



**Synthesis, Physicochemical and Atomistic  
Analysis of Templated Polymerisation in  
Metal-Organic Frameworks (MOFs)**

**Nimai Mehta**

Thesis submitted to Cardiff University for the degree of Doctor of Philosophy

September 2021

# Abstract

Metal-organic frameworks (MOFs) are porous three-dimensional coordination networks comprised of metal nodes that are covalently bound to organic linkers in an array. These materials are attractive due to their porosity and structural diversity. A variety of MOFs in the literature has been used as templates for polymerisation reaction, where MOFs act as hosts for guest monomers that then polymerise *in situ*, allowing synthesis of highly porous polymer networks. Many of the studies are focussed on achieving polymerisation under confinement, but there is a lack in understanding of the fundamental mechanistic interpretation of processes involved.

In this work, prototypical frameworks MOF-5 and HKUST-1 have been used as hosts for polymerising biocompatible and biodegradable monomers vinyl acetate, lactic acid, lactide, and  $\epsilon$ -caprolactone. A range of techniques have been used to characterise the MOFs, monomer@MOF, polymer@MOF composites, and polymers isolated from the MOFs. Characterisation of polymer@MOF composites by SEM confirmed intrinsic polymerisation, with typically 65 % conversion of monomer determined by  $^1\text{H-NMR}$  spectroscopy. Powder X-ray diffraction experiments showed an expansion of unit cell of both frameworks after monomer adsorption, followed by contraction after polymerisation.

For the vinyl acetate@MOF-5 system, guest specific binding, guest-framework interactions, polymerisation kinetics, and changes in local framework mobility have been investigated by *single crystal* X-ray diffraction, *solid-state* NMR, total neutron scattering, quasi-elastic neutron scattering and neutron spectroscopy. Experiments suggest binding of monomer at the MOF metal nodes, and close association with the linker groups, which are lost following polymerisation. Working with the Disordered Materials Group at ISIS Pulsed Neutron and Muon Source at Rutherford Appleton Laboratories (Oxfordshire, UK), the monomer@MOF composites were investigated in the first simulations of confined liquids in crystalline solid materials to be performed on the *Dissolve* simulation environment. The combination of simulation and experimental data has provided the first atomic-scale resolution of monomer@MOF composites.

## Summary of Chapters

Chapter 1 of the thesis introduces MOF structures, synthesis, and applications in hybrid materials and host template for polymer networks. Chapter 2 discusses the theory and background of templated polymerisation, and its significance towards influencing the goal of this project. It follows on to discuss the selection criteria, structure and properties of the host MOFs, MOF-5 and HKUST-1. A discussion of the polymers has also been covered in this chapter. In Chapter 3, a range of experimental techniques and characterisation methods have been discussed to show host-guest interactions and properties of polymer networks isolated from the host MOF.

In Chapter 4, it is shown that the pore filling of host with guest monomer results in expansion of unit cell dimensions of the MOF, observed through negative peak shifts in powder X-ray diffraction patterns. An opposite effect of framework contraction is observed during polymerisation of intrinsic guest monomers that result in an increase in *d*-spacing of the framework lattice. To confirm polymerisation, IR spectroscopy is used to confirm changes consistent with change in IR fingerprint observed by changes in vibrational frequencies through development of covalent bond structures and functional group identification. Thermal analyses have been carried out to determine the pore-filling content and compare the effect of confinement on the guest species. <sup>1</sup>H NMR spectroscopy has been employed to quantify polymer conversion and determine polymer characteristics through investigation of chemical structure and environment. Using SEM, changes in the MOF structure have been visually observed following guest adsorption and *in-situ* polymerisation. Other complementary techniques have been used to investigate differences between desolvated host and guest@host composites.

Vinyl acetate interactions in MOF-5 have been explored and polymerisation dynamics investigated by neutron scattering techniques have been discussed in Chapter 5. Total neutron scattering experiments at ISIS Pulsed Neutron and Muon Source have been performed to study monomer interaction and identify binding sites within the MOF-5 framework. Molecular dynamics and Monte-Carlo simulations have been performed using a new code

and simulation environment called '*Dissolve*' developed by the Disordered Materials Group at the ISIS Pulsed Neutron and Muon Source (Oxfordshire, UK). Simulations with confined liquid in crystalline materials is first of its kind to be performed using Dissolve. To further understanding of influence of guest species on the structure of MOF-5, QENS experiments were performed at the IRIS spectrometer (ISIS Pulsed Neutron and Muon Source).

Understanding of the guest motion and framework linker mobility was also an essential aim of this experiment. Complementary studies to determine polymerisation dynamics were subsequently carried out using  $^1\text{H}$ - $^{13}\text{C}$  *solid-state* NMR using cross-polarisation and high-powered decoupling methods to determine changes in guest mobility and kinetics of monomer conversion during the polymerisation process. *Single crystal* XRD was performed to map electron densities and determine structure of the guest@host composite.

Chapter 6 provides a brief summary of all the findings and probable conclusions from all characterisation methodologies used to understand the influence of guest adsorption on the host framework, characteristics of polymer synthesised by host-templated approach, identify interaction and binding of guest monomers, and determine the dynamics of the polymerisation reaction.

## Table of Contents

<b>List of Figures</b> .....	ii
<b>List of Tables</b> .....	xvi
<b>List of Schemes</b> .....	xix
<b>List of Abbreviations</b> .....	xx
<b>Contributions</b> .....	xxi
<b>Acknowledgements</b> .....	xxii
<b>1. Chapter 1: Introduction</b> .....	<b>1</b>
1.1 Metal-Organic Frameworks.....	2
1.2 Fundamentals of MOF Design.....	3
1.2.1 Secondary Building Units.....	3
1.2.2 Organic Linker.....	4
1.3 MOF Synthesis.....	6
1.3.1 Solvothermal and Hydrothermal.....	7
1.3.1.1 Effect of Temperature.....	8
1.3.1.2 Effect of Solvent.....	9
1.3.1.3 Effect of Modulators.....	9
1.3.2 Microwave Synthesis.....	11
1.3.3 Ultrasonic Synthesis.....	11
1.3.4 Electrochemical Synthesis.....	11
1.3.5 Mechanochemical Synthesis.....	12
1.4 Application.....	12
1.4.1 Gas Purification.....	13

## Table of Contents

1.4.2 Gas Separations.....	13
1.4.3 Gas Storage.....	15
1.4.4 Catalysis.....	17
1.4.5 Biological Applications.....	18
1.5 MOF Templated Polymerisation.....	20
1.5.1 Overview.....	20
1.5.2 Polymer Networks for Drug Delivery.....	23
1.6 Project Aims.....	25
1.7 Conclusion.....	27
1.8 References.....	29
<b>2. Chapter 2: Project Background.....</b>	<b>34</b>
2. Background Information on Key Materials.....	35
2.1 Metal-Organic Frameworks.....	35
2.1.1 MOF-5 (IRMOF-5) $[\text{Zn}_4\text{O}(\text{C}_8\text{H}_4\text{O}_4)_3]$ .....	35
2.1.2 HKUST-1 (MOF-199) $[\text{Cu}_3(\text{C}_9\text{H}_3\text{O}_6)_2]$ .....	42
2.2 Biodegradable Polymers.....	47
2.2.1 Polyvinyl Acetate – PVAc.....	48
2.2.2 Poly(Lactic Acid) – PLA.....	50
2.2.3 Poly( $\epsilon$ -caprolactone) – PCL.....	53
2.3 Conclusion.....	57
2.5 References.....	59

## Table of Contents

<b>3. Chapter 3: Methods</b> .....	<b>64</b>
3.1 Materials.....	65
3.2 Synthesis of Metal-Organic Frameworks (MOFs).....	65
3.2.1 Synthesis of HKUST-1 (MOF-199) .....	67
3.2.2 Synthesis of MOF-5 (IRMOF-1) .....,	68
3.2.2.1 H/D exchange of $\text{Zn}(\text{NO}_3)_2 \cdot 6\text{H}_2\text{O}$ for deuterated MOF synthesis.....	69
3.2.2.2 Synthesis of deuterated MOF-5 $[\text{Zn}_4\text{O}(\text{C}_8\text{D}_4\text{O}_4)_3]_n$ .....	69
3.2.2.3 Synthesis of H/D-MOF-5 $[\text{Zn}_4\text{O}(\text{C}_8\text{H}_x\text{D}_y\text{O}_4)_3]_n$ .....	70
3.3 Polymerisation of monomers in MOF pores. ....	70
3.3.1 Radical polymerisation of vinyl acetate in MOFs.....	70
3.3.2 Ring-opening polymerisation of $\epsilon$ -caprolactone in MOFs.....	71
3.3.3 Ring-opening polymerisation of D,L-Lactide.....	72
3.3.4 Condensation polymerisation of lactic acid.....	74
3.4 Framework Digestion and Polymer Isolation.....	75
3.5 Characterisation.....	75
3.5.1 Powder X-ray diffraction (PXRD).....	75
3.5.2 Nuclear Magnetic Resonance (NMR).....	77
3.5.3 Thermogravimetric Analysis (TGA).....	78
3.5.4 Infrared Spectroscopy.....	79
3.5.5 Mass Spectrometry.....	79
3.5.6 Gas Adsorption.....	81
3.5.7 Scanning Electron Microscopy (SEM).....	82

## Table of Contents

3.5.8 Gas Phase Chromatography (GPC).....	83
3.5.9 Other Methods.....	83
3.6 References.....	84
<b>4. Chapter 4: Characterisation and Analysis.....</b>	<b>87</b>
4.1 Scope.....	88
4.2 MOF-5.....	88
4.2.1 MOF-5: Powder X-Ray Diffraction.....	89
4.2.1.1 In-situ polymerisation: vinyl acetate in MOF-5.....	91
4.2.1.2 In-situ polymerisation: $\epsilon$ -Caprolactone in MOF-5.....	98
4.2.2 HKUST-1: Powder X-Ray Diffraction.....	101
4.2.2.1 In-situ polymerisation: vinyl acetate in HKUST-1.....	102
4.2.2.2 In-situ polymerisation: $\epsilon$ -caprolactone in HKUST-1.....	103
4.2.2.3 In-situ polymerisation: D,L-lactic acid and D,L-lactide in HKUST-1.....	105
4.3 IR Spectroscopy (ATR-FTIR).....	107
4.3.1 MOF-5 – FTIR Spectroscopy.....	107
4.3.1.1 Vinyl acetate polymerisation in MOF-5.....	110
4.3.1.2 $\epsilon$ -Caprolactone polymerisation in MOF-5.....	111
4.3.2 HKUST-1 – FTIR Spectroscopy.....	113
4.3.2.1 Vinyl acetate polymerisation in HKUST-1.....	114
4.3.2.2 $\epsilon$ -Caprolactone polymerisation in HKUST-1.....	115
4.4 Thermogravimetric Analysis (TGA).....	117
4.4.1 MOF-5 – TG and DTG Analysis.....	117

## Table of Contents

4.4.1.1 Vinyl acetate polymerisation in MOF-5.....	118
4.4.1.2 $\epsilon$ -Caprolactone Polymerisation in MOF-5.....	121
4.4.2 HKUST-1 – TG and DTG Analysis.....	123
4.4.2.1 Vinyl acetate polymerisation in HKUST-1.....	124
4.4.2.2 $\epsilon$ -Caprolactone Polymerisation in HKUST-1.....	126
4.4.2.3 D,L-Lactide Polymerisation in HKUST-1.....	128
4.5 NMR Analysis – Isolated Polymer.....	130
4.5.1 Poly(vinyl acetate) isolated from MOF – $^1\text{H}$ NMR.....	130
4.5.2 Poly(vinyl acetate) isolated from MOF – $^{13}\text{C}$ NMR.....	133
4.5.3 Poly( $\epsilon$ -Caprolactone) isolated from MOF – $^1\text{H}$ NMR.....	135
4.5.4 Poly( $\epsilon$ -Caprolactone) isolated from MOF – $^{13}\text{C}$ NMR.....	138
4.6 Mass Spectrometry.....	139
4.6.1 Poly(vinyl acetate) isolated from MOF.....	139
4.6.2 Poly( $\epsilon$ -Caprolactone) isolated from MOF.....	142
4.7 Emission Spectroscopy: ICP-AES.....	145
4.8 Adsorption Isotherms and BET Surface Area Analysis.....	145
4.8.1 MOF-5.....	146
4.8.2 HKUST-1.....	148
4.9 Scanning Electron Microscopy (SEM).....	150
4.9.1 MOF-5.....	150
4.9.2 Monomer@MOF-5 composite.....	152
4.9.3 Polymer@MOF-5 composite.....	154

## Table of Contents

4.9.4 HKUST-1.....	156
4.9.5 Monomer@HKUST-1 composite.....	157
4.9.6 Polymer@HKUST-1 composite.....	158
4.9.7 Isolated Polymer.....	159
4.10 Conclusions.....	161
4.11 References.....	164
<b>5. Chapter 5: Characterisation of Guest Interactions in VAc@MOF-5.....</b>	<b>167</b>
5.1 Total Neutron Scattering: Experimental Analysis (NIMROD).....	170
5.1.1 Diffraction Data Analysis.....	170
5.1.2 Calculations on MOF-5 Crystallographic Unit.....	172
5.2 Investigation of Vinyl Acetate Binding and Interaction in MOF-5.....	173
5.2.1 Materials and Sample Preparation.....	173
5.2.2 Monomer Addition.....	175
5.2.2.1 Vapour Deposition Method.....	175
5.2.2.2 Liquid Deposition Method – Monomer Addition.....	177
5.3 Results and Discussion.....	179
5.3.1 Calculation of number of guest molecules.....	179
5.3.2 Modelling of Experimental Data.....	180
5.3.2.1 Calculation of Bragg Peaks on <i>Dissolve</i> .....	181
5.3.2.2 Calculations for $G(r)$ .....	182
5.3.2.3 Implementing Forcefield on <i>Dissolve</i> .....	183
5.3.2.4 Building MOF-5 simulation box.....	184

## Table of Contents

5.3.2.5 General Atomistic Simulations .....	185
5.3.3 H- and D-MOF-5.....	186
5.3.4 Data Analysis: Monomer@MOF.....	188
5.3.4.1 h-VAc@H-MOF.....	189
5.3.4.2 h-VAc@D-MOF.....	189
5.3.4.3 Conclusions from h-VAc@MOF samples.....	193
5.3.4.4 d-VAc@D-MOF.....	194
5.3.4.5 d-VAc@H-MOF.....	196
5.3.4.6 Conclusions from d-VAc@MOF.....	197
5.4 Present Hypotheses and Future Outlook.....	197
5.5 Quasi-Elastic Neutron Scattering (QENS) Experiment.....	203
5.5.1 In-situ polymerisation of vinyl acetate monomer in MOF-5.....	203
5.5.1.1 Materials and Methods.....	203
5.5.1.2 Sample Containers.....	205
5.5.1.3 Experimental Samples.....	206
5.5.2 QENS Data Analysis – Underlying Theory.....	207
5.5.3 Results and Discussion.....	209
5.5.3.1 Elastic Fixed Window Scan (EFWS).....	209
5.5.3.2 EFWS: Observing MOF Dynamics.....	209
5.5.3.3 EFWS: Observing Guest Dynamics.....	211
5.5.3.4 Quasi-elastic Peak Fitting.....	213
5.5.3.5 Lorentzian Peak Area.....	214

## Table of Contents

5.5.3.6 Full Width at Half Maximum (FWHM).....	216
5.5.3.7 Elastic Incoherent Structure Factor (EISF).....	219
5.6 Conclusion of QENS Experiment.....	219
5.7 <sup>13</sup> C solid-state NMR analysis of VAc@MOF-5 Polymerisation.....	221
5.7.1 Sample Preparation.....	222
5.7.2 <sup>13</sup> C MAS NMR Experiments.....	223
5.7.3 <sup>1</sup> H- <sup>13</sup> C MAS NMR of MOF-5.....	224
5.7.4 Data Analysis and Fitting.....	228
5.7.5 Results and Discussion.....	230
5.7.5.1 Temperature Ramp Experiment.....	230
5.7.5.2 Polymerisation Experiment.....	232
5.8 Summary and Conclusion for Polymerisation.....	236
5.8.1 MOF Dynamics during Polymerisation.....	244
5.9 X-ray Structure Analysis.....	245
5.9.1 Powder XRD of <i>solid-state</i> NMR Samples.....	245
5.9.2 Single-crystal XRD (SCXRD).....	246
5.9.3 Conclusions from X-Ray Diffraction.....	248
5.10 Conclusions.....	250
5.11 References.....	254
<b>6. Chapter 6: Conclusions.....</b>	<b>257</b>
6.1 Conclusion .....	258
6.2 Future Work.....	263

**Table of Contents**

6.3 References..... 266

**Appendix..... 268**

## List of Figures

Fig 1.1: General representation of building blocks of metal organic frameworks.....**3**

Fig 1.2: Lattice structures (middle) and corresponding SBUs (metal nodes (left), and organic linkers (right)) of some of the MOFs discussed in this review. (Atom definition: blue – metal, red – oxygen, purple – nitrogen, grey – carbon, green – chlorine.).....**5**

Fig 1.3: Representation of the variety of linkers in the IRMOF family of MOFs. Yellow spheres indicate the void space in the crystal lattice. ....**6**

Fig 1.4: Overview of synthesis methods, possible reaction temperatures, and final reaction products in MOF synthesis. ....**8**

Fig 1.5: Adsorption isotherms of carbon dioxide on MIL-53(Cr) in comparison to carbon dioxide removal from flue gas by amine wash. ....**14**

Fig 1.6: H<sub>2</sub>-storage capacities for different MOFs (prototype trials). ....**16**

Fig 2.1: Reaction scheme for the synthesis of MOF-5 from zinc nitrate hexahydrate and terephthalic acid. The blue sphere in the MOF-5 structure is for visual aid depicting the spherical void space.....**36**

Fig 2.2: Magnification of the metal cluster and the organic linker from MOF-5 structure. The purple spheres represent five distinct sites for water adsorption and are labelled with Greek symbols. ....**40**

Fig 2.3: Reaction scheme for the synthesis of HKUST-1 from copper (II) nitrate trihydrate and trimesic acid. The yellow sphere in the HKUST-1 structure is for visual aid depicting the spherical void space, and the orange spheres depict the void space in the coordination sphere. Atoms: Blue – Cu; Red – O; Black – C. H-atom has been eliminated for clarity. ....**43**

## List of Figures

Fig 2.4: (a) Wireframe scheme for HKUST-1 framework viewed down the [100] direction, showing nanochannels with fourfold symmetry. (b) viewed along the cell body diagonal [111], showing a hexagonal-shaped 18 Å window at the intersection of the nanopores. Blue – Cu; Red – O; Black – C; H – Grey. ....**44**

Fig 2.6: Chemical structure diagrams of (a) vinyl acetate monomer (VAc) and (b) standard repeating unit of a poly(vinyl acetate) polymer. ....**48**

Fig 2.7: Approaches to obtain high molecular weight PLA. ....**50**

Fig 2.8: Chemical structure diagrams of  $\epsilon$ -caprolactone monomer ( $\epsilon$ -CL) and standard repeating unit of a poly( $\epsilon$ -caprolactone) polymer. ....**53**

Fig 3.1: Schematic of solvothermal autoclave (L) and image of an autoclave similar to the one used for MOF synthesis. ....**66**

Fig 4.1: PXRD pattern for synthesised MOF-5 (top) vs. simulated MOF-5 pattern (bottom) from CIF (CCDC: 175572). (\*' denoted additional peak arising from bound solvent DMF) ....**89**

Fig 4.2 PXRD patterns for as-synthesised MOF-5 (bottom) and interpenetrated MOF-5 synthesised by literature reported method (top).<sup>6</sup> Peaks corresponding to reflection planes are indexed, the pattern is baseline corrected (Section 3.5.1). Dashed lines indicate coordinated solvent peaks for corresponding MOF structures. ....**91**

Fig 4.3: PXRD pattern of synthesised MOF-5 (bottom), VAc@MOF-5 (middle), and PVAc@MOF-5 (top). Black arrows indicate the direction of shift for peak at 9.7° (Expansion for  $2\theta = 5-15^\circ$  range is shown in Appendix A4.3. The diffraction patterns shown are background subtracted) ....**92**

Fig 4.4: PXRD patterns of PVAc@MOF-5 from structural change–polymerisation time experiment. ....**95**

## List of Figures

Fig 4.5: MOF-5 crystallographic structure and corresponding Miller indices planes (200), (220), (400) and (420) responsible for diffraction peaks at  $2\theta = 6.9^\circ$ ,  $9.7^\circ$ ,  $13.7^\circ$ , and  $15.4^\circ$  respectively.....**97**

Fig 4.6 PXRD pattern of synthesised MOF-5 (bottom),  $\epsilon$ CL@MOF-5 (middle), and PCL@MOF-5 (top). (Expansion for  $2\theta = 5\text{--}15^\circ$  range is shown in Appendix A4.4. The diffraction patterns shown are background subtracted. PCL characteristic peak region is shown by black box) .....**99**

Fig 4.7 PXRD pattern of PCL@MOF-5, PCL isolated from PCL@MOF-5 (top), and PCL polymerised ex-situ (bottom). .....**100**

Fig 4.8: PXRD pattern for synthesised HKUST-1 (top) vs. simulated HKUST-1 pattern from CIF (CCDC: 112954) (bottom). .....**101**

Fig 4.9: PXRD patterns for HKUST-1 (bottom), VAc@HKUST-1 (middle), PVAc@HKUST-1 (top). (Expansion for  $2\theta = 5\text{--}15^\circ$  range is shown in Appendix A4.5. The diffraction patterns shown are background subtracted) .....**100**

Fig 4.10: PXRD patterns for HKUST-1 (top),  $\epsilon$ CL@HKUST-1 (middle), PCL@HKUST-1 (bottom). ( $2\theta = 5\text{--}20^\circ$  range expansion in Appendix A4.5. The diffraction patterns shown are background subtracted. PCL characteristic peak region is shown by black box,  $2\theta = 21.6^\circ$  and  $23.9^\circ$ ) .....**102**

Fig 4.11: PXRD pattern of PCL isolated from PCL@HKUST-1 (top), and PCL polymerised ex-situ (bottom). .....**103**

Fig 4.12 PXRD patterns for HKUST-1 (bottom), LAC@HKUST-1 (middle), PLAC@HKUST-1 (top). ( $2\theta = 5\text{--}14^\circ$  range expansion in Appendix A4.5. The diffraction patterns shown are background subtracted) .....**104**

## List of Figures

Fig 4.13 (a) ATR-FTIR spectrum of MOF-5 and H<sub>2</sub>BDC and (b) chemical bond structure of MOF-5 and contribution to the FTIR spectrum (*Schematic adapted and modified*).<sup>18</sup> (\* - 3650 cm<sup>-1</sup> from atmospheric water adsorption) .....**107**

Fig 4.14: ATR-FTIR spectra of MOF-5 (bottom), VAc@MOF-5 (middle) and PVAc@MOF-5 (top). Dashed green lines and corresponding arrows indicate changes in absorbance intensity with polymerisation. (Region between 2000–450 cm<sup>-1</sup> has been shown in Fig A4.8. The spectra have been normalised to  $\nu(\text{C}=\text{O})$  1350 cm<sup>-1</sup> absorbance peak of the MOF.) .....**109**

Fig 4.15: ATR-FTIR spectra of PVAc isolated from MOF-5 (top) and PVAc synthesised by ex-situ polymerisation (bottom). (The spectra have been normalised to the  $\nu(\text{C}=\text{O})$  of the MOF at 1350 cm<sup>-1</sup>) .....**110**

Fig 4.16: ATR-FTIR spectra of MOF-5,  $\epsilon\text{CL@MOF-5}$  and PCL@MOF-5. Dashed green lines and corresponding arrows indicate changes in absorbance intensity with polymerisation. (Region between 2000–450 cm<sup>-1</sup> has been shown in Fig A4.9. The spectra have been normalised to  $\nu(\text{C}=\text{O})$  of the MOF at 1350 cm<sup>-1</sup>) .....**111**

Fig 4.17: ATR-FTIR spectra of PCL isolated from MOF-5 and PCL synthesised by ex-situ polymerisation. ....**112**

Fig 4.18 (a) ATR-FTIR spectrum of HKUST-1 and H<sub>3</sub>BTC and (b) chemical bond structure of MOF-5 and contribution to the FTIR spectrum.....**113**

Fig 4.19: ATR-FTIR spectra of HKUST-1 (bottom), VAc@HKUST-1 (middle) and PVAc@HKUST-1 (top). Dashed green lines and corresponding arrows indicate changes in absorbance intensity with polymerisation. (Region between 2000–450 cm<sup>-1</sup> has been shown in Fig A4.10. The spectra have been normalised to  $\nu(\text{C}=\text{O})$  of the MOF at 1369 cm<sup>-1</sup>.) .....**114**

## List of Figures

Fig 4.20: ATR-FTIR spectra of HKUST-1 (bottom),  $\epsilon$ CL@HKUST-1 (middle) and PCL@HKUST-1 (top). Dashed green lines and corresponding arrows indicate changes in absorbance intensity with polymerisation. (Region between 2000–450  $\text{cm}^{-1}$  has been shown in Fig A4.11. The spectra have been normalised to  $\nu(\text{C}=\text{O})$  1369  $\text{cm}^{-1}$  absorbance peak of the MOF.) .....115

Fig 4.21: ATR-FTIR spectra of PCL isolated from HKUST-1 (top) and PCL synthesised ex-situ polymerisation (bottom). .....116

Fig 4.22: TGA profiles for empty MOF-5, VAc@ MOF-5, and PVAc@MOF-5. Regions I, II, and III correspond to the regions for vaporisation of moisture and surface species; removal of intrinsic and bound guest; and thermal decomposition of MOF-5, respectively. All samples were run under air. ....119

Fig 4.23: TGA profiles for empty MOF-5,  $\epsilon$ CL@MOF-5, and PCL@MOF-5. Regions I, II, and III correspond to the regions for vaporisation of moisture and surface species; removal of intrinsic and bound guest; and thermal decomposition of HKUST-1, respectively. All samples were run under air. ....121

Fig 4.24: TGA profiles for empty HKUST-1, VAc@HKUST-1, and PVAc@HKUST-1. Regions I, II, and III correspond to the regions for vaporisation of moisture and surface species; removal of intrinsic and bound guest; and thermal decomposition of HKUST-1, respectively. All samples were run under air. ....124

Fig 4.25: TGA profiles for empty HKUST-1,  $\epsilon$ CL@HKUST-1, and PCL@HKUST-1. Regions I, II, and III correspond to the regions for vaporisation of moisture and surface species; removal of intrinsic and bound guest; and thermal decomposition of HKUST-1, respectively. All samples were run under air. ....126

## List of Figures

Fig 4.26: TGA profiles for empty HKUST-1 and PLAC@HKUST-1. Regions I, II, and III correspond to the regions for vaporisation of moisture and surface species; removal of intrinsic and bound guest; and thermal decomposition HKUST-1, respectively. All samples were run under air.....**128**

Fig 4.27:  $^1\text{H}$  NMR spectra of (a) isolated PVAc from HKUST-1 (b) isolated PVAc from MOF-5 and (c) linear polymer PVAc. Detailed spectral assignments are shown in appendix A4.21. ....**131**

Fig 4.28:  $^{13}\text{C}$  NMR spectra of isolated PVAc from MOF-5. PVAc isolated from HKUST-1:  $^{13}\text{C}$  NMR (400 MHz,  $\text{CDCl}_3$ ): 19 ( $\text{CH}_3$ ); 31 ( $\text{CH}_2$ ); 65 ( $\text{CH}$ ), 171 ( $-\text{COO}$ ); PVAc isolated from MOF-5:  $^{13}\text{C}$  NMR (400 MHz,  $\text{CDCl}_3$ ): 19 ( $\text{CH}_3$ ); 31 ( $\text{CH}_2$ ); 65 ( $\text{CH}$ ), 171 ( $-\text{COO}$ ) .....**133**

Fig 4.29:  $^1\text{H}$  NMR spectra of (a) isolated PCL from HKUST-1 (b) isolated PCL from MOF-5 and (c) linear polymer PCL. ....**136**

Fig 4.30:  $^{13}\text{C}$  NMR spectra of PCL isolated from HKUST-1:  $^{13}\text{C}$  NMR (400 MHz,  $\text{CDCl}_3$ ): 24.6 ( $^a\text{CH}_2$ ); 25.5 ( $^b\text{CH}_2$ ); 28.3 ( $^c\text{CH}_2$ ), 34.1 ( $^d\text{CH}_2$ ), 64.49 ( $^e\text{CH}_2\text{O}$ ), 173.90 ( $\text{C}=\text{O}$ ) ppm. ....**138**

Fig 4.31: ESI GC-MS spectrum of isolated PVAc from HKUST-1.....**140**

Fig 4.32: MALDI-TOF spectrum of isolated PVAc from HKUST-1.....**140**

Fig 4.33: ESI GC-MS spectrum of isolated PVAc from MOF-5.....**141**

Fig 4.34: MALDI-TOF spectrum of isolated PVAc from MOF-5.....**141**

Fig 4.35: LC-MS spectrum of isolated PCL from HKUST-1.....**142**

Fig 4.36: MALDI-TOF spectrum of isolated PCL from HKUST-1.....**143**

## List of Figures

Fig 4.37: LC-MS spectrum of isolated PCL from MOF-5.....144

Fig 4.38: MALDI-TOF spectrum of isolated PCL from MOF-5.....144

Fig 4.39: N<sub>2</sub> adsorption isotherm for MOF-5 (black), PVAc@MOF-5 (red), and PCL@MOF-5 (blue) recorded at 77 K. ....146

Fig 4.40: N<sub>2</sub> adsorption isotherm for HKUST-1 (black) and PCL@HKUST-1 (blue). ....158

Fig 4.41: SEM images of crystalline MOF-5. (a) cubic shaped crystals of MOF-5, (b,c) agglomerates of cubic MOF-5 (d) sheet-like morphology of MOF-5 before synthesis optimisation. ....150

Fig 4.42: SEM images of monomer@MOF-5. (a-b) VAc@MOF-5 and (c-d) εCL@MOF-5. ....152

Fig 4.43: SEM images of polymer@MOF-5. (a) PVAc@MOF-5 at 0.4 g/g MOF loading, (b) PVAc@MOF-5 at an excess loading of 0.6g/g MOF. ....154

Fig 4.44: SEM images of polymer@MOF-5. (a) PCL@MOF-5 at 0.4 g/g MOF loading, (b) PCL@MOF-5 at an excess loading of 0.6g/g MOF.....155

Fig 4.45: SEM images of polymer@MOF-5 protrusions on. (a) PVAc@MOF-5 and (b) PCL@MOF-5 at an excess loading of 0.6g/g MOF (Magnification – x600).....155

Fig 4.46: SEM images of crystalline HKUST-1. (a) Octahedral crystals of HKUST-1 (b) aggregated crystallites of HKUST-1 upon excess moisture adsorption. ....156

Fig 4.47: SEM images of monomer@HKUST-1. (a) VAc@HKUST-1, (b) εCL@HKUST-1. ....157

## List of Figures

Fig 4.58: SEM images of in-situ polymerised monomer@HKUST-1. (a,b) PVAc@MOF-5 and (c,d) PCL@HKUST-1 at 0.4 g/g MOF loading. ....**158**

Fig 4.51: SEM images of (a) isolated PVAc from MOF-5, (b) isolated PCL from HKUST-1, (c) isolated PLAC from HKUST-1. ....**160**

Fig 5.1: Crystallographic MOF-5 unit cell. Only the atoms within the dotted blue line have been shown and considered to be in the unit cell, full linkers have been shown to aid visual representation. ....**172**

Fig 5.2: Schematic diagram of monomer addition by vapour deposition method. (Insets – Photographic image of cell container, monomer reservoir, and vacuum operated–vapour deposition system.) ....**175**

Fig 5.3: (a) Schematic diagram of monomer addition by liquid deposition method. (b) Photographic image of cell container with Swagelok and air-tight vacuum seal. ....**177**

Fig 5.4: Atomic structure of crystalline MOF-5 from simulation environment in Dissolve for empty MOF with solvent DMF and water. ....**184**

Fig 5.5: Atomic structure of crystalline MOF-5 from simulation environment in Dissolve for monomer@MOF without solvent (shown here is the h-monomer@H-MOF-5 sample with 414 monomer molecules per simulation box or 52 molecules/unit MOF cell loading before simulation) ....**184**

Fig 5.6: Comparison of powder XRD and TNS patterns for (a) H-MOF-5 and (b) D-MOF-5. (c) total structure factor  $F(Q)$  and (d) total pair distribution function  $G(r)$  for H- and D-MOF. ....**186**

## List of Figures

Fig 5.7: The experimental and calculated (a) total structure factor  $F(Q)$  and (b) total pair distribution function  $G(r)$  for h-VAc@H-MOF. Comparison between empty H-MOF and h-VAc@H-MOF (c) total structure factor  $F(Q)$  and (b) total pair distribution function  $G(r)$ .  
.....189

Fig 5.8: The experimental and calculated (a) total structure factor  $F(Q)$  and (b) total pair distribution function  $G(r)$  for h-VAc@D-MOF. Comparison between empty H-MOF and h-VAc@H-MOF (c) total structure factor  $F(Q)$  and (b) total pair distribution function  $G(r)$ .  
.....191

Fig 5.9: The experimental and calculated (a) total structure factor  $F(Q)$  and (b) total pair distribution function  $G(r)$  for d-VAc@D-MOF. Comparison between empty D-MOF and d-VAc@D-MOF (c) total structure factor  $F(Q)$  and (b) total pair distribution function  $G(r)$ .  
.....194

Fig 5.10: The experimental and calculated (a) total structure factor  $F(Q)$  and (b) total pair distribution function  $G(r)$  for d-VAc@D-MOF. Comparison between empty D-MOF and d-VAc@D-MOF (c) total structure factor  $F(Q)$  and (b) total pair distribution function  $G(r)$ .  
.....196

Fig 5.11: A comparison between simulation ensemble used during (a) preliminary simulations and (b) after introduction of disorder following simulated heating at 443 K.  
.....198

Fig 5.12: Schematic diagram of sample containers used for investigation of in-situ polymerisation of monomer@MOF-5 experiment by neutron spectroscopy on the IRIS instrument. ....205

Fig 5.13: EFWS of empty H-MOF and d-guest@H-MOF plotted as (a) absolute elastic intensity versus temperature, and as (b) normalised to elastic intensity measurement at 15 K versus temperature. ....210

## List of Figures

Fig 5.14: EFWS of empty D-MOF and h-guest@D-MOF plotted as (a) absolute elastic intensity versus temperature, and as (b) normalised to elastic intensity measurement at 15 K versus temperature. (The discrepancy between two data points at 260 K for oligomer@MOF-5 sample is due to recording measurements in two different times. Measurements at temperature 0–260 K were recorded two months prior to final 260–320 K measurements due to scheduled maintenance of the IRIS instrument) .....**212**

Fig 5.15: Height of Lorentzian peak vs Q for guest@MOF. (The Q dependence of scattering intensity for D-MOF, H-Monomer@D-MOF and H-Oligomer@D-MOF have not been fitted to Lorentzian model, shown here as a reference only). .....**215**

Fig 5.16: The Q dependence of the widths (FWHM) of the Lorentzian peaks for empty MOF and guest@MOF. (The inconsistency in data beyond  $Q = 1.7 \text{ \AA}^{-1}$  is due to weak signal at higher Q derived from the instrument detector for H-Monomer@D-MOF and H-Oligomer@D-MOF). .....**217**

Fig 5.17:  $^1\text{H}$ - $^{13}\text{C}$  MAS NMR spectrum of MOF-5 (a) CP and (b) HPDEC. ....**224**

Fig 5.18: (a) The  $2 \times 2 \times 2$  unit cell of MOF-5 formed by four A- and four B-subcells. (b) single crystallographic unit cell of MOF-5. ....**225**

Fig 5.19:  $^1\text{H}$ - $^{13}\text{C}$  MAS NMR spectrum of VAc@MOF-5 (a) CP and (b) HPDEC. The box (dotted lines) indicate key regions of the spectra, as described in the text. ....**226**

Fig 5.20:  $^1\text{H}$ - $^{13}\text{C}$  MAS NMR spectrum of PVAc@MOF-5 (a) CP and (b) HPDEC. The box (dotted lines) indicate key regions of the spectra, as described in the text. ....**227**

Fig 5.21:  $^{13}\text{C}$  CP MAS NMR spectrum of VAc@PVAc at set temperatures during the temperature ramp step.  $^{13}\text{C}$  NMR:  $\delta = 19$  ppm ( $\text{CH}_3$  – Monomer/Polymer), 31 and 38 ppm ( $\text{CH}_2$  – Polymer), 97 ppm ( $\text{CH}_2$  – Monomer), 128 ppm ( $\text{C}_1, \text{C}_2$  – MOF), 136 ppm ( $\text{C}_3$  – MOF), 138 ppm ( $\text{C}_4$  – MOF), 141 ppm ( $\text{CH}$  – Monomer), 168-170 ppm ( $\text{C}_5$  – MOF). ....**231**

## List of Figures

Fig 5.22:  $^{13}\text{C}$  (a) CP and (b) HPDEC exponential fits of peak integral values for all resonance peaks. (Blue and red crosses indicate the integral values and black lines indicate the fit.)

.....233

Fig 5.23:  $^{13}\text{C}$  (a) CP and (b) HPDEC exponential fits of peak integral values for resonance peak at 19 ppm. (Blue crosses indicate the integral values fit to exponential fit – black lines)

.....235

Fig 5.24:  $^{13}\text{C}$  (a, b) CP and (c, d) HPDEC exponential fits of peak integral values for resonance peak at 31 and 38 ppm. (Blue crosses indicate the integral values fit to exponential fit – black lines) .....236

Fig 5.25: 2D contour plots of  $^{13}\text{C}$  (a) CP and (b) HPDEC spectrum over the experiment time of 72 h. Black box with dotted line shows the region of development of methine signal from the polymer over time. ....238

Fig 5.26:  $^{13}\text{C}$  (a) CP and (b) HPDEC exponential fits of peak integral values for resonance peak at 19 ppm. (Blue crosses indicate the integral values fit to exponential fit – black lines)

.....239

Fig 5.27:  $^{13}\text{C}$  (a) CP and (b) HPDEC exponential fits of peak integral values for resonance peak at 141 ppm. (Blue crosses indicate the integral values fit to exponential fit – black lines)

.....240

Fig 5.28:  $^{13}\text{C}$  (a) CP and (b) HPDEC exponential fits of peak integral values for resonance peak at 168-171 ppm. (Blue crosses indicate the integral values fit to exponential fit – black lines) .....242

Fig 5.29:  $^{13}\text{C}$  (a) CP and (b) HPDEC exponential fits of peak integral values for MOF peaks at 168-171 ppm ( $\text{C}_4$ ). (Blue crosses indicate the integral values fit to exponential fit – black lines) .....244

## List of Figures

Fig 5.30: PXRD pattern for (a) MOF-5, VAc@MOF-5, PVAc@MOF-5 and PVAc@MOF-5 (L). Here PVAc@MOF-5 (L) is the sample polymerised during the solid-state NMR experiment.....**246**

Fig 5.31: Crystal structure of VAc@MOF-5 determined by SCXRD. The network atoms are depicted by solid sticks, whereas guest monomer molecules are represented by red (oxygen) and grey (carbon) stick/solid surfaces. Only partial MOF-5 framework has been shown for clarity.....**247**

Fig 5.32: Comparison of PXRD pattern of synthesised VAc@MOF-5 versus simulated powder pattern of VAc@MOF-5 following SCXRD analysis on the same sample. (Blue asterisks show additional peaks on the simulated pattern below  $2\theta = 20^\circ$  that is otherwise not present in the experimental PXRD).....**249**

Fig A4.1: PXRD pattern with  $2\theta = 5-11^\circ$  range expansion for synthesised MOF-5, VAc@MOF-5, and PVAc@MOF-5. ...**274**

Fig A4.2: PXRD pattern with  $2\theta = 11-15^\circ$  range expansion for synthesised MOF-5, VAc@MOF-5, and PVAc@MOF-5. ...**275**

Fig A4.3: PXRD pattern with  $2\theta = 5-15^\circ$  range expansion for synthesised MOF-5, VAc@MOF-5, and PVAc@MOF-5. (The diffraction patterns shown are background subtracted) ...**276**

Fig A4.4: PXRD pattern with  $2\theta = 5-15^\circ$  range expansion for synthesised MOF-5,  $\epsilon$ CL@MOF-5, and PCL@MOF-5. (The diffraction patterns shown are background subtracted) ...**277**

Fig A4.5: PXRD pattern with  $2\theta = 5-15^\circ$  range expansion for synthesised HKUST-1, VAc@HKUST-1, and PVAc@HKUST-1. (The diffraction patterns shown are background subtracted) ...**278**

## List of Figures

Fig A4.6: PXRD pattern with  $2\theta = 5\text{--}20^\circ$  range expansion for synthesised HKUST-1,  $\epsilon\text{CL@HKUST-1}$ , and PCL@HKUST-1. (The diffraction patterns shown are background subtracted) ...**279**

Fig A4.7: PXRD pattern with  $2\theta = 5\text{--}14^\circ$  range expansion for synthesised HKUST-1, LAC@HKUST-1, and PLAC@HKUST-1. (The diffraction patterns shown are background subtracted) ...**280**

Fig A4.8: ATR-FTIR spectra of MOF-5, VAc@MOF-5 and PVAc@MOF-5. Region between  $2000\text{--}450\text{ cm}^{-1}$ . Dashed green lines and corresponding arrows indicate changes in absorbance intensity with polymerisation. (The spectra have been normalised to  $\nu(\text{C=O})$   $1350\text{ cm}^{-1}$  absorbance peak of the MOF.) ...**281**

Fig A4.9: ATR-FTIR spectra of MOF-5,  $\epsilon\text{CL@MOF-5}$  and PCL@MOF-5. Region between  $2000\text{--}450\text{ cm}^{-1}$ . Dashed green lines and corresponding arrows indicate changes in absorbance intensity with polymerisation. (The spectra have been normalised to  $\nu(\text{C=O})$   $1350\text{ cm}^{-1}$  absorbance peak of the MOF.) ...**282**

Fig A4.10: ATR-FTIR spectra of HKUST-1, VAc@HKUST-1 and PVAc@HKUST-1. Region between  $2000\text{--}450\text{ cm}^{-1}$ . Dashed green lines and corresponding arrows indicate changes in absorbance intensity with polymerisation. (The spectra have been normalised to  $\nu(\text{C=O})$   $1350\text{ cm}^{-1}$  absorbance peak of the MOF.) ...**283**

Fig A4.11: ATR-FTIR spectra of HKUST-1,  $\epsilon\text{CL@HKUST-1}$  and PCL@HKUST-1. Region between  $2000\text{--}450\text{ cm}^{-1}$ . Dashed green lines and corresponding arrows indicate changes in absorbance intensity with polymerisation. (The spectra have been normalised to  $\nu(\text{C=O})$   $1350\text{ cm}^{-1}$  absorbance peak of the MOF.) ...**284**

Fig A4.12: TGA and DTGA profile of VAc@MOF-5 under air flow. (*The 1<sup>st</sup> order DTGA profile is smoothed to weighted average of 10 points equivalent to  $0.01^\circ\text{C}$* ). ...**285**

Fig A4.13: TGA and DTGA profile of PVAc@MOF-5 under air flow. (*The 1<sup>st</sup> order DTGA profile is smoothed to weighted average of 10 points equivalent to 0.01 °C*). ...**286**

Fig A4.14: TGA and DTGA profile of εCL@MOF-5 under air flow. (*The 1<sup>st</sup> order DTGA profile is smoothed to weighted average of 10 points equivalent to 0.01 °C*). ...**287**

Fig A4.15: TGA and DTGA profile of PCL@MOF-5 under air flow. (*The 1<sup>st</sup> order DTGA profile is smoothed to weighted average of 10 points equivalent to 0.01 °C*). ...**288**

Fig A4.16: TGA and DTGA profile of VAc@HKUST-1 under air flow. (*The 1<sup>st</sup> order DTGA profile is smoothed to weighted average of 10 points equivalent to 0.01 °C*). ...**289**

Fig A4.17: TGA and DTGA profile of PVAc@HKUST-1 under air flow. (*The 1<sup>st</sup> order DTGA profile is smoothed to weighted average of 10 points equivalent to 0.01 °C*). ...**290**

Fig A4.18: TGA and DTGA profile of PLAC@HKUST-1 under air flow. (*The 1<sup>st</sup> order DTGA profile is smoothed to weighted average of 10 points equivalent to 0.01 °C*). ...**291**

Fig A4.19: TGA and DTGA profile of εCL@HKUST-1 under air flow. (*The 1<sup>st</sup> order DTGA profile is smoothed to weighted average of 10 points equivalent to 0.01 °C*). ...**292**

Fig A4.20: TGA and DTGA profile of PCL@HKUST-1 under air flow. (*The 1<sup>st</sup> order DTGA profile is smoothed to weighted average of 10 points equivalent to 0.01 °C*). ...**293**

Fig A4.21: <sup>1</sup>H NMR spectra of PVAc isolated from MOF. Regions between 1.6 – 2.1 ppm have been expansion to show curve fitting and integral analysis. ...**294**

Fig A4.22: <sup>1</sup>H NMR spectra of PVAc isolated from MOF with detailed assignments. ...**295**

Fig A4.23: <sup>1</sup>H NMR spectra of PCL isolated from MOF with detailed assignments. ...**296**

Fig A5.1: <sup>1</sup>H-<sup>13</sup>C MAS NMR spectrum of MOF-5 (a) CP and (b) HPDEC. Expansion of the range 120 – 180 ppm is shown....**300**

## List of Tables

Table 1.1: Size determination of Zr-bdc MOFs from synthesis carried out in presence of benzoic acid as a modulator.....**10**

Table 2.1: A summary of structural, thermal, hydrogen isotherm properties for MOF-5. The data has been averages over literature review of most consistent values for 20 studies that use solvothermal synthesis. ....**37, 38**

Table 2.2: Location of each type of adsorption site depicted with the number of water molecules adsorbed. ....**41**

Table 3.1: Matrix, solvent and matrix-analyte concentration used for their MALDI analysis of polymer. ....**80**

Table 3.2: Elements analysed for the ICP-AES. ....**81**

Table 4.1: Sample identification and corresponding time of polymerisation for polyvinyl acetate in-situ polymerisation in MOF-5. ....**93**

Table 4.2: Characteristic diffraction peaks, corresponding Miller index plane and *d*-spacing for MOF-5. ....**94**

Table 4.3: Percentage mass loss of the observed in regions I, II and III from TGA profiles for empty HKUST-1, VAc@HKUST-1, and PVAc@HKUST-1 ....**125**

Table 4.4: Percentage mass loss of the observed in regions I, II and III from TGA profiles for empty HKUST-1, εCL@HKUST-1, and PCL@HKUST-1 ....**127**

Table 4.5: <sup>1</sup>H NMR conversion for templated PVAc determined by integral analysis. (Calculated using method described in Section 3.5.2) ....**132**

Table 4.6: <sup>1</sup>H NMR conversion for templated PCL determined by integral analysis. (Calculated using method described in Section 3.5.2) ....**136**

## List of Tables

Table 4.7: Measured concentrations of sodium (Na) and metal ions ( $M = \text{Cu}^{2+}$  for HKUST-1;  $\text{Zn}^{2+}$  for MOF-5) by ICP-AES. ....**145**

Table 4.8: Calculated BET surface area and maximum pore volume values for MOF-5. ....**147**

Table 4.9: Calculated BET surface area and maximum pore volume values for HKUST-1.....**149**

Table 5.1: Details of container and mass content of MOF in each container. (\* - H/D-MOF is 1:1 physical mixture of deuterated and hydrogenated reactants. Synthesis is described in section 3.2.2.3) .....**174**

Table 5.2: Comparison of calculated number of molecules of monomer per unit cell of MOF-5 in each sample container. (50/50-Monomer is an equimolar sample of hydrogenated and deuterated monomer prepared by physical mixing) .....**174**

Table 5.3: Comparison of Bragg reflections observed through PXRD and TNS. ....**187**

Table 5.4: Sample list and numbers for the neutron spectroscopy experiment. ....**206**

Table 5.5:  $^{13}\text{C}$  CP MAS NMR exponential fit  $R^2$  values with corresponding decay time and rate constants. ....**234**

Table 5.6:  $^{13}\text{C}$  HPDEC MAS NMR exponential fit  $R^2$  values with corresponding decay time and rate constants. ....**234**

Table 5.7: Estimated percentage conversion from Avrami-Erofeev equation compared to conversation values calculated from TGA and  $^1\text{H}$  NMR.....**240**

## List of Tables

Table 5.8: Estimated percentage conversion from Avrami-Erofeev equation compared to conversation values calculated from TGA (Section 4.4) and <sup>1</sup> H NMR (Section 4.5) .....	<b>241</b>
Table A2.1: Properties of Poly(vinyl acetate).....	<b>269, 270</b>
Table A2.2: Properties of Poly(lactic acid).....	<b>271, 272</b>
Table A2.3: Properties of Poly(ε-caprolactone)...	<b>273, 274</b>
Table A4.24: Characteristic absorbance bands and their assignments for MOF-5.....	<b>296</b>
Table A4.25: Characteristic absorbance bands and their assignments for PVAc. ....	<b>297</b>
Table A4.26: Characteristic absorbance bands and their assignments for PCL. ....	<b>297</b>
Table A4.27: Characteristic absorbance bands and their assignments for HKUST-1. ....	<b>298</b>
Table A4.28: ICP-AES analysis of isolated polymers from polymer@HKUST-1 composite. ....	<b>298</b>
Table A4.29: ICP-AES analysis of isolated polymers from polymer@MOF-5 composite.....	<b>299</b>
Table A5.1: Physical parameters of the flat-plate containers.....	<b>296</b>

## List of Schemes

Scheme 3.1: Schematic diagram of copper(II) nitrate reaction with trimesic acid to form HKUST-1. ....**67**

Scheme 3.2: Schematic diagram of zinc (II) nitrate reaction with terephthalic acid to form MOF-5. ....**68**

Scheme 3.3: Schematic for the reaction pathway for polymerisation of vinyl acetate to polyvinyl acetate. ....**71**

Scheme 3.4: Schematic for the reaction pathway for polymerisation of  $\epsilon$ -caprolactone to poly( $\epsilon$ -caprolactone). ....**72**

Scheme 3.5: Schematic for reaction mechanism of D,L-lactide to poly(lactic acid). ....**73**

Scheme 3.6: Schematic for reaction pathway of lactic acid to poly(lactic acid). ....**74**

Scheme 5.1: Steps in diffraction data analysis with Gudrun for reducing total scattering data. ....**161**

## List of Abbreviations

### *Materials*

MOF	Metal-organic frameworks
$\epsilon$ CL	$\epsilon$ -Caprolactone
HKUST	Hong Kong University of Science and Technology
IRMOF	Isorecticular metal-organic framework
LA	Lactic Acid
LAC	Lactide
MIL	Materials Institut Lavoisier
PVAc	Poly(vinyl acetate)
PCL	Poly( $\epsilon$ -caprolactone)
PLA	Poly(lactic acid)
PLAC	Poly(lactide)
SBU	Secondary building unit
UiO	Universitetet i Oslo
VAc	Vinyl acetate
ZIF	Zeolite imidazolate framework

### *Reaction*

AIBN	Azobisisobutyronitrile
BDC	Benzene dicarboxylate
BTC	Benzene tricarboxylate
DEF	Diethylformaide
DMF	N,N-dimethylformamide
HCl	Hydrochloric acid
THF	Tetrahydrofuran
Sn(II)Oct	Stannous (II) ethylhexanoate

### *Methods*

ATR-FTIR	Attenuated total reflectance Fourier-transform infrared spectroscopy
BET	Brunauer, Emmett and Teller
CP	Cross-polarisation
DTGA	Differential thermogravimetric analysis
DFT	Density functional theory

## List of Abbreviations

EFWS	Elastic Fixed Window Scan
FT	Fourier transform
FTIR	Fourier-transform infrared spectroscopy
FWHM	Full-width at half maximum
GPC	Gas phase chromatography
GC-MS	Gas chromatography – Mass spectrometry
HPDEC	High-powered decoupling
ICP-AES	Inductively coupled plasma atomic emission spectrometry
LC-MS	Liquid chromatography – Mass spectrometry
MALDI	Matrix assisted laser desorption/ionization
MALDI-TOF	Matrix assisted laser desorption/ionization Time-of-flight
MAS	Magic angle spinning
MC	Monte Carlo
MD	Molecular dynamics
MS	Mass spectrometry
NMR	Nuclear magnetic resonance
PXRD	Powder X-ray diffraction
QENS	Quasi-elastic neutron scattering
SEM	Scanning electron microscopy
SCXRD	Single Crystal XRD
TGA	Thermogravimetric Analysis
TNS	Total neutron scattering
UV	Ultraviolet
UV/vis	Ultraviolet – visible
XRD	X-ray diffraction

## Contributions

I would like to acknowledge the scientific contributions to the work described in this thesis.

The total neutron scattering experiment, I cannot thank Dr Thomas Headen and Dr Tristan Youngs (Disordered Materials Group – NIMROD at ISIS Pulsed Neutron and Muon Source, RAL, Oxfordshire, UK) enough for their efforts and guidance during the experiment, data analysis and simulation. They have dedicated much of their time to this study and at times, have gone above and beyond to deal with the complex system we had and tutoring me for using *Gudrun* and *Dissolve*. Dr Youngs was key in initial development of *Dissolve*, which allowed us to study confined liquids in MOF. Dr Headen spent most of the workday to help us make progress with the data analysis. I would also like to thank Calum Green (STFC Liquid Structure Simulation Placement Student, Imperial College London) for his time and work described in Chapter 5. The experiment was performed with Dr Craig James, whose help and guidance were invaluable.

For the QENS experiment, I would like to thank Dr Ian Silverwood (The IRIS instrument at ISIS Pulsed Neutron and Muon Source, RAL, Oxfordshire, UK) for performing the experiment to allow us to have the vital data from the experiment during scheduled maintenance closures, and amidst restrictions during COVID-19 global pandemic. Dr Silverwood ran our experiment after it had been cancelled or postponed indefinitely himself and I will never be able to appreciate him enough. He performed the following data analysis which allowed us to reach to the conclusions from the QENS experiment.

I would like to thank Dr Nia Richards (Cardiff University) for her help with the *solid-state* NMR experiment for repeatedly running our experiment and being a friend when experiment initially did not show what we expected. Dr Colan Hughes' (Cardiff University) input and expertise was invaluable in understanding the results from the experiment. Dr Hughes also did many of the integral calculations along-side so that the calculations were accurate.

I would also like to thank Dr Lauren Hatcher (Royal Society University Research Fellow, Cardiff University) for the *single-crystal* XRD experiments and data analysis with her expertise in crystallography.

## Acknowledgements

I have truly enjoyed my time as a PhD student at Cardiff School of Chemistry, Cardiff University and have made many friends along the way.

First, I would like to thank my amazing supervisors, Dr Alison Paul and Dr Timothy Easun. The both of you have been an inspiration both in my academic life and outside. I have learnt so much along the way and seen myself grow as a researcher with your guidance and encouragement. Dr Paul, thank you for being so kind and supportive of me during the years and allowing me to have many fantastic research opportunities during my PhD. Your support in my weightlifting has also been an important part for my progress in the sport. Dr Easun, thank you too for your kindness over the years and allowing me to be a member of your family in the Christmas of 2020 when I could not go home. Those memories will always be cherished. The depth of knowledge and the work ethic you both have; I hope can be as good as you some day. I could not have asked for better supervisors. “One more thing!”, neutrons are cooler than photons.

A big thank you for Alex and Corey for being the great friends and welcoming me with open arms in the research group. Your support and friendship have been invaluable. Thank you for the barbeque dinners, board games, listening to my rants on the phone, and your advice in all parts of the life. I have made a friendship to last a lifetime.

I would also like to thank Dan, Dom, and Josh for the support and laughs in the lab and in group meetings. Having group members like you made things better. Thank you, Chris, for running my PXRD samples when in need! I would also like to thank the staff at School of Chemistry (technical and admin) for all their help during my PhD and providing a safe working environment during COVID-19.

Another huge thank you to everyone at Synergi Weightlifting club (Matt, Verity, Elin, Ellie, Stu) for making me one of your own. I came in as just another student, and I have stayed there as the ‘top fan’ and part of the family. I would also like to convey a huge thank you to Fil for being the best, kindest, and the most hard working and supportive friend. Your support with my PhD and weightlifting alike has been monumental. Thank you Ania for being the

most amazing coach, friend, and mentor. Your advice and kindness have made me a better in every path of life (except at virtual competitions). Thank you to everyone at Synergi!

Finally, I would like to thank my parents for their continued support throughout my life in working towards what I always dreamt of. Your encouragement and support have been the reason I am what I am today. And, finally, Kanhai – I can't express in words what a big support you have been over the years. Thank you for believing in me when I didn't and encouraging me in pursuing my dreams. I am fortunate to have you as my brother.

*Dedicated to my parents  
and my brother.*

# Chapter 1

---

## Introduction

# Chapter 1: Introduction

---

## 1.1 Metal-Organic Frameworks

The idea of coordination polymers based on metal ions linked to each other by organic linkers has been in existence since 1960s.<sup>1</sup> However, it was not until late 1980s that porous three-dimensional networks with defined pores were synthesised.<sup>2</sup> Coordination networks are defined in the IUPAC Recommendations for the Nomenclature of Inorganic Chemistry as:

*“A coordination compound extending, through repeating coordination entities, in 1 dimension, but with cross-links between two or more individual chains, loops, or spiro-links, or a coordination compound extending through repeating coordination entities in 2 or 3 dimensions.”*<sup>3</sup>

The term *coordination polymer* is suggested as a generic term to describe all materials that extend in one, two or three-dimensions. Metal-organic frameworks and porous coordination polymers, colloquially known as MOFs. A MOF is a coordination network with organic ligands containing potential voids. This description accounts for the fact that many systems may show changes in structure in potential porosity, solvent and/or guest adsorbed within pores may occur depending on temperature, pressure, or external stimuli.<sup>4</sup>

Over the years since, metal-organic frameworks have emerged as a broad spectrum of crystalline materials with high porosity, with surface areas extending beyond 6,000 m<sup>2</sup>/g.<sup>5</sup> In addition to high porosity, MOFs possess properties such as low density, and the ability to tune its chemical functionality by altering the metal and linker combinations. These characteristics have allowed for studies investigating their use in a range of applications that cover catalysis, sensing, gas separation and storage, light-harvesting, and as drug delivery systems.<sup>6-10</sup>

The key for ‘designing’ a MOF involves assembly of secondary building units (SBUs) and multidentate organic molecules in desired network topology.<sup>11</sup> Structurally, MOFs are often compared to aluminosilicate zeolites due to their analogous open network with micro-pores. MOFs, however, can have much larger pores that fall in the mesoporous range (2-50 nm). A major difference in MOFs and zeolites lies in the synthesis conditions. Zeolites and aluminosilicates, which are formed entirely of inorganic corner-sharing tetrahedral units of AlO<sub>4</sub> and SiO<sub>4</sub>, generally require a template molecule or an ion to provide a three-

## Chapter 1: Introduction

---

dimensional structure. This contrasts with MOF syntheses, where no additional reagents are required; the two building blocks can differ enormously and contain both organic and inorganic species that define the structure without an imperative requirement of a templating agent.<sup>12</sup>

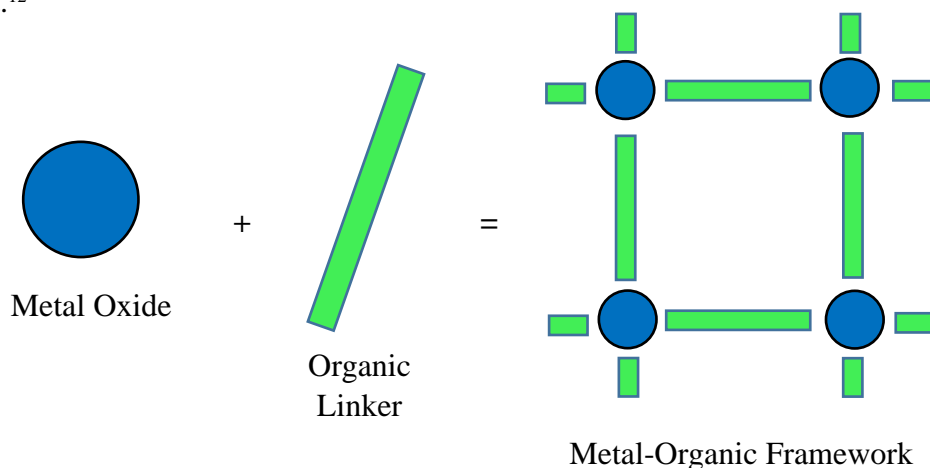


Fig 1.1: General representation of building blocks of metal organic frameworks.

The ability to synthesise MOFs using distinct combinations of metal-ion secondary building units (SBUs) and organic linker, provides an approach to obtain frameworks with variable pore sizes, topologies and internal surface area. These properties for MOFs can be tailored for intended specialised applications (Fig 1.1).<sup>13,14</sup>

## 1.2 Fundamentals of MOF Design.

### 1.2.1 Secondary Building Units

The term secondary building units (SBUs) was originally used for the description of zeolites, where metal oxide tetrahedra ( $\text{TO}_4$ ) primary building units form larger periodically recurring structural arrangements, *i.e.*, SBUs. Within a MOF, the SBUs serve as anchor points that form strong bonds with the struts of the multidentate functional groups of linking molecule, such as carboxylates, forming the stable geometric structure.

The choice of metal ions plays an important role in defining the geometry of the SBU. There are a few cations that have been used to create a MOF; transition metals are most common choice, however, recently lanthanides have been experimented with to show similar structures.<sup>15</sup> Each metal will have their own coordination preference for the respective

## Chapter 1: Introduction

---

valance state which can be used to define the geometry of both the SBU and the resulting MOF. In a classical study investigating significance of metal salt and the resulting SBU from the reactant salt, Hu *et al.* were able to exploit this metal-directed effect to synthesise six new MOFs based on polycarboxylate acids and V-shaped imidazole-based linker by a range of metal salts.<sup>16</sup> The study noted and compared the crystal structures and their resulting geometry from cadmium(II), zinc(II), cobalt(II), nickel(II), and manganese(II) salts. The Cd(II) and two Ni(II) frameworks were synthesised with different linkers which resulted in 6-coordinate metal centres giving a distorted octahedral geometry, Co(II) lies in a distorted trigonal bipyramidal coordination environment. Interestingly, Zn(II) shows two varied coordination: distorted tetrahedral nodes and an octahedrally coordinated node. The Mn(II) structure is also an interesting case with two types of Mn ions (5- and 6-coordinate) bridged by the carboxylate linker to give a binuclear cluster.

### 1.2.2 Organic Linker

Secondary building units can be combined into a framework structure through different linkers. Selection and substitution of a linker can lead to two situations: either the symmetry of the structure is retained when another linker is used and only the unit cell parameters change because of the elongation of the carbon chain, as seen in some isorecticular MOFs, or the symmetry can also change because of the change in the mutual arrangement of functionalities.<sup>17</sup>

The presence of different substituents and functional groups in the linker is then responsible for the selectivity and chemical properties of the pores. The organic linkers are most commonly carboxylates; however, they may also be other organic anions such as phosphonates, sulfonates, and heterocyclic compounds. 1,4-benzene dicarboxylate ( $\text{BDC}^{2-}$ , terephthalate), with a  $180^\circ$  angle between the two carboxylic groups, can form short link via a carboxylate end, thereby linking up to six metal ions, or it forms long bridges by the benzene ring, leading to a great variety of structures. 1,3-benzene dicarboxylate, in which the two carboxylate moieties are rigidly predisposed at  $120^\circ$ , is a good oxygen donor for building metal–organic networks.<sup>18</sup> 1,3,5-Benzene tricarboxylic acid ( $\text{H}_3\text{BTC}$ , trimesic acid) is a rigid, planar molecule and has been extensively used in the form of its three 1,3,5-benzene tricarboxylate anions  $\text{H}_n\text{BTC}^{(3-n)-}$  ( $n = 0, 1, 2$ ) as a bridging ligand in the synthesis of multidimensional MOFs (Fig 1.2).<sup>19,20</sup>

## Chapter 1: Introduction

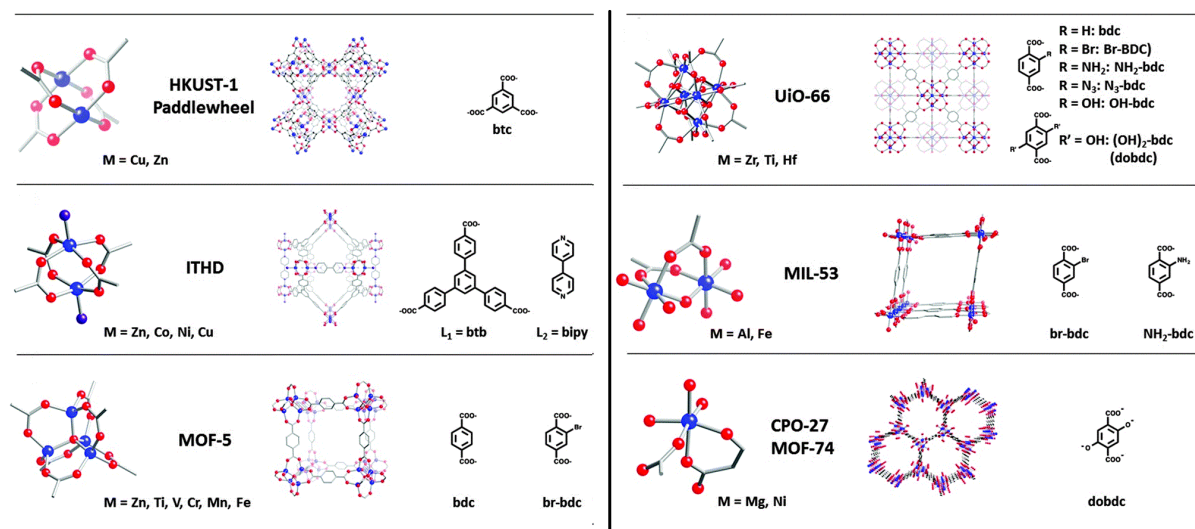


Fig 1.2: Lattice structures (middle) and corresponding SBUs (metal nodes (left), and organic linkers (right)) of some of the MOFs discussed in this review. (Atom definition: blue – metal, red – oxygen, purple – nitrogen, grey – carbon, green – chlorine.)<sup>21</sup> [Reproduced with permission]

The basic design principles of MOFs were first introduced by Robson<sup>22,23</sup>, describing a potentially novel class of materials formed by ‘scaffolding’ either tetrahedral or an octahedral array of valance rod-like connecting units. It was not until the early 2000s however, that Omar Yaghi coined the term ‘*reticular chemistry*’, describing reticular synthesis as:

*“In essence, reticular synthesis can be described as the process of assembling judiciously designed rigid molecular building blocks into predetermined ordered structures (network), which are held together by strong bonding.”*<sup>24</sup>

Yaghi and co-workers successfully applied this concept of modular chemistry combining SBUs of similar metal and organic linkers (Fig 1.3). This led to the discovery of one of the first MOFs, MOF-5, which consists of a  $[Zn_4O]^{6+}$  tetrahedral node linked by a  $BDC^{2-}$  linkers. Replacing the  $BDC^{2-}$  linker by other linear dicarboxylate led to classification of a new family of materials called ‘*Isorecticular MOF*’ (IRMOF).<sup>25</sup>

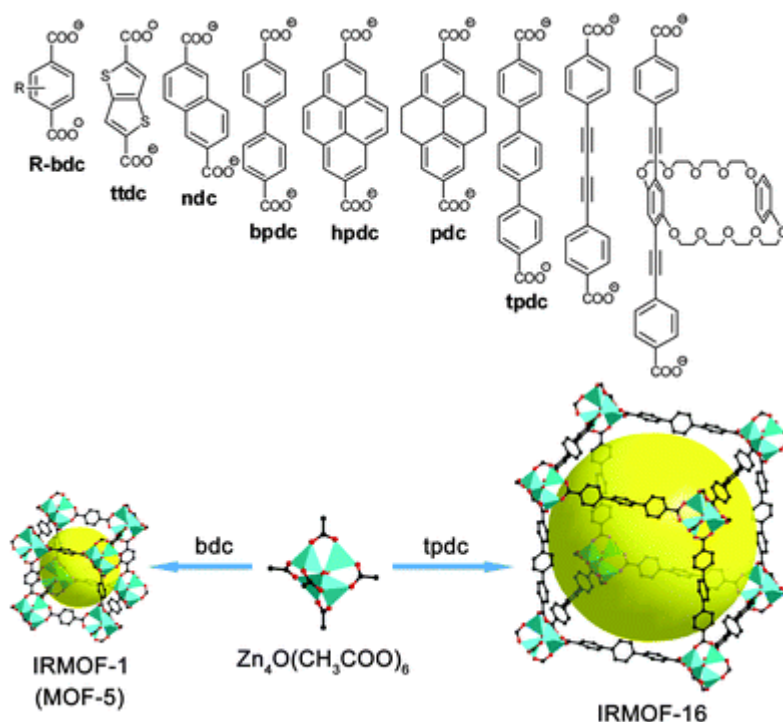


Fig 1.3: Representation of the variety of linkers in the IRMOF family of MOFs. Yellow spheres indicate the void space in the crystal lattice.<sup>26</sup> [Reproduced with permission]

The IRMOF series is the largest and most investigated series of MOFs, and along with the MIL (Materials Institute Lavoisier) series forms the large representation of materials with versatility of extending the framework using the same SBU. However, with thriving research studying MOFs, they form a small part of over 84,000 reported MOF structures in the Cambridge Structural Database (CSD) as of June 2018.<sup>27</sup>

### 1.3 MOF Synthesis

The synthesis of metal-organic frameworks (MOFs) has attracted immense attention over the years as researchers strive to synthesise a large variety of structures with different linker-metal combinations to explore potential applications and develop greener and cost-effective synthesis for MOFs.<sup>28</sup> The main goal during MOF synthesis is to create conditions that lead to defined inorganic building blocks without decomposition of the linkers at higher temperatures. Additionally, crystallization kinetics must allow nucleation and growth of the desired phase to occur.

MOFs are synthesised using hydrothermal and solvothermal synthesis. In the case of solvothermal synthesis, the reaction mixture is sealed in a pressure vessel and heated to temperatures greater than the boiling point of solvent mixtures.<sup>29</sup> As a reaction pressure is increased, the solubility of reactant increases. Reduced linker solubility often results in slowing down of the reaction rate and poor crystallinity.<sup>30</sup> Hence, to mitigate such effects, solvothermal and hydrothermal syntheses are performed at increased pressure to prevent reactant precipitation during the reaction. This increases the likelihood of obtaining products of higher crystallinity.<sup>30</sup>

### 1.3.1 Solvothermal and Hydrothermal Synthesis

Hydrothermal and solvothermal synthesis are the most prevalent of the conventional synthesis where the reactants are heated in presence of a solvent medium. In a typical solvent-based MOFs synthesis, reactants in presence of one or more solvents result in formation of a nanoporous material through nucleation and spreading. Multiple nucleation aggregates on the surface adsorb organic molecules into an inorganic–organic crystal. A drawback of this method is that the reaction time can range from several hours to days. Despite this, many of the MOF syntheses are carried out using this approach allowing the effects of different variables to be understood.

Alternative methods to ameliorate the issue of long synthesis time have been developed such as microwave-assisted,<sup>31</sup> sonochemical,<sup>32</sup> electrochemical,<sup>33</sup> and mechanochemical methods.<sup>34</sup> Many of these synthetic methods have been studied with a motive to scale-up for commercial interests as they offer advantages of shorter reaction times and lower temperatures compared to solvothermal synthesis methods. Fig 1.4 shows a comparison of various methods used for MOF synthesis.<sup>35</sup>

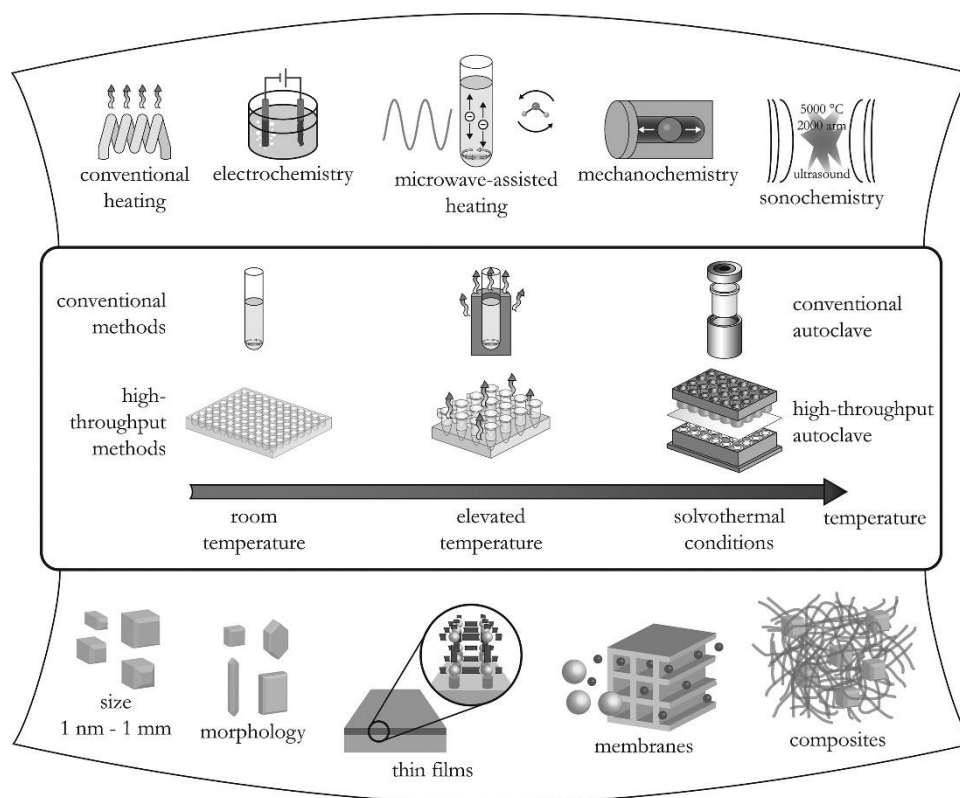


Fig 1.4: Overview of synthesis methods, possible reaction temperatures, and final reaction products in MOF synthesis.<sup>28</sup> [Reproduced with permission from N. Stock *et al.*]

Whilst the metal cations and organic ligands during synthesis define the structure and topology of the framework, reaction conditions play an important role in the resulting crystallite size and their morphology. Synthesis is sensitive to reaction conditions such as temperature, pressure, molar ratio of the reactants, solvent mixture and concentration used for synthesis, and pH.<sup>36</sup>

### 1.3.1.1 Effect of Temperature

Increasing the temperature and pressure increases the probability of crystallisation because of the increase in the solubility of the reactants and therefore self-assembly and the yield of crystals.<sup>37</sup> Forester *et al.* outlined the importance of synthesis temperature where they were able to produce five different phases of cobalt succinate by varying temperature as the only variable during the synthesis of the framework.<sup>38</sup> It was found that the overall dimensionality of the structures increased, with 1D chains up to 100 °C, 2D sheets at 150 °C, and 3D materials at 190 °C and above. At higher temperatures, dimensionality increases as well,

## Chapter 1: Introduction

---

beginning at isolated cobalt atoms or clusters through 100 °C, and continuing to 2D Co–O–Co sheets at 150 °C and above.

In the room temperature synthesis, nanoscale MOF-5 and a new phase was produced when triethylamine (TEA) was directly added into a DMF solution containing the reactants.<sup>39</sup> MOF-5 of different crystal shapes such as spherical (30x45 nm in diameter) and wire-shaped (~100 nm in diameter) nanocrystals were also synthesized with direct-mixing within liquid crystals or in ordered cylindrical channel (100 nm diameter) of an anodic alumina membrane, respectively.

The influence of the reaction parameters on the crystal size of HKUST-1 was systematically investigated in two reports.<sup>40,41</sup> The use of acetate as the counterion led to smaller crystal size, which is related to the change in nucleation rate. Increasing the reaction temperature leads to the formation of Cu<sub>2</sub>O as a by-product. At low reaction temperatures, octahedrally shaped crystals are formed, while at higher temperatures the crystals have less-defined faces and edges.

### 1.3.1.2 Effect of Solvent

The choice of solvent has also been shown to have effects on the resulting topology of the framework. Liu *et al.* demonstrated synthesis of two 3D supramolecular isomers of a Co(II) framework prepared by using similar reactants and methods, while only changing the solvent from DMF to MeOH.<sup>42</sup> The MOF resulting from the reaction in MeOH had linear constituent Co–O inorganic chains consisting of *trans*-isomeric Co(II) octahedra, whereas the form synthesised with DMF as the solvent resulted in zig-zag Co–O chains of half *trans*- and half less symmetric *cis*-isomeric Co(II) octahedra. The two isomers had dramatically different magnetic properties due to the difference in coordinative environment around the Co(II) ion.

### 1.3.1.3 Effect of Modulators

To exhibit further control on nucleation and morphology, modulators may be added into the reaction mixture. These are usually monodentate linkers that result in competitive binding at the metal sites during self-assembly process. Modulators are thus employed to adjust the size

## Chapter 1: Introduction

---

and shape of MOF crystals.<sup>43</sup> Mono-carboxylic acids and their salts are often used in synthesis of metal carboxylates, but N-heterocyclic compounds and alkylamines are also employed for the synthesis of certain MOFs such as ZIFs. In order to regulate the size and morphology of isorecticular Zr-based MOFs with UiO-66, -67, and -68 structures; acetic acid or benzoic acid are used as modulators.<sup>44</sup> Their findings are illustrated in Table 1.1. In absence of the modulators, the MOFs obtained were microsized aggregates of nanocrystals. As an example, by adding increasing amounts of the modulator, Zr-BDC samples increased in crystal size with an octahedral shape. For Zr-BPDC, increasing the amount of the modulator resulted in formation of individual octahedral microcrystals. Such behaviour exhibits the influence of modulators in defining the end morphology of the MOF.

Table 1.1: Size determination of Zr-bdc MOFs from synthesis carried out in presence of benzoic acid as a modulator.<sup>44</sup>

<b>Benzoic Acid (Equivalents)</b>	<b><math>d_{DLS,water}^{[a]}</math> (nm)</b>	<b><math>d_{DLS,EtOH}^{[b]}</math> (nm)</b>	<b><math>d_{XRD}^{[c]}</math> (nm)</b>
0	122-615 (220)	220-712 (295)	85
1	105-396 (255)	190-459 (220)	39
3	142-459 (164)	148-308 (198)	67
5	105-396 (164)	105-396 (142)	95
10	79-255 (105)	91-255 (122)	120
20	122-342 (164)	95-265 (128)	-
30	164-458 (190)	164-531 (164)	-

*([a] The equivalents of benzoic acid added are given with respect to  $ZrCl_4$ . [b] Data for particle sizes from dynamic light scattering (DLS) measurements (the maximum of the distribution is given in parentheses) in water ( $d_{DLS,water}$ ) and in ethanol ( $d_{DLS,EtOH}$ ), and crystallite sizes from the evaluation of powder XRD patterns using Scherrer's equation ( $d_{XRD}$ ). [c] Crystallite sizes were out of scope for determination by Scherrer's equation.)*

## Chapter 1: Introduction

---

### 1.3.2 Microwave Synthesis

Microwave synthesis has widely been used to achieve rapid synthesis of micro- and nano-porous MOFs in conjunction with hydrothermal conditions.<sup>45</sup> Besides increased rate of crystallization, phase selectivity, narrow particle size distribution are some of the advantages through microwave synthesis.<sup>31</sup>

In microwave synthesis, the reactant mixture along with a suitable solvent is transferred to a Teflon vessel, sealed and placed into a microwave. The mixture is stirred and heated for the appropriate time at the set temperature. The applied oscillating electric field, coupled with the permanent dipole moment of the molecules in the synthesis medium induces molecular rotations, resulting in rapid heating of the liquid phase.<sup>43,46</sup>

### 1.3.3 Ultrasonic Synthesis

Ultrasonic synthesis relies on homogeneous and rapid nucleation to aid synthesis with a reduced crystallization time. Compared to conventional solvothermal reactions, this method results in reduced crystallization time and significantly smaller particles size.<sup>47,48</sup> A reactant mixture for a given MOF is introduced to a conical Pyrex reactor fitted to a sonicator bar with an adjustable power output, without external cooling. Acoustic activation, which is the formation and collapse of bubbles formed in the solution after sonication produces very high local temperatures (~5,000 K) and pressures (~1,000 bar), and results in extremely fast heating and cooling rates (>1000 K/s) producing fine crystallites.<sup>49</sup>

### 1.3.4 Electrochemical Synthesis

The electrochemical synthesis applies the fundamentals of electrolysis where metal ions are continuously supplied through anodic dissolution as a metal source instead of metal salts, which react with the mixture of linker molecules and a conducting salt in the reaction medium. With the electrochemical route, it is possible to run a continuous process to obtain a higher yield with regards to the solids content compared to normal batch reactions.<sup>28</sup>

Electrochemical synthesis has several advantages over conventional syntheses: (1) faster synthesis at lower temperatures, (2) As metal salts are not required, separations of anions (such as,  $\text{NO}_3^-$  or  $\text{Cl}^-$ ) post-synthesis is not required eliminating the need for their removal,

(3) It is possible to achieve increased yield and virtual total utilization of the linker can be achieved in combination with high Faraday efficiencies.<sup>50</sup>

### 1.3.5 Mechanochemical Synthesis

In mechanochemical synthesis, the mechanical breakage of intramolecular bonds followed by a chemical transformation takes place. The interest in mechanically activated MOF synthesis is due to multiple reasons. One important consideration for this approach is for its environmental benefits. Reactions can be carried out at room temperature under solvent-free conditions, which is especially advantageous as organic solvents can be avoided.<sup>51</sup> The reaction times associated with mechanochemical syntheses are short, normally in the range of 10-60 min, and can lead to quantitative yields. Moreover, in some cases metal salts can be replaced by metal oxides as a starting material, which results in the formation of water as the only side product, making purification less tedious.

Other less common approaches have also been used such as employing Ionic Liquids (IL) as synthesis media,<sup>52</sup> using MOFs as microfluidic systems,<sup>53</sup> and Dry-gel conversion of the system.<sup>54</sup> Choosing the right approach often comes down to the yield, scale of synthesis, size and purity of the MOF to be obtained.

### 1.4 Applications

In the past decade there has been considerable growth in characterisation and studies concerning the application of MOFs. Due to their structural and functional tunability, MOFs have been recognised to have fascinating scope of applications in both industry and research.<sup>26,55,56</sup> As the interest in the real-world application has grown, MOFs have been studied for interests in the field of heterogeneous catalysis, energy trapping and transfer, gas storage and separation, chemical sensing, drug delivery, biomedical applications, and proton conduction.<sup>57-59</sup> Many early MOFs made from divalent metals, such as  $Zn^{2+}$  or  $Cu^{2+}$ , have shown exceptional porosity and promise for a wide variety of applications, but stability concerns have made it unsuitable for high-moisture conditions as MOFs are known to adsorb moisture very rapidly due to their exceptionally large surface area.

## Chapter 1: Introduction

---

For certain applications, their framework integrity must be guaranteed to maintain their intended function and characteristics. In applications such as catalysis, that often mandate stability toward aqueous acid/base or coordinating anions, a minimum degree of moisture is desirable to prevent any precipitation of these species during the synthesis. The chemical stability of MOFs has been receiving increased attention over the past few years and research has been directed to try and address the issue concerning the stability of MOFs in different environments, understand the possible decomposition pathways, and to develop more stable framework structures.<sup>60</sup>

### 1.4.1 Gas Purification

Of the potential application where MOFs can be useful is for removal or ppm-traces of sulphur components from various gases. MOF structures with accessible and open metal sites are suited to preferentially chemisorb electron-rich, odour-generating molecules, like alcohols, phosphines, amines, oxygenates, water, or sulphur-containing molecules.<sup>60</sup> Removal of tetra-hydrothiophene (THT, odorant) from natural gas is one such example investigated by Belmabkhout *et al.*<sup>57</sup> At room temperature, traces of 10–15 ppm sulphur were fully captured, to less than 1 ppm using an electrochemically synthesised Cu-EMOF in a fixed bed reactor. The overall capacity of the MOF material exceeded the performance of other commercially available activated carbon materials, Norit (type RB4) and CarboTech (type C38/4), as adsorbent by an order of magnitude.

### 1.4.2 Gas Separations

In gas separation processes, crude gas mixtures consisting of components of varying concentrations are separated by distillation or thermal adsorption-desorption is used to separate the mixture. Examples of existing technologies are nitrogen–oxygen (air), nitrogen–methane, and certain noble gas separations, some of these components are separated using zeolitic adsorbents. In recent times, separation of Kr–Xe by pressure swing adsorption, as well as the purification of methane in natural gas were tested on MOF-adsorbents.<sup>61,62</sup>

## Chapter 1: Introduction

MOFs with small pores have shown to be able to separate molecules by size or kinetic diameter.<sup>63,64</sup> Where the water uptake usually occurs, relatively larger molecules such as  $N_2$ ,  $O_2$ ,  $CO_2$ , and  $CH_4$  are barred from adsorption.<sup>65</sup> Adsorption isotherms of nitrogen and hydrogen for magnesium formate MOF (Basosiv M050) have shown the preferential adsorption of hydrogen over nitrogen.

Current trends in separation focusses on elimination of  $CO_2$  from low pressure flue gases that are emitted by burning of fossil fuel. Awareness of global warming over the past few years has attracted substantial interest in  $CO_2$  separation.<sup>66</sup> Chemisorption of  $CO_2$  is achieved by amine wash at room temperature.  $CO_2$  in MOFs is physisorbed in the same temperature region. Due to the lower energy of adsorption during physisorption, MOF adsorbents, such as MIL-53(Cr), require a greater  $CO_2$  partial pressure to reach sufficient adsorption capacities (Fig 1.5).<sup>67</sup> These studies suggest that MOFs currently can only be used in  $CO_2$  separation at high pressure for desired effectiveness. However, even under such conditions, MOFs do not yet perform as well as commercial amine scrubbers. Hence, further research into gas separations is required to develop effective solutions to the gas separation problems.

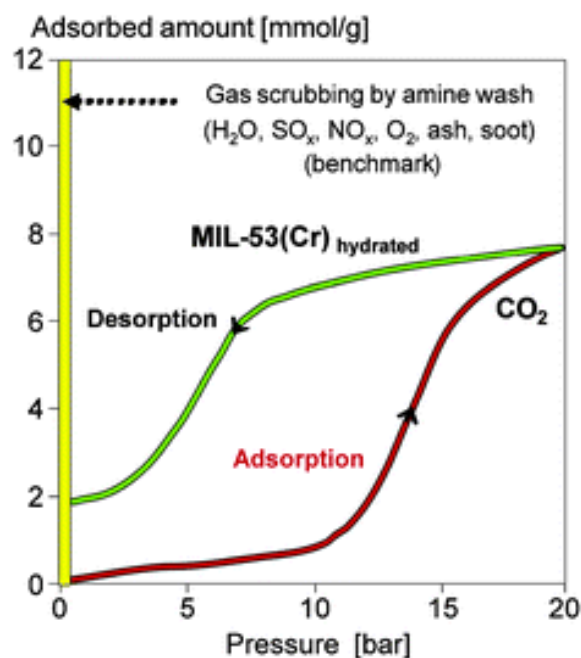


Fig 1.5: Adsorption isotherms of carbon dioxide on MIL-53(Cr) in comparison to carbon dioxide removal from flue gas by amine wash.<sup>68</sup>

### 1.4.3 Gas Storage

MOFs, by nature have a unique porous structure with considerable dead volume. With this characteristic property, it is possible to use this void volume to for volumetric gas storage. This effect can be very pronounced depending on the type of MOF and the adsorbent gas, its temperature and pressure.

It has been demonstrated that the gas-storage performance of a MOF strongly depends on the synthesis method, the scale of production and efficiency of activation. High uptakes of gases have been reported by Kitagawa *et al.*<sup>69</sup> The greatest challenge with storage of hydrogen is using materials that allow compact and lightweight storage, as well as a high storage density. In addition to the target values set by the US Department of Energy, the need for alternative fuel sources and energy carriers was recently reviewed.<sup>70</sup> The prospects of using hydrogen as a portable fuel has been attracting continued interest in both industry and research for many years. The advantages of using MOFs for hydrogen storage applications is that it works fully reversibly, avoids complicated heat treatments, and recharging proceeds within seconds or minutes.

MOF-5 has been studied to identify distinct locations of adsorbed hydrogen molecules using inelastic neutron scattering.<sup>25</sup> Experimental and DFT density functional theory (DFT) studies have shown proposed storage capacity of 10–12 molecules (up to 4 wt%) and 16–20 molecules of H<sub>2</sub> per Zn<sub>4</sub>O-cluster, respectively.<sup>71</sup>

Storage data are reported of up to 7.5 wt% of hydrogen on MOFs, (e.g. MOF-177) at 9 MPa and 77 K, which surpasses many of the other materials. Many other research groups have investigated overcoming the challenge of improving hydrogen storage with various studies reporting values in the range of 2–4 wt%.<sup>72,73</sup> Similar values were achieved by Yaghi's group with MOF-505 where Cu-paddle-wheels are connected by 3,3',4,4'-biphenyltetracarboxylic acid. However, uncertainty persists over whether large surface area materials like MOF-177, MIL-100 or MOF-5 and isoreticular compounds, materials with an average surface area of between 1000 to 1500 m<sup>2</sup>g<sup>-1</sup> or even small pore MOFs could potentially be the most promising storage media.<sup>60</sup> It is also difficult to deduce whether divalent or trivalent metal

## Chapter 1: Introduction

clusters are the most favourable ones. Nevertheless, a comparison to NaX-zeolite very clearly indicates the superior behaviour of MOFs over conventional microporous inorganic media.<sup>74</sup>

For applications that are limited by volume and portability, it is relevant to compare storage data on a volume-specific rather than a weight-specific storage capacity. Typically, the packing densities of MOF powders are around 0.2 to 0.4 g cm<sup>-3</sup> increasing to 0.5 to 0.8 g cm<sup>-3</sup> when shaped into tablets or extruded fibres.<sup>120</sup> The density of these material is so low that weight limitation for an application is usually irrelevant, unlike metal hydrides for storage media. The most important issue here is the amount of hydrogen which can be discharged from the storage media at a reasonable timescale. Within this context, MOFs really have a fully reversible uptake- and release-behaviour. Since the storage mechanism is based predominantly on physisorption, there are no huge activation energy barriers to be overcome when the stored hydrogen is released. A simple pressure reduction by controlling valve opening is enough to draw off hydrogen from MOFs within a few seconds. Fig 1.6 shows a comparison of hydrogen storage capacities of common MOFs

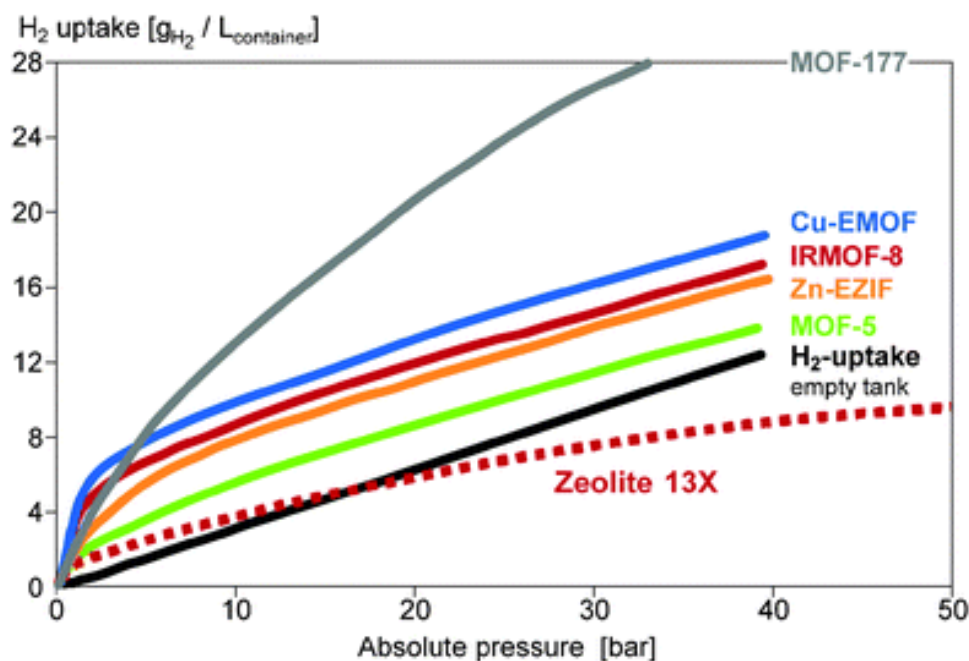


Fig 1.6: H<sub>2</sub>-storage capacities for different MOFs (prototype trials).<sup>75</sup>

## Chapter 1: Introduction

---

It is essential to determine the preferred adsorption sites for hydrogen in MOF structures that in principle should enable the prediction of storage capacities. In this respect, neutron scattering coupled with molecular modelling tools might become as important as extensive experimental synthesis efforts. Depending on the application and the associated temperature ranges, highly porous MOFs might be favourable for low temperatures, whereas materials with small porosity and flexible MOFs could be useful for room temperature hydrogen storage.<sup>76</sup>

### 1.4.4 Catalysis

Catalysis is of continuous importance due to its crucial role in many chemical processes. MOFs, due to their ability to tailor its pore size to yield selectivity, regioselectivity, and selectivity with shape and size, have demonstrated potential to be used as heterogeneous catalyst. Manipulating these factors allows creating appropriate environment around the catalytic centre in the restricted space available. Allowing incorporating or shielding the active sites of the MOFs as per requirements, it may be possible to avoid the omnipresent problem of catalyst degradation and product-catalyst separation known in homogeneous systems.<sup>77,78</sup>

MOFs may act as catalysts through (i) coordinatively unsaturated nodes (metal centres), (ii) ligands functionalized with organic groups (e.g., as Brønsted acids), (iii) metal-complexes (as with homogeneous catalysis) which are incorporated into the linking ligand (e.g., as metallo-ligands) or the pores.

The active catalyst sites in MOFs remain to be identified, even when considering the well-defined bulk structures of the MOFs. There is an opportunity to detect the sites with a view of controlling the synthesis mechanisms. Identifying these sites is an integral part of representing the performance of MOF as a catalyst in terms of intrinsic kinetics and turnover frequencies. Moreover, MOFs present unique challenges with regards to catalytic stability. Although some MOFs have been shown to withstand temperatures as high as 350 °C, it is however difficult to find applications of MOFs as catalysts at such extreme temperatures, because of their stability limitations and the challenges associated with the regeneration of

## Chapter 1: Introduction

---

organic linkers from the MOF. MOFs are connected by node–linker bonds that may be unstable under some catalytic reaction conditions, resulting into the decomposition of the MOF. There is an essential requirement to understand the destabilization phenomena to better refine the structure to endure decomposition during catalysis.

### 1.4.5 Biological Applications

Unceasing improvement in the medical diagnostics and therapeutic properties in recent years have driven the research exploring avenues for applications such as drug delivery and MRI contrasting agents. Besides polymers and mesoporous silica nanoparticles (MSNs), MOFs have been explored as potential materials of interest in both drug delivery and as MRI contrast agents either as a  $T_1$ - (spin-lattice relaxation time) or  $T_2$ - (spin-spin relaxation time) or combined  $T_1$ - and  $T_2$ - contrast agents for MRI image enhancement. In most cases, the MOFs are functionalized by post-synthetic modifications with bio-compatible polymers and/or ligands, to achieve either targeted drug delivery, improve MRI imaging, enhance stability and to mitigate the toxicity of the modified MOFs to be used for the desired applications. Although hurdles in commercialization are still a concern, important steps have been taken towards converting research into potential applications.<sup>79</sup>

### Drug Delivery

MOFs exhibit many characteristics that are desired for drug delivery applications such as exceptionally large surface area and pore size for drug encapsulation, intrinsic biodegradability as a result of relatively labile metal-ligand bonds, and versatile functionality for post-synthetic modification of molecules.<sup>80</sup> A range of MOFs with diverse structures and characteristics have been investigated for the application of drug delivery such as chiral MOFs, MOFs based on biocompatible metal, Ca-, Cr-, Cu-, Mg- and Zn-based MOFs, MIL family MOFs, MOFs containing lanthanide elements such as, Eu, Gd, or Tb, zeolite-based MOFs, Surface-Anchored MOFs (SURMOFs), Nanoscale Coordination Polymers (NCPs).<sup>81</sup>

A range of drugs and bioactive compounds have been investigated as a cargo on carrier MOFs either by encapsulation within the MOF pores, functionalising MOFs with molecules,

## Chapter 1: Introduction

---

or a novel indirect approach using MOFs as a template for synthesis of biocompatible polymer networks or membranes. Some of the drugs and/or bioactive compounds include: anticarcinogens (5-fluorouracil, busulfan, azido-thymidine triphosphate, cidofovir, doxorubicin, paclitaxel),<sup>82</sup> antiarrhythmia drug (procainamide HCl),<sup>83</sup> amphiphilic drug (caffeine, lidocaine),<sup>84</sup> pro-drug of cis-platin, iron-chelator drug (deferiprone),<sup>85</sup> bio-active gas (nitric oxide and iodine),<sup>86</sup> analgesic drug (ibuprofen),<sup>87</sup> luminescent dye (rhodamine-6G) etc. The release of guest molecules from a MIL container was detected in a study as less than an hour of an *in-vivo* intravenous testing subjected to rats with the release that could last for 14 days. The storage capacity depended on the pore size, pore functionalization and the MIL-particle size. For example, 40 mass% of doxorubin could be stored in iron (III) amino terephthalate (MIL-101-NH<sub>2</sub>).<sup>88</sup>

In addition to being used as carriers for drug delivery, the MOFs have also been studied to be used as a carrier for biologically active gases such as NO and I<sub>2</sub>. The MIL family of MOFs, that are composed of tetravalent central metal ions and carboxylic acid as the bridging ligand, are the most utilised materials for the controlled release of biological gases. Controlled and sustained release of biologically active gases in active concentrations may have great implications for potential applications in the biomedical applications. MOFs selectively adsorb and desorb many volatile molecules and other biologically active compounds. Due to their high surface area and high porosity, they allow greater adsorptive surface area per gram than other currently used encapsulating materials such as zeolites and cyclodextrins.<sup>89</sup>

While the systems that have been discussed above show some promise for the use of MOFs as drug delivery vehicles, drug loading is based on the ability of adsorb the guest drug molecules in the MOF during the development stages. In contrast to other nanoparticles, MOFs can hold a substantially larger amount of guest molecules but require a greater time period for loading into the matrices. One of the disadvantages of MOFs for controlled drug delivery is that the coordinated metal ions in the frameworks MOFs may leach out into the external environment. This may potentially be a hazard if some metal ions are released in excess that could impart severe toxicity. To circumvent this issue, the MOFs are modified with polymers and/or ligands to the MOFs framework with an aim to enhancing the stability of the MOFs, prevent aggregation of MOFs, and significantly reduce the leaching of metal

## Chapter 1: Introduction

---

ions present in the structure of the MOFs. Various functionalization of the MOFs with biopolymers and bio-ligands or cell-targeting ligands helped to mitigate the problems to an extent pertinent to the stability, biocompatibility and toxicity of the MOFs used.

### Hybrid Materials

One of the approaches considered to tailor the properties of MOFs for expanding the scope of applications is by integrating MOFs with other functional materials.<sup>90,91</sup> There have been various approaches investigated for developing these ‘hybrid’ materials that include post-synthetic modification (PSM) where the MOFs are synthesised with functionalised linker molecules. Integrating MOFs with nanoparticles, both organic and inorganic oxides, quantum dots, polymers, various carbon-based materials, enzymes, silicon-based materials, and even polyoxometalates have also been used to enhance properties of MOFs to increase their resistance towards the harsh conditions.<sup>92</sup>

## 1.5 MOF Templated Polymerisation

### 1.5.1 Overview

Polymer chains during polymerisation often entangle and create an amorphous bulk polymer. Synthesising polymers in confined spaces can prevent the entanglement and conformational disorder that occurs in bulk polymers, allowing a control over assembly of polymer chains.<sup>93,94</sup>

A combination of MOFs and polymers can enable chain regulations with regards to chain length and sequence of polymers, taking advantages of MOFs’ well defined structural porosity and large surface area to accomplish highly ordered polymer structures by transferring the spatial information of the host MOF to the monomer entities. Controlled polymerisation inside MOFs can be accomplished by polymerisation proceeding through the pores of the MOF – where the MOF acts as a template without being involved in any chemical reactions, or polymerisation propagating from MOFs – where the MOF itself acts as a catalytic system to promote polymerisation. Choosing the approach is largely dependent on the objective and the reaction conditions to achieve polymerisation.<sup>91,95</sup> Utilizing MOFs as a

## Chapter 1: Introduction

---

reaction environment for polymerisation influences the orientation of polymers to obtain specific regio- or stereoisomers. Additionally, polymerisation inside the channel allows control over chain growth processes and tacticity.<sup>96</sup>

The control over the tacticity of the polymer is one of the main reasons for using ordered materials as templating motifs.<sup>97</sup> To produce composites by direct insertion of polymers within the pores of the MOF, the polymer must be able to penetrate and move through the MOF windows. This limits the amount and the molecular size of the polymer depending on the MOF structure. Furthermore, insertion of high molecular weight polymers is extremely difficult because of their low diffusivities that sets another limit for the chain length of polymers that may be obtained, often limiting the approach to oligomers and short polymers.

MOF-mediated template polymerisation has been accomplished in three distinct ways: (1) polymerisation of guest monomers. This approach uses confinement effects resulting from monomer molecules being confined in the nanosized pores of the MOF.<sup>98</sup> Different MOFs, depending on their chemistry and structure, have distinct pore size and dimensionality. However, the strong confinement effects reduce the monomer mobility within the pores and therefore reduce the reactivity of the monomers. (2) copolymerisation between host and guest molecules. This approach allows for transcription of the MOFs ordered structure onto the resulting polymers. Depending on the reaction pathway and the distribution of the monomers that have been confined into the MOF, the alignment, polymer sequence and the resulting structures can be regulated with precision. (3) Topochemical polymerisation of difunctional ligands in MOFs by single-crystal-to-single-crystal (SCSC) manner is an approach with which it is possible to precisely control stereoregularity of the polymer. However, a drawback of this method is it requires arranging the monomer species in suitable positions before initiating polymerisation, which is challenging.<sup>99</sup>

Radical polymerisation is widely used as the preferred method to produce vinyl polymers on both industrial and laboratory scales. In this method, the molecular weight distribution (MWD) is generally wide because termination and chain transfer reaction steps occur simultaneously with chain propagation. Hence, suppressing the side reaction is an important

## Chapter 1: Introduction

---

aspect to be considered when trying to achieve a polymer with narrow MWD.<sup>100</sup> Pioneering work in this field was carried out by Uemura *et al.* on the radical polymerisation of styrene monomer (St) in pores of 1D  $[\text{Zn}_2(\text{BDC})_2(\text{TED})]_n$  (where, BDC = 1,4-benzenedicarboxylate; TED = triethyldiamine), demonstrating that polymers with narrow MWD can be obtained by achieving polymerisation within the pores of this MOF.<sup>101</sup> The radicals of monomers propagating in the system showed high stability in the MOF pores, resulting in suppression of common side-reactions such as radical quenching by termination and chain transfer steps. The study also used the Cu analogue of this MOF,  $[\text{Cu}_2(\text{BDC})_2(\text{TED})]_n$  which was not as effective as 1D, likely because of the  $\text{Cu}^{2+}$  ions in the MOF being coordinatively saturated by the dicarboxylate linkers and are protected from being attacked by radical species. This study also demonstrated that it is vital to choose a MOF and polymer system that result in effective polymerisation without any undesirable interactions that may inhibit the process.

The researchers carried out further studies to understand the dependency of pore dimensions and channel size.<sup>102</sup> In this study, they used a MOF whose pore size could be tailored with using various dicarboxylate ligands by reticular chemistry,  $[\text{M}_2(\text{L})_2(\text{TED})]_n$  ( $\text{M} = \text{Zn}^{2+}, \text{Cu}^{2+}$ ;  $\text{L} =$  dicarboxylate ligand). The studies revealed that with an increase in size of the pores of the MOFs, the MWD of polystyrene (PSt) became narrower. Other vinyl monomers such as methyl methacrylate (MMA) and vinyl acetate (VAc) were also polymerised in MOFs to yield polymers with lower MWD.

Since proving the templating proof-of-concept as an effective approach to obtain polymers with tuneable MWD studies have been carried out to evaluate a range of monomers that can successfully polymerise under confinement of MOF pores. Hwang *et al.* studied these effects of monomer size on radical polymerisation of vinyl ester in  $[\text{Zn}_2(\text{BDC})_2(\text{TED})]_n$  by investigating the MWD of poly(vinyl esters) which became narrower with an increasing in monomer size: 2.17 for poly(vinyl acetate) (PVAc), 1.71 of poly(vinyl propionate) (PVPr), and 1.51 for poly(vinyl butyrate) (PVBr).<sup>103</sup> Reversible addition-fragmentation chain transfer (RAFT) polymerisation was more recently performed in the MOF to demonstrate further control over the polymerisation system.<sup>104,105</sup> There is a linear molecular weight increase as the reaction time increased which clearly indicates the benefits of using RAFT as an approach for controlled polymerisation. Kinetics of RAFT polymerisation of vinyl esters with pores of

## Chapter 1: Introduction

---

MOF,  $[Zn_2(BDC)_2(DABCO)]_n$  (DABCO = 1,4-Diazabicyclo[2.2.2]octane) as a polymerisation environment, with AIBN as an initiator and (*S*)-2-(ethyl propionate)-(*O*-ethyl xanthate) as chain transfer agent was investigated.<sup>106</sup> Compared to free radical polymerisation, there was an increase in molar mass of the polymer with RAFT polymerisation. This is a clear indication that a reversible-deactivation radical polymerisation (RDRP) process takes place inside the MOF. In order to obtain information on the effect of steric requirement of monomer tacticity on polymerisation of VAc, vinyl propionate (VBu) and vinyl butyrate (VBr) were also investigated. Polymer reactions in MOFs improved control over tacticity. Intermediate monomer size leads to enhanced tacticity control which might be due to interplay between steric demand of the monomer and mobility in the nanochannel.<sup>107</sup>

In theory, ideal orientation and perfect tacticity can be achieved provided monomers align perfectly inside the porous channels and hold their place as the polymerisation occurs. However, such orientation is hard to accomplish in reality. In case of free radical polymerisation, a limited occurrence of chain termination reaction occurs due to the decreased likelihood of end chain radicals to meet. All approaches considered, there is a general lack of consensus on how the polymerisation proceeds in real-time from point of initiation of polymerisation to the end of reaction. At current point of time, there is no specific evidence on actual mechanism of RDRP in MOFs either. The key to translate the approach of template-based polymerisation from laboratory to real world applications is to understand the polymerisation mechanism. Control over polymerisation by MOF templating could provide multi-dimensional and network-like polymer structures that are otherwise difficult to achieve by the route of bulk polymerisation. Further understanding of the polymerisation mechanism, in particular, enhanced sequence control, is needed to fully determine the effectiveness of this approach on a larger scale.

### 1.5.2 Polymer Networks for Drug Delivery

Improvement in the pharmacological and therapeutic properties of drugs is the driving force behind research into novel methods for targeted drug delivery. The use of nanocarriers in medicine and nanoparticle-based therapeutics have been subject to increasing interest over

## Chapter 1: Introduction

---

the recent years, as these systems hold a potential to alleviate many drawbacks such as inability to improve efficacy and undesirable side effects of conventional therapy.<sup>108</sup> They typically consist of an active agent incorporated within a nanoparticle carrier, such as micelles, liposomes, and polymer matrices.<sup>109</sup>

Polymer networks for loading of drug molecules offer several advantages such as stability, high swelling capacities, biocompatibility, and biodegradability. All these characteristics play an important function in targeted and controlled drug delivery.<sup>110</sup> Polymer network (PN) mediated drug delivery has acquired appreciable focus in the pharmaceutical industry in the past two decades due to their utility in time-controlled targeted drug delivery and tissue engineering.

In principle, templated polymer networks extracted from MOFs, should result in a non-separable network with high tensile strength depending on their structural complexity. Polymer networks have been widely investigated in recent years for controlled release of drug molecules.<sup>111</sup> A few of the significant biomedical uses of these polymer networks are in diagnosis, dialysis membrane, artificial dental and tissue implants, systems of drug delivery and burn dressing. For such applications a mandatory property for polymer is their biocompatibility, and the ability to be eliminated from the body (with or without prior biodegradation).<sup>112</sup>

To be chemically degradable, polymers must have hydrolytically or proteolytically labile bonds in their polymer backbone. Most polymers that are biodegradable rely on hydrolytic cleavage of ester bonds or ester derivatives such as poly(lactic acid) and poly( $\epsilon$ -caprolactone).<sup>113,114</sup> Degradation proceeds by releasing an acid as a decomposition product that catalyses further degradation or ionizes the initial hydrophobic structure that allows water molecules to adsorb to the polymer. A common issue with biodegradable polymers is uncertainty with regards to the safety of degradation products as degradation often results in distribution of fragment sizes. Toxicity of the degraded fragments is also challenging to determine experimentally without *in-vivo* testing. Ideally, polymers would degrade into

## Chapter 1: Introduction

---

small, metabolic compounds that are known to be non-toxic and are small enough for natural clearance mechanisms. Hence, it is vital that the polymers chosen should meet the criteria.

Using biodegradable polymer matrices presents a promising avenue as they can be degraded to non-toxic monomers inside the body. Such polymer networks may have a potential for high drug loading capacities, making them an enticing and promising candidate for further development in therapeutic treatments via drug delivery.<sup>115</sup>

One approach for drug delivery involves using highly porous MOFs as a template for polymerisation to occur within its pores forming polymers with high internal volume. Nanocarriers such as polymer networks synthesised through MOF-templated polymerisation have shown promise for drug delivery applications such as drug encapsulation within nanocarriers.<sup>116</sup> The MOF can be digested to yield a polymeric network which itself can be loaded with a drug and used for controlled release within the body. The digested MOF components can be recycled to reform the original structure and hence be reused as a template, making this a cost-effective method for templating polymer networks.<sup>117</sup>

### 1.6 Project Aims

The fundamental aims of this project are to synthesise biodegradable porous polymer networks templated by MOFs, and to verify the structure of the formed polymer networks. Additionally, to understand the mechanism of the polymerisation under confinement of monomer precursors in the MOF, and identify the requirements for achieving effective polymerisation by MOF templated polymerisation approach.

MOFs with well-defined porous structure can be used as templates and a polymerisation environment for a variety of monomers. Hence, improved control over polymer tacticity compared to bulk polymerisation as well as precise polymer networks tailored to intended applications can be achieved using this approach. Despite the advantages mentioned above, much of research on template synthesis of polymers is still developing and to an extent, uncertain with lack of substantial evidence. Template polymerisation within MOF pores had been suggested as a method to synthesise polymer matrices in the literature.<sup>118</sup> However, the

## Chapter 1: Introduction

---

research investigating mechanism of polymer network synthesis based templated approach is scarce and experimental data supporting proposed mechanisms has not been reported to our knowledge. The studies for understanding interaction of larger monomer molecules under confinement of MOF pores is not clearly understood and has not been reported.

Through our research, we aim to address the lack of understanding of polymerisation mechanism and guest behaviour through static and dynamical studies. In addition to conventional characterisation methods (X-ray diffraction, thermal analysis, IR and NMR spectroscopy), we will use neutron scattering to investigate guest behaviour at an atomistic level. Interactions and mechanisms driving polymerisation under these confined conditions have not been examined in real time as polymerisation is taking place. We performed total neutron scattering (TNS) and quasi-elastic neutron scattering (QENS) experiments at the NIMROD and IRIS instruments, respectively, (ISIS Pulsed Neutron and Muon Source, RAL, Oxfordshire, UK) that will help understand monomer and polymer interactions as the polymerisation proceeds from its initial monomer stage to its ultimate stage as a polymer. Additionally, these studies will also determine pathways to regenerate degraded MOF structure to ensure its recyclability. In general, MOF and polymer systems are potentially a good combination for template polymerisation for polymer structures that otherwise are difficult to achieve by bulk polymerisation. Understanding the mechanism behind the polymerisation reaction holds the key to real-world application.

### 1.7 Conclusion

Metal-organic frameworks (MOFs) are formed by reticular synthesis allowing for strong bonding between inorganic SBUs and organic units, resulting into crystals with high porosity and, high thermal and chemical stability. The highly porous nature of the MOFs makes them suitable candidates for applications in gas separation, gas storage, guest adsorption, catalysis, drug loading and release, among other applications. MOFs whose chemical composition and shape of building units can be multiply varied within a particular structure already exist and may lead to materials that offer a synergistic combination of properties. Furthermore, well-defined pores with high internal surface area allow chemical reactions to be performed within the pores of the MOF and can be used for synthesising polymers *in-situ* to obtain highly controlled polymers with long-range order. As the MOFs act as templates during polymerisation reactions, conventional polymerisation methods can be performed to allow polymerisation of confined guest monomer species within the pores with little alteration to the method.<sup>119</sup>

Studies involving MOF template polymerisation, with an aim to achieve control over molecular weight distribution, stereo-regularity, and co-polymer sequence have been investigated over the last decade. The ability to isolate the polymer structures without altering the polymer morphology or causing structural breakdown allows for synthesis of polymer architecture with porosity that can be tailored for the intended application. Despite the many conceptual advantages of using MOF templated polymerisation for polymer network synthesis, there is a lack of understanding on how to effectively control polymerisation of liquid monomers that are confined in MOFs. Secondly, there is also very little understanding of the polymerisation mechanisms and interactions of the monomer in the MOF framework during polymerisation.

Thus, it is essential to gain understanding of the energetic and atomic-scale intermolecular interactions within the pores of the MOF to understand how to control initiation and propagation of polymerisation during such reactions. Hence, to gather understanding of these mechanisms through different characterisation approaches have been a key inspiration to develop the aims of the research project. Furthering the knowledge may lead to the subsequent stage of the research project where the use of polymer architectures can be used

## Chapter 1: Introduction

---

as drug delivery vehicles by evaluating their drug loading and drug release capacities and capabilities.

The research in enhancing drug delivery mechanisms has been focused so that drugs are distributed only to targeted therapeutic locations in relevant quantities. Furthermore, understanding how polymers and polymer products interface with biological systems that are synthesised by the approach mentioned in the thesis is of prime importance. Many studies in recent years have reported on novel chemical roots for advanced drug delivery systems, but often, biocompatibility studies are overlooked until late in development.

MOF and polymers constitute a good combination for formation of advanced materials where the host MOF acts as a template for the synthesis of polymer structures. The template-based approach for achieving polymer networks is desirable because of the potential of precision synthesis of polymer networks. Furthermore, exploring specific properties of monomer and polymer confinement and their effects on the host structure provide a desirable platform for studies aimed at filling the gap in understanding these mechanisms.

### 1.8 References:

- 1 E. A. Tomic, *J. Appl. Polym. Sci.*, 1965, **9**, 3745–3752.
- 2 B. F. Hoskins and R. Robson, *J. Am. Chem. Soc.*, 1989, **111**, 5962–5964.
- 3 J. R. Long and O. M. Yaghi, *Chem. Soc. Rev.*, 2009, **38**, 1213–1214.
- 4 H. A. Schwartz, S. Olthof, D. Schaniel, K. Meerholz and U. Ruschewitz, *Inorg. Chem.*, 2017, **56**, 13100–13110.
- 5 T. Uemura, G. Washino, S. Kitagawa, H. Takahashi, A. Yoshida, K. Takeyasu, M. Takayanagi and M. Nagaoka, *J. Phys. Chem. C* 2015, **119**, 37, 21504–21514
- 6 T. Zhang and W. Lin, *Chem. Soc. Rev.*, 2014, **43**, 5982–5993.
- 7 M. C. So, G. P. Wiederrecht, J. E. Mondloch, J. T. Hupp and O. K. Farha, *Chem. Commun.*, 2015, **51**, 3501–3510.
- 8 O. K. Farha, A. Ö. Yazaydin, I. Eryazici, C. D. Malliakas, B. G. Hauser, M. G. Kanatzidis, S. T. Nguyen, R. Q. Snurr and J. T. Hupp, *Nature Chemistry*, 2010, **2**, 944–948.
- 9 L. E. Kreno, K. Leong, O. K. Farha, M. Allendorf, R. P. Van Duyne and J. T. Hupp, *Chem. Rev.*, 2012, **112**, 2, 1105–1125.
- 10 B. Li, H. M. Wen, W. Zhou and B. Chen, *J. Phys. Chem. Lett.*, 2014, **5**, 3468–3479.
- 11 M. O’Keeffe, *Chem. Soc. Rev.*, 2009, **38**, 1215–1217.
- 12 S. Yuan, L. Feng, K. Wang, J. Pang, M. Bosch, C. Lollar, Y. Sun, J. Qin, X. Yang, P. Zhang, Q. Wang, L. Zou, Y. Zhang, L. Zhang, Y. Fang, J. Li and H. C. Zhou, *Adv. Mat.*, 2018, 1704303.
- 13 S. R. Venna and M. A. Carreon, *Chem. Eng. Sci.*, 2015, **124**, 3–19.
- 14 H. B. Tanh Jeazet, C. Staudt and C. Janiak, *Dalton Trans.*, 2012, **41**, 14003–14027.
- 15 M. J. Kalmutzki, N. Hanikel and O. M. Yaghi, *Sci. Adv.*, 2018, **4**, 9180.
- 16 J. Hu, L. Huang, X. Yao, L. Qin, Y. Li, Z. Guo, H. Zheng and Z. Xue, *Inorg. Chem.*, 2011, **50**, 2404–2414.
- 17 S. Qiu and G. Zhu, *Coord. Chem. Rev.*, 2009, **253**, 2891–2911.
- 18 P. P. Soufeena, K. Subin Kumar and K. K. Aravindhakshan, in *Materials Today: Proceedings*, Elsevier Ltd, 2018, **5**, 16790–16799.
- 19 H. X. Zhang, B. S. Kang, A. W. Xu, Z. N. Chen, Z. Y. Zhou, A. S. C. Chan, K. B. Yu and C. Rena, *J. Chem. Soc.*, 2001, 2559–2566.
- 20 S. A. Bourne, J. Lu, A. Mondal, B. Moulton and M. J. Zaworotko, *Angew. Chem. Int. Ed.*, 2001, **40**, 2111–2113.
- 21 P. Deria, J. E. Mondloch, O. Karagiari, W. Bury, J. T. Hupp and O. K. Farha, *Chem. Soc. Rev.*, 2014, **43**, 5896–5912.
- 22 B. F. Hoskins and R. Robson, *J. Am. Chem. Soc.*, 1989, **111**, 5962–5964.
- 23 B. F. Hoskins and R. Robson, *J. Am. Chem. Soc.*, 1990, **112**, 1546–1554.

## Chapter 1: Introduction

---

- 24 O. M. Yaghi, M. O’Keeffe, N. W. Ockwig, H. K. Chae, M. Eddaoudi and J. Kim, *Nature*, 2003, 423, 705–714.
- 25 N. L. Rosi, *Science*, 2003, **300**, 1127–1129.
- 26 W. Lu, Z. Wei, Z. Y. Gu, T. F. Liu, J. Park, J. Park, J. Tian, M. Zhang, Q. Zhang, T. Gentle, M. Bosch and H. C. Zhou, *Chem. Soc. Rev.*, 2014, **43**, 5561–5593.
- 27 S. Hausdorf, F. Baitalow, T. Böhle, D. Rafaja and F. O. R. L. Mertens, *J. Am. Chem. Soc.*, 2010, **132**, 10978–10981.
- 28 N. Stock, S. Biswas and S. M. Cohen, *Chem. Rev.*, 2012, **112**, 933–969.
- 29 V. V. Butova, M. A. Soldatov, A. A. Guda, K. A. Lomachenko and C. Lamberti, *Russ. Chem. Rev.*, 2016, **85**, 280–307.
- 30 D. J. Tranchemontagne, J. R. Hunt and O. M. Yaghi, *Tetrahedron Lett.*, 2008, **64**, 8553–8557.
- 31 S. H. Jhung, J.-H. Lee, J. W. Yoon, C. Serre, G. Férey and J.-S. Chang, *Adv. Matter.*, 2007, **19**, 121–124.
- 32 W. J. Son, J. Kim, J. Kim and W. S. Ahn, *ChemComm.*, 2008, 6336–6338.
- 33 M. Hartmann, S. Kunz, D. Himsl, O. Tangermann, S. Ernst and A. Wagener, *Langmuir*, 2008, **24**, 8634–8642.
- 34 T. Friščić, D. G. Reid, I. Halasz, R. S. Stein, R. E. Dinnebier and M. J. Duer, *Angew. Chem. Int. Ed.*, 2010, **49**, 712–715.
- 35 C. Dey, T. Kundu, B. P. Biswal, A. Mallick and R. Banerjee, *Acta. Crystallogr. B: Struct. Sci. Cryst. Eng. Mater.*, 2014, **70**, 3–10.
- 36 A. J. Howarth, A. W. Peters, N. A. Vermeulen, T. C. Wang, J. T. Hupp and O. K. Farha, *Chem. Mater.*, 2017, 29, 26–39.
- 37 R. Seetharaj, P. V. Vandana, P. Arya and S. Mathew, *Arab. J. Chem.*, 2019, 12, 295–315.
- 38 P. M. Forster, A. R. Burbank, C. Livage, G. Férey and A. K. Cheetham, *Chem. Commun.*, 2004, **4**, 368–369.
- 39 L. Huang, H. Wang, J. Chen, Z. Wang, J. Sun, D. Zhao and Y. Yan, *Micropor. Mesopor. Mat.*, 2003, **58**, 105–114.
- 40 E. Biemmi, S. Christian, N. Stock and T. Bein, *Micropor. Mesopor. Mat.*, 2009, **117**, 111–117.
- 41 S. Y. Kim, A. R. Kim, J. W. Yoon, H. J. Kim and Y. S. Bae, *Chem. Eng. Sci.*, 2018, **335**, 94–100.
- 42 D. Liu, Y. Liu, G. Xu, G. Li, Y. Yu and C. Wang, *Eur. J. Inorg. Chem.*, 2012, **2012**, 4413–4417.
- 43 Y. R. Lee, J. Kim and W. S. Ahn, *Korean J. Chem. Eng.*, 2013, 30, 1667–1680.
- 44 A. Schaate, P. Roy, A. Godt, J. Lippke, F. Waltz, M. Wiebcke and P. Behrens, *Chem. Eur.*, 2011, **17**, 6643–6651.
- 45 T. Jin, Y. K. Hwang, D. Y. Hong, S. H. Jhung, J. S. Hwang, S. E. Park, Y. H. Kim and J. S. Chang, *Res. Chem. Intermed.*, 2007, **33**, 501–512.
- 46 S. H. Jhung, J. S. Chang, Y. K. Hwang and S. E. Park, *J. Mater. Chem.*, 2004, **14**, 280–285.

## Chapter 1: Introduction

---

- 47 A. Gedanken, *Ultrasonics Sonochemistry*, 2004, 11, 47–55.
- 48 K. S. Suslick, S. B. Choe, A. A. Cichowlas and M. W. Grinstaff, *Nature*, 1991, **353**, 414–416.
- 49 K. S. Suslick, D. A. Hammerton and R. E. Cline, *J. Am. Chem. Soc.*, 1986, **108**, 5641–5642.
- 50 A. Martinez Joaristi, J. Juan-Alcañiz, P. Serra-Crespo, F. Kapteijn and J. Gascon, *Crys. Growth Dec.*, 2012, **12**, 3489–3498.
- 51 A. L. Garay, A. Pichon and S. L. James, *Chem. Soc. Rev.*, 2007, **36**, 846–855.
- 52 Y. R. Lee, J. Kim and W. S. Ahn, *Korean J. Chem. Eng.*, 2013, 30, 1667–1680.
- 53 R. Ameloot, F. Vermoortele, W. Vanhove, M. B. J. Roeffaers, B. F. Sels and D. E. De Vos, *Nature Chem.*, 2011, **3**, 382–387.
- 54 D. Witters, N. Vergauwe, R. Ameloot, S. Vermeir, D. De Vos, R. Puers, B. Sels and J. Lammertyn, *Adv. Mater.*, 2012, **24**, 1316–1320.
- 55 C. Férey, C. Mellot-Draznieks, C. Serre, F. Millange, J. Dutour, S. Surblé and I. Margiolaki, *Science*, 2005, **309**, 2040–2042.
- 56 H. Furukawa, K. E. Cordova, M. O’Keeffe and O. M. Yaghi, *Science*, 2013, **341**, 1230444.
- 57 U. Mueller, M. Schubert, F. Teich, H. Puetter, K. Schierle-Arndt and J. Pastré, in *J. Mat. Chem.*, The Royal Society of Chemistry, 2006, vol. 16, pp. 626–636.
- 58 A. U. Czaja, N. Trukhan and U. Müller, *Chem. Soc. Rev.*, 2009, **38**, 1284–1293.
- 59 M. Jacobi, *Chem. Eng. News*, 2008, **86**, 13–16.
- 60 A. U. Czaja, N. Trukhan and U. Müller, *Chem. Soc. Rev.*, 2009, **38**, 1284–1293.
- 61 *United States Pat.*, EP 1,674,555, 2005, 2005, 1,674,555.
- 62 *Germany. Pat.*, WO 2006072573 A2, 2005.
- 63 M. Dincă and J. R. Long, *J. Am. Chem. Soc.*, 2005, **127**, 9376–9377.
- 64 T. K. Maji, G. Mostafa, H. C. Chang and S. Kitagawa, *Chem. Commun.*, 2005, 2436–2438.
- 65 L. Pan, B. Parker, X. Huang, D. H. Olson, J. Y. Lee and J. Li, *J. Am. Chem. Soc.*, 2006, **128**, 4180–4181.
- 66 D. N. Dybtsev, H. Chun and K. Kim, *Chem. Commun.*, 2004, **4**, 1594–1595.
- 67 P. L. Llewellyn, S. Bourrelly, C. Serre, Y. Filinchuk and G. Férey, *ngew. Chem. Int. Ed.*, 2006, **45**, 7751–7754.
- 68 X. Zhang, I. Da Silva, H. G. W. Godfrey, S. K. Callear, S. A. Sapchenko, Y. Cheng, I. Vitorica-Yrezabal, M. D. Frogley, G. Cinque, C. C. Tang, C. Giacobbe, C. Dejoie, S. Rudić, A. J. Ramirez-Cuesta, M. A. Denecke, S. Yang and M. Schröder, *J. Am. Chem. Soc.* 2017, **139**, 16289–16296.
- 69 R. Matsuda, R. Kitaura, S. Kitagawa, Y. Kubota, R. V. Belosludov, T. C. Kobayashi, H. Sakamoto, T. Chiba, M. Takata, Y. Kawazoe and Y. Mita, *Nature*, 2005, **436**, 238–241.
- 70 G. Férey, M. Latroche, C. Serre, F. Millange, T. Loiseau and A. Percheron-Guégan, *Chem. Soc. Rev. Commun.*, 2003, **3**, 2976–2977.
- 71 T. Mueller and G. Ceder, *J. Ohys. Chem. B*, 2005, **109**, 17974–17983.

## Chapter 1: Introduction

---

- 72 D. N. Dybtsev, H. Chun and K. Kim, *Angew. Chem. Int. Ed.*, 2004, **43**, 5033–5036.
- 73 K. Seki and W. Mori, *J. Phys. Chem. B*, 2002, **106**, 1380–1385.
- 74 Q. Yang and C. Zhong, *J. Phys. Chem. B*, 2005, **109**, 11862–11864.
- 75 Y. H. Hu and L. Zhang, *Adv. Mat.*, 2010, **22**, E117–E130.
- 76 R. B. Lin, S. Xiang, W. Zhou, and B. Chen, *Chem.*, 2020, **6**, 337–363.
- 77 K. C. Szeto, K. O. Kongshaug, S. Jakobsen, M. Tilset and K. P. Lillerud, *J. Chem. Soc.*, 2008, 2054–2060.
- 78 C. Janiak and J. K. Vieth, *New J. Chem.*, 2010, **34**, 2366–2388.
- 79 F. D. Duman and R. S. Forgan, *J. Mater. Chem. B*, 2021, **9**, 3423–3449
- 80 M. Oh and C. A. Mirkin, *Nature*, 2005, **438**, 651–654.
- 81 M. A. Chowdhury, *J. Biomed. Mater. Res. A*, 2017, **105**, 1184–1194.
- 82 P. Horcajada, T. Chalati, C. Serre, B. Gillet, C. Sebrie, T. Baati, J. F. Eubank, D. Heurtaux, P. Clayette, C. Kreuz, J. S. Chang, Y. K. Hwang, V. Marsaud, P. N. Bories, L. Cynober, S. Gil, G. Férey, P. Couvreur and R. Gref, *Nature Mat.*, 2010, **9**, 172–178.
- 83 J. An, S. J. Geib and N. L. Rosi, *J. Am. Chem. Soc.*, 2009, **131**, 8376–8377.
- 84 N. Liédana, A. Galve, C. Rubio, C. Téllez and J. Coronas, *ACS Appl. Mater. Interfaces*, 2012, **4**, 5016–5021.
- 85 K. M. L. Taylor-Pashow, J. Della Rocca, Z. Xie, S. Tran and W. Lin, *J. Am. Chem. Soc.*, 2009, **131**, 14261–14263.
- 86 I. I. Slowing, J. L. Vivero-Escoto, C. W. Wu and V. S. Y. Lin, *Adv. Drug Deliv. Rev.*, 2008, **60**, 1278–1288.
- 87 P. Horcajada, C. Serre, M. Vallet-Regí, M. Sebban, F. Taulelle and G. Férey, *Angew. Chem. Int. Ed.*, 2006, **45**, 5974–5978.
- 88 M. A. Chowdhury, *J. Chem.*, 2017, **7**, 1–22.
- 89 S. Chopra, S. Dhumal, P. Abeli, R. Beaudry and E. Almenar, *Postharvest Biol. Tec.*, 2017, **130**, 48–55.
- 90 M. L. Foo, R. Matsuda and S. Kitagawa, *Chem. Mater.*, 2014, **26**, 310–322.
- 91 T. Kitao, Y. Zhang, S. Kitagawa, B. Wang and T. Uemura, *Chem. Soc. Rev.*, 2017, **46**, 3108–3133.
- 92 S. Li and F. Huo, *Nanoscale*, 2015, **7**, 7482–7501.
- 93 P. Sozzani, S. Bracco, A. Comotti, R. Simonutti, P. Valsesia, Y. Sakamoto and O. Terasaki, *Nature Mater.*, 2006, **5**, 545–551.
- 94 K. Tajima and T. Aida, *Chem. Commun.*, 2000, 2399–2412.
- 95 S. Mochizuki, T. Kitao and T. Uemura, *Chem. Commun.*, 2018, **54**, 11843–11856.
- 96 R. Q. Zou, H. Sakurai and Q. Xu, *Angew. Chem. Int. Ed.*, 2006, **45**, 2542–2546.

## Chapter 1: Introduction

---

- 97 T. Uemura, R. Kitaura, Y. Ohta, M. Nagaoka and S. Kitagawa, *Angew. Chem. Int. Ed.*, 2006, **45**, 4112–4116.
- 98 T. S. Koblenz, J. Wassenaar and J. N. H. Reek, *Chem. Soc. Rev.*, 2008, **37**, 247–262.
- 99 T. Uemura, *Kinetic Control in Synthesis of Polymers Using Nanoporous Metal-Organic Frameworks*, Elsevier, New York, 2018.
- 100 B. Le Ouay and T. Uemura, *Isr. J. Chem.*, 2018, **58**, 995–1009.
- 101 T. Uemura, K. Kitagawa, S. Horike, T. Kawamura, S. Kitagawa, M. Mizuno and K. Endo, *Chem. Commun.*, 2005, 5968–5970.
- 102 T. Uemura, Y. Ono, K. Kitagawa and S. Kitagawa, *Macromolecules*, 2008, **41**, 87–94.
- 103 J. Hwang, H.-C. Lee, M. Antonietti and B. V. K. J. Schmidt, *Polym. Chem.*, 2017, **8**, 6204–6208.
- 104 G. Moad, E. Rizzardo and S. H. Thang, *Aus. J. Chem.*, 2005, **58**, 379–410.
- 105 G. Moad, E. Rizzardo and S. H. Thang, *Aus. J. Chem* 2009, **62**, 1402–1472.
- 106 J. Hwang, H.-C. Lee, M. Antonietti and B. V. K. J. Schmidt, *Polym. Chem.*, 2017, 6204–6208.
- 107 B. V. K. J. Schmidt, *Macromol. Rapid Commun.*, 2020, **41**, 1900333.
- 108 D. F. Emerich and C. G. Thanos, *Biomol. Eng.*, 2006, **23**, 171–184.
- 109 E. Andronescu and A. Grumezescu, *Nanostructures for Drug Delivery - 1st Edition*, Elsevier, 2017, vol. 2.
- 110 N. Raina, R. Rani, A. Khan, K. Nagpal and M. Gupta, *Polym. Bull.*, 2019, 1–24.
- 111 Daniel Klempner, L. H., *American Chemical Society – Division of Polymeric Materials: Science and Engineering Meeting – Chemical Congress of North America*, 1994.
- 112 D. K. Gilding and A. M. Reed, *Polymer*, 1979, **20**, 1459–1464.
- 113 L. S. Nair and C. T. Laurencin, *Prog. Polym. Sci.*, 2007, **32**, 762–798.
- 114 F. O. Eschbach, S. J. Huang, J. A. Cameron, *Journal of Bioactive and Compatible Polymers*, 1994, **9**, 234–235.
- 115 N. Mehta, PhD Annual Progression Review Report, Cardiff University, 2018.
- 116 M. Chamundeeswari, J. Jeslin and M. L. Verma, *Environ. Chem. Lett.*, 2019, **17**, 849–865.
- 117 S. Han and M. S. Lah, *Crys. Growth Des.*, 2015, **15**, 5568–5572.
- 118 B. V. K. J. Schmidt, *Macromol. Rapid Commun.*, 2020, **41**, 1900333.
- 119 A. C. Mescall and S. T. Easun, M.Sc. Report, Cardiff University, 2007.
- 120 B. Yeskendir, D. P. Dacquin, Y. Lorgouilloux, C. Cortois, S. Royer, and J. Dahanaut, *Mater. Adv.*, 2021, **2**, 7139–7186.

# Chapter 2

---

## Project Background

## Chapter 2: Project Background

---

### 2 Background Information on Key Materials

#### 2.1 Metal–Organic Frameworks

The work presented in this thesis is concentrated on two prototypical metal-organic frameworks, a zinc-based dicarboxylate, MOF-5 and copper tricarboxylate, HKUST-1. The choice of metal-organic framework for the project was on the basis of earlier studies establishing the credibility of ‘template synthesis’ of polymers in MOFs, previous research carried out in the Easun laboratory suggested that MOF-5, HKUST-1, and MIL-53 were good candidates for the template synthesis of the polymers.<sup>1</sup>

MOF-5 and HKUST-1 were selected for the study considering their characteristics such as pore dimensions, inability of zinc and copper to bioaccumulate in the body that may hinder the application of drug delivery, ease of breaking down the structure for polymer extraction, and recyclability of the MOF.

##### 2.1.1 MOF-5 (IRMOF-1) [Zn<sub>4</sub>O(C<sub>8</sub>H<sub>4</sub>O<sub>4</sub>)<sub>3</sub>]

MOF-5 is a zinc-based MOF that consists of [Zn<sub>4</sub>O]<sup>6+</sup> building units that are connected with linear 1,4-benzenedicarboxylate struts to form a cubic network (Fig 2.1). MOF-5 (IRMOF-1) was first discovered by Rosi *et al.* as one of the MOFs exhibiting ‘reticular chemistry’ and presented MOF-5 as a promising candidate for hydrogen storage.<sup>2</sup> MOF-5 has open skeleton structure, controlled pore structure and pore surface area and high thermal stability function, which has been widely studied in gas storage and separation, electrochemistry, catalysis, and medicine.<sup>3-5</sup>

## Chapter 2: Project Background

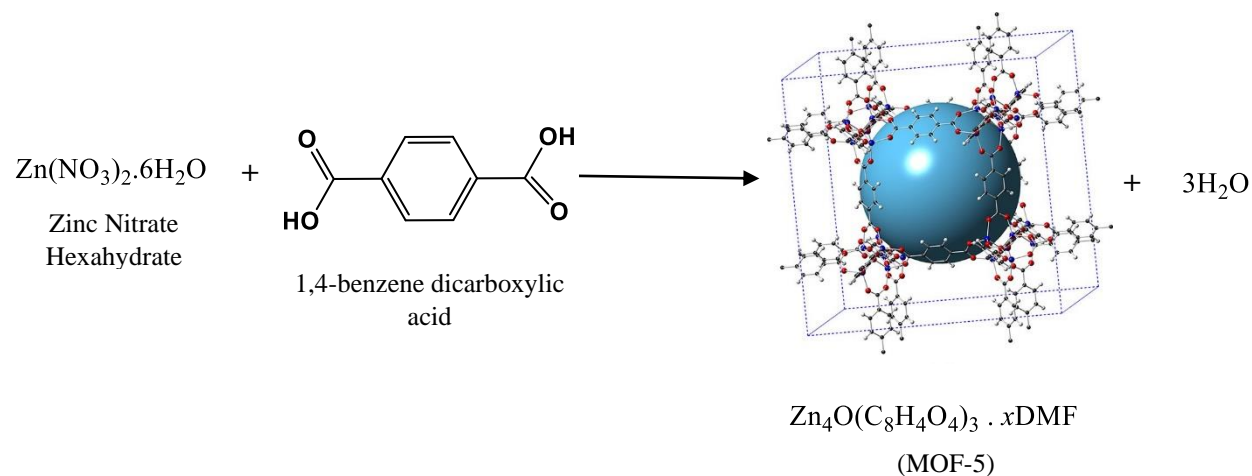


Fig 2.1: Reaction scheme for the synthesis of MOF-5 from zinc nitrate hexahydrate and terephthalic acid. The blue sphere in the MOF-5 structure is for visual aid depicting the spherical void space.

### ***'Reticular Chemistry'***

Reticular chemistry is responsible for the large number of MOFs known to date: an isorecticular series based on MOF-5 (the IRMOF series) was one of the first and the largest to be discovered. In its essence, reticular chemistry is concerned with linking secondary building units into extended porous frameworks with strong covalent bonds.<sup>2</sup> For a given framework shape it is possible to prepare a series of analogues that exhibit the same topology but differing only in the nature and size of the links — an isorecticular series. The series of isorecticular MOFs (IRMOFs) was the first such series and based on this concept, the IRMOF family has expanded over the years with several new additions using different benzene carboxylate ligands and tetranuclear and tetrahedral  $\text{Zn}_4\text{O}$  building units, IRMOF- $n$  ( $n = 1-16$ ), with larger and tunable pore sizes ranging from 3.8 to 29 Å, and pore volumes up to 1  $\text{cm}^3/\text{g}$  with high porosity.<sup>6</sup> (Shown in Fig. 2.2 as a representation of ditopic carboxylate linkers and illustration of formation of extended IRMOF networks by replacing acetate with rigid dicarboxylates.<sup>7</sup>)

## Chapter 2: Project Background

---

It was suggested that using other ditopic carboxylate linkers that are closely related, and by employing identical conditions would yield the same type of frameworks with diverse pore sizes and functionalities.<sup>8</sup> Using the range of linkers  $R_n$ -BDC (where,  $n = 2-7$ ), 2,6-NDC, BPDC, HPDC, PDC, and TPDC instead of BDC yielded a series of MOFs from IRMOF-2 through -16, including the non-interpenetrating structures of BPDC, HPDC, PDC, and TPDC. Comparison of the percent free volume in crystals of IRMOF-1 through -16 shows that it varies in small increments (1 to 5%) from 55.8% in IRMOF-5 to 91.1% in IRMOF-16. Although the increments are relatively small, their free volume is considerably higher than most open zeolites.

### *Structure and Properties*

MOF-5 exhibits a simple cubic structure with a  $[Fm\bar{3}m]$  space group and a unit cell length of  $a = 25.44 \text{ \AA}$ . The MOF-5 structure has a square shaped pore of  $7 \times 7 \text{ \AA}$ . The surface area and pore volume are the decisive properties that warrants the use of MOF for many applications such as gas storage, gas adsorption, drug loading etc. MOF-5 isolated and desolvated in air has been reported to have surface area range of about  $SA_{\text{BET}} = 950 - 3500 \text{ g/cm}^2$  and  $SA_{\text{Langmuir}} = 1250 - 4400 \text{ g/cm}^2$ .<sup>3</sup> Noticeably, MOF-5 desolvated under nitrogen has shown to possess a larger surface area.<sup>9</sup>

Table 2.1: A summary of structural, thermal, hydrogen isotherm properties for MOF-5. The data are averages of the most consistent values from 20 literature studies that use solvothermal synthesis.<sup>10</sup>

	Units	Value	Conditions
<b><i>Structure Properties</i></b>			
Bulk Density	$\text{g cm}^{-3}$	0.13	Fixed tapping.
		0.22	Tapping with Jolt.
Skeletal Density		0.59	Single Crystal Density
BET Surface Area	$\text{m}^2 \text{ g}^{-1}$	3800	$\text{N}_2$ Isotherm at 77 K
Micropore Volume	$\text{cm}^3 \text{ g}^{-1}$	1.55	Ar Isotherm at 87 K

## Chapter 2: Project Background

Skeletal Volume	cm <sup>3</sup>	1.65 x 10 <sup>-20</sup>	Single Crystal
Lattice Parameter	Å	25.4	PXRD
Mean Particle Diameter	µm	0.36	
<b><i>Thermal Properties</i></b>			
Heat Capacity (c <sub>p</sub> )	J g <sup>-1</sup> K <sup>-1</sup>	0.09	300 K, ρ = 0.35 g/cm <sup>3</sup>
Thermal Conductivity (k)	W m <sup>-1</sup> K <sup>-1</sup>	0.72	300 K
<b><i>Hydrogen Isotherm Parameters</i></b>			
α	J mol <sup>-1</sup>	2240	-
β	J mol <sup>-1</sup> K <sup>-1</sup>	19.5	
η <sub>max</sub>	mol kg <sup>-1</sup>	125	
P <sub>o</sub>	MPa	1692	
V <sub>a</sub>	ml g <sup>-1</sup>	2.00	

The Zn–O bond length in the single-crystal structure of MOF-5, the single-crystal structure of zinc nitrate that contributes to the SBU in MOF-5, and the hexagonal ZnO SBU are very similar in the order of ~ 1.9 Å.<sup>11</sup> The C–C and C–H bond length in the MOF structure is also consistent with those found on carboxylates (1.4 – 1.5 Å and 0.9 Å respectively), the C–O bond linking the SBU and the carboxylate linker has a length is at the order of 1.3 Å.<sup>12</sup> These similarities suggest that the energetic differences between the dense assemblages and the final MOF stem from the void space in MOF-5. ZnO has a framework density (FD) of 42.0 Zn•nm<sup>-3</sup>, while for MOF-5 is 1.9 Zn•nm<sup>-3</sup>. The large difference reiterates the high porosity character that desolvated MOF-5 possesses.

## Chapter 2: Project Background

---

### Interaction of MOF-5 with water and solvent DMF molecules.

The extremely porous nature of MOF-5 also contributes to much of its framework instability that results from water adsorption. The degradation of MOF-5 following exposure to moisture or air with relatively high humidity has been reported in several studies.<sup>13–15</sup> Long *et al.* reported the hydrolysis of MOF-5 by measuring hydrogen isotherms and X-ray diffraction patterns of samples before and after exposure to humid air.<sup>14</sup> Schröck and co-workers identified the water loading threshold for the degradation of MOF-5; irreversible decomposition was observed after an uptake of 8 wt % water.<sup>16</sup> Cychoz and Matzger also analysed the structure of several MOFs: MOF-177 MOF-5, HKUST-1, MOF-505, UMCM-150, MIL-100, and Zn(2-methylimidizolate).<sup>17</sup> Following exposure to dimethylformamide (2 mL) solutions containing 50 to 2000  $\mu\text{L}$  of water; they concluded that the MOF stability was related to the composition and geometry of the metal cluster of MOFs. Many of these studies conclude that MOF-5 has a characteristic and drastic increase in water uptake (type V isotherm) coinciding with a rapid, irreversible structure change upon exposure to air with a relative humidity of 50% or higher.<sup>18</sup> Below this threshold humidity, the uptake of water was limited and resulted in little change in structure over an exposure times up to several hours. The faster rates of structure decomposition of MOF-5 hint that the water coverage on the adsorption sites within the MOF may affect the energies associated with irreversible hydrolysis of the framework.<sup>18</sup>

A small number of studies have investigated how the water-induced degradation mechanism proceeds and have employed molecular dynamics (MD) and first-principle calculations to understand the effects leading to the degradation. The earliest studies of water in adsorption in MOF-5 by Greathouse and Allendorf revealed that the adsorbed water interacts more strongly with Zn sites as compared to the carboxylate linker. Furthermore, the water molecules can insert into the MOF-5 upon breaking of Zn–O bonds.<sup>19</sup> Han *et al.* further expanded the study by predicting a reaction mechanism associated with MOF hydrolysis where the adsorbed water dissociates into a hydroxyl group and a proton. This is followed by the –OH group bonds to Zn breaking the Zn–O bond between the metal cluster and the linker. The remaining hydrogen then joins with the organic linker to form carboxylic acid.<sup>20</sup>

## Chapter 2: Project Background

---

A study by Siegel *et al.* evaluated the energetics associated with water adsorption and insertion into MOF-5 framework as a function of coverage using van der Waals-aware functional to capture dispersion interactions present during molecular adsorption. A key finding of their study was that the thermodynamics of water insertion into MOF-5 is dependent of coverage of the water molecules on the framework.<sup>21</sup> The water molecule insertion becomes thermodynamically favourable only when a critical number of water molecules are adsorbed as relatively compact clusters on the same  $Zn_4O$  secondary building unit of the MOF.

Ming *et al.* calculated the thermodynamics of water adsorption at various sites in MOF-5. Subsequently, the energetics for hydrolysis are evaluated as a function of the local coverage of water near the Zn–O insertion point.<sup>21</sup> They identified five distinct sites at which water molecules interact with MOF-5. These sites are illustrated as large purple spheres in Fig 2.2 and labelled with Greek letters  $\alpha$ ,  $\beta$ ,  $\gamma$ ,  $\delta$ , and  $\epsilon$ .

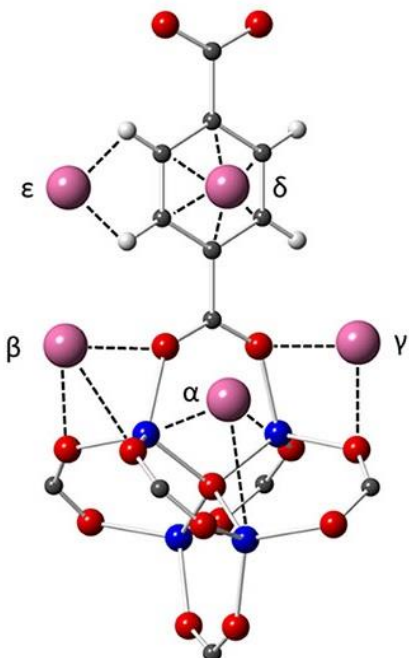


Fig 2.2: Magnification of the metal cluster and the organic linker from MOF-5 structure. The purple spheres represent five distinct sites for water adsorption and are labelled with Greek symbols. (*Image reproduced with permission*)<sup>16</sup>

## Chapter 2: Project Background

---

The three sites  $\alpha$ ,  $\beta$ , and  $\gamma$  exist on the Zn–O metal cluster, whereas  $\delta$  and  $\epsilon$  are present on the linker around the benzene ring. Site  $\alpha$  is the closest site to the central oxygen in the Zn cluster and is equidistant to three of the Zn atoms bonded to the central oxygen. Site  $\beta$  is closest to one of the four Zn atoms in the cluster and is equidistant to three of the four oxygen atoms bonded to Zn. Site  $\gamma$  is within the proximity two oxygen atoms bonded to Zn. On the linker, site  $\delta$  is located above the face of the benzene ring. Site  $\epsilon$  is positioned at the edge of the benzene, with equal distances to two hydrogen atoms. Table 2.2 lists the number of each type of site on a single metal cluster or linker. In total, there are 20 adsorption sites on the metal cluster and 12 sites on the linker.

Table 2.2: Location and number of each type of adsorption site in a unit cell depicted with the number of water molecules adsorbed.

Location	Site Name	Number of Sites
Zn–O Cluster	$\alpha$	4
	$\beta$	4
	$\gamma$	12
Linker	$\delta$	6
	$\epsilon$	6

Over the years, interest in studies concerning MOF-5 has steadily increased with majority of the studies concentrated over gas adsorption and storage. The consistent attention towards MOF-5 is due to its ease of synthesis that can be scaled up for a industrial application in addition to its attractive properties such as large surface area and pore volume as mentioned earlier. A major hindrance for its application on a larger scale remains its instability towards moisture. Currently, a large portion of research is focussed on identifying the ‘stability window’ or the conditions where the MOF-5 is stable to take advantage of its characteristics.

## Chapter 2: Project Background

---

### 2.1.2 HKUST-1 (MOF-199) [Cu<sub>3</sub>(C<sub>9</sub>H<sub>3</sub>O<sub>6</sub>)<sub>2</sub>],

HKUST-1 (Hong Kong University of Science and Technology-1) is a copper-based MOF made with copper ions coordinated with 1,3,5–benzene tricarboxylate (BTC) in a cubic  $[Fm-3m]$  lattice, and was first reported by Chui *et al.* in 1999.<sup>22</sup> Since its discovery, HKUST-1 has been used for a range of applications such as gas adsorption and storage,<sup>23</sup> gas sensing,<sup>24</sup> catalysis,<sup>25</sup> electrochemistry,<sup>26</sup> and biomedical applications.<sup>27</sup> Due to its ease of preparation and wide-spread usage in research, it has been commercialized by ACS Material, Plasma Chem, Advanced Chemical Synthesis and Manufacturing (ACSYNAM) and sold under the tradename Basolite C300 by BASF.

#### *Structure and Properties*

HKUST-1 consists of a 3-D intersecting system of large square-shaped pores of 9 x 9 Å. The framework of HKUST-1 consists of Cu (II) ions as dimers, where each copper atom is coordinated by four oxygen from BTC linkers and water molecules (Fig 2.3). The presence of water molecules in the first coordination sphere of Cu ions has been suggested as a way to obtain a coordinative valency on Cu (II) species.<sup>28</sup> The pores can hold up to 10 additional water molecules per formula unit.

## Chapter 2: Project Background

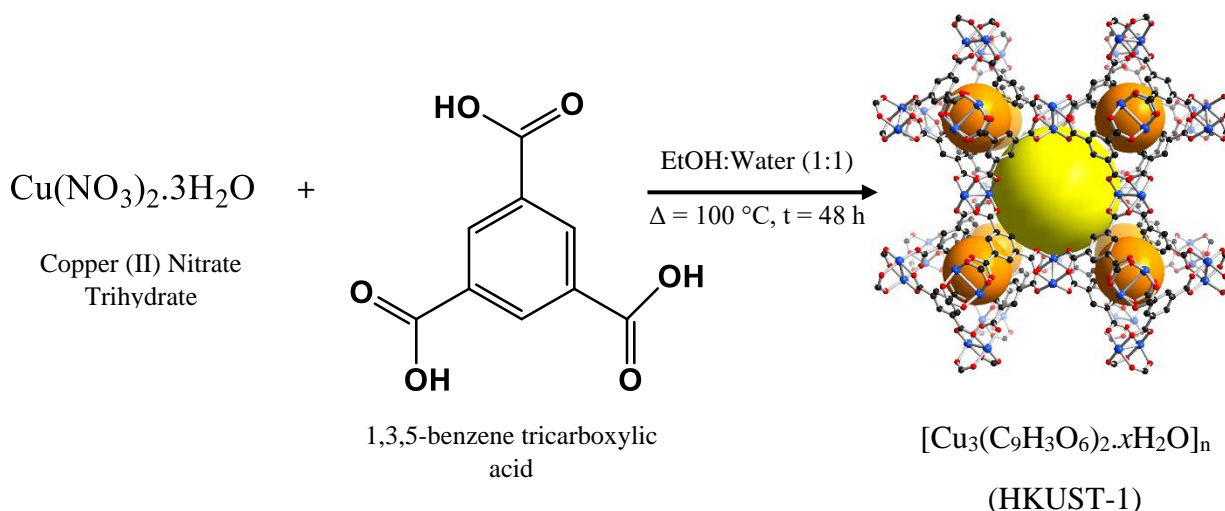


Fig 2.3: Reaction scheme for the synthesis of HKUST-1 from copper (II) nitrate trihydrate and trimesic acid. The yellow sphere in the HKUST-1 structure is for visual aid depicting the spherical void space, and the orange spheres depict the void space in the coordination sphere. Atoms: Blue – Cu; Red – O; Black – C. H-atom has been eliminated for clarity.

The polymeric framework of HKUST-1 is composed of dimeric cupric tetra-carboxylate units with the interatomic distance between Cu-Cu metal ions being 2.628 Å. The framework overall has a neutral charge with 12 carboxylate oxygens from the two BTC linkers bound to four coordination sites for each of the three Cu(II) ions of the formula unit. Such bimetallic tetracarboxylate units are a common occurrence for MOFs with *tbo* topology in space group  $[Fm\bar{3}m]$ .<sup>22</sup> Fig 2.4 shows HKUST-1 framework structure viewed down the [100] direction (a), showing nanochannels with fourfold symmetry and a hexagonal-shaped 18 Å window (b) when viewed along [111] direction. The occurrence of this highly stable arrangement is not just for Cu-based framework, but also for many other transition metal carboxylates such as quadruple-bonded molybdenum MOF  $[\text{Mo}_2(\text{O}_2\text{CCH}_3)_4]^{29}$  and its catalytically active rhodium analogue  $[\text{Rh}_2(\text{O}_2\text{CCH}_3)_4]^{30}$

## Chapter 2: Project Background

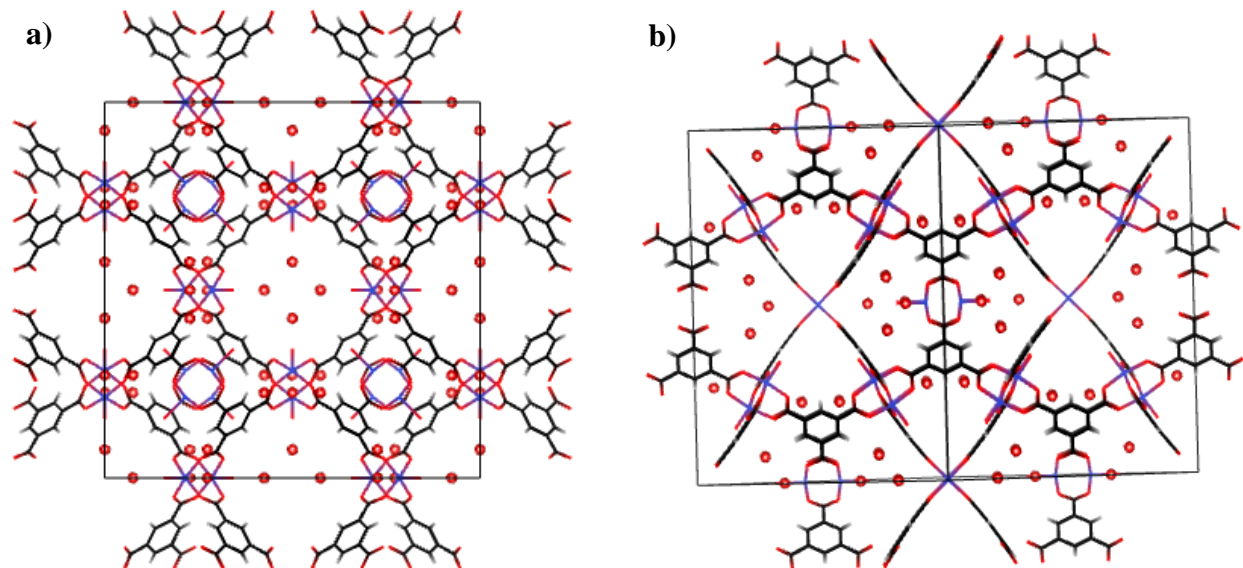


Fig 2.4: (a) Wireframe scheme for HKUST-1 framework viewed down the [100] direction, showing nanochannels with fourfold symmetry. (b) viewed along the cell body diagonal [111], showing a hexagonal-shaped 18 Å window at the intersection of the nanopores. Blue – Cu; Red – O; Black – C; H – Grey.

HKUST-1 is thermally stable up to 240°C and offers potential for chemical functionalization of the organic linkers. It has a high surface area ( $SA_{\text{BET}} = 1500\text{-}2100 \text{ m}^2/\text{g}$ ), good stability, and relatively straightforward synthesis. Despite its commercialization and widespread availability, research trends for HKUST-1 has continued to grow ever since its discovery.

### *Host-Guest Interactions*

An important characteristic of HKUST-1 that is especially attractive for applications such as gas adsorption is that the solvent molecules contained in the channels after the synthesis can be removed by thermal treatment, resulting in efficient removal of guest and producing an activated MOF.<sup>31</sup> The vacant coordination sites at the metal ions present in the framework are the main site for guest molecules to interact to the framework along with the sites where there may be defects present in the MOF motif. In other words, the interaction energy only depends on the distribution of electron density around  $\text{Cu}^{2+}$  centers. The electron density is equivalent in both its

## Chapter 2: Project Background

---

high-spin ferromagnetic state and low-spin antiferromagnetic states, and does not change if the  $\text{Cu}^{2+}$  centers are ferro- or antiferromagnetically coupled.<sup>32</sup>

Supronowicz *et al.* studied the host-guest interactions of several guest molecules in HKUST-1 such as CO, CO<sub>2</sub>, OCS, SO<sub>2</sub>, NO, NO<sub>2</sub>, N<sub>2</sub>O, NH<sub>3</sub>, PH<sub>3</sub>, and other small molecules with the undercoordinated metal centers of the HKUST-1 by means of density functional theory.<sup>33</sup> IR measurements of CO adsorption indicate the defects are due to the presence of  $\text{Cu}^+$  centers.. Carbon monoxide binds strongly to  $\text{Cu}^+$ , whereas nitrogen monoxide prefers binding to  $\text{Cu}^{2+}$  as two recent studies for HKUST-1 have shown.<sup>34</sup>

In general, the type of interactions can be classified in three categories: weak physisorption, polarization and electrostatics, and strong acid–base interactions. The nature of these interactions largely depends on the chemistry of the molecules adsorbed. Interactions of molecules in HKUST-1 are significantly stronger for the uncoordinated metal sites when compared to the carboxylate linker for water molecules, suggesting that water interacts with the metal sites in a Lewis acid-base type interaction. Only ammonia is adsorbed stronger to the metal sites than water. Hydrogen sulfide and phosphane on the other hand are less strongly bound than water. Interactions for these four cases are too strong to be classified as physisorption and fall in the regime of chemisorption.<sup>35,36</sup>

For larger molecules, Souza *et al.* reported characterization of 5-fluorouracil (5-FU) drug in HKUST-1 through inelastic neutron scattering (INS).<sup>37</sup> The popular anti-cancer drug, 5-FU was encapsulated within HKUST-1 host framework, yielding a drug@MOF conjugate, 5-FU@HKUST-1. The interaction of the guest drug in HKUST-1 and the confinement studies of guest@MOF was studied through vibrational spectroscopy. Using time-resolved infrared spectra with density functional theory calculations, they examined dynamics of vibrational motions dissociation of 5-FU bound to the framework of HKUST-1 upon water exposure. It was found that HKUST-1 creates hydrophilic channels within the hydrophobic polyurethane matrix enabling control over drug release rates. The combination of hydrophilic MOF with a

## Chapter 2: Project Background

---

hydrophobic polymer can be harnessed to engineer a tunable composite that reduces the potential of unwanted burst effect commonly encountered in drug delivery. The researchers demonstrated that INS spectroscopy as a powerful technique to study the interactions between the drug molecule and the MOF and confinement effects through vibrational motions of the molecule.

### *Outlook*

Translation from research to real world applications for HKUST-1 has been rapidly developing for various industries. Like MOF-5, one of the major concerns for HKUST-1 is its sensitivity towards moisture. The defects created due to moisture attack, impede the gas adsorption and diffusion, catalytic activity, in addition to the optical and other electronic properties.<sup>38</sup> Besides post synthetic modifications of HKUST-1 that results in hydrophobicity, reconstructing and utilizing the buffer action of sacrificial bonds has a potential for enhancing the tolerance towards moisture.

Gas adsorption in HKUST-1 is both through physical and chemical adsorption. However, the total adsorption and desorption for applications in industry is usually considered by adjusting the balance of these two adsorptions. The selective adsorption for O<sub>2</sub> and CO<sub>2</sub> on HKUST-1 shows a visible potential for commercial and industrial application once the defects are overcome. HKUST-1 also has a relatively large pore diameter of 13 Å. This limits the practical application of loading catalysts and therapeutically active molecules to those of a relatively small molecular size.<sup>39</sup> Thus, it becomes important to investigate methods to design the structure of HKUST-1 so that it can be used as a preferable carrier for drug molecules by restricting the pore diameter. Although the large pore may limit the application for drug encapsulation, it may be advantageous towards template synthesis approach allowing penetration of guest molecules within the pores. Monomers and other organic molecules are capable of penetrating through these voids in the structure and interact with the coordinated metal centers as well as organic linker molecules. Template polymerisation strategies have been proven to be successful in our experiment and effective extraction of polymer networks and ease of disassembly of the HKUST-1 structure make it an attractive host for the approach (Discussed later in Chapter 4).

## Chapter 2: Project Background

---

### 2.2 Biodegradable Polymers

Polymers have played an important role in advancing the application of drug delivery by providing controlled release of both hydrophobic and hydrophilic pharmaceutical drugs. Whilst some recent advances in drug delivery have been predicated towards rational design of polymers tailored for specific drug molecules and/or engineered to exert distinct biological functions,<sup>40</sup> there is a vast amount of unexplored scope.

The fundamental requirement for polymers to be considered for drug delivery and other therapeutic applications is their ability to degrade naturally by dissolution of chain fragments in non-crosslinked systems without chemical alterations or not form byproducts that are toxic or harmful to the biological system.<sup>41,42</sup>

Degradation and erosion of a polymer can either be a surface or a bulk phenomenon. Surface degradation occurs when the polymer matrix is slowly removed from the surface, but the polymer volume fraction remains largely unaffected. On the other hand, bulk degradation results in no significant changes in the physical size and shape of the polymer until it fully collapsed as a result of degradation, but the fraction of polymer remaining in the carrier decreases over time. The dominant process is determined by the relative rates of solvent penetration into the polymer, diffusion of the degradation product, and degradation or dissolution of its macromolecular structure.<sup>43</sup> In an ideal scenario, polymers degrade into small metabolic compounds that are known to be nontoxic and are small enough for natural clearance mechanisms. Hence, in the studies outlined in the theses we have made consideration of selecting polymer systems that have been extensively studied and are widely used in industry for biological among other applications.<sup>44</sup>

## Chapter 2: Project Background

---

### 2.2.1 Polyvinyl Acetate (PVAc)

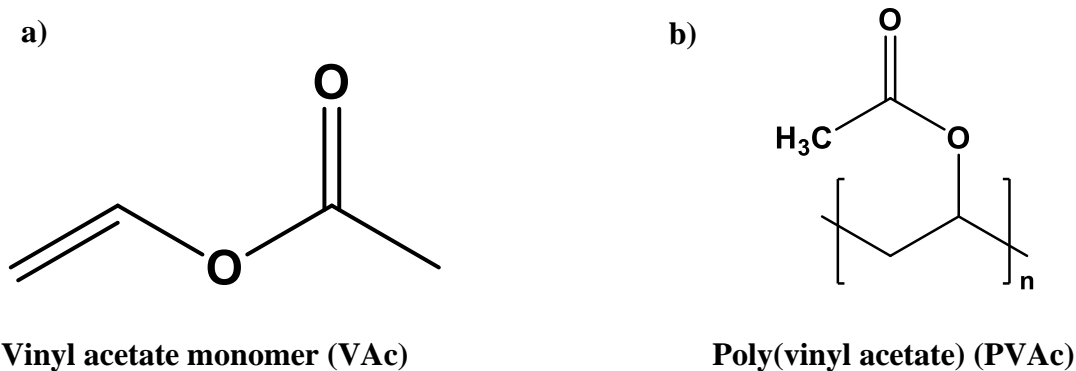


Fig 2.5: Chemical structure diagrams of (a) vinyl acetate monomer (VAc) and (b) standard repeating unit of a poly(vinyl acetate) polymer.

**Polyvinyl acetate (PVAc)** is a polyvinyl ester with a backbone formula of  $(C_4H_6O_2)_n$ , with the general formula  $-[RCOOCHCH_2]-$  (Fig 2.5). It is a colourless, non-toxic, atactic, highly branched, and non-crystalline thermoplastic, prepared by conventional free-radical polymerisation of vinyl acetate.<sup>45</sup> Vinyl acetate was discovered in 1912 by Dr Fritz Klatte in Germany, he found that the catalysed reaction of acetylene with acetic acid gave a low boiling liquid readily polymerised into a range of dense solid material, PVAc.<sup>46</sup> It has good resistance to UV and oxidation, but is rather brittle below its glass transition temperature ( $T_g$ ) and very sticky above it. PVAc resins produce clear, hard films that have good weather resistance and withstand water, grease, oil, and petroleum fuels. Additional properties are high initial tack, almost invisible bond line, softening at 30-45 °C, good biodegradation resistance, poor resistance to creep under load, and low cost. PVAc possess good adhesive properties with many porous substrates but are not effective on non-porous surfaces. As a result, PVAc is one of the main ingredients of water-based glues, commonly referred to as wood glue, carpenter's glue, Elmer's glue (USA), or white glue. PVAc resins and copolymers are also used as hot-melt adhesives, sealants, fabric finishing, plastic wood, and inks.<sup>47</sup>

## Chapter 2: Project Background

---

### Applications

Polyvinyl acetate is used in vast number of different applications.<sup>48</sup> The most common of the applications is in manufacturing of PVAc-based dispersions and dispersible polymer powders in the construction and adhesives industry. The polymeric binders are used as an additive to enhance the properties industrial binders such as tile adhesives, mortars and self-levelling compounds. PVAc dispersions are also used in many other adhesive formulations. PVAc forms the main ingredient in wood glues (white glue). It is also commonly used as a binder in the paper industry and as a binder in latex paints, although binders based on acrylics are far more common in paint technology. Almost one third of the PVAc produced goes into binder and adhesive applications.<sup>49</sup>

PVAc is approved by the Food and Drug Administration (FDA) for its use in the food and consumer industry. PVAc also constitutes as one of the main ingredients in every chewing gum. It is a major component in the so called 'gumbase', a mixture of different polymers that in combination with sugar, sweeteners, flavours, and other additives make up a chewing gum.<sup>50</sup> More often, PVAc is used as a major component of a copolymer (VAc, terpolymers, vinylacrylics, etc.) than a homopolymer itself. Additionally, in the applications mentioned above, PVAc and the related polymers are usually used as a part of complex mixture such as in fillers, plasticisers, impact modifiers, compatibilizers, or other polymers.

Polyvinyl acetate is also the raw material to make other polymers such as polyvinyl alcohol (PVA) which is used in a variety of medical applications because of its biocompatibility, low adherence towards proteins, and low toxicity. Specific uses include cartilage replacements, contact lenses, and eye drops.<sup>51,52</sup> Another important polymer derived from PVAc by partial hydrolysis followed by esterification with phthalic acid is polyvinyl acetate phthalate (PVAP), which forms the main component of enteric coatings for pharmaceutical tablets and capsules.<sup>53</sup> Summary of properties of poly(vinyl acetate) is provided in Appendix A2.1.<sup>‡</sup>

---

‡ - The appendix follows the following nomenclature: **A**<Chapter #>.<Fig/Table #>

## Chapter 2: Project Background

### 2.2.2 Poly(Lactic Acid) – PLA

**Poly(lactic acid, or polylactide (PLA))** is a thermoplastic polyester with backbone formula  $(C_3H_4O_2)_n$  or  $[-C(CH_3)HC(=O)O-]_n$ . PLA is a biodegradable thermoplastic polyester formally obtained by condensation polymerisation of lactic acid with loss of water (Fig 2.6). An alternative approach of polymerisation is by ring-opening polymerisation of lactide, the cyclic dimer of the basic repeating unit.<sup>54</sup>

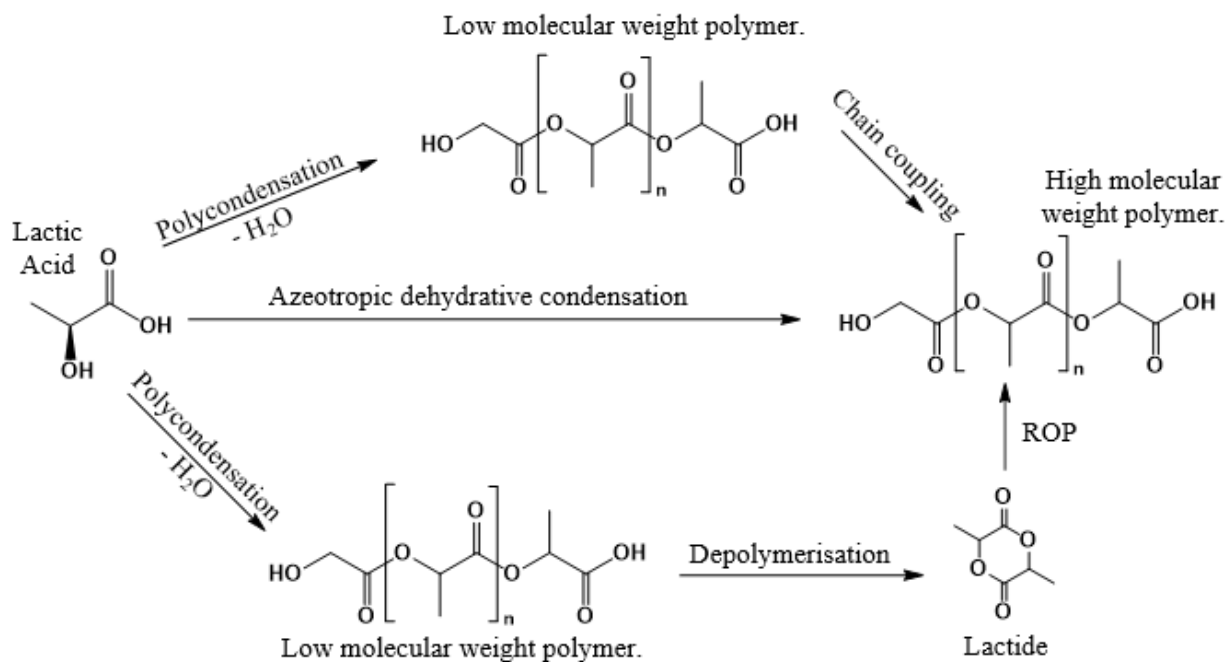


Fig 2.6: Approaches to obtain high molecular weight PLA.

Poly(lactic acid) was first developed in the 1980s in Japan. By 2010 it was the second most used bioplastic in the world by consumption volume.<sup>55</sup> Its widespread use is a credit to its availability from fermented plant sources, such as beet, corn starch, cassava roots, or sugarcane.

## Chapter 2: Project Background

---

The more common route of obtaining PLA is the ring-opening polymerisation of lactide aided by metal catalysts, typically tin octoate or metal alkoxides. The metal-catalysed reaction often results in a racemization of the PLA, reducing its stereoregularity compared to the starting material (usually corn starch).<sup>56</sup> ROP of L-lactide is generally the most preferred route for preparing high molecular weight PLA due to a greater ability to establish control over the chemistry and, as a result, varying the property of the polymer in a more controlled fashion. Polymerisations of lactide has been carried out by using melt polymerisation, bulk polymerisation, solution polymerisation, and suspension polymerisation techniques. Each of these methods has its own advantages and disadvantages, but melt polymerisation is generally considered the most simple and reproducible method of all listed above.<sup>57</sup>

Another approach to PLA is the direct condensation of lactic acid monomers. This process is carried out at temperatures less than 200 °C; above that temperature, the entropically favoured lactide monomer is generated. The condensation reaction generates one equivalent of water for every condensation or esterification step. The condensation reaction is reversible and subject to equilibrium, so removal of water is required to generate high molecular weight species. This route is a two-step reaction that usually requires an additional purification step that significantly drives up the overall cost. Achieving high molecular weight PLA for industrial applications by a direct dehydration condensation reaction is not feasible as the equilibrium does not favour a polymer of high molecular weight. As a result, PLA prepared from polycondensation reaction has low molecular weight and poor mechanical properties and therefore is not suitable for many applications.<sup>56</sup>

### Applications

PLA has a potential for use in a wide range of applications from packaging in the food industry to manufacturing of biomedical devices. A study in 2010 estimated an increase in other applications as well by 2020, especially in fibres and fabric.<sup>38</sup> In the field of packaging especially, high-value films and rigid-thermoformed containers are of high interest. PLA is also a growing alternative as a 'green' food packaging and are increasingly being used as food

## Chapter 2: Project Background

---

containers for fruits, vegetables, and salads.<sup>38</sup> PLA is used as a feed material in desktop fused filament fabrication 3D printers. PLA-printed solids can be encased in plaster-like moulding materials, then burned out in a furnace, so that the resulting void can be filled with molten metal. These not only can be used as moulds, but also for applications such as household décor or ornaments.<sup>58</sup>

A stereo-complex of D- and L-PLA has a higher glass transition temperature compared to racemic PLA, resulting in a greater mechanical strength. It has a wide range of applications, such as woven wrinkle-free shirts, microwavable trays, hot-fill applications and as an additive in engineering plastics such as ABS. Such blends also have good form stability and visual transparency, making them useful for low-end packaging applications.<sup>38</sup>

PLA undergoes degradation to form innocuous lactic acid, and thus is safe to use in medical implants in the form of anchors, screws, plates, pins, rods, and as a mesh.<sup>59</sup> Lactic acid is a natural product associated with muscular construction in humans, which can be decomposed by the body's normal metabolic pathways. Lactic acid is converted to pyruvic acid and enters the tricarboxylic acid cycle to yield carbon dioxide and water. As L-lactic acid (LLA) is the naturally occurring stereoisomer of lactic acid, PLLA is more commonly used for medical applications than poly(D-lactic acid) (PDLA), which breaks down into D-lactic acid (DLA). PLA and other poly( $\alpha$ -hydroxy acid)s as well as their copolymers have been approved by the U.S. Food and Drug Administration (FDA) and by other regulatory agencies in many countries for implantation in the human body.<sup>56</sup> A variety of products are commercially available and have successfully been used for medical applications. Depending on the exact type and molecular weight of PLA used, it can break down inside the body within 6 months to 2 years. This gradual degradation is desirable for a support structure such as medical implants because it gradually transfers the load to the body, allowing the bone or tissue to heal. Pure poly-L-lactic acid (PLLA) is also a main ingredient in Sculptra, a long-lasting facial volume enhancer, primarily used for treating lipoatrophy of cheeks.<sup>60</sup>

## Chapter 2: Project Background

---

Despite these advantages, some disadvantages of PLA remain to be overcome, which include degradation products and its hydrophobic nature. Despite its bioavailability, LA is a relatively strong acid and its accumulation at the implant site, due to the “burst” release by the bulk degradation of PLA, will result in lowering of local pH that may potentially trigger an anti-inflammatory response.<sup>61</sup> Another disadvantage of PLA stems from the removal of water molecule during condensation reaction which often results in an agglomerate of polymer as with the template approach described in the thesis. PLA envelopes fine MOF crystals into a thick paste which especially hinders intrinsic penetration of polymer in the micropores of the MOF. Summary of properties of poly(lactic acid) is provided in Appendix A2.2).

### 2.2.3 Poly( $\epsilon$ -caprolactone)

**Polycaprolactone (PCL)** is a biodegradable polyester with a backbone formula  $(C_6H_{10}O_2)_n$  or  $[-OCH_2(CH_2)_4C=O-]$ . PCL has a low melting point of around  $60\text{ }^\circ\text{C}$  and a glass transition temperature of about  $-60\text{ }^\circ\text{C}$  and is commonly prepared by ring opening polymerisation of  $\epsilon$ -caprolactone using a catalyst such as stannous octoate. By nature, PCL is a biocompatible, biodegradable, bioresorbable polymer, an aliphatic polyester belonging to the poly- $\alpha$ -hydroxy acid group, in the same chemical group as polylactic and polyglycolic acids.<sup>62</sup>

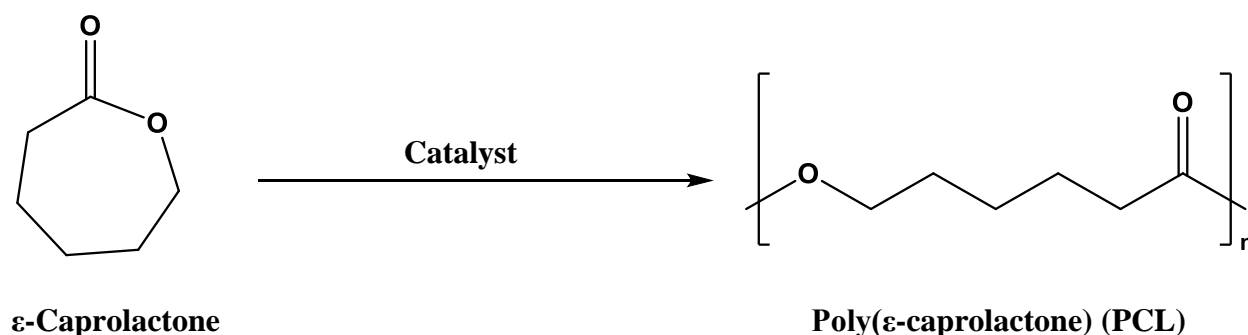


Fig 2.7: Chemical structure diagrams of  $\epsilon$ -caprolactone monomer ( $\epsilon$ -CL) and standard repeating unit of a poly( $\epsilon$ -caprolactone) polymer.

## Chapter 2: Project Background

---

PCL was first synthesised by the Carruthers group in the early 1930s by ring-opening polymerisation of the cyclic monomer of  $\epsilon$ -caprolactone (Fig 2.7).<sup>63</sup> The length (n) of the PCL chain or the corresponding molecular weight of the polymer determines the time of its degradation via ester-bond hydrolysis and its persistence. Many microbes in nature are able to completely biodegrade PCL.<sup>64</sup> The amorphous phase undergoes degradation first and decreases the overall crystallinity as a consequence, while the molecular weight remains constant.<sup>65</sup> Then, cleavage of ester bonds results in mass loss.

PCL is hydrophobic and semi-crystalline, it has better viscoelastic properties than many other biodegradable polymers, and is thus easy to manufacture and manipulate, allowing a large range of structures such as microspheres, fibres, micelles, nanofibers, films, foams, etc. It can also be easily blended with other polymers to produce copolymers exhibiting different physicochemical properties and biodegradability.<sup>66</sup> It became commercially available following efforts to identify synthetic polymers that could be degraded by microorganisms.<sup>67</sup> In industry, PCL finds its most common use in the production of speciality polymers. Polycaprolactones impart good resistance to water, oil, solvent, and chlorine to the polyurethane produced. Summary of properties of poly( $\epsilon$ -caprolactone) is provided in Appendix A2.3.

### Applications

PCL has uses in different fields such as tissue scaffolding, in long-term drug delivery systems – in particular contraceptives delivery, in microelectronics, as adhesives, and in packaging.<sup>63</sup> The properties of PCL such as control over degradation, miscibility with other polymers, biocompatibility and potential to be made from monomers derived from renewable sources, makes it a very useful polymer if its properties can be controlled and it can be made inexpensively. A range of metals have been studied for catalysts and catalytic systems for polymerisation of  $\epsilon$ -caprolactone.<sup>53</sup>

## Chapter 2: Project Background

---

The numerous advantages and wide array of functions of PCL systems have led to product development and its use for biomedical applications. PCL implants and PCL-based collagen stimulators. Sutures were among the first devices made of synthetic absorbable polymers with the advantage of slow degradation in biological tissue as well as slow and controlled degradation. The copolymer of polycaprolactone and polyglycolide enters into the composition of the well-known monofilament suture Monocryl™ (Ethicon, Inc.; Somerville, New Jersey, USA), widely used in several surgery fields for many years.<sup>68</sup> It sufficiently maintains high tensile strength and induces minimal tissue reaction after implantation in addition to its safety.

PCL is suitable for long-term drug delivery due to its high permeability to many drugs, excellent biocompatibility, slow biodegradability, and bioerodability as a drug carrier. Among drug release systems, the biodegradable contraceptive capsule Capronor™ made of PCL containing levonorgestrel has particularly been investigated regarding its design and long-term experimental (up to 2 years) and clinical development, providing important information on the global safety of PCL and confirming the PCL slow degradation process and the long-term safety of those drug release systems.<sup>69</sup> Many other drugs have been encapsulated in PCL microspheres for research as an anticancer, antipsychotic, non-steroidal anti-inflammatory, anti-hypertensive drugs.<sup>70-73</sup>

PCL is used as a feedstock material for 3D printers and is often in implants in tissue engineering for its use in scaffolds produced by 3D printing, accredited to its physicochemical (low melting point), mechanical properties and longevity. 3D printing produces structures through successive layer deposition using a computerized process, to repair and replace tissues and/or organs.<sup>74</sup> Recent advances have also used PCL in tracheal surgery as whole tracheal 3D scaffold to promote repair and healing. Scaffolds are also being investigated in congenital heart defect, gastric wall damage (hollow organ) and periodontal repair. Such an application has attracted a considerable interest in orthopedics for meniscus replacements, which affects many people around the world and current and alternate materials have faced issues with weathering and fabrication of parts.<sup>75,76</sup> The applications demonstrate that PCL is an important polymer for tissue engineering, and in conjunction with 3D-printing technology will be a key area of research and applications.

## Chapter 2: Project Background

---

PCL is used as a component of "night guards" (dental splints) and in root canal filling. It performs like gutta-percha, possessing similar handling properties, and can be easily softened by applying heat or dissolved in solvents such as chloroform for its re-use. Due to excellent moldability of PCL, dental splints can be fabricated in all shapes and sizes that may be required. The major difference between the polycaprolactone-based root canal filling material and other widely used replacement is that the PCL-based material is biodegradable.<sup>77</sup>

PCL and PCL-based polymer networks provide an interesting opportunity to design drug delivery systems due to their relevant advantages, such as the easy removal of polymer metabolites and degradation products following drug release, and the ability to synthesise it in form of micro- and nanoparticulate systems to finely control site-specific and targeted drug delivery.<sup>78</sup> Its compatibility with a wide range of drugs allows uniform drug distribution in the matrix, whereas its long-term degradation facilitates drug release up to several months.<sup>77</sup> The main advantages of PCL for drug delivery are its high permeability to small drug molecules, and its negligible tendency to generate an acid during degradation so it does not create an acidic environment, as compared to other polyesters such as PLA and polyglycolic acid (PGAs). The degradation of PCL homopolymer is very slow compared to other polyesters, making it more suitable for long-term delivery systems extending to a period of more than 1 year, with an ability to increase and decrease effective release by proper physical or chemical modifications.<sup>79</sup> Drug release rates from PCL based substrates may depend on specific formulations and synthesis, such as PCL content, size and percentage of the relative drug fraction used. Control over these parameters can be achieved by polymer networks with varying sizes that can be controlled using templating with microporous materials to accurately control drug release rates.

## Chapter 2: Project Background

---

### 2.3 Conclusion

In conclusion, the background of key MOF and polymer materials is presented in this chapter, detailing the synthesis, polymerisation reactions. The chapter also describes the properties of polymer@MOF composite that make them attractive to be used in the application for developing multi-dimensional polymer structures and architectures.

The exceptionally large surface area due to MOFs characteristic porosity, together with processable synthetic methods and flexibility of the polymer have been sought to enhance the properties of polymer@MOF composite and synthesise MOF-templated polymer networks.<sup>80</sup> Materials have been used to synthesise polymer@MOF by a combination of bottom-up synthesis where the MOF is initially synthesised. This is followed by incorporation of monomer within the MOF pores, and subsequently allowing polymerisation to occur *in-situ*. Upon completion of polymerisation, the polymer surrounding MOF structure is dissolved to isolate and obtain a multi-dimensional polymer network. The aim of following this approach is to obtain well-defined porous polymer of relatively high surface area compared to what is obtained from conventional solution polymer approaches. Additionally, the template-based approach allows to adopt various chemical approaches to obtain specific regio- and stereoisomers.<sup>81</sup> Template based approach allows tailor-made polymer systems to obtain highly controlled polymer structures.<sup>82</sup>

Exploiting the ability to polymerise from monomers *in-situ*, the above described composite materials provide a route to the highly porous soft structures that are suitable for drug uptake and release. Accordingly, we have chosen to combine the classical MOF-5 and HKUST-1 templates with PVAc, PLA, and PCL in order to pursue a better understanding of MOF-monomer/polymer interactions influence the final soft porous framework obtained. The selection of linear (rather than branched) target polymers is influenced by previously published studies<sup>75,81</sup>, which report formation of 3-D network structures, as this physically intertwined construct is expected to be more easily degraded, as befits the intended ultimate application in drug delivery.

## **Chapter 2: Project Background**

---

MOF and polymers constitute a good combination for developing advanced materials that result in composites that features desirable properties of both type of materials suitable for various applications. The area of polymerisation under MOF confinement holds several hurdles that need overcoming to fully understand the effect of confinement in crystalline solids. Improved understanding of the processes and mechanisms will allow investigation in large-scale applications such as heterogeneous catalysis and drug delivery. Overall, MOFs and polymers are an interesting combination of materials for various applications and hold promise with future developments with further research. Especially in the quest of precisely controlled material structures, the connection between MOF and polymers seems to be a valuable approach.

## Chapter 2: Project Background

---

### 2.5 References

- 1 A. C. Mescall and S. T. Easun, MSc MOF Report, *Cardiff University*, 2017.
- 2 N. L. Rosi, J. Eckert, M. Eddaoudi, D. T. Vodak, J. Kim, M. O’Keeffe and O. M. Yaghi, *Science*, 2003, **300**, 1127–1129.
- 3 A. D. Burrows, L. C. Fisher, D. Hodgson, M. F. Mahon, N. F. Cessford, T. Düren, C. Richardson and S. P. Rigby, *Cryst. Eng. Comm.*, 2012, **14**, 188–192.
- 4 U. Mueller, M. Schubert, F. Teich, H. Puetter, K. Schierle-Arndt and J. Pastré, *J. Mater. Chem.*, 2006, **6**, 626–636.
- 5 S. Hausdorf, F. Baitalow, T. Böhle, D. Rafaja and F. O. R. L. Mertens, *J. Am. Chem. Soc.*, 2010, **132**, 10978–10981.
- 6 D. J. Tranchemontagne, J. R. Hunt and O. M. Yaghi, *Tetrahedron*, 2008, **64**, 8553–8557.
- 7 W. Lu, Z. Wei, Z. Y. Gu, T. F. Liu, J. Park, J. Park, J. Tian, M. Zhang, Q. Zhang, T. Gentle, M. Bosch and H. C. Zhou, *Chem. Soc. Rev.*, 2014, **43**, 5561–5593.
- 8 M. Eddaoudi, J. Kim, N. Rosi, D. Vodak, J. Wachter, M. O’Keeffe and O. M. Yaghi, *Science*, 2002, **295**, 469–472.
- 9 S. Hausdorf, J. Wagler, R. Mossig and F. O. R. L. Mertens, *J. Phys. Chem. A*, 2008, **112**, 7567–7576.
- 10 Y. Ming, J. Purewal, D. Liu, A. Sudik, C. Xu, J. Yang, M. Veenstra, K. Rhodes, R. Soltis, J. Warner, M. Gaab, U. Müller and D. J. Siegel, *Micropor. Mesopor. Mater.*, 2014, **185**, 235–244.
- 11 J. T. Hughes and A. Navrotsky, *J. Am. Chem. Soc.*, 2011, **133**, 9184–9187.
- 12 J. Hafizovic, M. Bjørgen, U. Olsbye, P. D. C. Dietzel, S. Bordiga, C. Prestipino, C. Lamberti and K. P. Lillerud, *J. Am. Chem. Soc.*, 2007, **129**, 3612–3620.
- 13 L. Huang, H. Wang, J. Chen, Z. Wang, J. Sun, D. Zhao and Y. Yan, *Micropor. Mesopor. Mater.*, 2003, **58**, 105–114.
- 14 S. S. Kaye, A. Dailly, O. M. Yaghi and J. R. Long, *J. Am. Chem. Soc.*, 2007, **129**, 14176–14177.
- 15 S. Hausdorf, J. Wagler, R. Mossig and F. O. R. L. Mertens, *J. Phys. Chem. A*, 2008, **112**, 7567–7576.
- 16 K. Schröck, F. Schröder, M. Heyden, R. A. Fischer and M. Havenith, *Phys. Chem. Chem. Phys.*, 2008, **10**, 4732–4739.
- 17 K. A. Cychosz and A. J. Matzger, *Langmuir*, 2010, **26**, 17198–17202.

## Chapter 2: Project Background

---

- 18 Y. Ming, J. Purewal, J. Yang, C. Xu, R. Soltis, J. Warner, M. Veenstra, M. Gaab, U. Müller and D. J. Siegel, *Langmuir*, 2015, **31**, 4988–4995.
- 19 J. A. Greathouse and M. D. Allendorf, *J. Am. Chem. Soc.*, 2006, **128**, 10678–10679.
- 20 S. S. Han, S. H. Choi and A. C. T. Van Duin, *Chem. Commun.*, 2010, **46**, 5713–5715.
- 21 Y. Ming, N. Kumar and D. J. Siegel, *ACS Omega*, 2017, **2**, 4921–4928.
- 22 S. S. Y. Chui, S. M. F. Lo, J. P. H. Charmant, a G. Orpen and I. D. Williams, *Science*, 1999, **283**, 1148–1150.
- 23 H. Li, K. Wang, Y. Sun, C. T. Lollar, J. Li and H. C. Zhou, *Mater. Today*, 2018, **21**, 108–121.
- 24 V. V. Guerrero, Y. Yoo, M. C. McCarthy and H. K. Jeong, *J. Mater. Chem.*, 2010, **20**, 3938–3943.
- 25 P. Guo, C. Froese, Q. Fu, Y. T. Chen, B. Peng, W. Kleist, R. A. Fischer, M. Muhler and Y. Wang, *J. Phys. Chem. C*, 2018, **122**, 21433–21440.
- 26 L. L. Jiang, X. Zeng, M. Li, M. Q. Wang, T. Y. Su, X. C. Tian and J. Tang, *RSC Advances*, 2017, **7**, 9316–9320.
- 27 M. Mozafari, *Metal-Organic Frameworks for Biomedical Applications*, Elsevier, New York, 2020.
- 28 C. Prestipino, L. Regli, J. G. Vitillo, F. Bonino, A. Damin, C. Lamberti, A. Zecchina, P. L. Solari, K. O. Kongshaug and S. Bordiga, *Chem. Mater.*, 2006, **18**, 1337–1346.
- 29 F. A. Cotton, Z. C. Mester and T. R. Webb, *Acta. Crystallogr. B. Struct. Sci. Cryst. Eng. Mater.*, 1974, **30**, 2768–2770.
- 30 P. Ceccherelli, M. Curini, M. C. Marcotullio and O. Rosati, *Tetrahedron*, 1991, **47**, 7403–7408.
- 31 S. Loera-Serna, M. A. Oliver-Tolentino, M. De Lourdes López-Núñez, A. Santana-Cruz, A. Guzmán-Vargas, R. Cabrera-Sierra, H. I. Beltrán and J. Flores, *J. Alloys Compd.*, 2012, **540**, 113–120.
- 32 P. St. Petkov, G. N. Vayssilov, J. Liu, O. Shekhah, Y. Wang, C. Wöll and T. Heine, *Chem. Phys. Chem.*, 2012, **13**, 2025–2029.
- 33 B. Supronowicz, A. Mavrandonakis and T. Heine, *J. Phys. Chem. C*, 2013, **117**, 14570–14578.
- 34 J. Szanyi, M. Daturi, G. Clet, D. R. Baer and C. H. F. Peden, *Phys. Chem. Chem. Phys.*, 2012, **14**, 4383–4390.
- 35 G. W. Peterson, G. W. Wagner, A. Balboa, J. Mahle, T. Sewell and C. J. Karwacki, *J. Phys. Chem. C*, 2009, **113**, 13906–13917.

## Chapter 2: Project Background

---

- 36 C. Petit, L. Huang, J. Jagiello, J. Kenvin, K. E. Gubbins and T. J. Bandosz, *Langmuir*, 2011, **27**, 13043–13051.
- 37 B. E. Souza, S. Rudić, K. Titov, A. S. Babal, J. D. Taylor and J. C. Tan, *Chem. Commun.*, 2019, **55**, 3868–3871.
- 38 T. Wang, H. Zhu, Q. Zeng and D. Liu, *Adv. Mater. Inter.*, 2019, **6**, 1900423.
- 39 W. Wong-Ng, J. A. Kaduk, D. L. Siderius, A. L. Allen, L. Espinal, B. M. Boyerinas, I. Levin, M. R. Suchomel, J. Ilavsky, L. Li, I. Williamson, E. Cockayne and H. Wu, *Powder Diffr.*, 2015, **30**, 2–13.
- 40 M. A. Chowdhury, *Rev. J. Chem.*, 2017, **7**, 1–22.
- 41 L. S. Nair and C. T. Laurencin, *Prog. Polym. Sci.*, 2007, **32**, 762–798.
- 42 Z. Zhang, O. Ortiz, R. Goyal and J. Kohn, *Principles of Tissue Engineering*, 2014, 441–473.
- 43 J. A. Tamada and R. Langer, *Proc. Natl. Acad. Sci. U. S. A.*, 1993, **90**, 552–556.
- 44 Kinam. Park, W. S. W. Shalaby and Haesun. Park, *Biodegradable hydrogels for drug delivery*, CRC Press, Boca Raton, 1993.
- 45 Poly(vinyl Acetate) - PVAc, [http://polymerdatabase.com/Polymer Brands/PVA.html](http://polymerdatabase.com/Polymer%20Brands/PVA.html), (accessed June 9, 2020).
- 46 Polyvinyl Acetate – The Plastics Historical Society, [http://plasticquarian.com/?page\\_id=14234](http://plasticquarian.com/?page_id=14234), (accessed June 9, 2020).
- 47 N. K. Agwan, A.R. Khan and, K. Agwan, *Chem. Phys. Chem.*, 1968, **9**, 157–169.
- 48 M. Amann and O. Minge, *Adv. Polym. Sci.*, 2011, **245**, 137–172.
- 49 Polyvinyl Acetate - Chemical Economics Handbook (CEH) | IHS Markit, <https://ihsmarkit.com/products/polyvinyl-acetate-chemical-economics-handbook.html>, (accessed June 11, 2020).
- 50 W. M. Carpenter, M. F. Grower and G. Nash, *Oral Surg. Oral Med. Oral Pathol. Oral Radiol. Endol.*, 1976, **42**, 461–469.
- 51 M. I. Baker, S. P. Walsh, Z. Schwartz and B. D. Boyan, *J. Biomed. Mater. Res. Part B Appl. Biomater.*, 2012, **100 B**, 1451–1457.
- 52 ASM International., *Characterization and failure analysis of plastics.*, ASM International, 2003.
- 53 P. J. Tarcha, *Polymers for Controlled Drug Delivery*, CRC Press, Florida, 1st edn., 2000.
- 54 Polylactic acid, PLA - Conservation and Art Materials Encyclopedia Online (CAMEO), [http://cameo.mfa.org/wiki/Polylactic\\_acid](http://cameo.mfa.org/wiki/Polylactic_acid), (accessed June 10, 2020).

## Chapter 2: Project Background

---

- 55 Bioplastics - Study: Market, Analysis, Trends | Ceresana, <https://web.archive.org/web/20171104212623/http://www.ceresana.com/en/market-studies/plastics/bioplastics>, (accessed June 10, 2020).
- 56 R. Auras, L. T. Lim, S. E. M. Selke and H. Tsuji, *Poly(Lactic Acid)*, John Wiley & Sons, Inc., Hoboken, NJ, USA, 2010.
- 57 J. Nieuwenhuis, *Clin. Mater.*, 1992, **10**, 59–67.
- 58 Metal Casting with Your 3D Printer | Make:, <https://makezine.com/projects/guide-to-3d-printing-2014/metal-casting-with-your-3d-printer/>, (accessed June 10, 2020).
- 59 S. Suzuki and Y. Ikada, in *Poly(Lactic Acid)*, John Wiley & Sons, Inc., Hoboken, NJ, USA, 2010, pp. 443–456.
- 60 Sculptra® Aesthetic: A Poly-L-lactic Acid Facial Injection, <https://www.sculptraaesthetic.com/>, (accessed June 10, 2020).
- 61 M. J. Yaszemski, R. G. Payne, W. C. Hayes, R. Langer and A. G. Mikos, *Biomaterials*, 1996, **17**, 175–185.
- 62 M. O. Christen and F. Vercesi, *Clin. Cosmet. Investig. Dermatology*, 2020, 13, 31–48.
- 63 F. J. Van Natta, J. W. Hill and W. H. Carruthers, *J. Am. Chem. Soc.*, 1934, **56**, 455–459.
- 64 C. X. F. Lam, S. H. Teoh and D. W. Hutmacher, *Polym. Int.*, 2007, **56**, 718–728.
- 65 R. A. Gross and B. Kalra, *Science*, 2002, 297, 803–807.
- 66 M. Labet and W. Thielemans, *Chem. Soc. Rev.*, 2009, **38**, 3484–3504.
- 67 M. A. Woodruff and D. W. Hutmacher, *Prog. Polym. Sci.*, 2010, 35, 1217–1256.
- 68 R. S. Bezwada, D. D. Jamiolkowski, I. Y. Lee, V. Agarwal, J. Persivale, S. Trenka-Benthin, M. Ernet, J. Suryadevara, A. Yang and S. Liu, *Biomaterials*, 1995, **16**, 1141–1148.
- 69 P. D. Darney, S. E. Monroe, C. M. Klaisle and A. Alvarado, *Am. J. Obstet. Gynecol.*, 1989, **160**, 1292–1295.
- 70 M. Hombreiro Pérez, C. Zinutti, A. Lamprecht, N. Ubrich, A. Astier, M. Hoffman, R. Bodmeier and P. Maincent, *J. Controlled Release*, 2000, **65**, 429–438.
- 71 P. Giunchedi, B. Conti, L. Maggi and U. Conte, *J. Microencapsul.*, 1994, **11**, 381–393.
- 72 R. K. Chang, J. C. Price and C. W. Whitworth, *Drug Dev. Ind. Pharm.*, 1986, **12**, 2355–2380.
- 73 N. Carreras, V. Acuña, M. Martí and M. J. Lis, *Colloid Polym. Sci.*, 2013, **291**, 157–165.
- 74 M. Gao, H. Zhang, W. Dong, J. Bai, B. Gao, D. Xia, B. Feng, M. Chen, X. He, M. Yin, Z. Xu, N. Witman, W. Fu and J. Zheng, *Scientific Reports*, 2017, **7**, 1–12.

## Chapter 2: Project Background

---

- 75 G. D. Mogoşanu and A. M. Grumezescu, *Int. J. Pharm.*, 2014, **463**, 127–136.
- 76 E. Avolio, M. Caputo and P. Madeddu, *Front. Cell Dev. Biol.*, 2015, **3**, 1-17.
- 77 N. Hiraishi, J. Y. Y. Yau, R. J. Loushine, S. R. Armstrong, R. N. Weller, N. M. King, D. H. Pashley and F. R. Tay, *J. Endod.*, 2007, **33**, 952–956.
- 78 N. Raina, R. Rani, A. Khan, K. Nagpal and M. Gupta, *Polym. Bull.*, 2019, 1–24.
- 79 D. R. Paul, *Polymer Blends.*, Elsevier Science, 1978.
- 80 B. V. K. J. Schmidt, *Macromol. Rapid Commun.*, 2020, **41**, 1900333.
- 81 M.-L. Hu, M. Y. Masoomi and A. Morsali, *Coord. Chem. Rev.*, 2019, **387**, 415–435.
- 82 B. Voloskiy, K. Niwa, Y. Chen, Z. Zhao, N. O. Weiss and X. Zhong, *ACS Nano*, 2015, **28**, 3044-3049.

# Chapter 3

---

Methods

## Chapter 3: Methods

---

### Introduction

The details of the synthesis methods, experimental procedures and characterisation methods employed throughout this work are summarised in this chapter. Details information about raw materials used, sample preparation procedure, conditions, and characterisation techniques are given. Polymerisation methods for *in situ* MOF templated polymerisation and *ex situ*, solution polymerisation have been described in the chapter.

### 3.1 Materials

All the starting reactants were obtained from chemical vendors: Copper (II) nitrate trihydrate, terephthalic acid, disodium-EDTA, methanol, ethanol, and chloroform, were obtained from Fisher Scientific UK. Zinc (II) nitrate hexahydrate, trimesic acid, *N,N* – dimethylformamide, deuterium oxide, tin (II) 2-ethylhexanoate,  $\epsilon$ -caprolactone, vinyl acetate, D,L – lactide, lactic acid were all obtained from Sigma Aldrich (Merck). Deuterated vinyl acetate monomer was acquired from QMX Laboratories UK. Deuterated terephthalic acid was synthesised by and acquired from ISIS Pulsed Neutron and Muon Source deuteration laboratory at Science and Technology Facilities Council (STFC), Oxfordshire, UK. The reactants were used without further purification, unless otherwise stated.

### 3.2 Synthesis of Metal-Organic Frameworks (MOFs)

This section outlines details of solvothermal synthesis of both MOFs, HKUST-1 and MOF-5. As described earlier in chapter 2, solvothermal synthesis is a widely employed procedure during the synthesis of the inorganic and hybrid organic-inorganic solids.<sup>1-3</sup> In general, over a period the solvents are heated to temperature above their boiling point in a pressurised, sealed vessel (Fig 3.1). These conditions activate the chemical reaction between dissolved reactants which result in formation of the reaction product. Solvothermal synthesis has proven to be an efficient procedure to control particle size and morphology of a range of metal-oxides such as zeolites,<sup>4</sup> perovskites,<sup>5</sup> and MOFs. All synthesis in this work has been performed in a 20 mL Teflon-lined autoclave, with 10 mL filling of the reaction mixture at the start of synthesis. The autoclave has operating temperatures and pressures up to a maximum of 250 °C and

## Chapter 3: Methods

---

1800 psig, thick-walled PTFE liner with a flanged seal. As a safety measure, the autoclave consist of a blow-off disc in the vessel head which is designed such that it blows out to release pressure through an opening in the cover at approximately 3500 psig.<sup>6</sup>

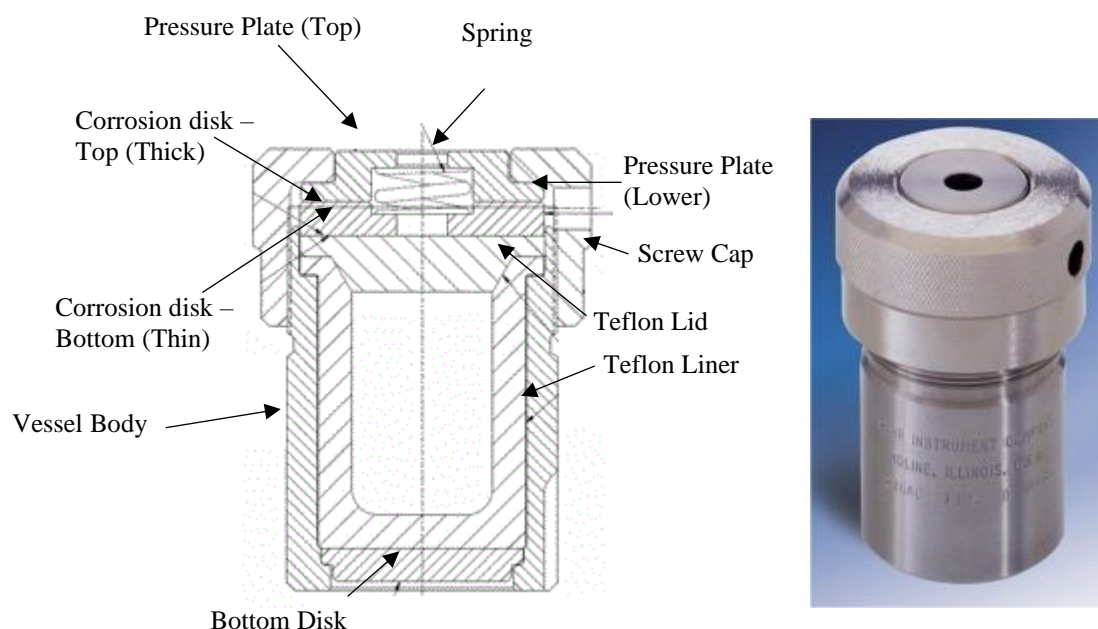


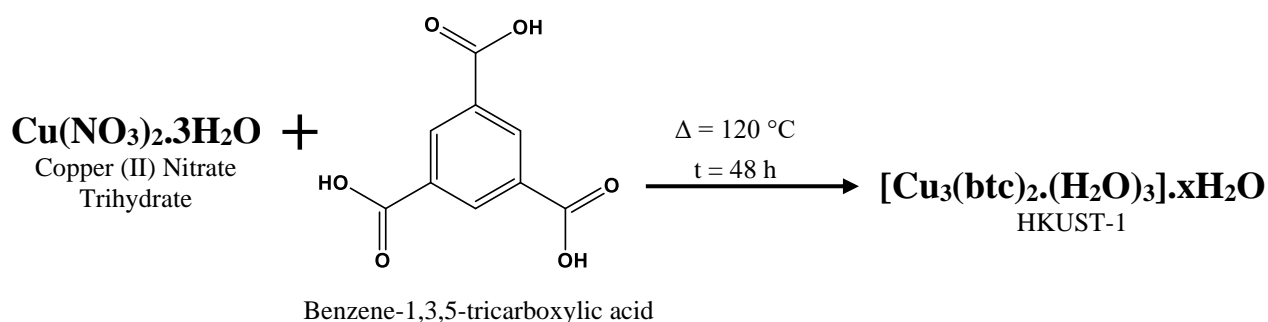
Fig 3.1: Schematic of solvothermal autoclave (L) and image of an autoclave similar to the one used for MOF synthesis.<sup>7</sup>

MOFs are known to readily adsorb atmospheric moisture, especially MOF-5 and HKUST-1. Before addition of monomers, the MOFs were activated by heating them to 170 °C under vacuum for 18 to 24 hours to ensure removal of residual solvent and coordinated water. This ensures that there is maximum accessible surface area for the monomer molecules to penetrate within the MOF pores.

## Chapter 3: Methods

### 3.2.1 Synthesis of HKUST-1 (MOF-199) $[\text{Cu}_3(\text{BTC})_2 \cdot x(\text{H}_2\text{O})_3]_n$

Solvothermal synthesis of HKUST-1, also known as Cu-BTC framework or MOF-199, was first reported by Chui *et al.* involving heating the reaction mixture for 12 hours at a temperature of 180 °C in a Teflon-lined autoclave.<sup>8</sup> This reaction, however, results in formation of CuO due to high reaction temperature. HKUST-1 was synthesised using a modified method by Schlichte *et al.* that was optimized changing the molar ratio to achieve a better yield and crystallinity.<sup>9</sup> A typical solvothermal reaction is as follows;  $\text{Cu}(\text{NO}_3)_2 \cdot 3\text{H}_2\text{O}$  (0.55 g, 0.3 mmol) was dissolved in de-ionized (Milli-Q) water (10 mL) and mixed with a solution of trimesic acid (benzene-1,3,5-tricarboxylic acid) 0.38 g (0.18 mmol) in ethanol (10 mL). After 10 minutes of stirring the solution was transferred to a 20 ml Teflon liner, placed in an autoclave, and heated to 120 °C for 24 h. (Scheme 3.1)



Scheme 3.1: Schematic diagram of copper(II) nitrate reaction with trimesic acid to form HKUST-1.

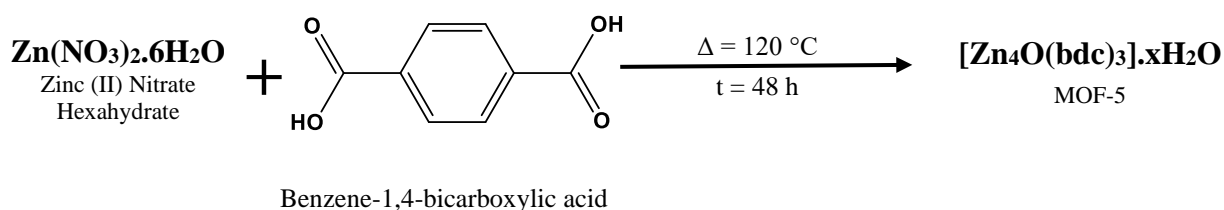
HKUST-1 samples (~1 g) were stirred in excess ethanol (~10 mL) at room temperature for approximately an hour to displace any unreacted agents from the framework. This method was repeated 4-5 times. The samples were filtered and dried in air for 24 h. The samples were heated to 160 °C overnight prior to characterisations. Upon activation and loss of co-ordinated water, HKUST-1 changed colour from azure blue to royal blue.

## Chapter 3: Methods

### 3.2.2 Synthesis of MOF-5 (IRMOF-1) $[\text{Zn}_4\text{O}(\text{C}_8\text{H}_4\text{O}_4)_3]_n$

The solvothermal synthesis reported by Yaghi *et al.* involves crystallisation of a mixture of zinc nitrate and terephthalic acid solution in *N,N*-dimethylformamide, and forms the basis of our synthesis approach. However, to develop a repeatable and effective synthetic procedure involved much trial-and-error with changes in molar ratio and addition of trace amounts of water to aid solubility and proton exchange. The adopted final synthesis method is described below.

For our synthesis approach  $\text{Zn}(\text{NO}_3)_2 \cdot 6\text{H}_2\text{O}$  (2.2 g, 123.25 mmol) was dissolved in *N,N*-dimethylformamide (60 mL) and stirred for 10 minutes before adding deionized water (0.6 mL, 1% volume of DMF) and of terephthalic acid (benzene-1,4-bicarboxylic acid) (0.49 g, 49.2 mmol) and leaving it to stir until full dissolution. The solution mixture evenly distributed in six 20 ml Teflon liners and placed in an autoclave and heated to 120 °C for 48 h (Scheme 3.2). To activate samples of MOF-5, the samples (~1 g) were stirred in an excess of chloroform (~10 mL) at room temperature approximately for an hour; chloroform displaces majority of the residual DMF molecules and unreacted agents. This method is repeated 4-5 times. The samples were filtered and dried in an oven at 120 °C for 24 h.



Scheme 3.2: Schematic diagram of zinc (II) nitrate reaction with terephthalic acid to form MOF-5.

For hydrogenated, deuterated, and a mixed H/D (1:1) MOF-5 isotopologues required for contrast variation neutron scattering experiments, the synthetic procedures were modified.

## Chapter 3: Methods

---

MOF-5 samples (~1 g) were stirred in excess chloroform (~10 mL) at room temperature for approximately an hour to displace any unreacted agents and residual solvent from the framework. This method was repeated 4-5 times. The samples were filtered and dried in air for 24 h. The samples were heated to 160 °C overnight prior to characterisations. This procedure was consistent for all MOF-5 sample isotopologues.

### 3.2.2.1 H/D exchange of Zn(NO<sub>3</sub>)<sub>2</sub>·6H<sub>2</sub>O for deuterated MOF synthesis.

The metal salt used for the synthesis of deuterated MOF; Zn(NO<sub>3</sub>)<sub>2</sub>·6H<sub>2</sub>O (10 g), was recrystallised from an aqueous solution that was saturated and partially dehydrated at 45 °C. Crystals were dissolved in an excess of D<sub>2</sub>O and slowly concentrated by vacuum distillation at 80 °C for 3 h. The mixture was replenished with D<sub>2</sub>O and the process was repeated twice. Crystals obtained following this process were recrystallised in D<sub>2</sub>O solution saturated at room temperature and pressure. Once crystallisation was initiated, the solution was stored at 5 °C to accelerate recrystallisation. After 6 h, the crystals account for 6 – 8 g of deuterium exchanged zinc salt. The deuterium exchange was confirmed with ATR-IR spectroscopy.

### 3.2.2.2 Synthesis of deuterated MOF-5 [Zn<sub>4</sub>O(C<sub>8</sub>D<sub>4</sub>O<sub>4</sub>)<sub>3</sub>]<sub>n</sub>

The synthesis of deuterated MOF-5 follows a similar method to synthesis of its hydrogenated counterpart, albeit replacing the metal salt and water with deuterium exchanged salt and deuterium oxide, respectively, and using a deuterated terephthalic acid.

Zn(NO<sub>3</sub>)<sub>2</sub>·6D<sub>2</sub>O (2.2 g, 123.25 mmol) was dissolved in *N,N*-dimethylformamide (60 ml) and stirred for 10 minutes before adding deuterium oxide (0.6 ml, 1% volume of DMF) and *d*<sub>4</sub>-terephthalic acid (*d*<sub>4</sub>-benzene-1,4-bicarboxylic acid) (0.49 g, 48 mmol) and leaving it to stir for 15 to 20 minutes or until dispersion. The solution mixture was evenly distributed in six 20 ml Teflon liners and placed in an autoclave and heated to 120 °C for increased reaction time for 72 h. Trial experiments suggested slow reaction kinetics and rate and the yield achieved with 48 h was low (18-20 %). Thus, the reaction time was extended to improve the yield and

## Chapter 3: Methods

---

crystallinity (32-38 %). The activation and work-up procedures are similar to that of MOF-5 (Section 3.2.2).

### 3.2.2.3 Synthesis of H/D-MOF-5 [ $\text{Zn}_4\text{O}(\text{C}_8\text{H}_x\text{D}_y\text{O}_4)_3$ ]<sub>n</sub>

Hydrogenated and deuterated hybrid MOF-5 was synthesised by using equal parts by weight mixtures of the starting reactants.  $\text{Zn}(\text{NO}_3)_2 \cdot 6\text{H}_2\text{O}$  (1.1 g, 61.6 mmol) and  $\text{Zn}(\text{NO}_3)_2 \cdot 6\text{D}_2\text{O}$  (1.1 g, 66.6 mmol) were mixed and dissolved in N,N-dimethylformamide (60 mL) and stirred for 10 minutes before adding deuterium oxide and  $\text{H}_2\text{O}$  in 1:1 ratio (0.6 ml, 1% volume of DMF), terephthalic acid (0.25 g, 24.0 mmol) and *d*<sub>4</sub>-terephthalic acid (*d*<sub>4</sub>-benzene-1,4-bicarboxylic acid) (0.25 g, 24.6 mmol) and leaving it to stir for 15 to 20 minutes or until dispersion. The solution mixture evenly distributed in six 20 ml Teflon liners, placed in an autoclave and heated to 120 °C for an extended time of 72 h. The activation and work-up procedures are similar to that of MOF-5 (Section 3.2.2).

## 3.3 Polymerisation of monomers in MOF pores.

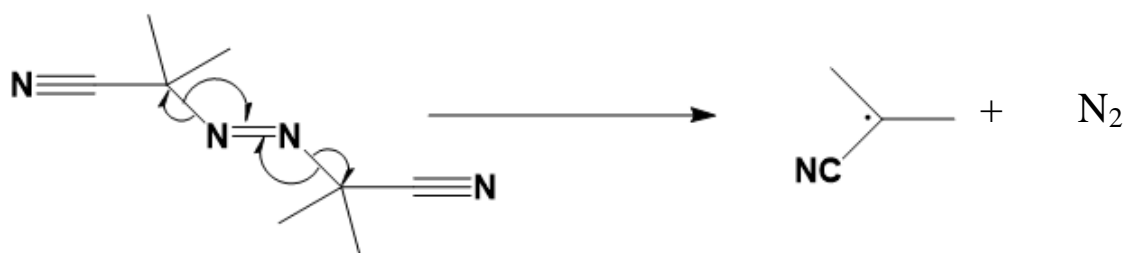
### 3.3.1 Radical polymerisation of vinyl acetate in MOFs

The MOF (80 mg) was dried by evacuation at 170 °C for 24 h, and cooled to room temperature under nitrogen. A mixture of vinyl acetate (40 mg) with 2% equivalent weight of 2,2'-azobis(isobutyronitrile) (AIBN; 0.8 mg) initiator was added to the MOF and soaked in monomer for 24 h at room temperature, this allows the monomer to seep into the intrinsic pores of the MOF. Extrinsic monomer was completely removed by controlled evacuation under vacuum at 40 °C for 18 h. The reaction flask was then filled with nitrogen and heated to 70 °C for 48 h to perform the polymerisation (Scheme 3.3). Upon completion of the polymerisation time, the reaction flask was cooled to room temperature and the polymer@MOF composites were washed in ethanol (20 mL) and dried at room temperature under continuous nitrogen flow.

## Chapter 3: Methods

---

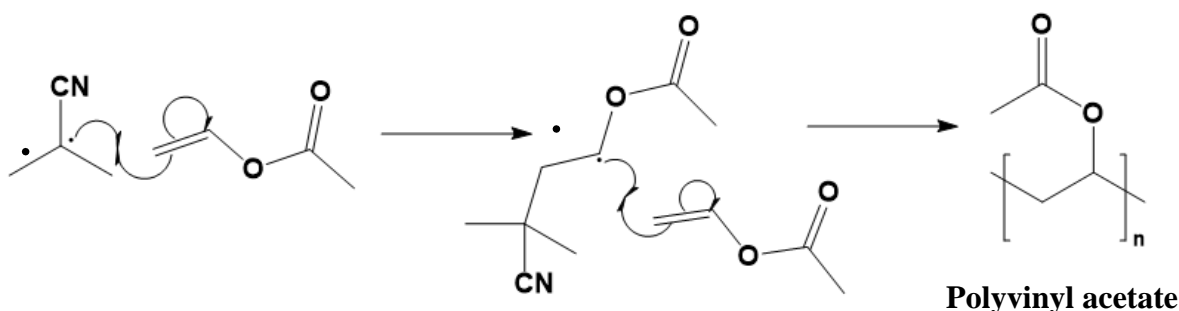
a) Free radical formation step.



2,2'-Azobis(2-methylpropanenitrile)

(AIBN)

b) Reaction of free radical with vinyl acetate monomer.



Scheme 3.3: Schematic for the reaction pathway for polymerisation of vinyl acetate to polyvinyl acetate.

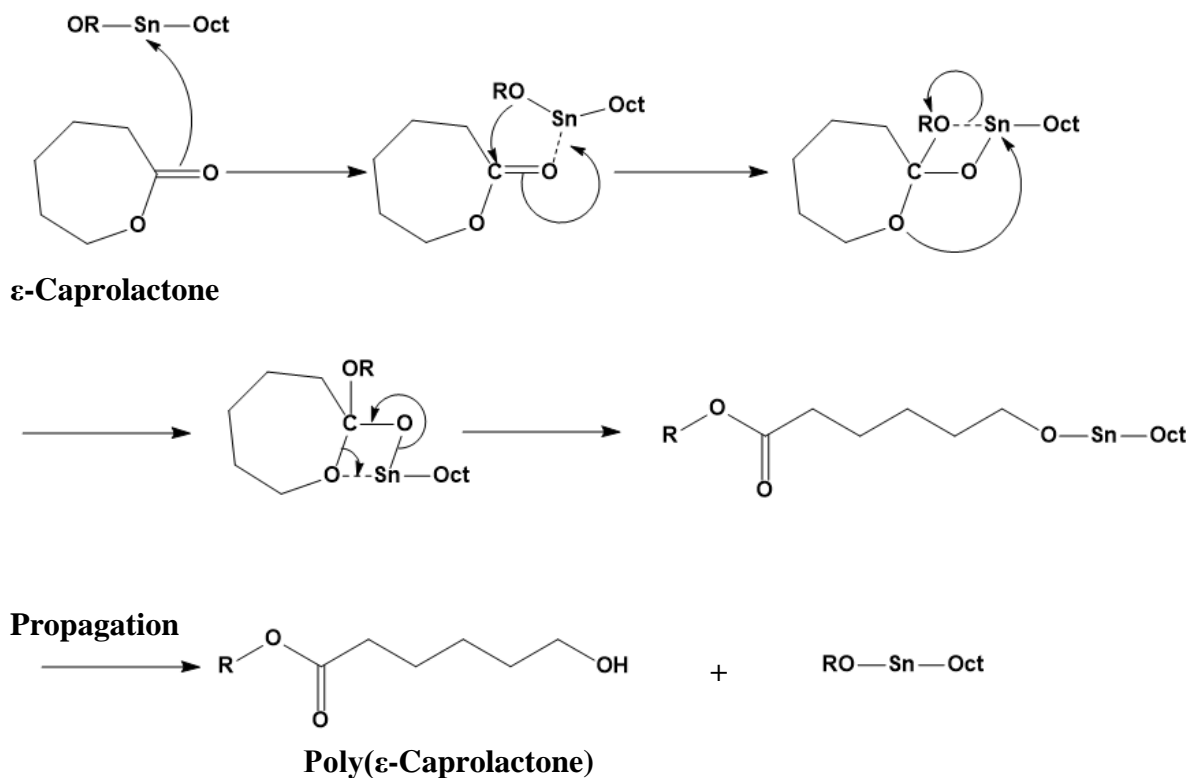
### 3.3.2 Ring-opening polymerisation of $\epsilon$ -caprolactone in MOFs

The MOF (0.8 g) was dried by evacuation at 170 °C for 24 h and cooled to room temperature under nitrogen. A  $\approx$  2 mL solution was prepared by dissolving a mixture of 2 mL toluene, tin (II) 2-ethylhexanoate catalyst (1.8 mg), and  $\epsilon$ -caprolactone (0.8 g) [molar ratio – 9 : 0.04 : 12]. Monomer (0.4 g) dissolved in the catalyst and initiator solvent was added, allowing the MOF to soak under nitrogen at room temperature for 24 h. Extrinsic monomer was evacuated under vacuum at 70 °C for 16 h. The reaction flask was then filled with nitrogen and heated to 120 °C for 48 h to polymerise (Scheme 3.4). Upon completion of the polymerisation time,

## Chapter 3: Methods

the reaction flask was cooled to room temperature and the polymer@MOF composites were washed in ethanol (20 mL) and dried at room temperature under continuous nitrogen flow.

### Tin (II) 2-ethylhexanoate



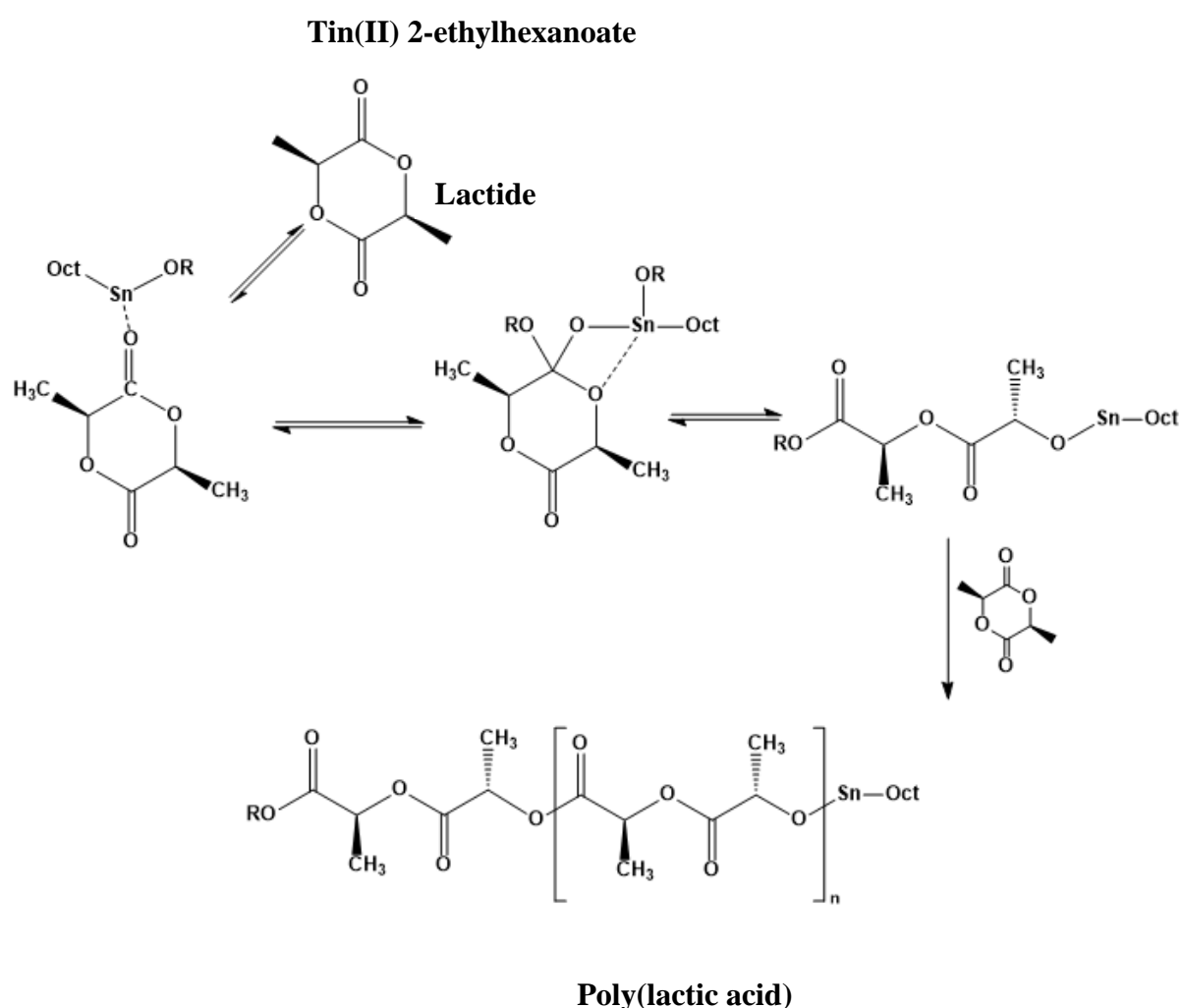
Scheme 3.4: Schematic for the reaction pathway for polymerisation of  $\epsilon$ -caprolactone to poly( $\epsilon$ -caprolactone).

### 3.3.3 Ring-opening polymerisation of D,L-Lactide.

The MOF (80 mg) was dried and activated under nitrogen by method described in Section 3.2.3. Once the MOF was allowed to cool down under nitrogen to room temperature, D,L – lactide (0.5 g) was added to the MOF. A solution of 0.4 mL benzyl alcohol with Sn(II)Oct catalyst (2 mg) was prepared and added to the reaction flask containing MOF along with the monomer. For the case of lactide, the monomer was added first without dissolution in the initiator solvent and the catalyst due to its melting point being considerably higher than other monomers used (mp = 116 – 120 °C)<sup>10</sup>. The temperature of the reaction mixture was

## Chapter 3: Methods

gradually increased to 130 °C and the MOF was allowed to soak in the liquid monomer, initiator and catalyst mixture for 24 h under nitrogen at this temperature. Extrinsic monomer was evacuated under vacuum at 130 °C for 16 h. The reaction flask was then filled with nitrogen at heated to 140 °C for 48 h to allow polymerisation (Scheme 3.5). Upon completion of the polymerisation time, the reaction flask was cooled to room temperature and the polymer@MOF composites were washed in ethanol (20 mL) and dried at room temperature under continuous nitrogen flow.

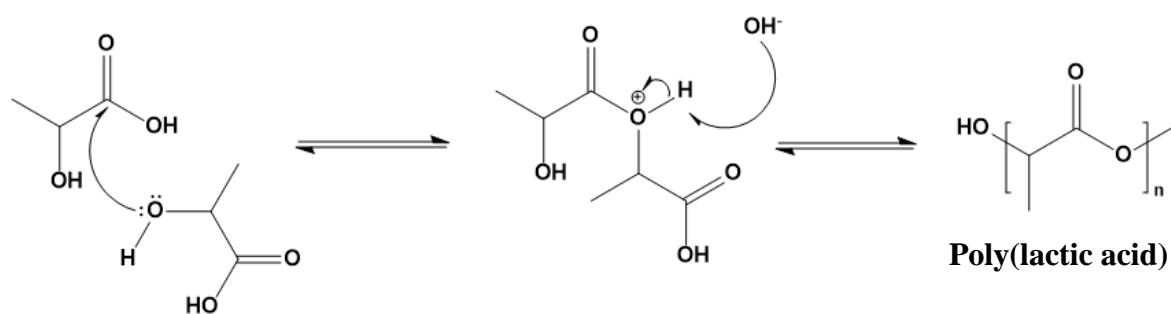


Scheme 3.5: Schematic for reaction mechanism of D,L-lactide to poly(lactic acid).<sup>38</sup> [The mechanism is conceptually the same as Scheme 3.4]

## Chapter 3: Methods

### 3.3.4 Condensation polymerisation of lactic acid.

The MOF (80 mg) was dried and activated as per the method described in Section 3.2.3. Lactic acid was dried over  $\text{MgSO}_4$  overnight and dehydrated under vacuum for 6 h at  $50\text{ }^\circ\text{C}$ . A mixture of 0.4 mL dehydrated lactic acid monomer with 1% wt.  $\text{Sn(II)Oct}$  was injected into the sealed reaction vessel containing the activated MOF. The MOF was left to soak under nitrogen for 24 h before the excess monomer was removed under vacuum at  $55\text{ }^\circ\text{C}$  to remove additional extrinsic monomer. The reaction temperature was increased to  $110\text{ }^\circ\text{C}$  for 30 h to allow polymerisation (Scheme 3.6). Upon completion of the polymerisation time, the reaction flask was cooled to room temperature and the polymer@MOF composites were washed in ethanol (20 mL) and dried at room temperature under continuous nitrogen flow.



Scheme 3.6: Schematic for reaction pathway of lactic acid to poly(lactic acid).

## Chapter 3: Methods

---

### 3.4 Framework Digestion and Polymer Isolation.

An aqueous solution of 0.5 M Na<sub>2</sub>EDTA was prepared by dissolving 1.45 g of Na<sub>2</sub>EDTA in 10 mL deionized water. The mixture was heated to 45 °C under constant stirring for 24 h and allowed to equilibrate for 1 h. 1 g of polymer@MOF composite was added to the EDTA solution and stirred for 18 h to allow complete digestion of the MOF framework and extraction of the polymer network. The solution mixture was rested for 4 h to allow complete separation of the phases. The white precipitate consists of solid polymer mixed with linker and a gel-like polymer floating in the solution. The mixture was centrifuged to isolate the polymer from the Cu/EDTA solution and washed repeatedly (10 washes) with ethanol to remove any residual linker and with water 3–5 times to remove any residual copper complexes. Between each set of washes, the solid precipitate was dried in vacuum at room temperature, overnight. After the washes, the isolated polymer precipitate was collected and stored under nitrogen.

### 3.5 Characterisation

Prior to any characterisation on MOF, all empty MOF samples without guests were activated as per method described in section 3.2.3. To remove unreacted reagents and solvent molecules within the pores of the framework. This is an essential step to maximise the capacity of the pores for the subsequent adsorption of the guest molecules and for characterisation when studying structural effects through powder X-ray diffraction or surface area analyses to be used for an accurate direct comparison with the guest loaded sample.

#### 3.5.1 Powder X-ray diffraction (PXRD)

Powder diffraction was performed using a PANalytical X'Pert PRO Chiller 59 diffractometer using Ni-filtered CuK $\alpha$  radiation source ( $\lambda = 1.5418 \text{ \AA}$ ) scanning a range of  $2\theta = 4 - 50^\circ$ , at room temperature. The samples were loaded on zero-background Si-wafers after drying. The comparison between experimental data and crystallographic data was performed on X'Pert Highscore Plus software by PANalytical; using Rietveld refinement DICVOL for indexing the powder pattern and Le Bail fitting for identifying space groups of the

## Chapter 3: Methods

---

indexed pattern. In addition, Cambridge Crystallography Data Centre (CCDC) database<sup>11</sup>, International Centre for Diffraction Data (ICDD)<sup>12</sup>, Crystallography Open Database (COD)<sup>13</sup>, were used for accessing literature and comparative data.

The  $d$ -spacing has been calculated from the Bragg's law equation [ $\lambda = 2d \sin \theta$ ]; where  $\theta$  is the diffraction angle. Characteristic diffraction peaks positions ( $2\theta$ ) were measured from the recorded patterns on X'Pert Highscore Plus software assuming cubic symmetry and average values over ten samples for each MOF were compared with average values for guest@MOF composite. Percentage change in  $d$ -spacing was calculated by determining and comparing the difference in lattice parameters of the as synthesised MOF and guest@MOF composite. The percentage change in lattice from initial value (PCI $v$ ) is defined by Eq. 3.5.

$$PCIv = \frac{(Initial-Final)_{d-spacing}}{Initial_{d-spacing}} \times 100 \quad (3.5)$$

A more accurate approach of interpreting data to understand changes in lattice  $d$ -spacing would be to perform indexing and Rietveld refinement for each powder pattern to quantify the structural changes in the diffraction patterns between MOF, monomer@MOF, and polymer@MOF composite. However, due to time constrains at the time of submission of this thesis, they have not been performed. Further work on studying structural changes in the MOF will account for indexing and structural refinement.

Peak full-width at half maximum (FWHM) was determined by using the Debye-Scherrer equation (Eq. 3.6) using particles size of 0.2 and 0.09  $\mu\text{m}$  for MOF-5 and HKUST-1, respectively. The shape factor ( $K$ ) was used as 0.91 for both cubic and octahedral crystal of MOF-5 and HKUST-1, respectively. ( $\lambda_{\text{Cu}} = 1.5406 \text{ \AA}$ )

$$\tau = \frac{K\lambda}{\beta \cos\theta} \quad (3.6)$$

## Chapter 3: Methods

---

### 3.5.2 Nuclear Magnetic Resonance (NMR)

$^1\text{H}$  and  $^{13}\text{C}$  nuclear magnetic resonance (NMR) spectra were recorded on either a Bruker 300 Fourier, Bruker 400 UltraShield<sup>TM</sup> or a Bruker 500 MHz Avance NMR spectrometer. All the 2D COSY correlation-spectra were recorded on Bruker 500 MHz Avance NMR spectrometer.

The obtained chemical shifts ( $\delta$ ) are reported in ppm and are referenced to the residual solvent signal. Spin-spin coupling constants (J) are given in Hz. The chemical shift assignment and peak properties were determined using MestReNova software by Mestrelab Research S.L.

#### Calculation of number average molecular weight ( $M_n$ ) and conversion from NMR data.

The number-average molecular weight  $M_n$  and degree of polymerisation (DP) of polymer units were calculated from the integral values of methylene of polymer chain proton signals at 1.6–2.2 ppm for PVAc and PCL. The integral per proton was calculated by summing end group proton integrals and divided by the number of protons. The number of repeating units ( $n$ ) were calculated using Eq. 3.8.

$$n = \frac{(\text{Sum of } \text{CH}_2 \text{ proton integrals} / \text{number of } \text{CH}_2 \text{ protons})}{\text{Integral per proton values}} \quad (3.7)$$

$M_n$  was calculated by multiplying the formula weight of end groups and repeating units using Eq. 3.7.

$$M_n = FW_{\text{end-groups}} + n * FW_{\text{repeating unit}} \quad (3.8)$$

The conversion to polymer was calculated from the dried isolated polymers from the MOF (Eq 3.9). Conversion of VAc monomer to polymer was calculated from the summation of normalised integration of characteristic polymer methylene peak to the normalised

## Chapter 3: Methods

---

integration of monomer and polymer methylene peaks. (PVAc conversion, VAc: CH<sub>2</sub> – 4.56 ppm; PVAc: CH<sub>2</sub> – 4.85 ppm). The conversion of ε-CL to PCL was determined by using the discrete signals of the protons in γ-position for ε-CL, and the respective protons of monomer and the polymer. While the signal at δ = 4.15 ppm is assigned to the ε-CL, the signal for the polymer is found at δ = 3.97 ppm if the spectrum is measured in CDCl<sub>3</sub>.

$$\text{Conversion (\%)} = \frac{\int \text{Polymer}_{CH_2}}{\int \text{Monomer}_{CH_2} + \int \text{Polymer}_{CH_2}} \times 100 \quad (3.9)$$

### 3.5.3 Thermogravimetric Analysis (TGA)

Thermogravimetric (TG) data was recorded using a PerkinElmer Pyris 1 thermogravimetric instrument. Approximately 15 mg of the powdered material was loaded into an alumina crucible and heated in a flow of air (20 mL/min) from room temperature to 700 °C at the rate of 5 °C/min. The data was also acquired in nitrogen flow. (Cardiff Catalysis Institute (CCI), Cardiff University).

For all TGA results where the empirical formula was known the first and second order differential curves were used to identify small changes and the inflection points in the data. The first and second order differentials were calculated using the Origin 2017 software's data analysis functions. The first order differential is indicative of changes in mass, whereas the second order difference identifies inflection points in the data.

Using the experimental mass losses at different stages in the TGA profile of the MOF, estimating the composition of the MOF is possible. This includes the amount of moisture, residual solvent in the MOF and the amount of monomer present in MOF-Polymer composite. In principle, Eq. 3.10 could be used to assist in these calculations but the variable solvent content in our systems made this approach troublesome.

$$R_{EXP} = \frac{M_w[T_t \text{ }^\circ\text{C}]}{M_w[\text{Residue}]} = \frac{M_w[\text{Desolvated MOF}]}{M_w[\text{Residue}]} \quad (3.10)$$

Where,  $R_{exp}$  is the experimental MOF/residue ratio,  $M_w$  is the molecular weight,  $T_t$  is the temperature at which the linker decomposition is initiated.

### 3.5.4 Infrared Spectroscopy

Infrared spectroscopy was carried out on a SHIMADZU IRAffinit-1S spectrometer. All spectra were acquired by scanning between the range of 500 – 4000  $\text{cm}^{-1}$  and averaging 32 scans.

### 3.5.5 Mass Spectrometry

All mass spectrometry characterisation was carried out by CHEMY Analytical Services at Cardiff School of Chemistry.

**GC-MS:** Electron-spray (ES-MS) data was collected on a Waters LCT-Premier mass spectrometer. The mobile phase was 50:50  $\text{H}_2\text{O}/\text{ACN}$  (ACN – acetonitrile) with 1 % hydrochloric acid. For every sample run, four scans were taken, a blank run prior to the sample being added and then the sample was run under the modes ES+, ES-, and APCI+ (APCI – atmospheric pressure chemical ionisation). Samples were shown in ES+ mode. Sample analyte (10  $\mu\text{L}$ ) was injected via an autosampler and lock mass was employed (directly infused via a second pump) to ensure accuracy.

**MALDI:** was performed on a Bruker Autoflex Speed mass spectrometer, time-of-flight instrument equipped with a pulsed  $\text{N}_2$  laser (337 nm, 4 ns pulse width) and time delayed extraction source. All spectra were recorded in positive ion mode under delayed extraction conditions (220 ns) and in reflector mode. The accelerating voltage was 20 kV. The matrix

## Chapter 3: Methods

---

was dissolved in THF or acetone and was mixed with the polymerisation mixture in a 25:1 v/v ratio before ionization. The matrix used for each of the polymer is outlined in Table 3.1.

Table 3.1: Matrix, solvent and matrix-analyte concentration used for their MALDI analysis of polymer.

Polymer	Matrix	Matrix/Analyte conc.	Solvent
Polyvinyl Acetate	2,5 – dihydroxybenzoic acid (DHB)	5 mg/mL	Acetone
Poly(lactic acid)	2,4,6 - Trihydroxyacetophenone (THPA)	10 mg/mL	THF
Poly( $\epsilon$ -caprolactone)	2,5 – dihydroxybenzoic acid (DHB)	10 mg/mL	THF

**ICP-AES:** ICP-AES was performed to determine the element content in the analyte samples, Table-3.2. Data were collected on an Agilent 7900 ICP-MS with I-AS autosampler. Samples were run against an external calibration - Blank, 0.001, 0.01, 0.1 and 1 mg/L (ppm) using PerkinElmer Multi-Element Standard 3 and compared it against Agilent IS Standard P/N 5188-6525 72 Ge. Instrument was run in He mode. (Table 3.2: Elements analysed, on the next page)

## Chapter 3: Methods

---

Table 3.2: Elements analysed for the ICP-AES.

Element Analysed	Compound	
$\text{Cu}^{2+}$	Polymers extracted from HKUST-1	Residual metal content in the polymer.
$\text{Zn}^{2+}$	Polymers extracted from MOF-5	Residual metal content in the polymer.
$\text{Na}^{2+}$	Terephthalic Acid	Confirmation whether deuterated material was the salt form or the acid post acidification.

### 3.5.6 Gas Adsorption

$\text{N}_2$  adsorption isotherms were measured on a Micrometrics 3Flex gas adsorption analyser at 77 K. Samples were first degassed at 100 °C for 24 hours using degasser on Quantachrome Quadrasorb evo gas sorption surface area and pore size analyser. The isotherms were obtained using a  $\varnothing 9$  mm sample tube containing 100-150 mg of samples under study.

BET surface areas were calculated from the isotherms using Microactive data reduction and control software for pore BET surface area and pore-size distribution analysis. (Cardiff Catalysis Institute (CCI), Cardiff University). The BET analysis was performed by plotting  $x/v(1-x)$  vs  $x$ , where  $x = (P/P_0)$  ( $P_0 = 1$  bar) and  $v$  is the volume of nitrogen adsorbed per gram of MOF at STP. This output is a curve with three distinctive regions: low pressure – concave region, a linear region at intermediate pressures, and a convex region for high pressure.

## Chapter 3: Methods

---

The slope ( $[c - 1]/v_m c$ ) and y intercept ( $1/v_m c$ ) of this linear region gives the monolayer capacity ( $v_m$ ), which can be used to calculate the surface area from Eq. 3.11.

$$A = v_m \sigma_0 N_{AV} \quad (3.11)$$

Where,  $\sigma_0$  is the cross-sectional area of the adsorbate at solid or liquid density ( $16.2 \text{ \AA}^2$  for nitrogen)<sup>14</sup>.

It is to be noted that the BET model assumes adsorption of gases onto a flat surface. In case of three-dimensional MOFs, adsorption takes place at vacant metal centres and at the pore walls within the void spaces by pore-filling mechanism. Despite this caveat, the BET model is often used to measure the surface area of these materials.<sup>15-17</sup> The BET model is able to reproduce the isotherm shapes in the low pressure region to reasonable accuracy and for this reason, the points corresponding to the final uptake in the adsorption of the isotherm between  $P/P_0 = 0.2-2$  mbar are plotted as  $P/P_0$  against  $P_n/(P-P_0)$  for BET surface area determination. In this thesis, the BET surface area has been calculated using 3Flex v4.00 for BET surface area and gas adsorption measurements.

### 3.5.7 Scanning Electron Microscopy (SEM)

Scanning Electron Microscopy images were collected using a HITACHI TM-3030 Plus Tabletop Microscope at 15 keV under high vacuum. Samples were mounted on a carbon tape and images were collected on the data software. Energy Dispersive X-ray (EDX) analysis was carried out on the Bruker Quantax 70 software.

## Chapter 3: Methods

---

### 3.5.8 Gas Phase Chromatography (GPC)

GPC measurements were taken on Agilent 1260 Infinity II instrument coupled with a PL Gel 5  $\mu\text{m}$  mixed-d column mass selective detector (Agilent, Santa Clara, CA). Samples were dissolved in HPLC-grade THF and filtered to remove any particulates with a 0.2  $\mu\text{m}$  syringe filter. The mass spectral scan rate 50 scans per second. The GC was operated with a flow rate of 1.0 mL/min. The mass spectrometer was operated in electron impact (EI) mode using an ionization voltage of 70 eV and a source temperature of 35  $^{\circ}\text{C}$ .

### 3.5.9 Other Methods

In addition to the methods described above, other non-standard characterisation methods were also used. Details for these methods are given in Chapter 4 and 5 with the description of the methods and their data analysis.

### 3.6 References

- 1 V. R. Remya and M. Kurian, *Int. Nano Lett.*, 2019, **9**, 17–29.
- 2 A. Kirchon, L. Feng, H. F. Drake, E. A. Joseph and H. C. Zhou, *Chem. Soc. Rev.*, 2018, **47**, 8611–8638.
- 3 X. Guo, S. Geng, M. Zhuo, Y. Chen, M. J. Zaworotko, P. Cheng and Z. Zhang, *Coord. Chem. Rev.*, 2019, **391**, 44–68.
- 4 Z. A. D. Lethbridge, J. J. Williams, R. I. Walton, K. E. Evans and C. W. Smith, *Microporous Mesoporous Mater.*, 2005, **79**, 339–352.
- 5 J. Tian and G. Cao, *Coord. Chem. Rev.*, 2016, **320–321**, 193–215.
- 6 The Parr Instrument Company, <https://www.parrinst.com/products/sample-preparation/acid-digestion/general-purpose-acid-digestion-vessel-model-4749-23-ml/documents/>, (accessed 26 March 2020).
- 7 OSP - Autoclave Hydrothermal Experiments | Safety Web | Oregon State University, <https://chemsafety.chem.oregonstate.edu/content/osp-autoclave-hydrothermal-experiments>, (accessed 9 April 2020).
- 8 S. S. Y. Chui, S. M. F. Lo, J. P. H. Charmant, a G. Orpen and I. D. Williams, *Science*, 1999, **283**, 1148–1150.
- 9 K. Schlichte, T. Kratzke and S. Kaskel, *Microporous Mesoporous Mater.*, 2004, **73**, 81–88.
- 10 3,6-Dimethyl-1,4-dioxane-2,5-dione 99% | Lactide | Sigma-Aldrich, <https://www.sigmaaldrich.com/catalog/product/aldrich/303143?lang=en&region=GB>, (accessed 3 April 2020).
- 11 Home - The Cambridge Crystallographic Data Centre (CCDC), <https://www.ccdc.cam.ac.uk/>, (accessed 15 April 2020).
- 12 The International Centre for Diffraction Data - ICDD, <http://www.icdd.com/>, (accessed 15 April 2020).
- 13 Crystallography Open Database, <http://www.crystallography.net/cod/index.php>, (accessed 15 April 2020).
- 14 K. S. Walton and R. Q. Snurr, *J. Am. Chem. Soc.*, 2007, **129**, 8552–8556.
- 15 F. J. Uribe-Romo, J. R. Hunt, H. Furukawa, C. Klöck, M. O’Keeffe and O. M. Yaghi, *J. Am. Chem. Soc.*, 2009, **131**, 4570–4571.
- 16 D. J. Tranchemontagne, K. S. Park, H. Furukawa, J. Eckert, C. B. Knobler and O. M. Yaghi, *J. Phys. Chem. C*, 2012, **116**, 13143–13151.

## Chapter 3: Methods

---

- 17 Y. Yan, X. Lin, S. Yang, A. J. Blake, A. Dailly, N. R. Champness, P. Hubberstey and M. Schröder, *Chem. Commun.*, 2009, 1025–1027.
- 18 B. D. Cullity, *Elements of DIFFRACTION*, Wiley, New York, 1978.
- 19 What is a Crystal?, <https://nature.berkeley.edu/classes/eps2/wisc/Lect4.html>, (accessed 3 April 2020).
- 20 A. West, *Solid State Chemistry and its Applications, 2nd Edition, Student Edition*, 2014.
- 21 Bravais lattices :: Condensed Matter Physics :: Rudi Winter's web space, <http://users.aber.ac.uk/ruw/teach/334/bravais.php>, (accessed 6 April 2020).
- 22 N. W. Ashcroft, *Solid State Physics*, Harcourt School, Internatio., 1987.
- 23 M. T. Weller, *Inorganic Materials Chemistry*, Oxford University Press, 1995.
- 24 Diffraction; Encyclopedia Britannica, <https://www.britannica.com/science/diffraction>, (accessed 6 April 2020).
- 25 Braggs Law, [https://serc.carleton.edu/research\\_education/geochemsheets/BraggsLaw.html](https://serc.carleton.edu/research_education/geochemsheets/BraggsLaw.html), (accessed 3 April 2020).
- 26 E. Zolotoyabko, *Basic Concepts of X-Ray Diffraction*, Wiley-VCH Verlag, 2011.
- 27 M. F. Moody, *Struct. Biol. Using Electrons X-rays*, 2011, 277–298.
- 28 Crystallography. Scattering and diffraction. The Bragg's Law, [https://www.xtal.iqfr.csic.es/Cristalografia/parte\\_05\\_5-en.html](https://www.xtal.iqfr.csic.es/Cristalografia/parte_05_5-en.html), (accessed 6 April 2020).
- 29 Y. Waseda, E. Matsubara and K. Shinoda, *X-Ray Diffraction Crystallography*, Springer International Publishing, 2016, vol. 46.
- 30 P. D. Hatten, S. B. Wilkins, T. A. W. Beale, T. K. Johal, D. Prabhakaran and A. T. Boothroyd, *J. Synchrotron Rad.*, 2005, **12**, 434–441.
- 31 N. Iwashita, in *Materials Science and Engineering of Carbon*, Elsevier, 2016, pp. 7–25.
- 32 X-ray Detectors, <http://pd.chem.ucl.ac.uk/pdnn/inst1/detects.htm>, (accessed 7 April 2020).
- 33 X-Ray Goniometer | Article about X-Ray Goniometer by The Free Dictionary, <https://encyclopedia2.thefreedictionary.com/X-Ray+Goniometer>, (accessed 7 April 2020).
- 34 G. S. Smith and R. L. Snyder, *J. Appl. Crystallogr.*, 1979, **12**, 60–65.

## Chapter 3: Methods

---

- 35 Zhang Xu, Zhang Ying, Wang Dong and Qu Fengyu, *J. Nanomater.*, 2014, **2014**, 1–6.
- 36 Powder Diffraction, <http://pd.chem.ucl.ac.uk/pdnn/diff2/kinemat2.htm>, (accessed 7 April 2020).
- 37 M. Liang, R. Harder and I. K. Robinson, *IUCrJ*, 2014, **1**, 172–178.
- 38 K. Masutani and Y. Kimura, *Poly(lactic acid) Science and Technology: Processing, Properties, Additives and Applications*, Royal Society of Chemistry, London, 2015.

# Chapter 4

---

## Characterisation and Analysis

## Chapter 4: Characterisation and Analysis

---

### 4.1 Scope

This chapter discusses the characterisation of HKUST-1 and MOF-5, and changes induced by guest incorporation in the MOF pores. Further guest@MOF composites will be discussed in detail by different characterisation methods to determine efficiency of polymerisation of vinyl acetate,  $\epsilon$ -caprolactone, and lactic acid confined in the microporous MOF.

The samples were characterised via PXRD for observing structural changes in the MOF and FTIR spectroscopy was used to determine successful polymerisation. Both samples were also set aside for complementary characterisations by TGA, gas adsorption and desorption, SEM microscopy, and BET surface area analysis.

Dried polymer following isolation (Section 3.4) from the MOF was stored in a sealed glass vial. The sample was used for characterised by FTIR spectroscopy,  $^1\text{H}$  and  $^{13}\text{C}$  NMR, TGA, ESI and GC-MS, MALDI-TOF, ICP-AES, GPC, and SEM microscopy will be discussed in this chapter.

### 4.2 MOF-5

MOF-5 was synthesised by the solvothermal synthesis method explained in section 3.2.2. MOF-5, monomer@MOF-5 and polymer@MOF-5 guest were prepared as described in Section 3.3. The results of characterisation analyses of MOF-5, monomer@MOF-5 composite, and polymers@MOF-5 isolated from MOF-5 by various methods will be described in this section.

## Chapter 4: Characterisation and Analysis

### 4.2.1 MOF-5: Powder X-Ray Diffraction

The crystallinity of the synthesised MOFs structures and guest modified MOF composites was characterised by PXRD and compared with the examples reported in literature and simulated data. The diffraction pattern of as-synthesised MOF-5 is shown in Figure 4.1. All diffraction peaks were indexed and were in accordance with the literature reported values.<sup>1,2</sup>

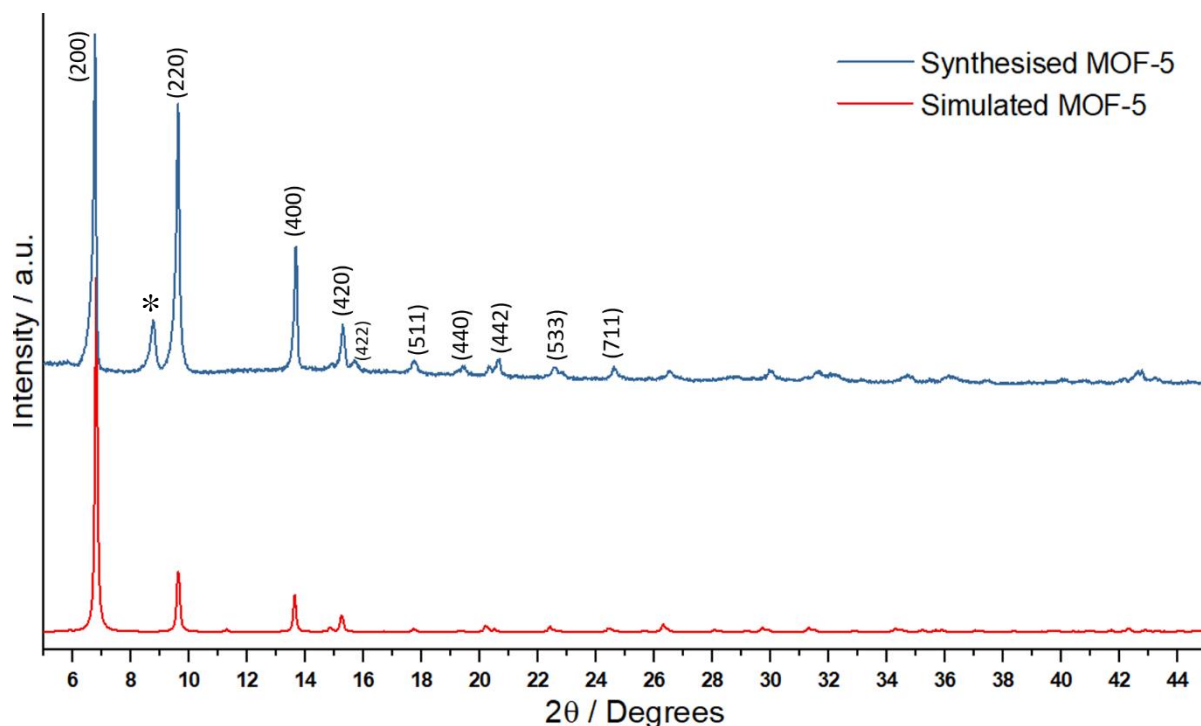


Fig 4.1: PXRD pattern for synthesised MOF-5 (top) vs. simulated MOF-5 pattern (bottom) from CIF (CCDC: 175572). (\* denoted additional peak arising from bound solvent DMF)

There is an additional peak observed at  $8.9^\circ$  [adjacent to the peak at  $9.7^\circ$  (200)] in the presence of guest DMF solvent molecules in the framework. The peak diminishes in intensity after repeat washing, solvent exchanging with chloroform and upon drying ( $120^\circ\text{C}$  for 24 h+). In cases where the solvent is not completely removed, the peak at  $8.9^\circ$  is present. Removal of solvent DMF molecules increases the flexibility of the MOF-5 leading to a higher cubic [ $Fm\bar{3}m$ ] symmetry in the framework and consequently, resulting in disappearance of the peak at  $8.9^\circ$  in the powder pattern.<sup>3</sup> DMF has preferential binding to the  $\text{Zn}_4\text{O}$  metal node of the MOF linked to the C-O of the linker, thus inhibiting the flexibility of

## Chapter 4: Characterisation and Analysis

---

MOF.<sup>4</sup> Further information regarding the number of DMF molecules per lattice for the samples calculated is in section 5.1.2.

The peak at 13.8° corresponds to reflection from (400) planes in a cubic MOF-5 (c-MOF-5) structure, and appears as an intense peak ( $I_{13.8^\circ}/I_{9.7^\circ} \leq 0.5$ ), whereas the intensity of this peak in the interpenetrated MOF is very low.<sup>3</sup> As the (400) planes diffract half as intense compared to what is expected from (200) planes, the relative high peak intensity of the 13.8° ( $\leq 0.5$ ) may suggest a trigonal or rhombohedral (t-MOF-5) structure.<sup>3</sup> Based on powder diffraction patterns, it is not possible to conclusively identify the crystal structure of MOF-5 and further investigation is needed through TGA, BET surface area analysis and SCXRD (Section 4.3.1 and 5.9.2).

The simulated and experimental powder patterns for the c-MOF-5 and t-MOF-5 strongly suggest that they represent the same phase. It is reported that t-MOF-5 possess a smaller BET surface area compared to c-MOF-5.<sup>5</sup> The c-MOF-5 powder pattern reported in the literature by Yaghi *et al.* is consistent with the simulated pattern.<sup>6</sup> However, the two represent an ideal desolvated MOF-5 phase and at ambient temperature and pressure, it is unlikely that the MOF maintains this structure. Hence, the broadening of peak at 9.7°, appearance of peak at 8.9° from coordinated solvent DMF, and following BET surface area analysis (Section 4.8.1), TG analysis (Section 4.4.1), and structure refinement with SCXRD (Section 5.9.2) all suggest a t-MOF-5 phase. Another possible explanation for additional peaks in the diffraction patterns may be from an interpenetrated structure of MOF-5 (int-MOF-5), where two cubic nets of MOF-5 are found as interpenetrated lattices.<sup>5</sup> For int-MOF-5, the 13.8° peak corresponds to the (2, 0, -4) plane, and the 6.8° arises from the (1, 0, -2) planes. The simulated XRD pattern of non-interpenetrated MOF-5 based on the crystal structures has a different peak intensity ratio to those of int-MOF-5. Shown in Fig 4.2 are the diffraction pattern for laboratory synthesised non-interpenetrated MOF-5 and int-MOF-5. It can be seen that intensity ratios for characteristic MOF-5 peaks differ, where the peak at 6.8° is slightly shifted and less intense and the 8.9° is the dominating peak for int-MOF-5. Moreover, there is significant broadening of peaks at 9.7° and at higher  $2\theta$  from multiple scattering.

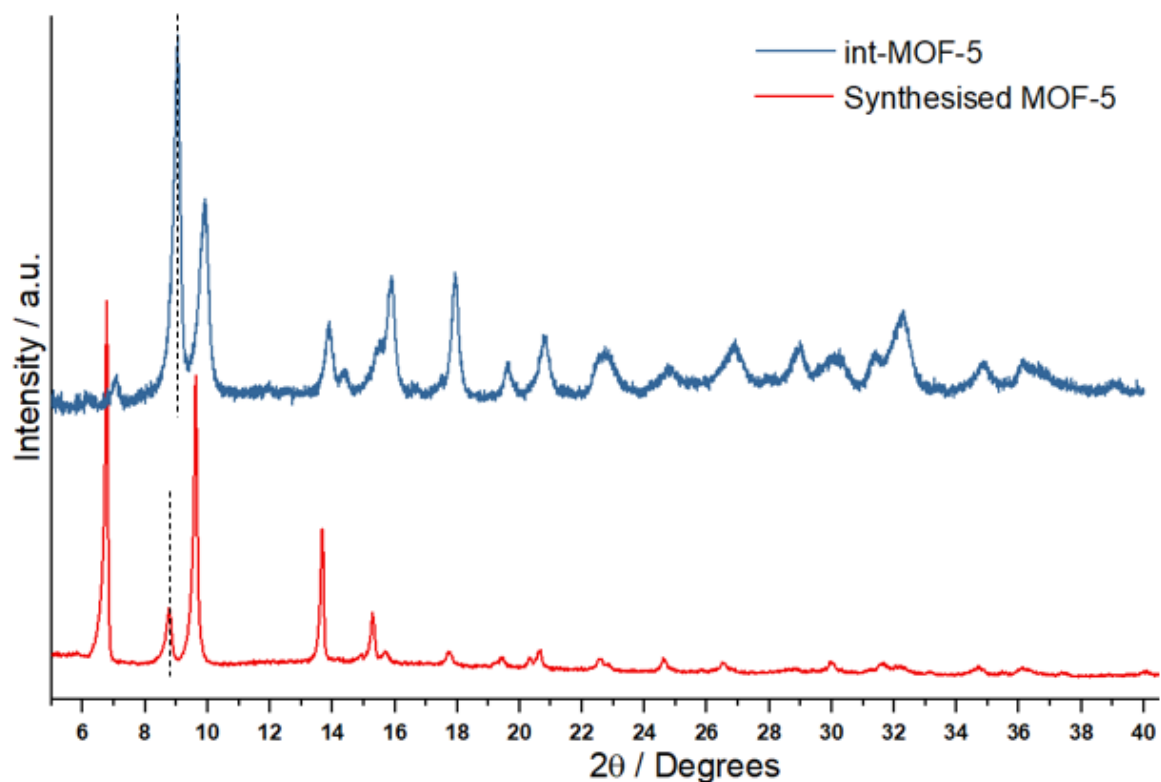


Fig 4.2 PXRD patterns for as-synthesised MOF-5 (bottom) and interpenetrated MOF-5 synthesised by literature reported method (top).<sup>5</sup> Peaks corresponding to reflection planes are indexed, the pattern is baseline corrected (Section 3.5.1). Dashed lines indicate coordinated solvent peaks for corresponding MOF structures.

### 4.2.1.1 In-situ polymerisation: vinyl acetate in MOF-5

The XRD patterns of monomer@MOF-5 and polymer@MOF-5 composites were in good agreement with that of empty MOF-5, indicating that microstructures of the MOF are well-retained without significant structural deformation with monomer adsorption and post-polymerisation. It can be observed through the powder pattern that MOF-5 undergoes minute structural deformation upon loading with guest molecules (Fig 4.3). The changes are in effect, expansion upon monomer adsorption and framework contraction following polymerisation of the monomer. The expansion effect is observed as a decrease in  $2\theta$  angle of the peak position that are most observable on the  $6.7^\circ$ ,  $8.9^\circ$ , and  $13.7^\circ$  peaks. These changes are may be a result of an increase in amorphous nature of the monomer-adsorbed structure of the MOF due to increase in disorder, resulting in decrease in signal-to-noise ratio.<sup>7</sup> The second effect is of framework contraction upon polymerisation of intrinsic monomer within

## Chapter 4: Characterisation and Analysis

the pores of the MOF resulting in a increase in  $d$ -spacing observed by an increase in different peak positions. Although the crystalline nature of the original empty MOF is not regained, there is a considerable increase in signal-to-noise ratio compared to the monomer@MOF suggesting an increase in overall crystallinity of the material.

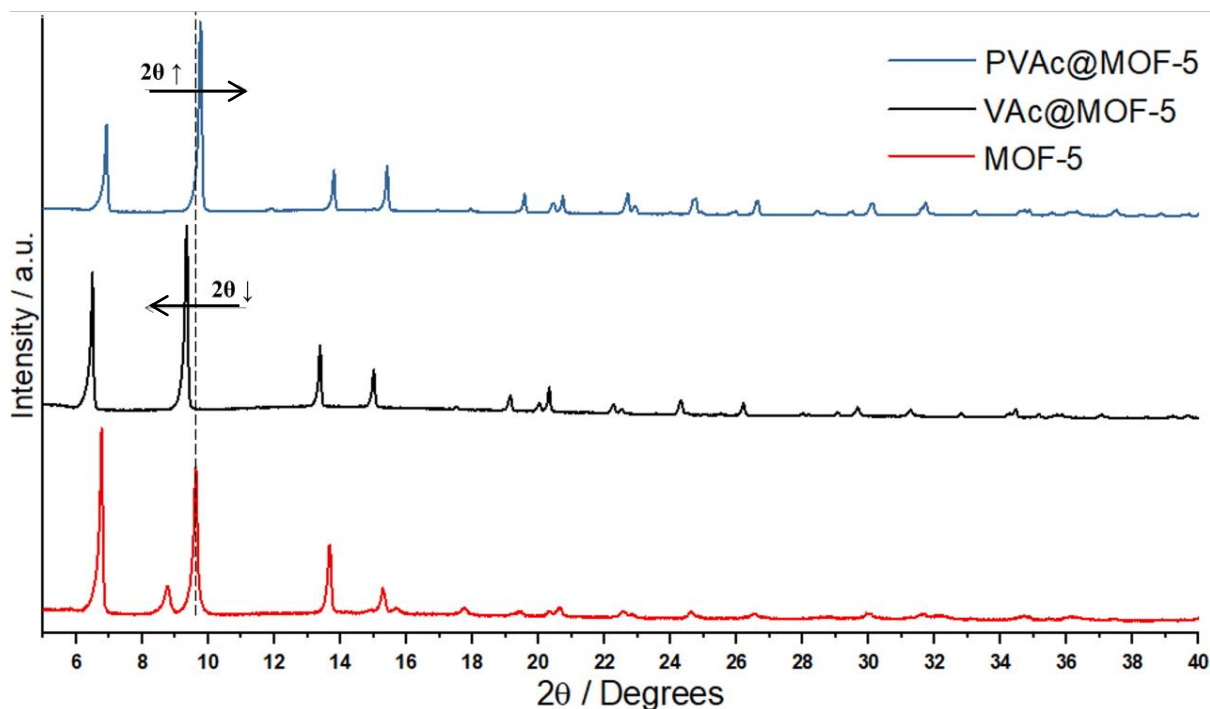


Fig 4.3: PXRD pattern of synthesised MOF-5 (bottom), VAc@MOF-5 (middle), and PVAc@MOF-5 (top). Black arrows indicate the direction of shift for peak at  $9.7^\circ$  (Expansion for  $2\theta = 5\text{--}15^\circ$  range is shown in Appendix Fig A4.1. The diffraction patterns shown are background subtracted)

The changes in peak intensity arise because of introduction of guest molecules within the pores of the MOF. The expansion and subsequent contraction of the MOF lattice observed as changes in  $2\theta$  is may be explained as an effect arising from adsorption of the monomer guest that results in saturation of the pores to an extent that it exerts stress on the crystal structure, enough to result in framework expansion.<sup>8</sup> Following polymerisation, contraction of the framework suggests that there is a threshold time stage at 21 h for VAc@MOF-5 where the

## Chapter 4: Characterisation and Analysis

---

MOF structure begins to contract suggesting that polymer chains act to reinforce the crystal lattice of the MOF.

To further analyse the changes in the crystal structure of MOF-5 during the polymerisation process, samples were taken at individual time points during polymerisation and their powder diffraction pattern were recorded. MOF-5 was dried, activated and soaked in monomer as described in section 3.2.2. The reaction temperature was increased to polymerisation temperature (70 °C) to initiate polymerisation. The samples were collected from the same experiment during polymerisation without cooling the sample from 70 °C, and under a nitrogen atmosphere. Individual time points for the experiment are presented in Table 4.1.

Table 4.1: Sample identification and corresponding time of polymerisation for polyvinyl acetate in-situ polymerisation in MOF-5. Error on individual measurements of  $2\theta$  ( $\pm 0.05$ ).

<b>Sample Identification</b>	<b>Elapsed Polymerisation Time</b>	<b>Sequential change in <math>2\theta</math></b>
Sample <b>M0</b>	0 h	6.9 (Starting value)
Sample <b>M1</b>	12 h	0.0
Sample <b>M2</b>	18 h	+0.1
Sample <b>M3</b>	21 h	+0.2
Sample <b>M4</b>	24 h	0.0
Sample <b>M5</b>	42 h	+0.2
Sample <b>M6</b>	45 h	+0.2
Sample <b>M7</b>	48 h	+0.2
Sample <b>M8</b>	66 h	+0.2
Sample <b>M9</b>	69h	-0.1
Sample <b>M10</b>	72 h	-0.1

## Chapter 4: Characterisation and Analysis

---

Table 4.2: Characteristic diffraction peaks, corresponding Miller index plane and  $d$ -spacing for MOF-5.

Diffraction Peak ( $2\theta$ deg)	Miller Plane (hkl)	$d$ -Spacing ( $\text{\AA}$ )
6.9	(200)	12.8
9.7	(220)	9.1
13.7	(400)	6.4
15.4	(420)	5.7

Fig 4.4 shows the displacement and changes in the peak positions of the PXRD diffractograms during the experiment. Sample M1 (12 h) shows negligible changes when compared to monomer@MOF composite. Past sample M4 (24 h), structural changes are more significant with a noticeable increase in  $2\theta$ , corresponding to a decrease in  $d$ -spacing and indicating contraction of the framework. The changes remain consistent with an increase in  $2\theta$  up to sample M5 (42 h), after which peak positions show little or no change.

## Chapter 4: Characterisation and Analysis

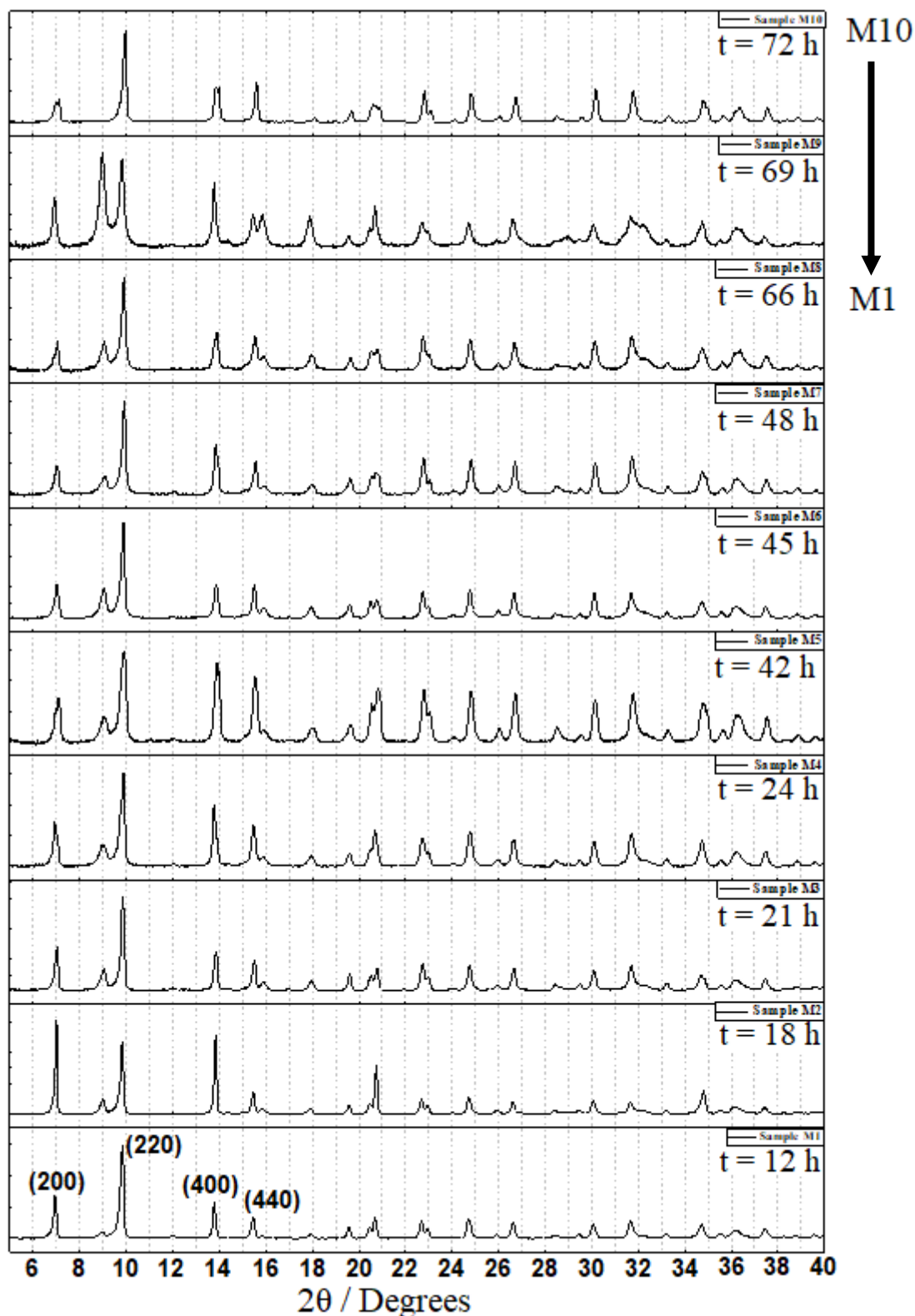


Fig 4.4: PXRD patterns of PVAc@MOF-5 from structural change–polymerisation time experiment. (Expansion for  $2\theta = 5\text{--}15^\circ$  range is shown in Appendix A4.2 and A4.3. The diffraction patterns shown are background subtracted)

## Chapter 4: Characterisation and Analysis

---

Any changes in  $2\theta = 9.7^\circ$  peak reflect changes arising on the metal nodes of the framework. There are little to no observable changes from sample M1 (12 h) to M3 (21 h). However, changes in diffraction pattern appear after M3 with consistent increase in  $2\theta$  corresponding to a decrease in  $d$ -spacing to M7 (48 h). Beyond sample M7 (48 h) the shifts in the peak are insignificant and there are negligible observable changes from samples M8 (66 h) to M10 (72 h). Changes observed in this region may support the argument that the monomer preferentially binds with the metal nodes, resulting in lattice frustrations and continuous contraction of the framework as the polymerisation process is ongoing and the monomer content reduced. This phenomenon is supported by characterisation methods described in Chapter 5. However, to accurately present this hypothesis based on PXRD patterns, a detailed investigation by indexing and Reitveld refinement is necessary to draw conclusions.

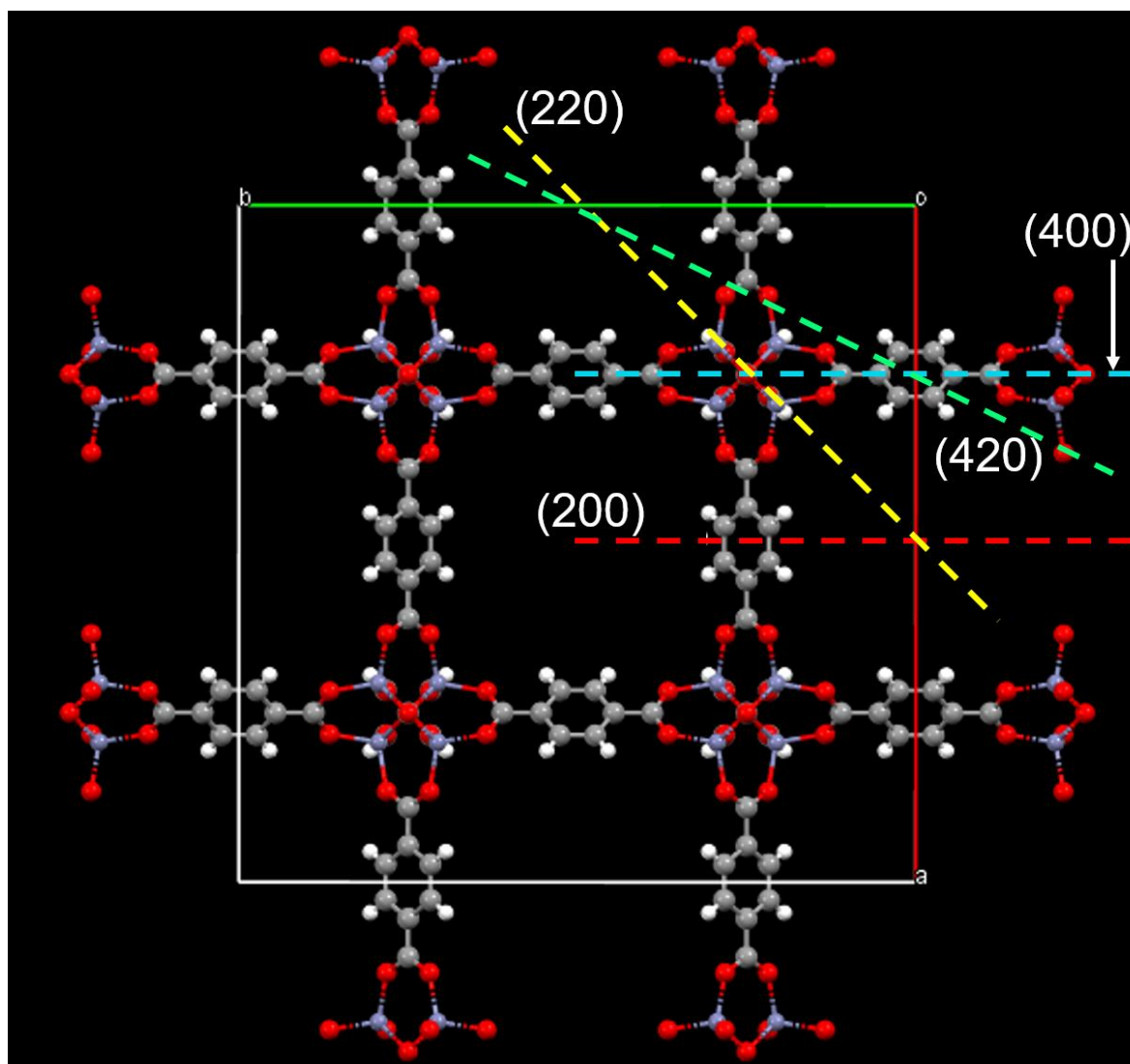


Fig 4.5: MOF-5 crystallographic structure and corresponding Miller indices planes (200), (220), (400) and (420) responsible for diffraction peaks at  $2\theta = 6.9^\circ$ ,  $9.7^\circ$ ,  $13.7^\circ$ , and  $15.4^\circ$  respectively.

Structural changes seen on the (220) plane of the lattice is consistent with the changes observed on the  $2\theta = 15.4^\circ$  peak ((420) plane) which shows simultaneous structural changes that occur between the metal-node and the BDC linker on the MOF-5 (Fig 4.5). The changes in  $d$ -spacings of the lattice for characteristic diffraction peaks from MOF-5 at  $2\theta = 6.9^\circ$ ,  $9.7^\circ$ ,  $13.7^\circ$ , and  $15.4^\circ$  are shown in A4.1 and A4.2 in the appendix.

The diffraction peak at  $2\theta = 13.7^\circ$  shows changes consistent changes observed with diffraction peaks at  $6.9^\circ$  and  $9.7^\circ$ . The changes here reflect the observations from the (220)

## Chapter 4: Characterisation and Analysis

---

and (420) plane with an initial decrease in  $d$ -spacing followed by continuous decrease to sample M7 (48 h), and no observable changes past M8 (66 h).

The reflection along the centre of the unit cell is responsible for the  $2\theta = 6.9^\circ$  peak, and thus shows any structural changes that may occur because of the phenyl ring displacement in the crystallographic cell. As the polymerisation progresses, we see slight changes in the  $d$ -spacing; an initial decrease, followed by an increase in the overall  $d$ -spacing. Without indexing and full structure refinement, it is not possible to draw firm conclusions, however, the qualitative increase in  $d$ -spacing observed is consistent with pore filling that affect the (220) and (420) plane reflections [CCDC Identifier: SAHYIK]. These reflections are known to be caused by the linker and metal-node bonds, and therefore suggest contraction of the framework during polymerisation.

### 4.2.1.2 In-situ polymerisation: $\epsilon$ -Caprolactone in MOF-5

The structural changes observed in MOF-5 before monomer addition and following polymerisation of  $\epsilon$ -caprolactone are consistent with the changes observed with in-situ polymerisation of vinyl acetate in MOF-5 with appearance of an additional peak at  $8.9^\circ$  and broadening of  $6.9^\circ$ ,  $9.7^\circ$ , and  $13.7^\circ$  peaks. Fig 4.6 shows a comparison of PXRD patterns of as-synthesised MOF-5,  $\epsilon$ -CL@MOF-5, and PCL@MOF-5. The increase in  $d$ -spacing upon adsorption of the monomer resulting in framework expansion ( $\epsilon$ -CL@MOF-5), followed by framework contraction observed by a decrease in the  $d$ -spacing as a result of polymer chains ‘reinforcing’ the framework is also observed with PCL@MOF-5 composites. This is observed with a decrease in peak width at full width at half minimum (FWHM) observed by Jian *et al.*<sup>9</sup> There is an additional peak visible at  $2\theta = 8.9^\circ$  (discussed in Section 4.2.1) that decreases in intensity upon guest sorption possibly due to sorbate molecules driving the coordinated solvent DMF molecules out of the framework.

In addition, diffraction peaks characteristic of PCL are observed in the PCL@MOF-5 composite and in isolated polymer from the MOF. PCL homopolymer crystallises with characteristic diffraction pattern with peaks at  $2\theta = 21.9^\circ$  and  $24.2^\circ$  corresponding to (110) and (200) planes of its orthorhombic crystal structure. It has been reported that the diffraction

## Chapter 4: Characterisation and Analysis

peaks broaden as the polymer loses its crystallinity.<sup>10</sup> PCL isolated from PCL@MOF show the characteristic peaks at  $2\theta = 21.6^\circ$  and  $23.9^\circ$  as two defined sharp peaks confirming the crystalline nature of the isolated polymer. (Fig 4.7)

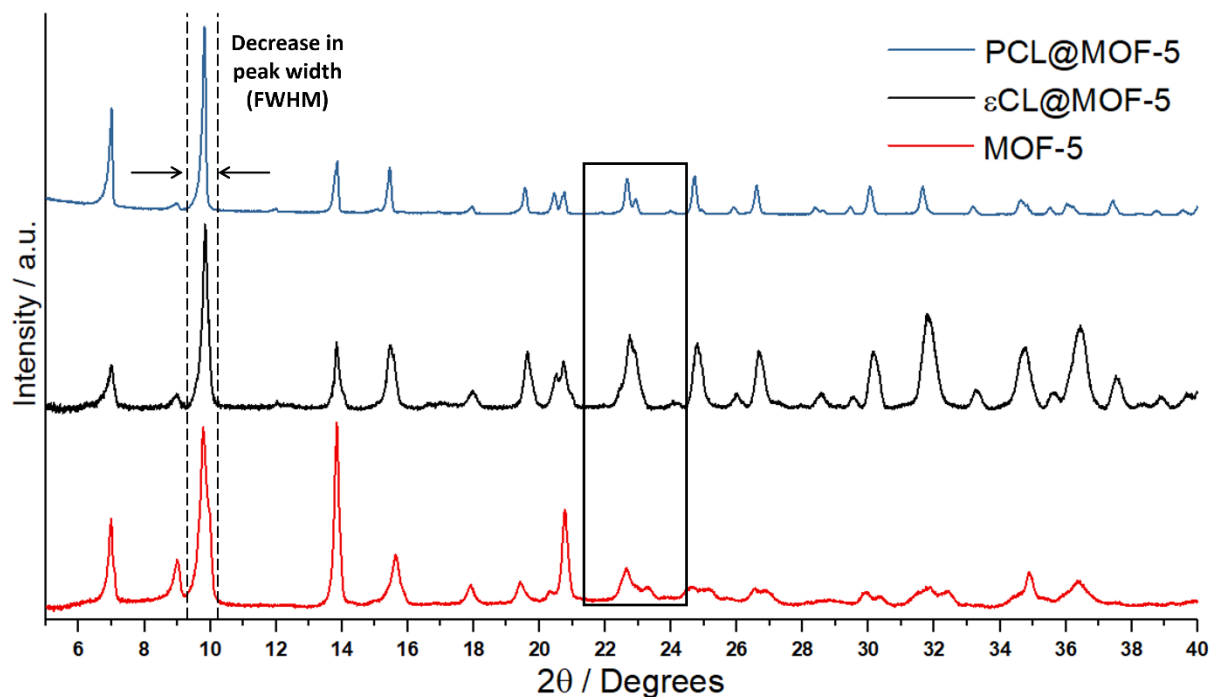


Fig 4.6 PXRD pattern of synthesised MOF-5 (bottom),  $\epsilon$ CL@MOF-5 (middle), and PCL@MOF-5 (top). (Expansion for  $2\theta = 5-15^\circ$  range is shown in Appendix A4.4. The diffraction patterns shown are background subtracted. PCL characteristic peak region is shown by black box)

## Chapter 4: Characterisation and Analysis

---

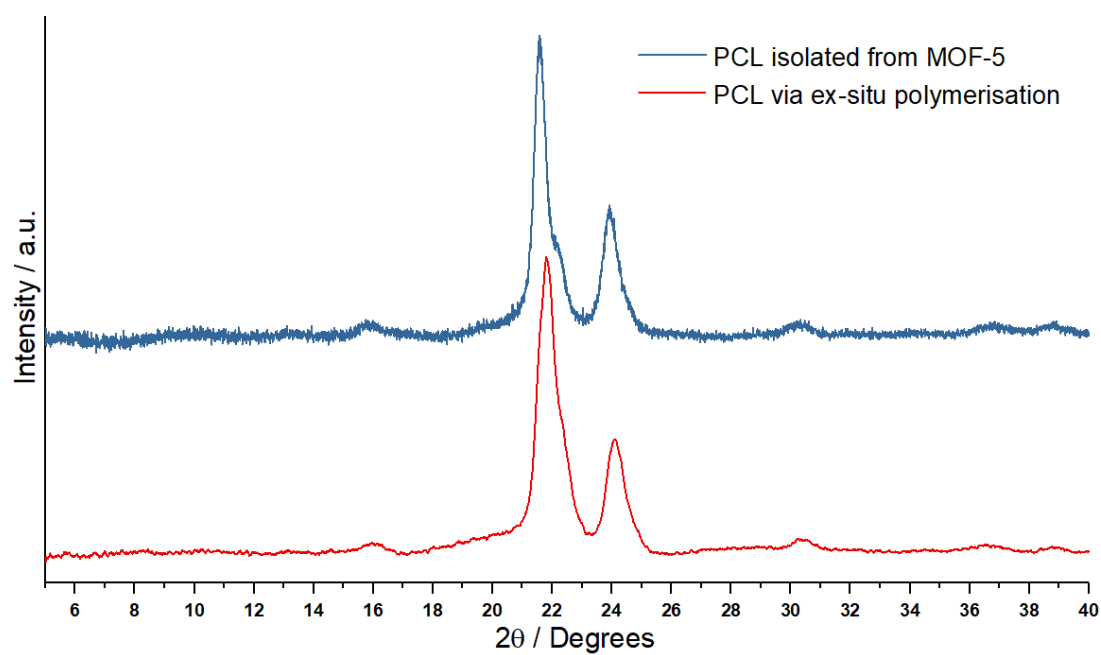


Fig 4.7 PXRD pattern of PCL@MOF-5, PCL isolated from PCL@MOF-5 (top), and PCL polymerised ex-situ (bottom).

## Chapter 4: Characterisation and Analysis

### 4.2.2 HKUST-1: Powder X-Ray Diffraction

The powder XRD pattern of as-synthesised HKUST-1 are shown in Fig 4.8.

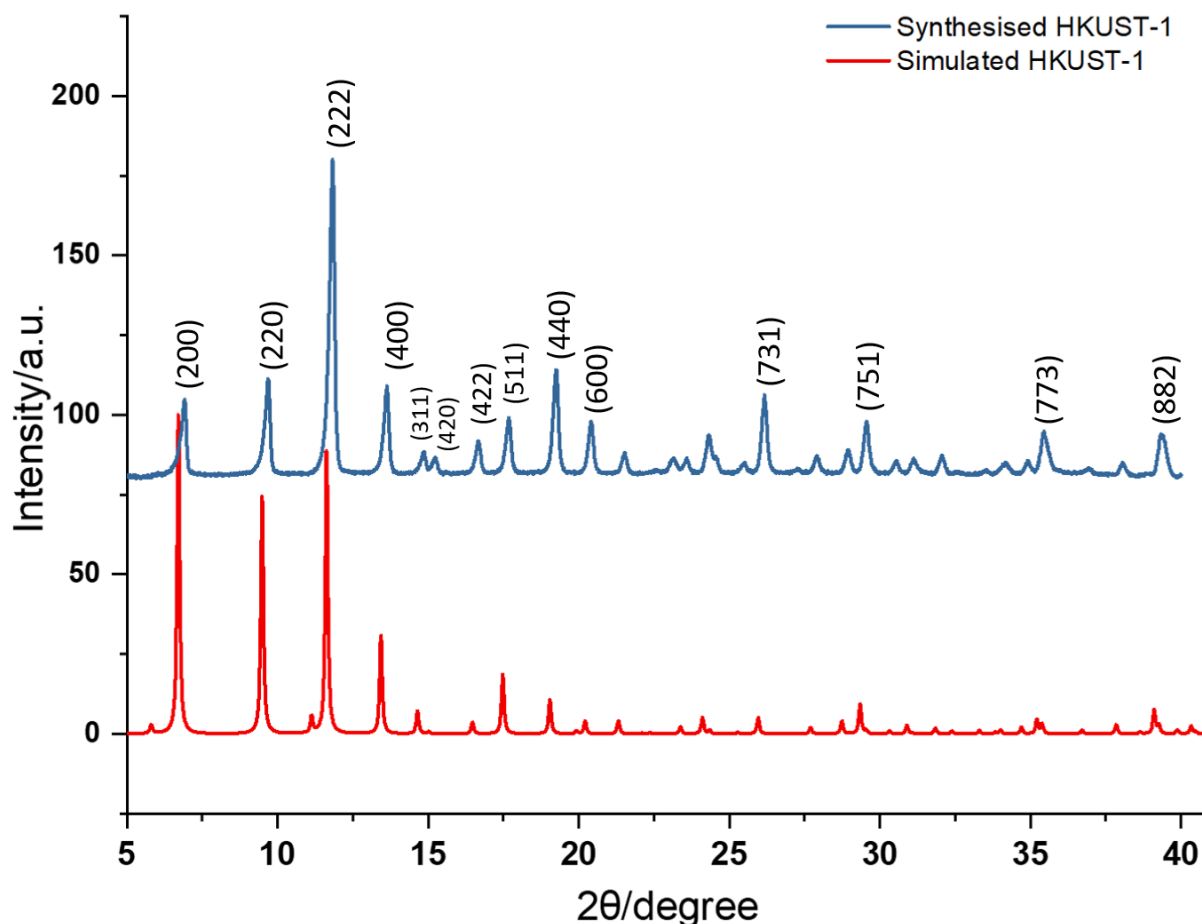


Fig 4.8: PXRD pattern for synthesised HKUST-1 (top) vs. simulated HKUST-1 pattern from CIF (CCDC: 112954) (bottom).

All characteristic diffraction peaks of HKUST-1 were in accordance with those reported in literature.<sup>11–13</sup> No obvious impurity peaks can be detected in the powder XRD patterns of HKUST-1 showing high crystallinity. The strong peaks at  $2\theta = 6.4^\circ$ ,  $9.1^\circ$ ,  $11.26^\circ$  and  $13.08^\circ$  matched well with the (200), (220), (222) and (400) planes confirming the cubic lattice. Further, small differences were observed with the simulated pattern with the intensity ratios of (311) to (420) plane, and (200) to (220) plane, which are both higher for the simulated pattern. This is likely because the simulated pattern represents a dehydrated HKUST-1 sample. HKUST-1 is very hygroscopic and hydration effects resulting in this phenomenon

## Chapter 4: Characterisation and Analysis

has been reported in literature.<sup>14</sup> It is challenging to avoid this discrepancy between simulated and synthesised samples as HKUST-1 rapidly adsorbs moisture from air during sample preparation for PXRD. Studies reported in literature also state that the reduction in intensity of peak at  $2\theta = 6.4^\circ$  is related to the FCC crystal structure loss due to hydration effects on HKUST-1.<sup>65</sup> The PXRD pattern shows negligible diffraction from potential unreacted copper nitrate and trimesic acid may have remained in the samples. Although there may be CuO and Cu(OH)<sub>2</sub> impurities present that results in diffraction peaks between  $2\theta = 32\text{-}40^\circ$ , it is difficult to conclude that without further characterisation (elemental analysis, TGA) due to possible secondary Bragg reflections effects from the highly crystalline structure.

### 4.2.2.1 In-situ polymerisation: vinyl acetate in HKUST-1

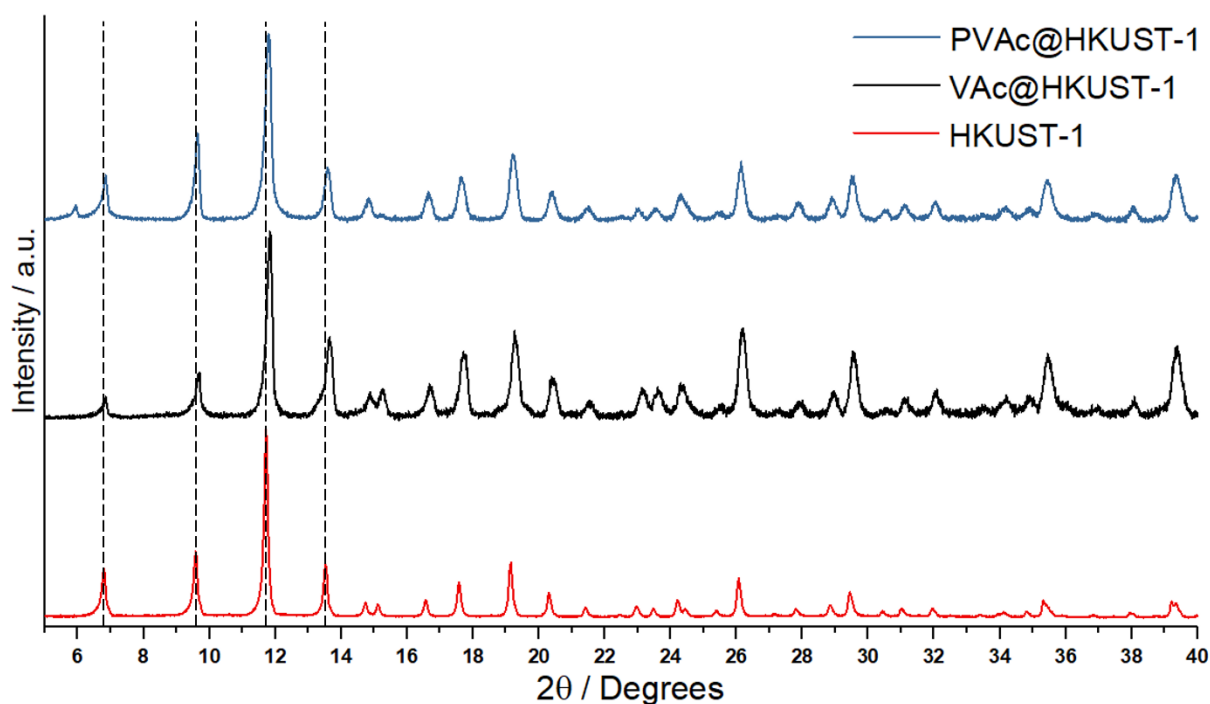


Fig 4.9: PXRD patterns for HKUST-1 (bottom), VAc@HKUST-1 (middle), PVAc@HKUST-1 (top). (Expansion for  $2\theta = 5\text{--}15^\circ$  range is shown in Appendix A4.5. The diffraction patterns shown are background subtracted)

PXRD patterns of VAc@HKUST-1 and PVAc@HKUST-1 composites were in good agreement with empty MOF (Fig 4.9), indicating that overall geometry of the MOF is well-retained upon monomer adsorption, or following in-situ polymerisation. Contrary to what is

## Chapter 4: Characterisation and Analysis

seen in the case of PVAc@MOF-5 composites, for PVAc@HKUST-1 there is an *increase* in  $2\theta$  observed upon monomer adsorption and subsequently, polymerisation. Also unlike PVAc@MOF-5, PVAc@HKUST-1 composite does not regain its original structure of the host MOF. The final  $d$ -spacing of PVAc@HKUST-1 is less than the initial  $d$ -spacing measured for desolvated host HKUST-1.

### 4.2.2.2 In-situ polymerisation: $\epsilon$ -caprolactone in HKUST-1

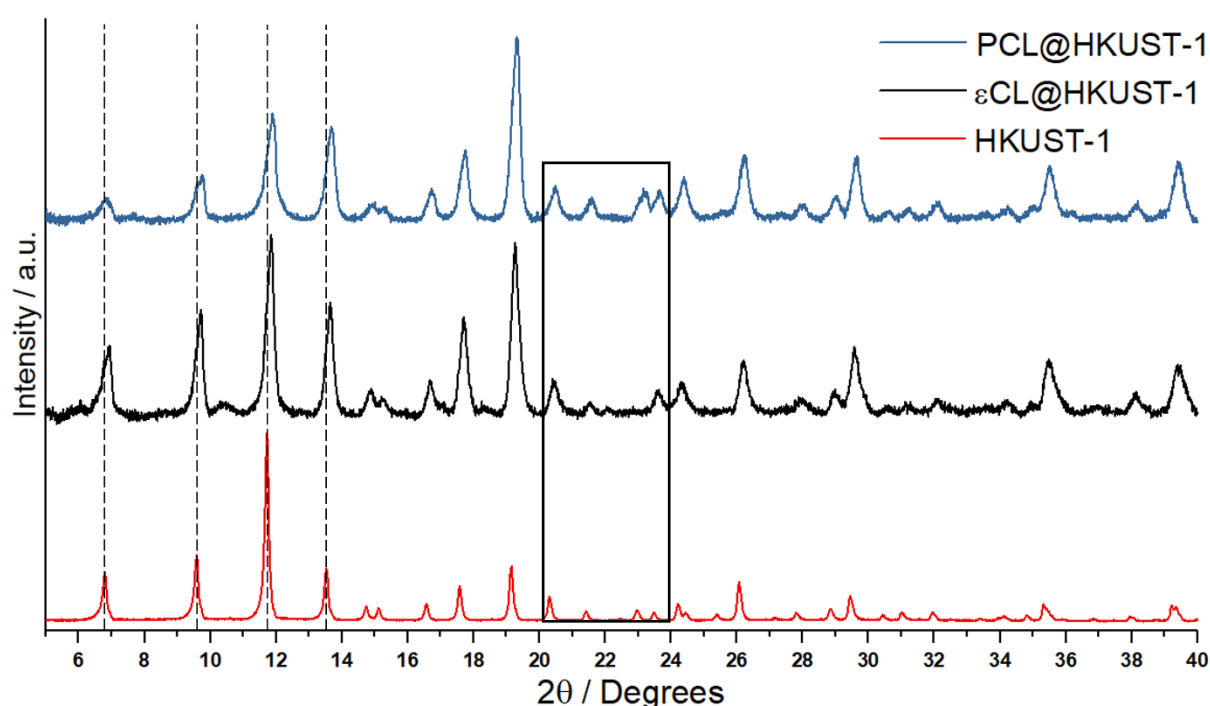


Fig 4.10: PXRD patterns for HKUST-1 (top),  $\epsilon$ CL@HKUST-1 (middle), PCL@HKUST-1 (bottom). ( $2\theta = 5\text{--}20^\circ$  range expansion in Appendix A4.6. The diffraction patterns shown are background subtracted. PCL characteristic peak region is shown by black box,  $2\theta = 21.6^\circ$  and  $23.9^\circ$ )

The PXRD patterns observed for HKUST-1,  $\epsilon$ CL@HKUST-1 and PCL@HKUST-1 were consistent and confirmed that the microstructure of the MOF was retained without structural deformation following polymerisation. The relative changes in  $2\theta$  position observed with in-situ polymerisation of  $\epsilon$ CL in HKUST-1 is likely due to introduction of guest molecules within the pores of the MOF. Changes in corresponding diffraction pattern at each stage are

## Chapter 4: Characterisation and Analysis

shown in Fig 4.10. The observations are consistent with those observed from PVAc@HKUST-1 where there is a decrease in the corresponding  $d$ -spacing and peak broadening due to loss of crystallinity following guest adsorption and polymerisation when compared to the desolvated HKUST-1.

Diffraction peaks characteristic of PCL ( $2\theta = 21.6^\circ$  and  $23.9^\circ$ ) are also observed in both PCL@HKUST-1 composite and isolated polymer from the MOF. The intense diffraction peaks of isolated polymer confirm crystalline nature (Fig 4.11).

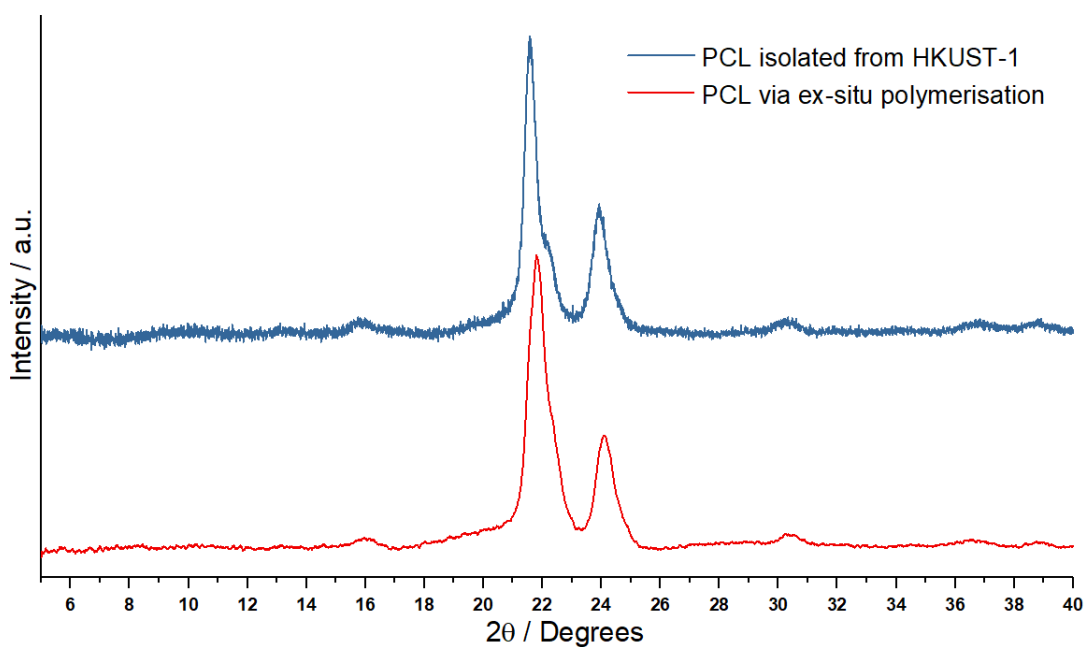


Fig 4.11: PXRD pattern of PCL isolated from PCL@HKUST-1 (top), and PCL polymerised ex-situ (bottom).

## Chapter 4: Characterisation and Analysis

### 4.2.2.3 In-situ polymerisation: D,L-lactic acid and D,L-lactide in HKUST-1

Condensation polymerisation of lactic acid (LA) and ring-opening polymerisation of lactide (LAC) monomer within HKUST-1 pores was carried out as described in sections 3.3.3 and 3.3.4, respectively. This is also evident visually with a paste-like composite, as opposed to free-flowing crystalline material that is obtained upon polymerisation of VAc and  $\epsilon$ CL. To mediate this problem, ROP of lactide was carried out. This resulted in less aggregation of crystal, although a free-flowing solid material was not achieved. We suspect that the in-situ polymerisation of LA was unsuccessful with majority of polymerisation occurring outside MOF pores. Water molecules are generated during polycondensation reaction of lactic acid during the chain propagation step, where the carboxyl and hydroxyl groups of two or more monomers link together to form an oligomer. As a result, we hypothesize that water molecules saturate the pores by preferentially binding to the metal node, forcing monomer molecules out of the microporous MOF. This results in a highly viscous post-polymerisation product usually with low molecular weight.

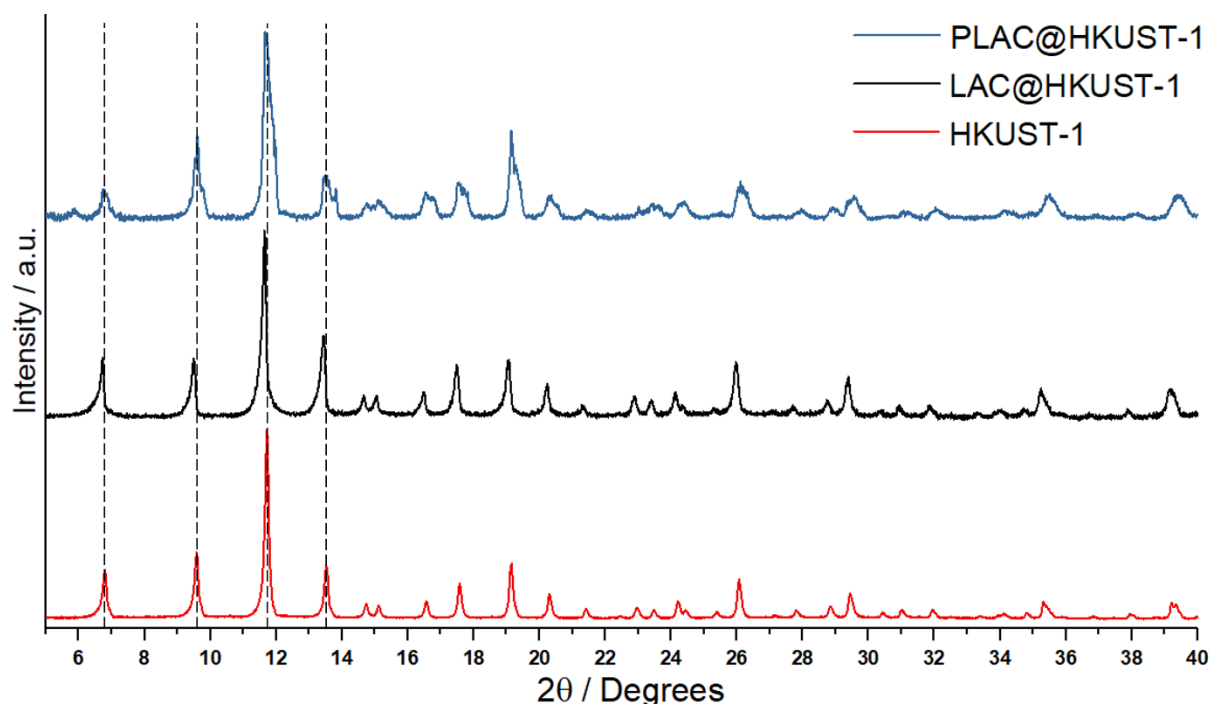


Fig 4.12 PXR D patterns for HKUST-1 (bottom), LAC@HKUST-1 (middle), PLAC@HKUST-1 (top). ( $2\theta = 5\text{--}14^\circ$  range expansion in Appendix A4.7. The diffraction patterns shown are background subtracted)

## **Chapter 4: Characterisation and Analysis**

---

PXRD studies of PLA@HKUST-1 show diffraction peaks from the MOF, albeit with poor signal-to-noise ratio. For polymer@MOF composites synthesised by polymerisation of LAC, PLAC@HKUST-1 showed improvement in signal-to-noise ratio with HKUST-1 retaining its crystal structure following polymerisation step (Fig 4.12). Due to the nature of the particles, suspected ex-situ polymerisation, and difficulties with polymerisation, the decision was made not to perform further synthesis and analysis on improving in-situ polymerisation methods for PLA@HKUST-1 and PLAC@HKUST-1.

## Chapter 4: Characterisation and Analysis

### 4.3 IR Spectroscopy (ATR-FTIR)

ATR-FTIR spectroscopy was used to determine the presence of monomers following addition to the empty MOF samples and any changes in peak positions and/or intensities arising following polymerisation. Where possible, reference spectra for isolated polymer are also shown, unfortunately these were not available for all the samples. It should be noted that FTIR alone is unable to provide conclusive evidence for incorporation of (intrinsic) monomer. However, other experimental data (SEM, BET – gas adsorption measurements, TGA, NMR, neutron scattering) suggest this is the case.

#### 4.3.1 MOF-5 – FTIR Spectroscopy

The FTIR spectra of as-synthesised MOF-5 and H<sub>2</sub>BDC linker and corresponding bond structure of the reported MOF-5 is shown in Fig 4.13. The FTIR spectrum of the as-synthesised MOF-5 is in good agreement with the literature reported spectrum.<sup>15,16</sup>

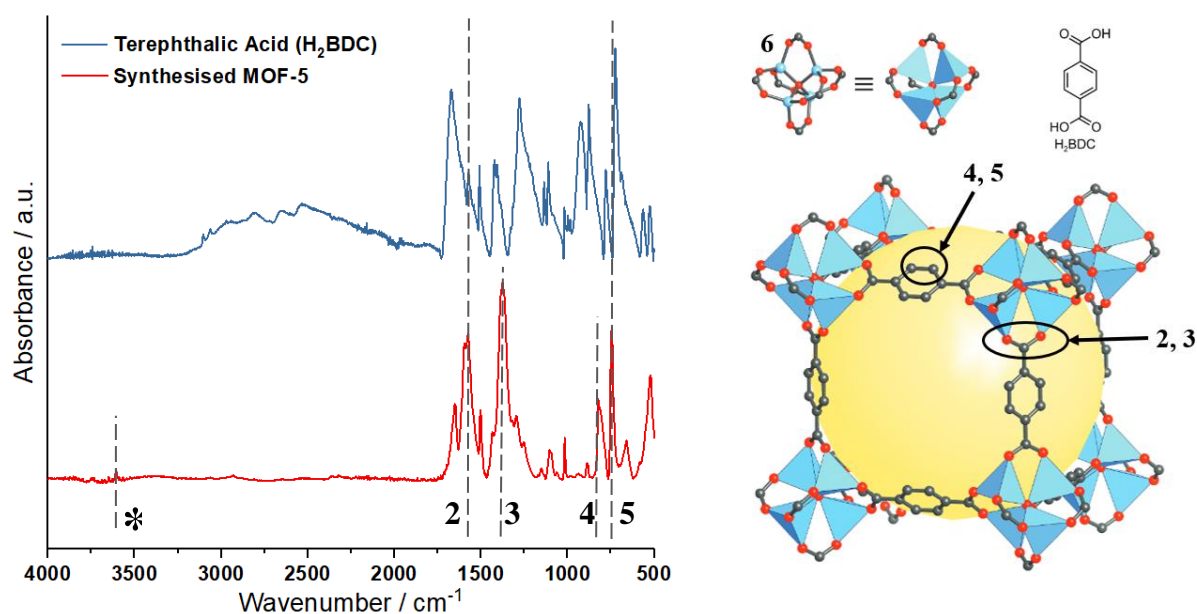


Fig 4.13 (a) ATR-FTIR spectrum of MOF-5 and H<sub>2</sub>BDC and (b) chemical bond structure of MOF-5 and contribution to the FTIR spectrum (*Schematic adapted and modified*).<sup>17</sup> (\* - 3650 cm<sup>-1</sup> from atmospheric water adsorption)

## Chapter 4: Characterisation and Analysis

---

The primary bond connectivity in the MOF structure is associated with FTIR band observed from two vibration bands located at  $1573\text{ cm}^{-1}$  and  $1370\text{ cm}^{-1}$ , with strong absorbance intensity due to carboxylic (COO) asymmetric and symmetric stretching vibrations, respectively.<sup>18</sup> The vibration bands at  $700\text{--}1200\text{ cm}^{-1}$  can be considered as the fingerprint of terephthalate compounds. Two sharp peaks observed at  $810\text{ cm}^{-1}$  and  $1014\text{ cm}^{-1}$  are a contribution from out of plane and in-plane bending of C-H in the phenyl ring of terephthalic acid.<sup>19</sup> Furthermore, the absorption peak at  $935\text{ cm}^{-1}$  is relevant to the SBU of MOF-5 representing Zn-O stretching vibration of  $\text{Zn}_4\text{O}$  tetrahedron. The peak at  $3650\text{ cm}^{-1}$  is likely contribution from any residual co-ordinated water or adsorbed atmospheric moisture present due to the hygroscopic nature of MOF-5. Further spectral assignments are given in Table A4.24 of the appendix.

## Chapter 4: Characterisation and Analysis

### 4.3.1.1 Vinyl acetate polymerisation in MOF-5 - FTIR Spectroscopy

ATR-IR spectra of MOF-5, VAc@MOF-5, and PVAc@MOF-5 were recorded and analysed (Fig 4.14). The presence of VAc and/or PVAc in guest@MOF composites can be confirmed by observation of their characteristic absorbance peaks.

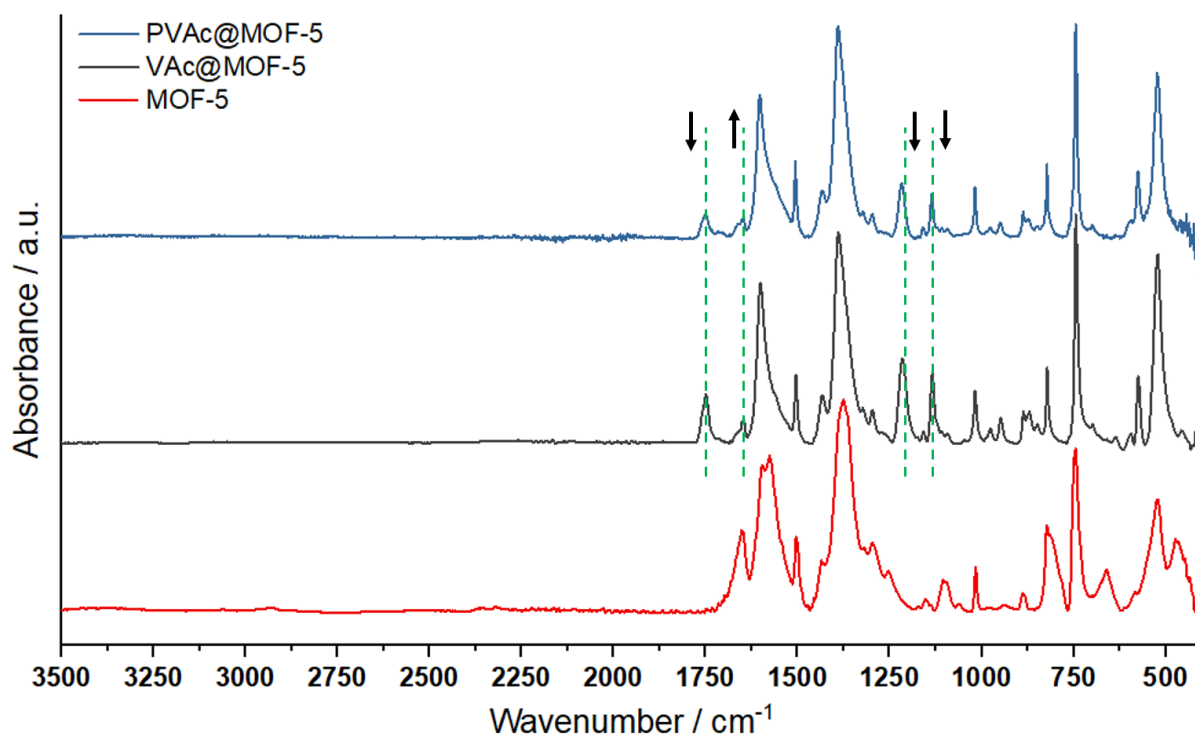


Fig 4.14: ATR-FTIR spectra of MOF-5 (bottom), VAc@MOF-5 (middle) and PVAc@MOF-5 (top). Dashed green lines and corresponding arrows indicate changes in absorbance intensity with polymerisation. (Region between 2000–450  $\text{cm}^{-1}$  has been shown in Fig A4.8. The spectra have been normalised to  $\nu(\text{C}=\text{O})$  1350  $\text{cm}^{-1}$  absorbance peak of the MOF. This has been done to evaluate increase or decrease in characteristic guest peaks.)

Specific absorbance bands for the PVAc molecule are absorb wavelength of light around: 1430, 1370, 1210 and 1140  $\text{cm}^{-1}$ .<sup>66</sup> The 1210 and 1140  $\text{cm}^{-1}$  are used to quantify and identify the presence of PVAc. The absorbance peak intensities at 1766, 1684, 1212 and 1140  $\text{cm}^{-1}$  decreased during polymerisation, while those at 1729 and 1233  $\text{cm}^{-1}$  increased. This decrease in peak intensity at 1684  $\text{cm}^{-1}$  from C=C stretching vibrations and 1140  $\text{cm}^{-1}$  from O-C-C asymmetric stretching is an indicates conversion of vinyl acetate to poly(vinyl acetate).<sup>20</sup> The  $\nu(\text{C}=\text{O})$  vibration shifts from 1766 to 1729  $\text{cm}^{-1}$ , and the C-C-O asymmetric stretching

## Chapter 4: Characterisation and Analysis

vibration shifts from 1212 to 1233  $\text{cm}^{-1}$  indicating the transfer of ester groups of the monomer to polymer chains.<sup>21</sup>

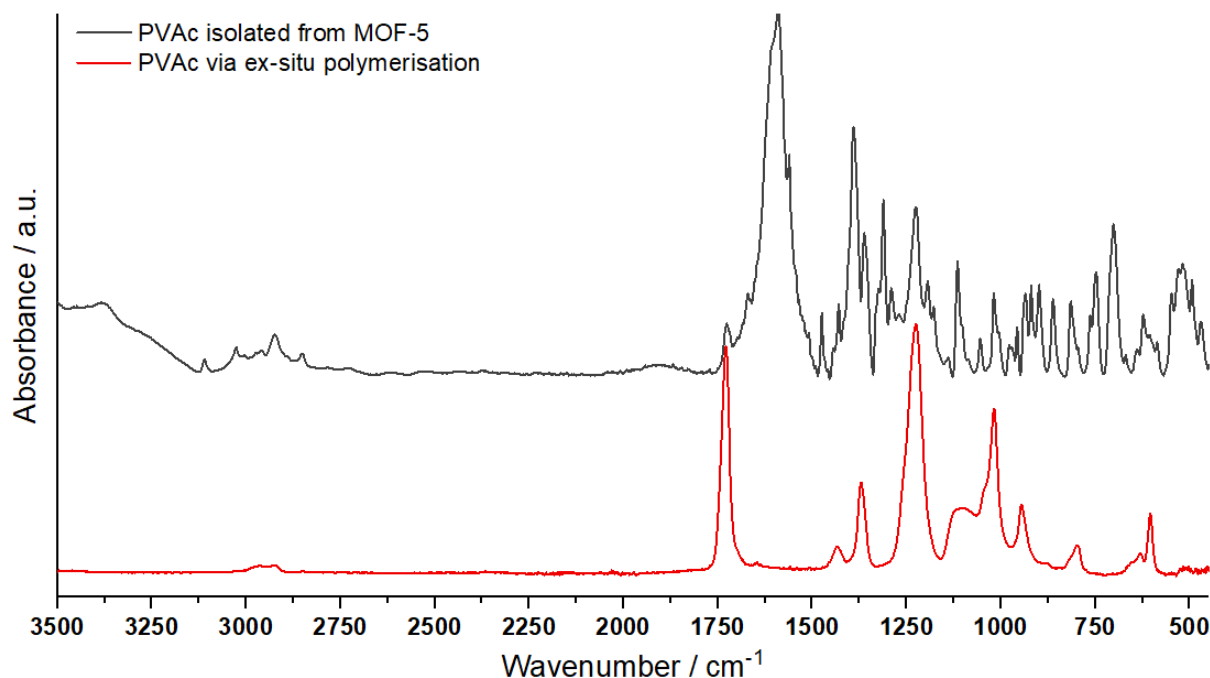


Fig 4.15: ATR-FTIR spectra of PVAc isolated from MOF-5 (top) and PVAc synthesised by ex-situ polymerisation (bottom). (The spectra have been normalised to the  $\nu(\text{C}=\text{O})$  of the MOF at 1350  $\text{cm}^{-1}$ )

In Fig 4.15, PVAc isolated from MOF-5 shows the characteristic bands are present following isolation and drying. Characteristic PVAc IR absorbance band assignments are shown in Table A4.25 in the appendix (The broad peak between 1500-1700  $\text{cm}^{-1}$  is residual fragments of degraded MOF components that remain present in the sample).

## Chapter 4: Characterisation and Analysis

### 4.3.1.2 $\epsilon$ -Caprolactone polymerisation in MOF-5 - FTIR Spectroscopy

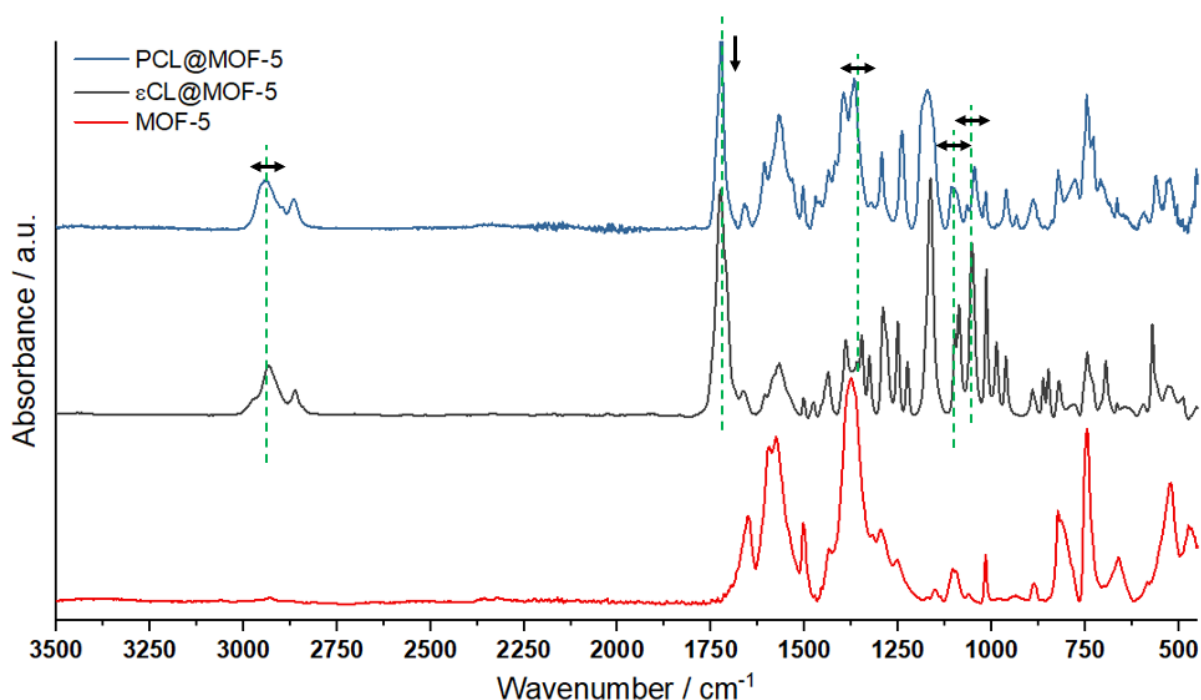


Fig 4.16: ATR-FTIR spectra of MOF-5,  $\epsilon$ CL@MOF-5 and PCL@MOF-5. Dashed green lines and corresponding arrows indicate changes in absorbance intensity with polymerisation. (Region between 2000–450  $\text{cm}^{-1}$  has been shown in Fig A4.9. The spectra have been normalised to  $\nu(\text{C}=\text{O})$  of the MOF at 1350  $\text{cm}^{-1}$ )

ATR-IR spectra were recorded and measured for  $\epsilon$ CL@MOF-5 and PCL@MOF-5 samples at room temperature to confirm polymerisation of  $\epsilon$ CL. There are visible peak broadening effects that are evident between  $\epsilon$ CL@MOF-5 and PCL@MOF-5 samples suggesting successful polymerisation of  $\epsilon$ CL. Polymer isolated from MOF-5 also shows bands that are characteristic to PCL (Fig 4.16).

The characteristic vibrations of linear ester carbonyl groups ( $\text{C}=\text{O}$ ) and ( $\text{C}-\text{O}$ ) bonds in the polymer were observed at 1729  $\text{cm}^{-1}$  and 1193  $\text{cm}^{-1}$ . The spectrum of the polymer shows two sharp peaks at 1015  $\text{cm}^{-1}$  and 988  $\text{cm}^{-1}$  that do not appear in the monomer spectrum.

Additionally, the PCL@MOF-5 spectrum shows two additional smaller peaks at 1415 and 931  $\text{cm}^{-1}$  that are not present in the monomer spectrum.

## Chapter 4: Characterisation and Analysis

There is a doublet present between 2800 and 3000  $\text{cm}^{-1}$  due to the  $\nu(\text{C-H})$  stretching of the methylene groups that shows broadening upon polymerisation. Noticeably, the bands between 700-1500  $\text{cm}^{-1}$  are a contribution from the polymer chain's backbone from bending, wagging and stretching from the methylene with gauche and trans isomeric configurations of the ester group. Bands present due to  $\nu(>\text{CH}_2)$  asymmetric and symmetric stretching are observed on all  $\epsilon\text{CL}@$ MOF-5, PCL@MOF-5, and the isolated PCL. The evident broadening of the peak at 1193, 1395, 1050, and 750  $\text{cm}^{-1}$  is further evidence of successful polymerisation.<sup>22</sup>

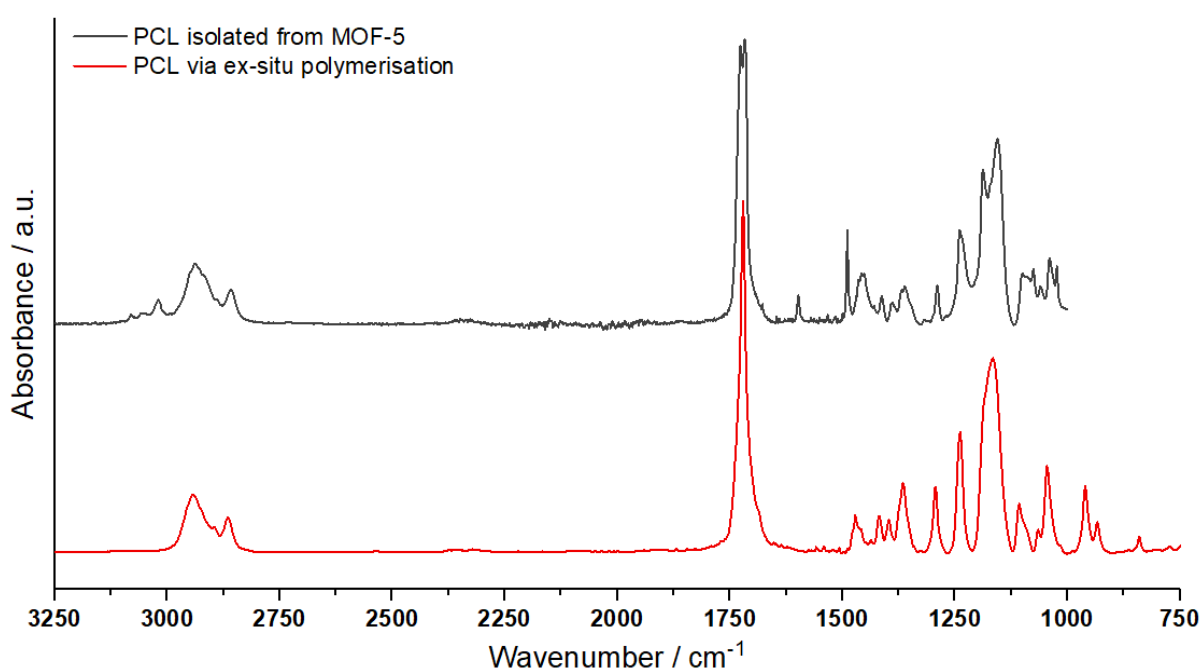


Fig 4.17: ATR-FTIR spectra of PCL isolated from MOF-5 and PCL synthesised by ex-situ polymerisation.

It is possible to demonstrate the crystalline nature of the isolated polymer extracted from the MOF through FTIR. Upon crystallisation, the asymmetric  $\nu(\text{C-H})$  band sharpens, and a minor band develops a shoulder at 2960  $\text{cm}^{-1}$  that are assigned to the symmetric and asymmetric stretching of PCL polymer (Fig 4.17). This observation is consistent with IR studies reported in the literature for PCL.<sup>23</sup> A narrow band develops around 1724  $\text{cm}^{-1}$  that is attributed to amorphous and crystalline regions of PCL since the changes are reversible and can be used to measure the crystallinity of PCL by resolving the overlapping carbonyl

## Chapter 4: Characterisation and Analysis

bands.<sup>24</sup> This further supports our observation of the crystalline nature of the isolated polymer from PXRD patterns (Fig 4.7). Characteristic PCL IR assignments are shown in Table A4.26 in the appendix.

### 4.3.2 HKUST-1 – FTIR Spectroscopy

The FTIR spectroscopy was used to identify the main functional groups of HKUST-1. The FTIR spectrum of H<sub>3</sub>BTC ligand is shown in Fig 4.18 (a). The FTIR spectrum of the synthesised HKUST-1 is in good agreement with literature reported spectrum.<sup>25,26</sup> The corresponding bond structure of the reported HKUST-1 is shown in Fig 4.18 (b).

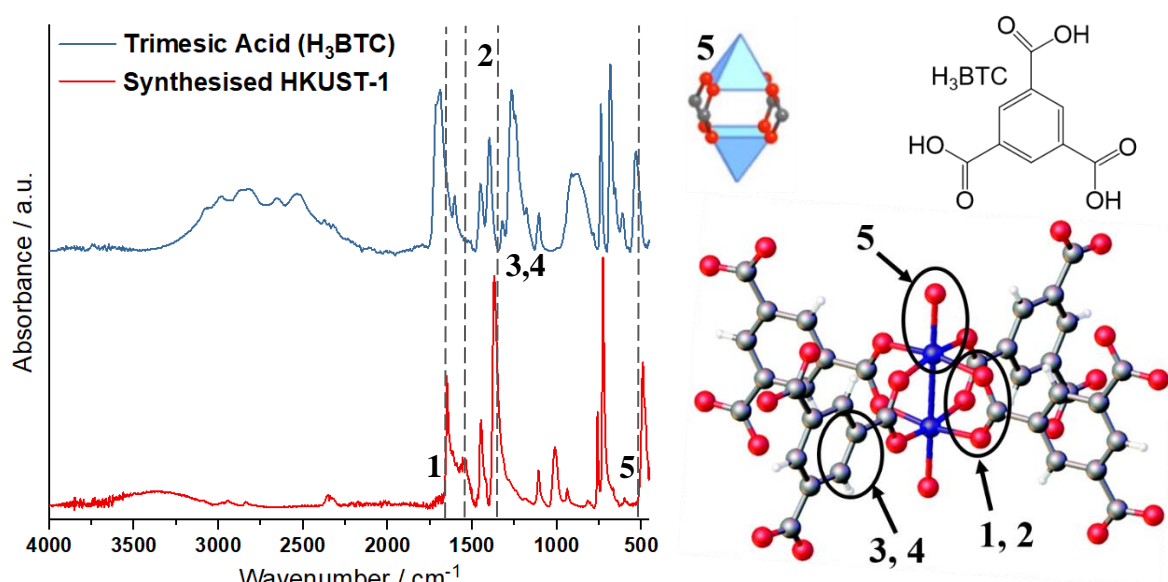


Fig 4.18 (a) ATR-FTIR spectrum of HKUST-1 and H<sub>3</sub>BTC and (b) chemical bond structure of MOF-5 and contribution to the FTIR spectrum.<sup>27</sup>

The wide band observed in the HKUST-1 spectrum around 3550-3200 cm<sup>-1</sup> is attributed to  $\nu(\text{OH})$  stretching modes because of atmospheric moisture adsorption. Unresolved signals of lesser intensity in 1640-1520 cm<sup>-1</sup> range and around 920 cm<sup>-1</sup> originate from the bending and libration modes of H<sub>2</sub>O respectively.<sup>27</sup> The vibration bands on the spectrum from 1300–1700 cm<sup>-1</sup> belong to the carboxylate linker, attributed to the coordination of BTC with the Cu sites; specifically, the symmetric and asymmetric stretching of COO<sup>-</sup> at 1659 cm<sup>-1</sup> and 1590 cm<sup>-1</sup>, and  $\delta(\text{C}=\text{O})$  bending modes. The peaks at 1375 cm<sup>-1</sup> and 1252 cm<sup>-1</sup> correspond to the

## Chapter 4: Characterisation and Analysis

symmetric stretching modes of the carboxylate groups  $\nu(\text{C}=\text{C})$  and  $\nu(\text{C}=\text{O})$  of the BTC linker. Furthermore, in-plane and out-of-plane bending modes from  $\delta(\text{C}-\text{H})$  appear at  $1107\text{ cm}^{-1}$  and  $935\text{ cm}^{-1}$ . Vibration mode from  $\text{Cu}-\text{O}$  bonds on the metal node of HKUST-1 appears in the low wavelength region at  $494\text{ cm}^{-1}$ . Further spectral assignments are given in Table A4.27 of the appendix.

### 4.3.2.1 Vinyl acetate polymerisation in HKUST-1 - FTIR Spectroscopy

Polymerisation of vinyl acetate in HKUST-1 shows similar trends as those observed with MOF-5 with intensities at  $1766$ ,  $1684$ ,  $1212$  and  $1140\text{ cm}^{-1}$  decreased during for the PVAc@HKUST-1 sample, while those at  $1729$  and  $1233\text{ cm}^{-1}$  were observed to increase relative to the VAc@HKUST-1 sample (Fig 4.19).

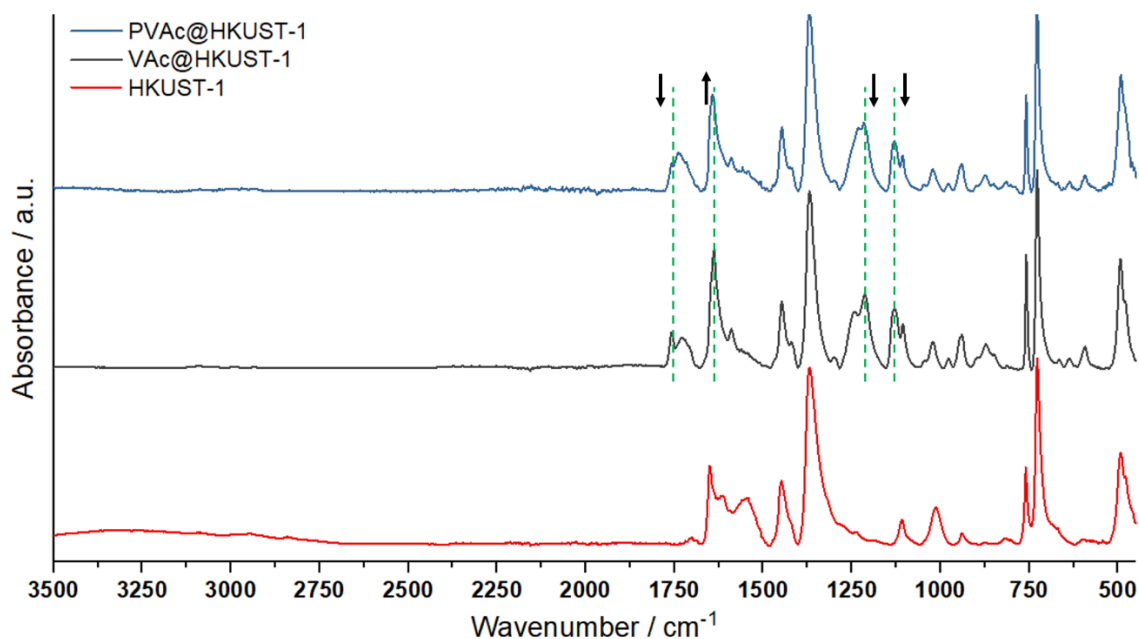


Fig 4.19: ATR-FTIR spectra of HKUST-1 (bottom), VAc@HKUST-1 (middle) and PVAc@HKUST-1 (top). Dashed green lines and corresponding arrows indicate changes in absorbance intensity with polymerisation. (Region between  $2000\text{--}450\text{ cm}^{-1}$  has been shown in Fig A4.10. The spectra have been normalised to  $\nu(\text{C}=\text{O})$  of the MOF at  $1369\text{ cm}^{-1}$ .)

## Chapter 4: Characterisation and Analysis

The characteristic absorbance bands for the PVAc molecule are absorb wavelength of light around: 1430, 1370, 1210 and 1140  $\text{cm}^{-1}$ .<sup>29</sup> The 1210 and 1140  $\text{cm}^{-1}$  are used to quantify and identify the presence of PVAc. The decrease in peak height of absorbance band at 1684  $\text{cm}^{-1}$  from C=C stretching vibrations and 1140  $\text{cm}^{-1}$  from O-C-C asymmetric stretching is indicative of vinyl acetate conversion to poly(vinyl acetate).<sup>20</sup> There is also a noticeable shift of C=O vibration peaks from 1766 to 1729  $\text{cm}^{-1}$ , and the C-C-O asymmetric stretching vibration shifts from 1212 to 1233  $\text{cm}^{-1}$  indicating the transfer of ester groups of the monomer to polymer chains.<sup>21</sup>

### 4.3.2.2 $\epsilon$ -Caprolactone polymerisation in HKUST-1 - FTIR Spectroscopy

ATR-IR spectra were recorded and measured for  $\epsilon\text{CL@HKUST-1}$  and  $\text{PCL@HKUST-1}$  to confirm polymerisation of  $\epsilon\text{CL}$  (Fig 4.20).

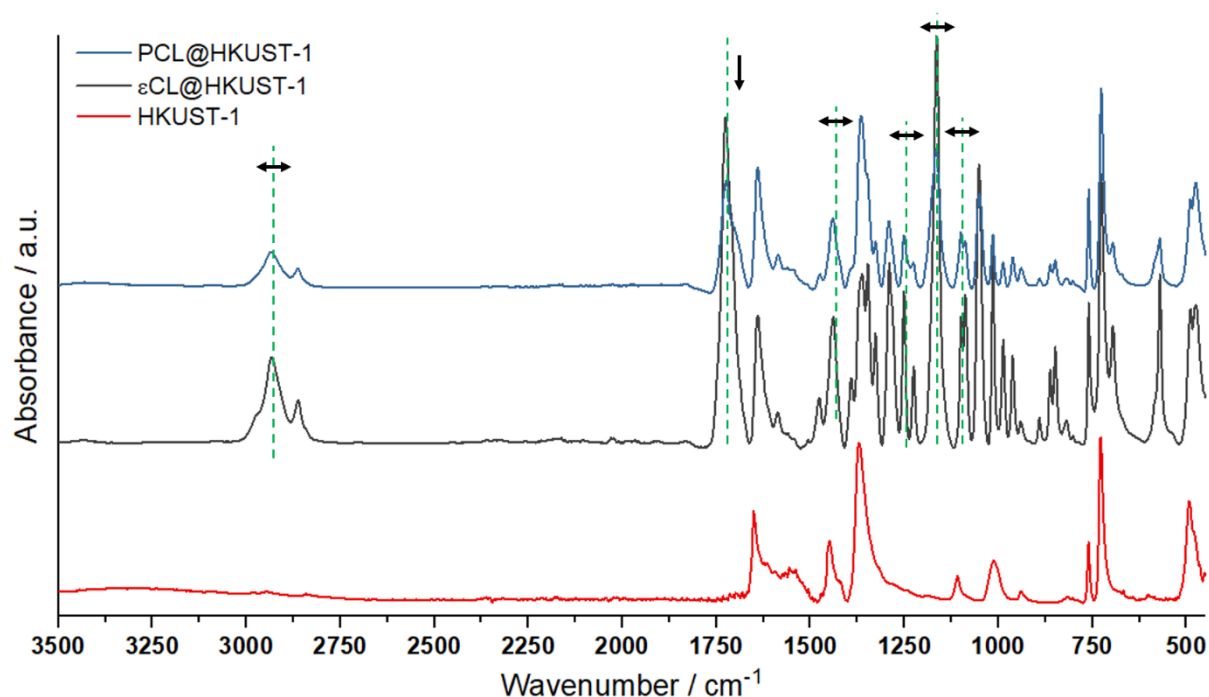


Fig 4.20: ATR-FTIR spectra of HKUST-1 (bottom),  $\epsilon\text{CL@HKUST-1}$  (middle) and  $\text{PCL@HKUST-1}$  (top). Dashed green lines and corresponding arrows indicate changes in absorbance intensity with polymerisation. (Region between 2000–450  $\text{cm}^{-1}$  has been shown in Fig A4.11. The spectra have been normalised to  $\nu(\text{C}=\text{O})$  1369  $\text{cm}^{-1}$  absorbance peak of the MOF.)

## Chapter 4: Characterisation and Analysis

PCL has characteristic absorbance peaks at 1730 and 1390  $\text{cm}^{-1}$  from  $\nu(\text{C}=\text{O})$  and  $\nu(\text{C}-\text{O})$ , respectively. Additionally, C–H bending and stretching bands are observed at 1415 and 1270  $\text{cm}^{-1}$ , respectively. The broad band around 2950  $\text{cm}^{-1}$  is a result of symmetric  $\text{CH}_2$  stretching. The vibrations from carbonyl groups ( $\text{C}=\text{O}$ ) and  $\text{C}-\text{O}$  of the polymer were observed at 1729  $\text{cm}^{-1}$  and 1193  $\text{cm}^{-1}$  in the PCL@MOF. PCL shows two sharp absorbance bands at 1015  $\text{cm}^{-1}$  and 988  $\text{cm}^{-1}$  that do not appear in the monomer spectrum. PCL@HKUST-1 spectrum shows two additional smaller peaks at 1415 and 931  $\text{cm}^{-1}$  that are not present in the  $\epsilon\text{CL@HKUST-1}$  sample from  $\delta(\text{C}-\text{H})$  and  $\delta(\text{C}-\text{O})$  bending. The  $\nu(>\text{CH}_2)$  asymmetric and symmetric stretching bands are observed on  $\epsilon\text{CL@HKUST-1}$ , PCL@HKUST-1, and the isolated PCL. The evident broadening of the peak at 1193, 1395, 1050, and 750  $\text{cm}^{-1}$  peaks is further evidence of successful polymerisation.<sup>22</sup>

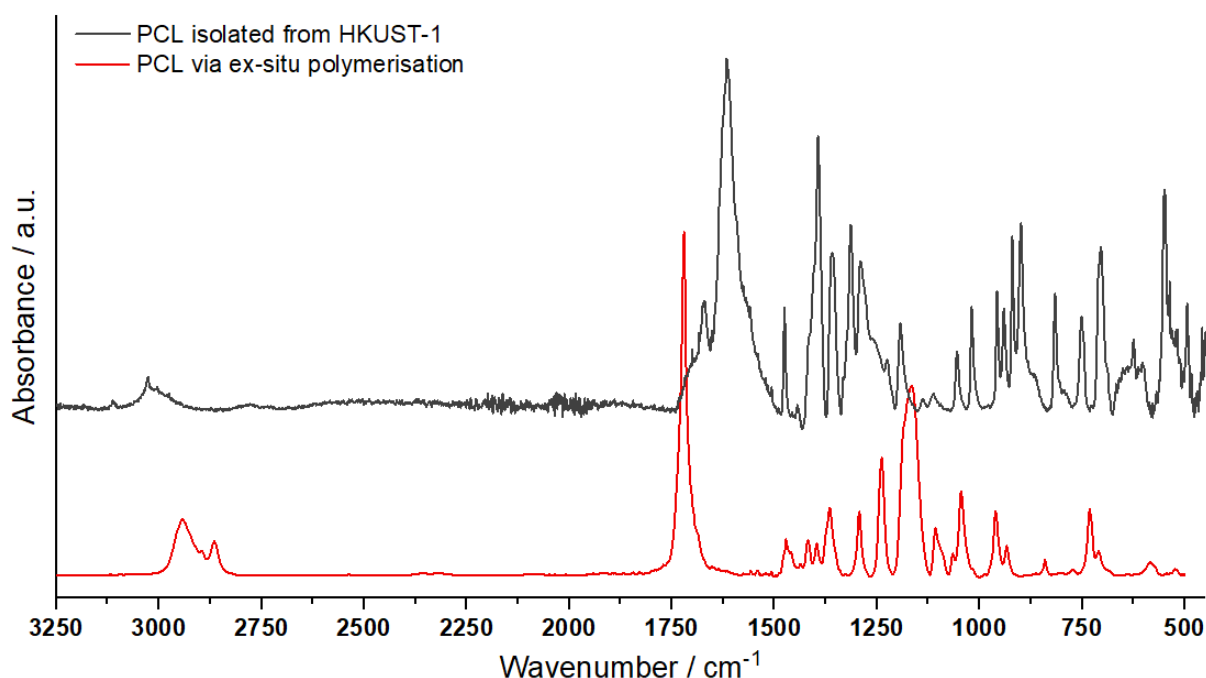


Fig 4.21: ATR-FTIR spectra of PCL isolated from HKUST-1 (top) and PCL synthesised ex-situ polymerisation (bottom).

The crystalline nature of the isolated polymer can be confirmed by sharpening of the asymmetric band at 2960  $\text{cm}^{-1}$ , and a shoulder developing on the same band (Fig 4.21). The PXRD of isolated polymer also confirms the crystalline nature of the isolated PCL from both MOFs (Section 4.2.2.2). (The broad peak between 1500-1700  $\text{cm}^{-1}$  is residual fragments of degraded MOF components that remain present in the sample).

## Chapter 4: Characterisation and Analysis

---

### 4.4 Thermogravimetric Analysis (TGA)

TGA is a valuable characterisation method to determine thermal stability of MOFs, pore volumes, and quantification of MOF's composition. TG and DTG analyses were used to determine the composition of the MOFs and to quantify the guest species present in guest@MOF composites. The number of solvent molecules calculated from synthesised MOF sample was used as a basis to calculate the monomer loading, polymer yield, and the degree of polymerisation in guest@MOF composites.

#### 4.4.1 MOF-5 – TG and DTG Analysis

The normalised TGA profile of dry and activated MOF-5 (heating rate of 5 °C/min under air flow of 50.0 mL/min) shows onset of structural decomposition around 425 °C with complete degradation and pyrolysis at 550 °C. Experimental temperature ranges for decomposition were consistent with TGA profiles for MOF-5 reported in literature.<sup>28</sup>

The TGA profile of MOF-5 shows three-step mass losses. The mass loss observed between 35 °C to 150 °C are a result of a mass loss from adsorbed atmospheric moisture due to the hygroscopic nature of MOF-5. The second step between 150 °C to 325 °C is likely due to coordinated water molecules and solvent DMF molecules within the framework. This is followed by a region of thermal stability for the MOF where there is negligible mass loss. The majority of mass losses occurs in the range of 425 °C to 550 °C as result of thermal decomposition.<sup>29,30</sup> In MOF-5, the carboxylates of the linker bridging the Zn<sub>4</sub>O tetrahedra are the weakest link in its structural framework.<sup>33–36</sup> Theoretically, the formula unit for MOF-5, Zn<sub>4</sub>O[C<sub>8</sub>H<sub>4</sub>O<sub>4</sub>]<sub>3</sub> consists of 2 equivalent CO<sub>2</sub> in a plane and six CO<sub>2</sub> molecules in the perpendicular plane. The evolution of one of the two CO<sub>2</sub> on the BDC accounts for initial loss of the total mass lost. The sample mass loss for temperatures greater than 400 °C is in good agreement with the initial loss of all equivalent CO<sub>2</sub> molecules and 1 equivalent of benzene ring molecules, and consequently further decomposition of the benzene ring.

## Chapter 4: Characterisation and Analysis

---

The mass losses between 150-325 °C were assigned to DMF and accounted for during calculations. The measured percentage mass of ZnO decomposition residue is approximately 38 wt%, in line with reported values of 42 wt%.<sup>28</sup> The additional mass present in the samples is likely due to unreacted starting reactants. The observed TGA profile was consistent with all the measured samples throughout this project.

### 4.4.1.1 Vinyl acetate polymerisation in MOF-5 – TGA

The TGA profiles of as-synthesised MOF, MOF with adsorbed guest monomer, and MOF-5 with polymer guest are shown in Fig 4.22. Like MOF-5, the profile can be divided into three distinct regions. Losses of mass in regions I and II are dominated by removal of guest molecules, whereas the loss in region III are a result of thermal degradation of MOF's framework.

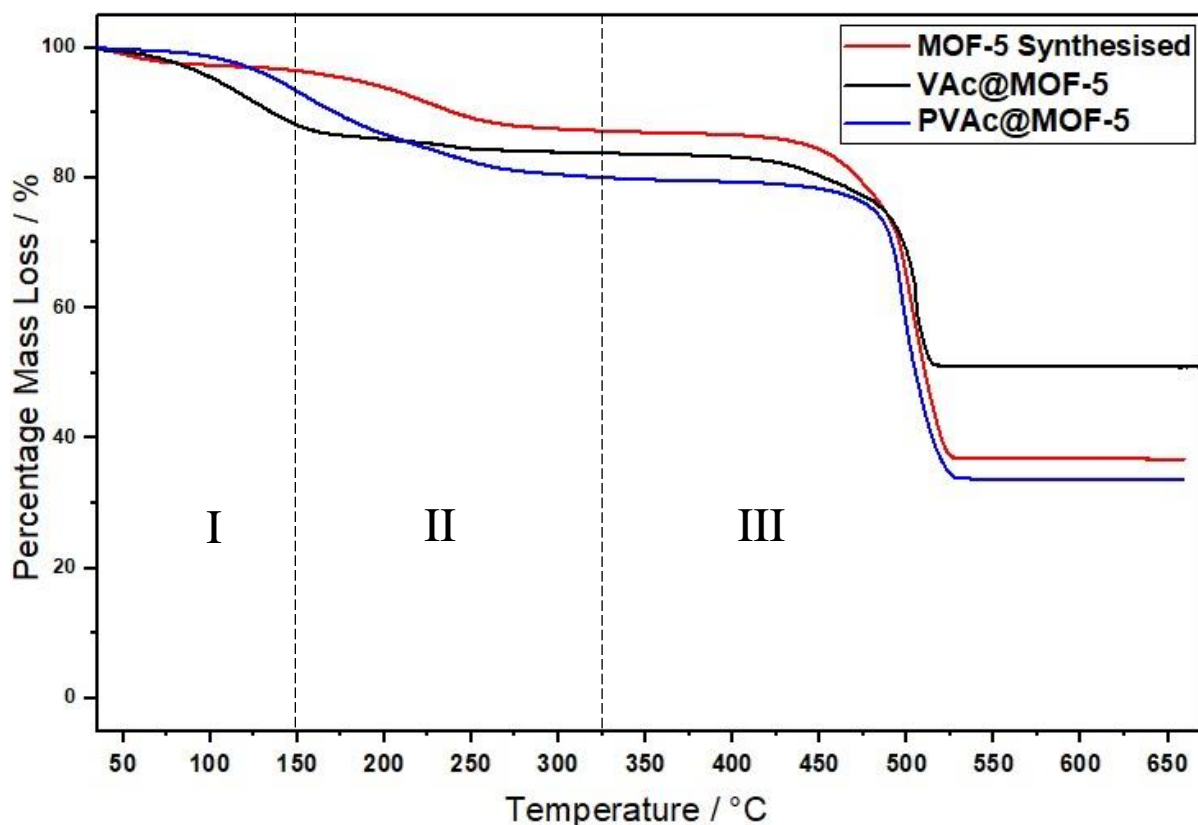


Fig 4.22: TGA profiles for empty MOF-5, VAc@ MOF-5, and PVAc@MOF-5. Regions I, II, and III correspond to the regions for vaporisation of moisture and surface species; removal of intrinsic and bound guest; and thermal decomposition of MOF-5, respectively. All samples were run under air.

Region I range from room temperature to 150 °C. For the guest-MOF composite, losses in this range account for 14 wt% and 10 wt% mass loss for monomer@MOF and polymer@MOF composites, respectively. The loss within this region may be a result of adsorbed moisture, surface solvent DMF molecules and extrinsic monomer that may be present on the crystal framework.

Region II account for the mass loss that comes from intrinsic, bound, or coordinated guest molecules within the MOF-5 structure. This accounts for 6 wt% for VAc@MOF-5 and 12 wt% for PVAc@MOF-5. The difference in this region with a noticeable two step loss can be

## Chapter 4: Characterisation and Analysis

---

a contribution from two phenomena. First is the removal of coordinated solvent DMF molecules present in the system. This is followed by evaporation on degradation of intrinsic free uncoordinated monomer in VAc@MOF-5 and, unreacted monomer in the case of PVAc@MOF-5.

Region III constitutes the losses due to the collapse of the framework. For VAc@MOF-5, the larger measured value is likely due to human error during monomer addition. The other likely reasons can be moisture adsorption before addition of the monomer, residual solvent, or unreacted linker that may have been present in the sample. The PVAc@MOF-5 samples show a higher measured percentage for polymer which may be from unreacted monomer that may be present in the system or additional intrinsic polymer that may be present and has not vapourised in region II.

During this project, attempts to characterise MOF-5 and guest@MOF-5 by TGA-IR were made, however, the resulting IR data were inconsistent due to instrumental problems that it was not possible to resolve under COVID-19 restrictions. These data would be useful addition to any future studies.

## Chapter 4: Characterisation and Analysis

### 4.4.1.2 $\epsilon$ -Caprolactone Polymerisation in MOF-5 – TGA

The TGA profiles of MOF,  $\epsilon$ CL@MOF-5, and PCL@MOF-5 are shown in Fig 4.23.

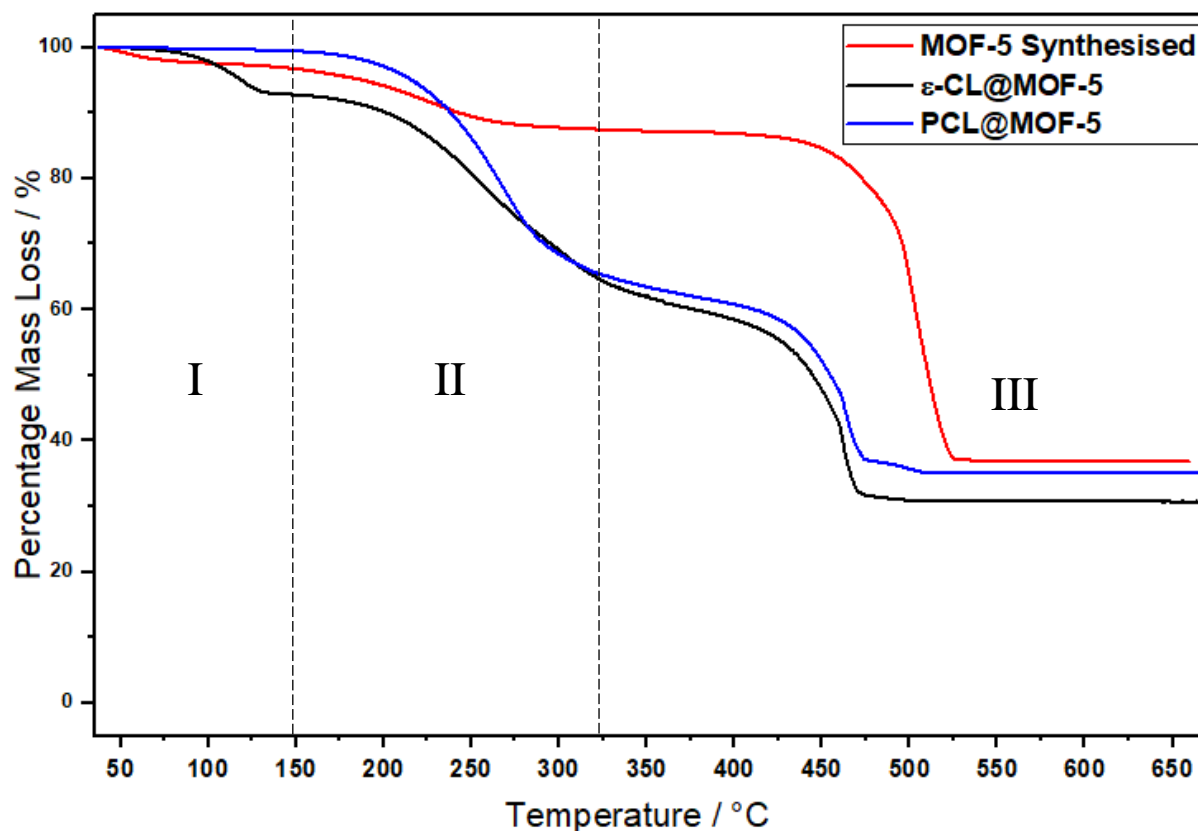


Fig 4.23: TGA profiles for empty MOF-5,  $\epsilon$ CL@MOF-5, and PCL@MOF-5. Regions I, II, and III correspond to the regions for vaporisation of moisture and surface species; removal of intrinsic and bound guest; and thermal decomposition of HKUST-1, respectively. All samples were run under air.

Similar to VAc polymerisation, the TGA profile can be divided into three distinct regions. Losses of mass in regions I and II are dominated by removal of guest molecules, whereas the losses in region III are a result of thermal degradation of MOF's framework. However, due to the higher boiling point of  $\epsilon$ -caprolactone, the mass losses from the monomer are absent for region I. For  $\epsilon$ CL, this range is reduced to 130 °C, beyond which losses occur from solvent DMF vaporisation possibly due to  $\epsilon$ CL molecules driving the physically adsorbed solvent DMF molecules out of the framework. For  $\epsilon$ CL@MOF-5, there is removal of atmospheric water corresponding to a change of mass of 10 wt% compared to  $\leq 1$  wt% with the PCL@MOF-5 sample. This supports our conclusion that the polymer chains reinforce the

## Chapter 4: Characterisation and Analysis

---

MOF structure, thereby resulting in restriction of space in the voids (discussed later in Chapter 5). Consequently, additional guest molecules are driven out of the composite during polymerisation. It is difficult to differentiate the onset of region III due to an overlap between regions for thermal breakdown of the polymer and the region of thermal stability of the MOF and subsequent breakdown of structure.

Losses in region I in  $\epsilon$ -CL@MOF-5 are due to evaporation of adsorbed moisture. The initial weight loss in region II is residual solvent molecules vaporising till 200 °C. After this, there is a step weight loss from 200 °C to 325 °C for  $\epsilon$ -CL@MOF-5 sample that is a contribution from monomer evaporation and decomposition. There is a steady loss between 325 °C to 425 °C, after which there is a loss from framework decomposition at higher temperatures in region III from 425 °C to 525 °C.

For PCL@MOF-5 samples, there is consistent weight loss after initial losses from DMF removal to 200 °C. The step loss for PCL@MOF-5 continues from 200 °C to 425 °C after which thermal breakdown of framework is initiated at temperatures above 425 °C. We suspect that there is still some polymer present in the framework beyond 425 °C which would explain the two-step loss on the derivative curve and the overestimation of metal oxide present as the residue.

## Chapter 4: Characterisation and Analysis

---

### 4.4.2 HKUST-1 – TG and DTG Analysis

TGA profile of HKUST-1 (heating rate of 5 °C/min under air flow of 50.0 mL/min) matched the profile reported in literature for HKUST-1 crystals.<sup>15,35,36</sup>

Losses between room temperature to 110 °C are due to evaporation of physically adsorbed water in region I, shown in Fig 4.25. In region II, there is a region of continuous mass loss between 110 and 250 °C followed by region of thermal stability of the MOF to 315 °C. These regions dictate the release of coordinated water molecules that are chemically bound on the Cu-OCO position on the copper paddlewheel, and the physically adsorbed solvent molecules within the HKUST-1 pores are lost.<sup>37</sup> The overall mass loss of 20 wt% corresponds to three or more water molecules per  $\text{Cu}_3(\text{BTC})_2$  formula unit of HKUST-1, which is consistent with widely reported values for HKUST-1 as  $[\text{Cu}_3(\text{BTC})_2(\text{H}_2\text{O})_3]_n$ .<sup>15,38–40</sup>

Losses at higher temperatures (> 300 °C) are due to the thermal decomposition of the desolvated framework accounting for 46 wt% of the total mass loss.

## Chapter 4: Characterisation and Analysis

### 4.4.2.1 Vinyl acetate polymerisation in HKUST-1 – TGA

To evaluate composition and quantify guest adsorbed by the MOF, TGA was carried out on guest@MOF composites and compared with the empty MOF. The TGA profiles of as synthesised HKUST-1, VAc@HKUST-1, and PVAc@HKUST-1 are shown in Fig 4.24.

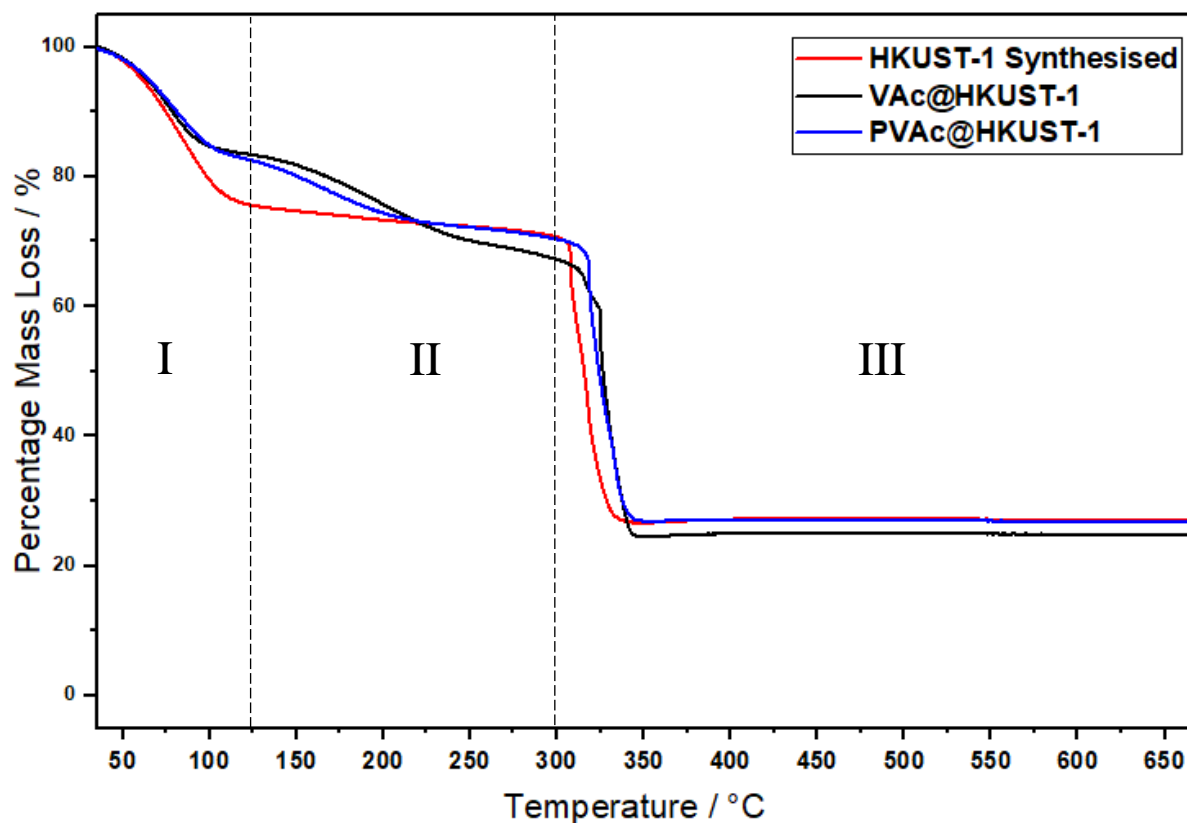


Fig 4.24: TGA profiles for empty HKUST-1, VAc@HKUST-1, and PVAc@HKUST-1. Regions I, II, and III correspond to the regions for vaporisation of moisture and surface species; removal of intrinsic and bound guest; and thermal decomposition of HKUST-1, respectively. All samples were run under air.

Like HKUST-1, the TGA profiles can be divided into three distinct regions. Losses of mass in regions I and II are dominated by removal of physically and chemically bound guest molecules whereas the loss in region III are a result of thermal degradation of the MOF frameworks. Table 4.3 shows the percentage mass loss observed in the case of VAc@HKUST-1 and PVAc@HKUST-1.

## Chapter 4: Characterisation and Analysis

---

Table 4.3: Percentage mass loss observed in regions I, II and III from TGA profiles for empty HKUST-1, VAc@HKUST-1, and PVAc@HKUST-1. (Error  $\pm 2$  %)

	<b>HKUST-1</b>	<b>VAc@HKUST-1</b>	<b>PVAc@HKUST-1</b>
<b>Region I</b>	25 %	15 %	15 %
<b>Region II</b>	3 %	18 %	15 %
<b>Region III</b>	47 %	43 %	47 %

## Chapter 4: Characterisation and Analysis

### 4.4.2.2 $\epsilon$ -Caprolactone Polymerisation in HKUST-1 – TGA

The TGA profiles of as synthesised HKUST-1,  $\epsilon$ CL@HKUST-1, and PCL@HKUST-1 with polymer guest for  $\epsilon$ -caprolactone is shown in Fig 4.25. The TGA profiles show similar trends seen in the VAc@MOF composite with three-region mass loss.

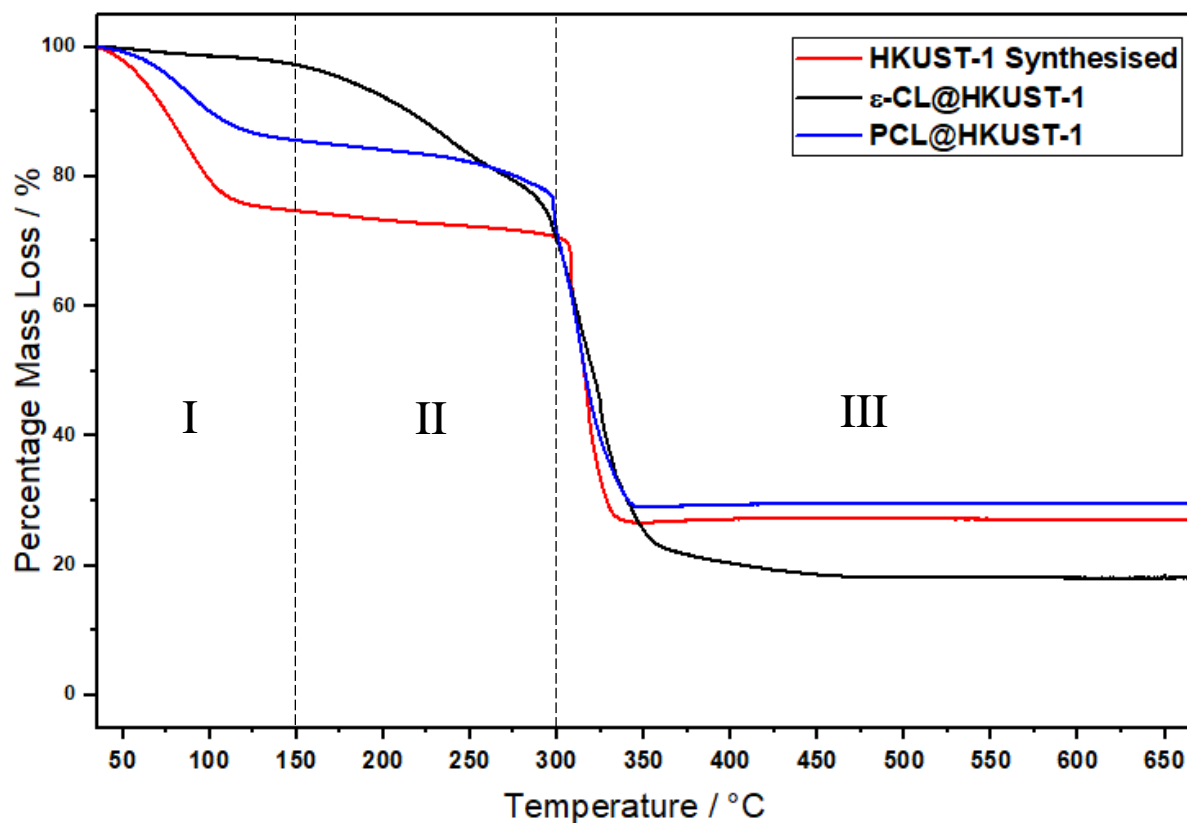


Fig 4.25: TGA profiles for empty HKUST-1,  $\epsilon$ CL@HKUST-1, and PCL@HKUST-1. Regions I, II, and III correspond to the regions for vaporisation of moisture and surface species; removal of intrinsic and bound guest; and thermal decomposition of HKUST-1, respectively. All samples were run under air.

Table 4.4 shows the percentage mass loss observed in the case of  $\epsilon$ CL@HKUST-1 and PCL@HKUST-1.

## Chapter 4: Characterisation and Analysis

---

Table 4.4: Percentage mass loss observed in regions I, II and III from TGA profiles for empty HKUST-1,  $\epsilon$ CL@HKUST-1, and PCL@HKUST-1. (Error  $\pm 2$  %)

	<b>HKUST-1</b>	<b><math>\epsilon</math>CL @HKUST-1</b>	<b>PCL@HKUST-1</b>
<b>Region I</b>	25 %	4 %	15 %
<b>Region II</b>	3 %	14 %	5 %
<b>Region III</b>	47 %	58 %	50 %

## Chapter 4: Characterisation and Analysis

### 4.4.2.3 D,L-Lactide Polymerisation in HKUST-1 – TGA

The TGA profiles of as synthesised HKUST-1, PLAC@HKUST-1 with polymer guest for D,L-lactide is shown in Fig 4.26.

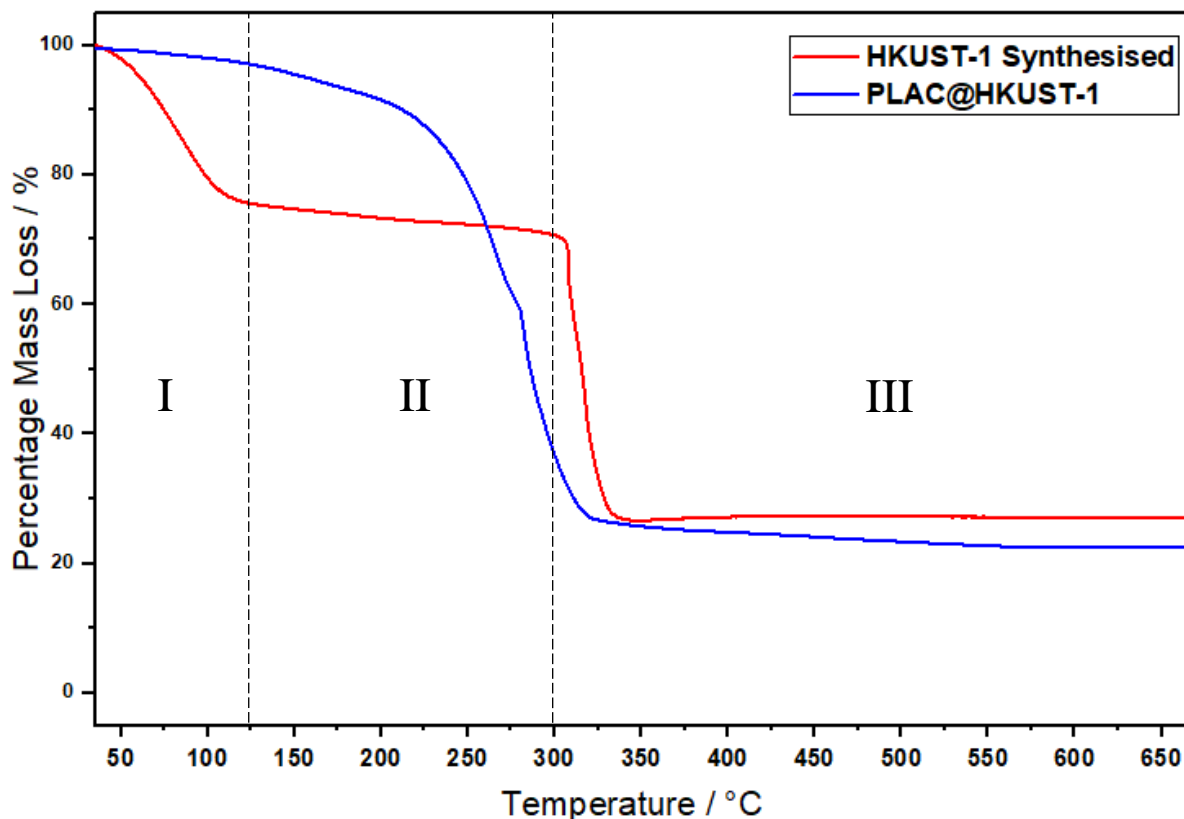


Fig 4.26: TGA profiles for empty HKUST-1 and PLAC@HKUST-1. Regions I, II, and III correspond to the regions for vaporisation of moisture and surface species; removal of intrinsic and bound guest; and thermal decomposition HKUST-1, respectively. All samples were run under air.

The D,L-lactide monomer has a melting point of 120-125 °C and initiates ring-opening polymerisation between 130-135 °C, at atmospheric pressure. Hence, only PLAC@HKUST-1 was studied using TG and DTG analyses.

Following the losses of water at  $T < 110$  °C, the TGA profile in region II shows a significant drop. This can be partially attributed to the polymer decomposition in the PLAC@HKUST-1 composite. The lack of distinct regions in PLAC@HKUST-1 suggests that the polymerisation

## Chapter 4: Characterisation and Analysis

---

here is extrinsic to the MOF, and the monomer is unable to penetrate the pores of the MOF likely due to its high viscosity at the monomer stage and incomplete melting to allow in-situ polymerisation. As a result, there is an overall 60 wt% loss in the region II that combines polymer decomposition, residual monomer vaporisation, and removal of bound water and solvent molecules in HKUST-1. It is possible through DTG analysis to identify the temperature step at which there is onset of MOF degradation at 275 °C (Appendix A4.18). The mass loss step continues until 350 °C where the metal oxides are obtained as decomposition product. Based on interpretation of the data, it is not possible to correlate experimental data to theoretical data for calculating in-situ degree of polymerisation without data from the monomer loaded sample, and due to suspected extrinsic polymerisation.

It was not possible to carry out an ex-situ monomer evacuation step under vacuum for LAC as this resulted in partial polymerisation of the monomer due to reduction in experimental pressure. For later experiments, this step was bypassed. Instead, mass percentage equal to the monomer loading of  $\epsilon$ CL, an addition of 40 wt% to the overall mass of the MOF was used for polymerisation experiments.

## Chapter 4: Characterisation and Analysis

---

### 4.5 NMR Analysis – Isolated Polymer

In our combinatorial systems, hydrogen bonding and coordinative interaction of solvent or additive with the polar groups of the monomer, and the chain growth can also be investigated through  $^1\text{H}$  and  $^{13}\text{C}$  NMR spectroscopy.  $^1\text{H}$  and  $^{13}\text{C}$  NMR spectra were evaluated to determine successful isolation of polymers from the MOF following  $\text{Na}_2\text{EDTA}$  extraction method (Section 3.4).

In-situ polymerisation of adsorbed guest monomer largely depends on the pore size of the MOF and its ability to penetrate and saturate the MOF pores to allow polymerisation within the MOF. Since there is no covalent chemical interaction between the adsorbed monomer or the polymer with the pore walls, but only physical and effective space interactions within the pores of the MOF, here polymer isolated from the MOF structure can be studied by NMR through isotropic chemical shift, assignments by harnessing neighbourhood relations from  $J$  coupling and peak integral analyses.

#### 4.5.1 Poly(vinyl acetate) isolated from MOF – $^1\text{H}$ NMR

Polymer extracted from MOF-5 showed all characteristic PVAc peak environments on the  $^1\text{H}$  spectrum (Fig 4.27, on the next page).

The large signature in the  $^1\text{H}$  NMR spectrum is attributed to the repeating units of VAc at 1.8 to 2.1 ppm. These are characteristic signals originating from the methyl, methylene, and methine protons at the lower chemical shift regions of the spectrum at 1.97-2.02, 4.84, and 1.84 ppm, respectively. Peaks appearing in this region were fitted to a second polynomial curve for integral analysis (Appendix – Fig A4.21). The terminal methyl end groups on – $\text{CH}_2\text{-O}(\text{C}=\text{O})\text{CH}_3$  groups appear at 3.8 ppm. Additional peaks in the spectrum are from AIBN initiator and appear between 1.4-1.5 ppm. There is residual and unreacted monomer present but in negligible amounts compared to the polymer.

## Chapter 4: Characterisation and Analysis

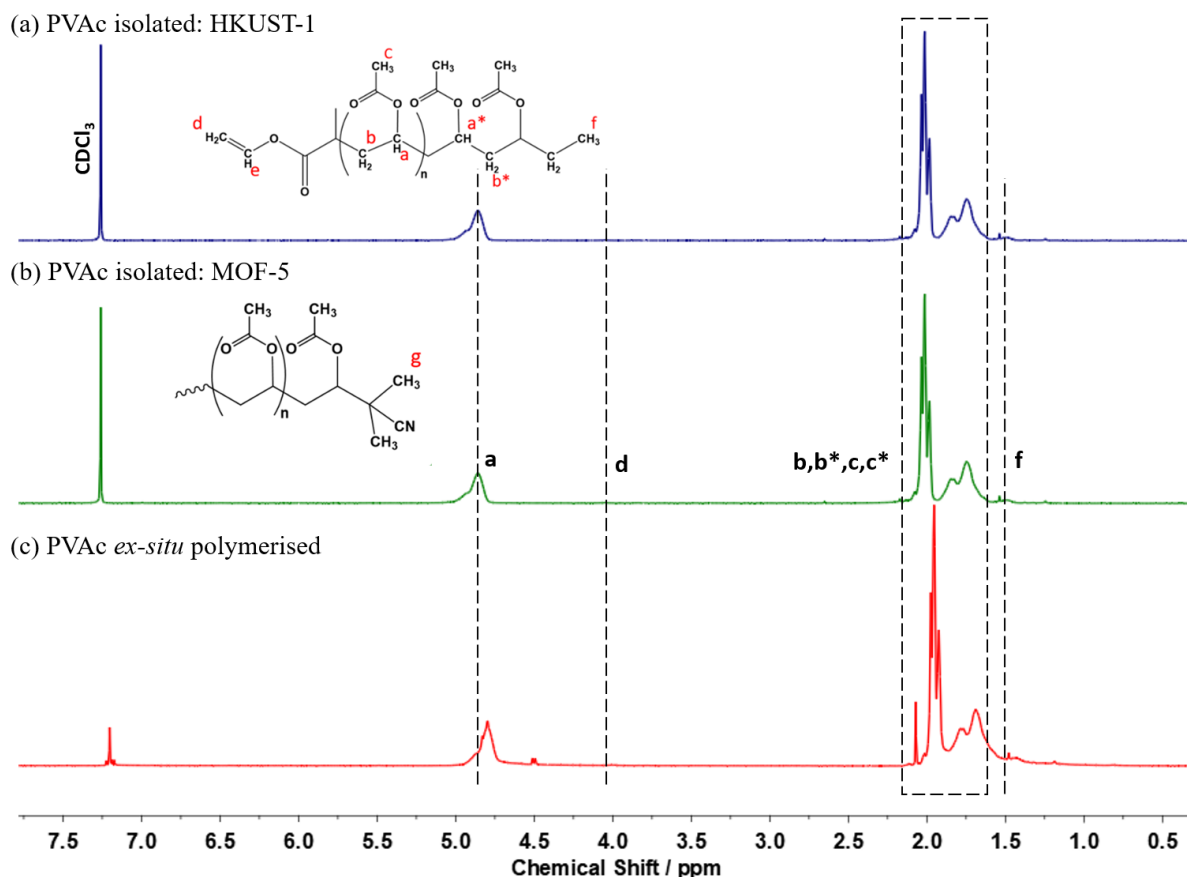


Fig 4.27:  $^1\text{H}$  NMR spectra of (a) isolated PVAc from HKUST-1 (b) isolated PVAc from MOF-5 and (c) linear polymer PVAc. Detailed spectral assignments are shown in appendix A4.21.  $^1\text{H}$ -NMR (400 MHz,  $\text{CDCl}_3$ ): 1.25 (d,  $-\text{CH}_3$ ); 1.84 (q, 4H); 1.97 (rr, s, 3H); 2.0 (mr, s, 3H); 2.02 (mm, s, 3H); 4.84 (s, 2H); 8.76 (s, 3H, COOH).

Percentage conversion of VAc monomer was calculated by comparing the peak integral area of the  $^1\text{H}$  of vinylic  $\text{CH}_2$  proton of the monomer at 4.6 ppm with the total peak integral area of the monomer and the  $^1\text{H}$  of the methine (CH) proton on the polymer backbone at 4.84 ppm. To compare the number average molecular weight of the polymer from the  $^1\text{H}$  NMR spectra, the peak area of the methine proton of the polymer at 4.84 ppm was compared with the methylene protons of the chain terminating end group at 4.6 ppm to calculate the number average molecular weight ( $M_n$ ). The results of the calculations are shown in Table 4.5 below.

## Chapter 4: Characterisation and Analysis

---

Table 4.5:  $^1\text{H}$  NMR conversion for templated PVAc following isolation from MOF, determined by integral analysis. (Calculated using method described in Section 3.5.2)

Host MOF	Conversion (%)	$M_n$ (Experimental)	$M_n$ (Theoretical)
MOF-5	68%	4150	6200
HKUST-1	64%	3950	6200

Number average molecular weight for polymer isolated from MOF-5 and HKUST-1 are calculated to be 64 and 68%, respectively. Calculated number average molecular weight of isolated PVAc polymer was less than theoretical molecular weight that was calculated by *ex-situ* solution polymerisation. The lower molecular weight by MOF templated approach is expected due to the confinement effects and steric hindrance imposed within the MOF pores on the monomer species.

## Chapter 4: Characterisation and Analysis

### 4.5.2 Poly(vinyl acetate) isolated from MOF – $^{13}\text{C}$ NMR

Fig 4.28 shows the  $^{13}\text{C}$  NMR spectra of isolated PVAc from the MOF-5.

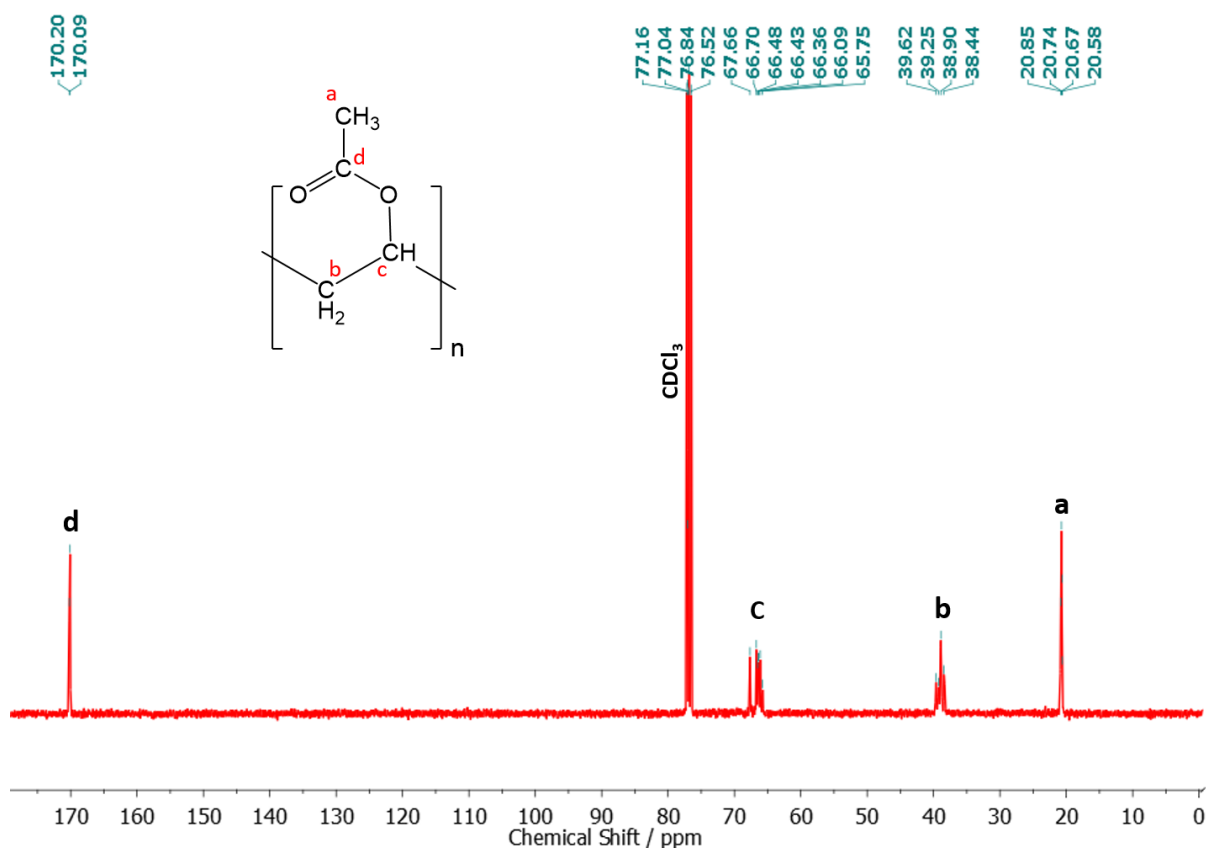


Fig 4.28:  $^{13}\text{C}$  NMR spectra of isolated PVAc from MOF-5. PVAc isolated from HKUST-1:  $^{13}\text{C}$  NMR (400 MHz,  $\text{CDCl}_3$ ): 19 ( $\text{CH}_3$ ); 31 ( $\text{CH}_2$ ); 65 ( $\text{CH}$ ), 171 ( $-\text{COO}$ ); PVAc isolated from MOF-5:  $^{13}\text{C}$  NMR (400 MHz,  $\text{CDCl}_3$ ): 19 ( $\text{CH}_3$ ); 31 ( $\text{CH}_2$ ); 65 ( $\text{CH}$ ), 171 ( $-\text{COO}$ )

A sharp singlet at 20 ppm originates from the methyl carbons on the acetyl group on the polymer. There is an overlap for the monomer and polymer characteristic methyl carbon peak between 19-20 ppm which is difficult to differentiate on the solution state NMR. However, on solid state  $^{13}\text{C}$  MAS NMR, the monomer peak appears as a finely resolved sharp singlet whereas the polymer appears as a broad hump in this region.

For VAc the methylene and methine carbon peaks appear at 97 and 141 ppm, respectively, and diminish in intensity as the monomer is converted to polymer. The characteristic methine

## Chapter 4: Characterisation and Analysis

---

on the polymer backbone of PVAc appears in the region between 65–70 ppm as a broad peak. The region between 37–40 ppm appears from the three methylene carbon features peaks at 38.4, 38.9 and 39.6 ppm.

The  $^{13}\text{C}$  spectra of isolated PVAc from HKUST-1 and MOF-5 showed all characteristic peaks with little to no signal from residual linker and unpolymerized monomer, post-washing with respective solvent and water. The  $^{13}\text{C}$  NMR spectrum of the methine carbon of PVAc consists of two primary peaks shown as 'c' in Fig 4.30 and gives rise to a complicated spectrum of lines between 65–69 ppm due to configurational and compositional splitting. The relative intensity between the two peaks between 60–69 ppm peaks can be used to determine the tacticity of the polymer. When the lower field peaks are prevalent, the polymer tends to be more isotactic in nature. On the other hand, higher field peaks dominating the intensity suggest a heterotactic and syndiotactic triad on the polymer. In the polymers isolated from the MOF-5 and HKUST-1, the relative intensities between these two peaks were 0.47 and 0.53 for the lower, and 0.53 and 0.47 for the upper field peaks, respectively. This suggests a more homogeneous mixture of isotactic and syndiotactic polymer in nature.

The carbonyl carbon on PVAc is a single peak showing that the resonances of side-chain carbon atoms are not affected by the tacticity or stereochemistry of the polymer. The carbonyl peak for VAc appears at 168 ppm and shifts downfield at 170 ppm for PVAc. There is a splitting of the carbonyl peak in the polymer spectrum giving rise to resolved lines at 170.09 and 170.20 ppm. Further details on  $^{13}\text{C}$ -NMR spectrum of for PVAc polymerisation is given in section 5.5 by solid state NMR.

## Chapter 4: Characterisation and Analysis

### 4.5.3 Poly( $\epsilon$ -Caprolactone) isolated from MOF – $^1\text{H}$ NMR

The  $^1\text{H}$ -NMR spectrum of isolated PCL shows clear presence of the groups characteristic of successful ROP of  $\epsilon\text{CL}$  (Fig 4.29). The protons on the benzyl alcohol group appear at 7.36 and 5.11 ppm. The multiplet of peaks between 1.25 and 1.65 ppm are assigned to proton resonance of methylene groups present in the repetitive unit on the polymer backbone. The peaks around 2.31 ppm are assigned to the methylene proton originating from the ( $-\text{CO}-\text{CH}_2$ ), whereas triple splitting peaks at 4.06 ppm are assigned to resonance signal from the methylene connected to the ester group ( $-\text{CH}_2-\text{O}-\text{CO}-$ ).

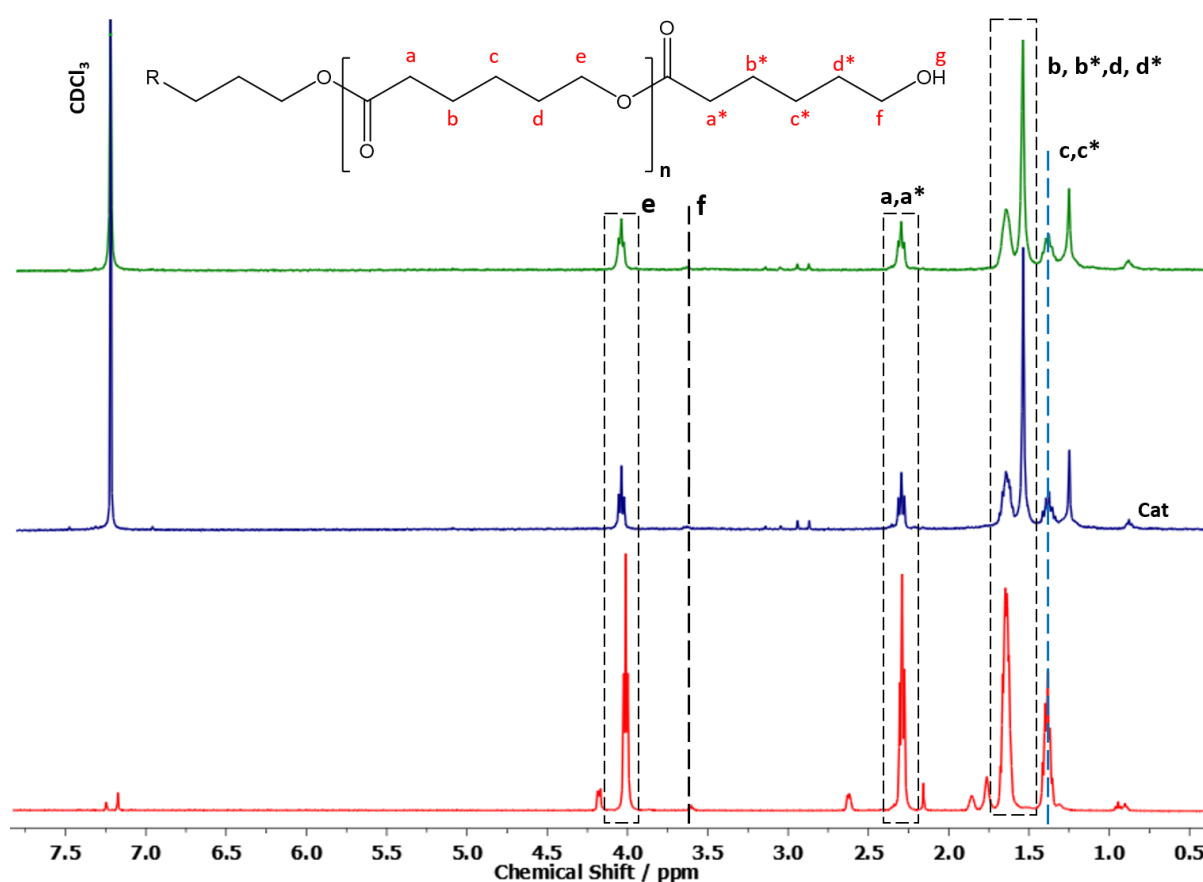


Fig 4.29:  $^1\text{H}$  NMR spectra of (top) isolated PCL from HKUST-1; (middle) isolated PCL from MOF-5, and (bottom) linear polymer PCL.  $^1\text{H}$ -NMR (400 MHz,  $\text{CDCl}_3$ , 25  $^\circ\text{C}$ ):  $\delta$  = 4.06 (t;  $\text{CH}_2 - \text{e}$ ), 3.60 (t;  $\text{CH}_2 - \text{f}$ ), 2.31 (t;  $\text{CH}_2 - \text{g}$ ), 1.5-1.7 (m;  $\text{CH}_2 - \text{b}, \text{b}^*, \text{d}, \text{d}^*$ ), 1.25-1.45 ppm (m;  $\text{CH}_2 - \text{c}, \text{c}^*$ ); 1.54 (s; OH), 0.87–0.97 (m; AIBN), 7.20 (s,  $\text{CDCl}_3$ ).

## Chapter 4: Characterisation and Analysis

---

Additional peaks belonging to the CH<sub>2</sub>O protons are found around the region of 5.09–5.02 ppm and are relatively weak compared to the other proton signals and the region is difficult to extract integral value due to noise.

The CH<sub>2</sub>OH protons appear in the isolated PCL spectrum at 3.64–3.45 ppm. A new peak at 4.20 ppm corresponding to the new ester group environment of the CH<sub>2</sub> protons of PCL is present in the control spectrum of ex-situ linear PCL but may be embedded under the noise due to the solubility difficulty during sample preparation for NMR. While the ex-situ polymerised linear PCL is readily soluble in chloroform and DMSO, isolated PCL is insoluble or sparingly soluble in most deuterated solvents available. Upon heating, the polymer solubility increases but the polymer precipitates in a few minutes making finely resolved <sup>1</sup>H and <sup>13</sup>C NMR acquisitions increasingly difficult as it is cooled down to room temperature. This effect may likely be due to presence of –ONa as functional end groups from the polymer isolation process with Na<sub>2</sub>EDTA instead of hydroxyl end groups that are present on the linear PCL. This conclusion is supported by ICP-AES that shows presence of Na<sup>+</sup> ions in the isolated polymer, and ESI-MS fragment analysis.

Additional peaks that belonging to Sn(II)Oct<sub>2</sub> initiator used for polymerisation of εCL are present in the spectrum of PCL, and can be identified with signal around 0.87 – 0.97 and 1.25 – 1.67 ppm regions. The single peak at 1.54 ppm is likely from hydroxyl groups on residual water that may still be present following drying of isolated PCL in air.

Table 4.6: <sup>1</sup>H NMR conversion for templated PCL following isolation from MOF, determined by integral analysis. (Calculated using method described in Section 3.5.2)

Host MOF	Conversion (%)	M <sub>n</sub> (Experimental)	M <sub>n</sub> (Theoretical)
MOF-5	59%	5350	7410
HKUST-1	65%	4800	7410

## Chapter 4: Characterisation and Analysis

---

Number average molecular weight for polymer isolated from MOF-5 and HKUST-1 are calculated to be 59 and 65%, respectively (Table 4.6). PCL isolated from MOF-5 shows a lower conversion compared to the polymer isolated from HKUST-1. It is unclear why the conversion in the case of MOF-5 was low and would need further investigation to determine the possible reason. It was suspected that a reason for this might be due to poor penetration of the monomer within the pores of MOF-5 but this was ruled out following a comparison between as-synthesised MOF weight and monomer@MOF weight for HKUST-1 and MOF-5. Values for number average molecular weight of isolated PCL polymer was less than theoretical molecular weight that was calculated by *ex-situ* solution polymerisation. The lower molecular weight by MOF templated approach is expected due to the confinement effects and steric hindrance imposed within the MOF pores on the monomer species which is also seen in the case of PVAc@MOF.

## Chapter 4: Characterisation and Analysis

### 4.5.4 Poly( $\epsilon$ -Caprolactone) isolated from MOF – $^{13}\text{C}$ NMR

Due to difficulties in solubilities due to reasons mentioned in section 4.5.3, acquiring  $^{13}\text{C}$  spectrum of only isolated PCL from HKUST-1 was possible. This is possible because of residual zinc metal complexes present in PCL isolated from MOF-5. The  $^{13}\text{C}$  NMR spectrum of isolated PCL also shows the characteristic peaks of PCL with resonance peaks at 176.4–173.9 ppm from the carbonyl group of the polymer (Fig 4.30). A single sharp resonance at 64.49 ppm appears in the spectrum from ( $-\text{CO}-\text{CH}_2-$ ). Further, upfield in the spectrum in the region between 34.1–23.40 ppm, resonance signals from each methylene carbons on the polymer backbone are present at 34.1, 28.3, 25.5, and 24.6 ppm.

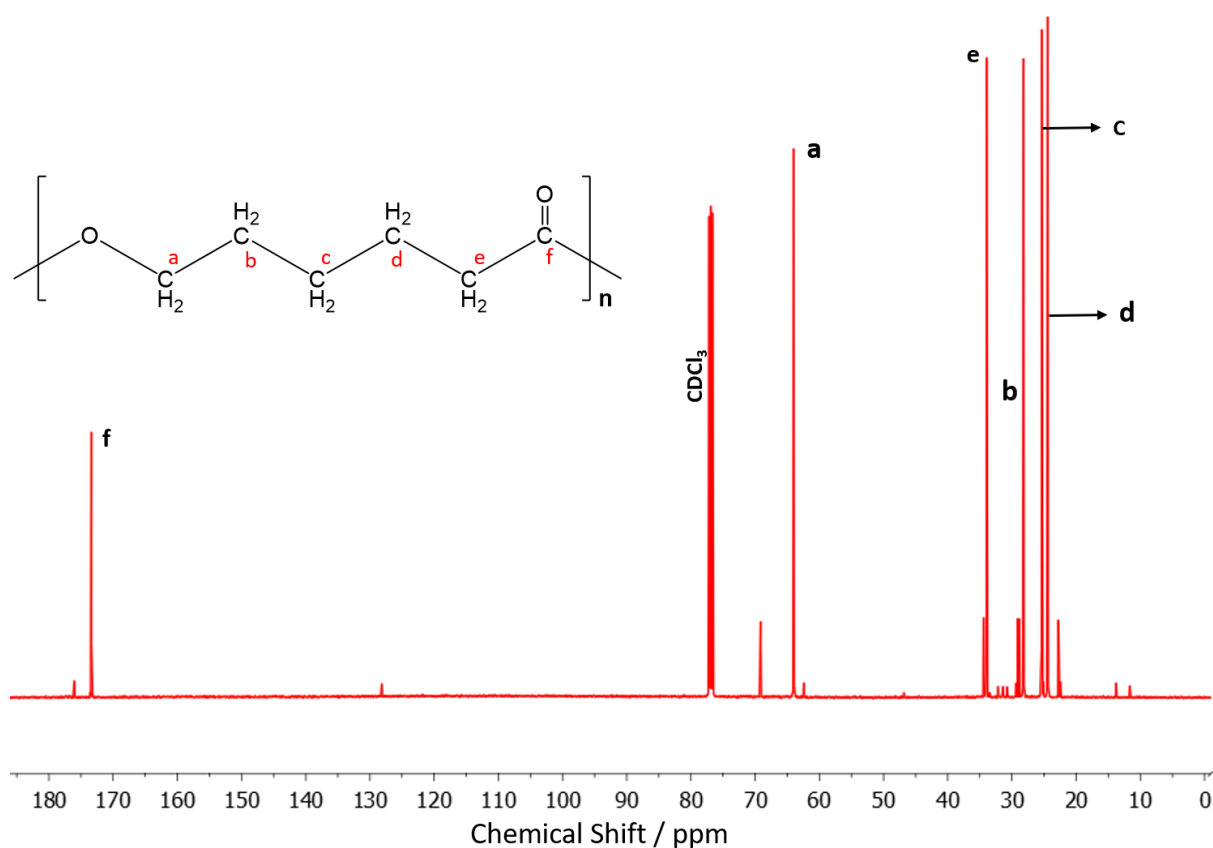


Fig 4.32:  $^{13}\text{C}$  NMR spectra of PCL isolated from HKUST-1:  $^{13}\text{C}$  NMR (400 MHz,  $\text{CDCl}_3$ ): 24.6 ( $^{\text{a}}\text{CH}_2$ ); 25.5 ( $^{\text{b}}\text{CH}_2$ ); 28.3 ( $^{\text{c}}\text{CH}_2$ ), 34.1 ( $^{\text{d}}\text{CH}_2$ ), 64.49 ( $^{\text{e}}\text{CH}_2\text{O}$ ), 173.90 ( $\text{C}=\text{O}$ ) ppm.

## Chapter 4: Characterisation and Analysis

---

### 4.6 Mass Spectrometry

Mass spectrometry (ESI) and MALDI-TOF was carried out on isolated polymers to identify and confirm the species present, polymer structure and nature of end groups, efficiency of the templating process and molecular weight distribution of the of the polymer. Furthermore, analysis was carried out to identify and resolve the homopolymer end groups using equation 4.3.

$$M_{n\text{-mer}} = n(M_{\text{RU}}) + M_{\text{EG1}} + M_{\text{EG2}} + M_{\text{ion}} \quad (4.3)$$

Where,  $M_{n\text{-mer}}$  = Mass of polymer,  $n$  = Degree of polymerisation,  $M_{\text{EG1}}$  = Mass of  $\alpha$ -end group,  $M_{\text{EG2}}$  = Mass of  $\beta$ -end group,  $M_{\text{RU}}$  = Mass of repeating unit of the polymer,  $M_{\text{ion}}$  = Mass of ion that complexes with the polymer. Polydispersity index (PDI) was calculated from the MALDI spectrum using  $M_w/M_n$  ratio.

#### 4.6.1 Poly(vinyl acetate) isolated from MOF

ESI GC-MS and MALDI-TOF spectra of PVAc isolated from HKUST-1 are shown in Fig 4.31 and 4.32, and spectra for PVAc isolated from MOF-5 are shown in Fig 4.33 and 4.34. Isolated PVAc from both MOFs show intense peaks that can be assigned to repeating monomer units for PVAc. Isolated polymers from MOF show a number average molecular weights to be 1215.4 and 1199.6 g/mol for HKUST-1 and MOF-5, respectively. From the MALDI spectrum of polymer isolated from HKUST-1 (Fig 4.32), the dispersity of 1.02 was calculated for PVAc using the  $M_w/M_n$  ratio. The PDI for PVAc isolated from MOF-5 was found to be 1.03. Both isolated polymers from MOF suggested an isolated short-chain polymer with 14 monomer units with  $-\text{OH}$  end groups at  $\alpha$  and  $\beta$  sites.

## Chapter 4: Characterisation and Analysis

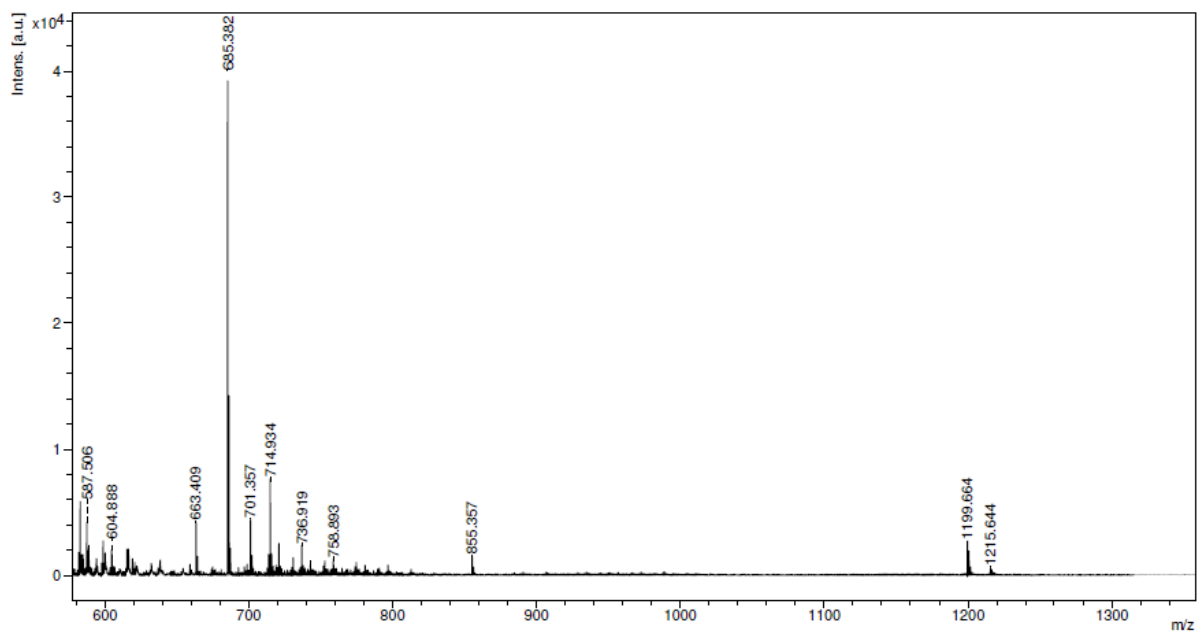


Fig 4.31: ESI GC-MS spectrum of isolated PVAc from HKUST-1

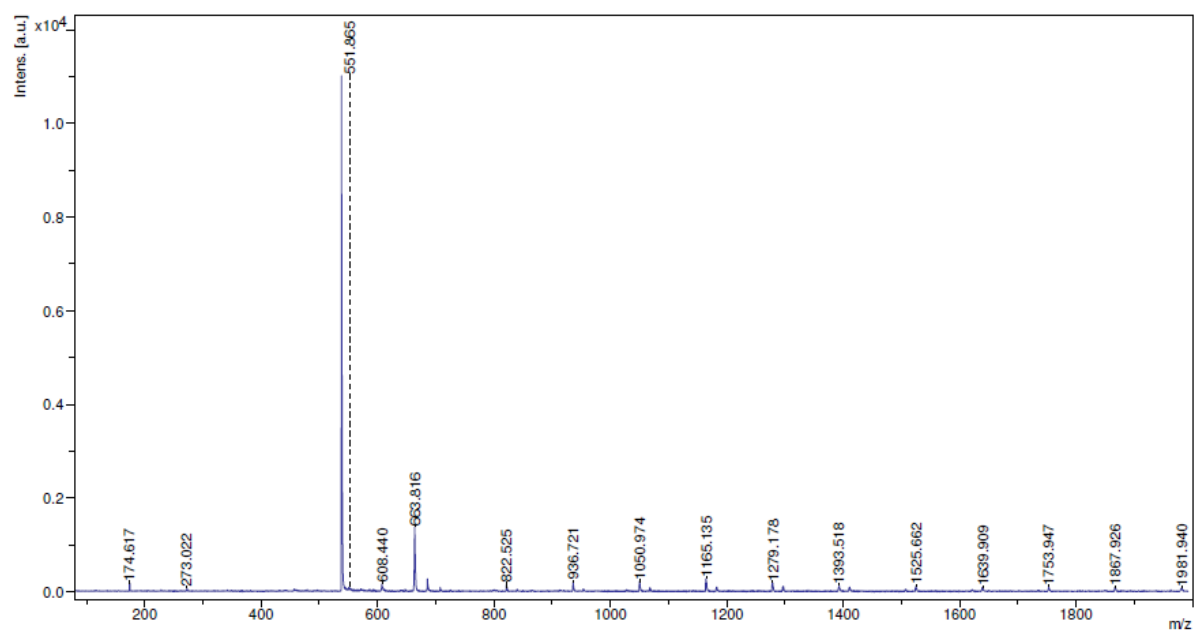


Fig 4.32: MALDI-TOF spectrum of isolated PVAc from HKUST-1

## Chapter 4: Characterisation and Analysis

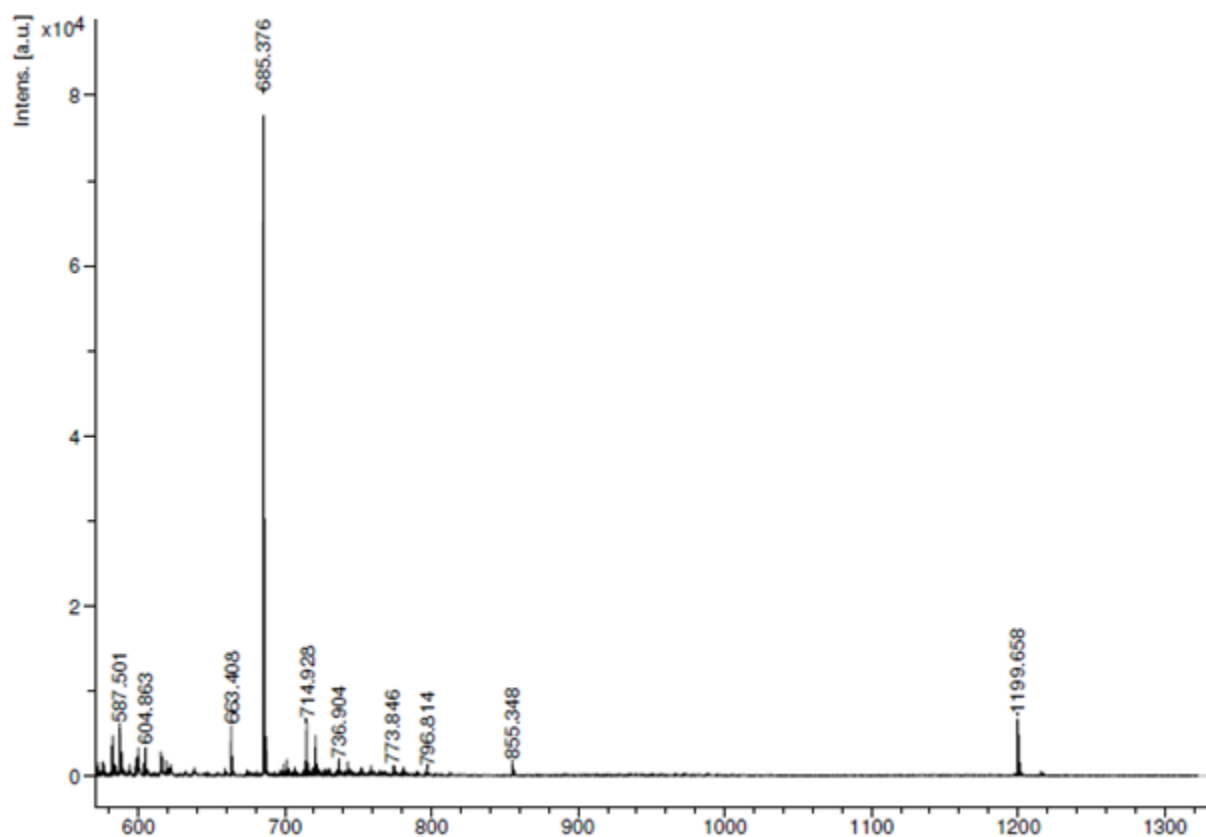


Fig 4.33: ESI GC-MS spectrum of isolated PVAc from MOF-5

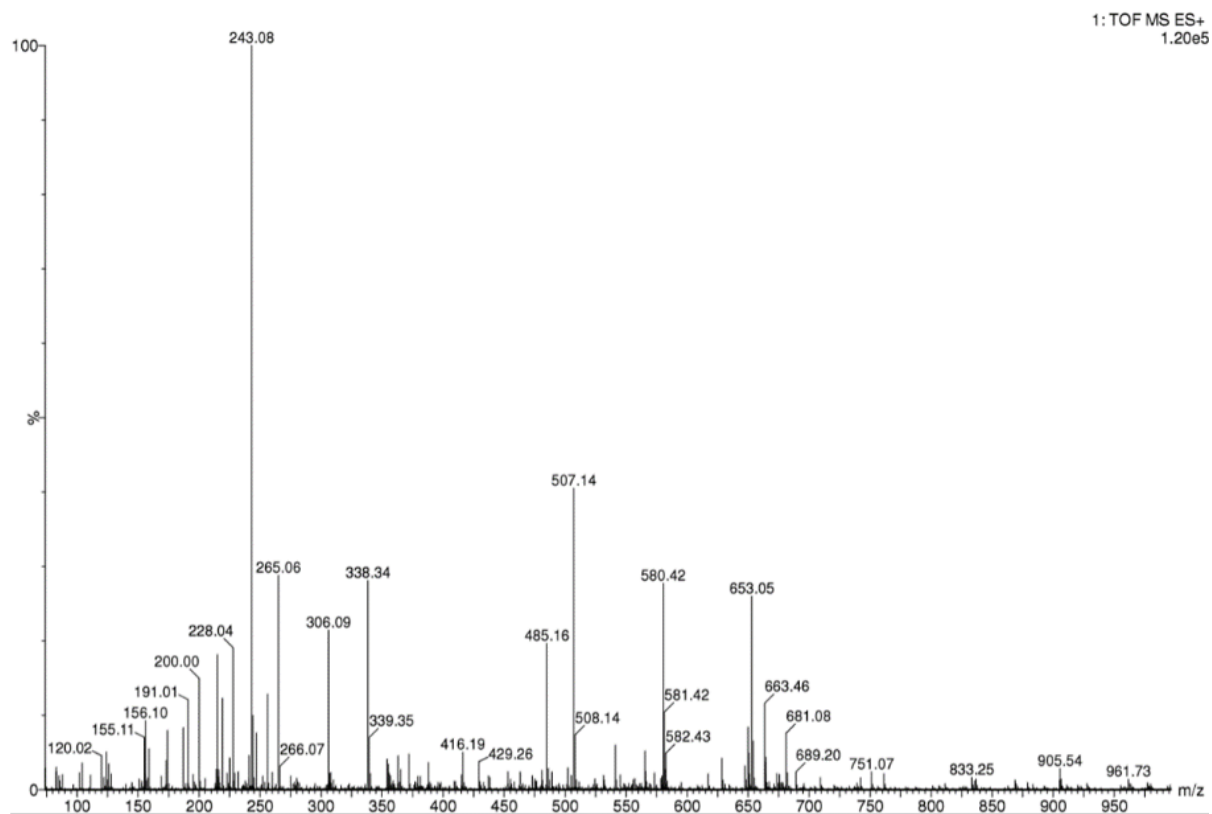


Fig 4.34: MALDI-TOF spectrum of isolated PVAc from MOF-5

## Chapter 4: Characterisation and Analysis

### 4.6.2 Poly( $\epsilon$ -Caprolactone) isolated from MOF

Fig 4.35 shows LC-MS chromatogram for PCL isolated from HKUST-1. The intense peaks are assigned to each of the monomer units. The fine structure observed at higher peak clusters is assigned to the PCL isomers. Analysing the distribution of the peaks from MALDI-TOF spectra, the resulting  $M_n$  values were 2875.89 and  $M_w$  of 3308.88 giving a PDI of 1.15. PCL isolated from HKUST-1 reveals successful polymerisation (Fig 4.36). Average number of monomer units from all HKUST-1 extraction were 20 monomer units ( $M_n = 2200$ ). These values correlate with those obtained from GPC (Gel Permeation Chromatography) and NMR. End group analysis reveal that unlike PVAc isolation following in-situ template polymerisations in MOFs, PCL extracted from HKUST-1 results in  $-OH$  end groups on  $\alpha$  and  $\beta$  end group sites. The high molecular weight and polydispersity is a promising result for polymers templated from MOFs and a potential candidate for drug loading studies.

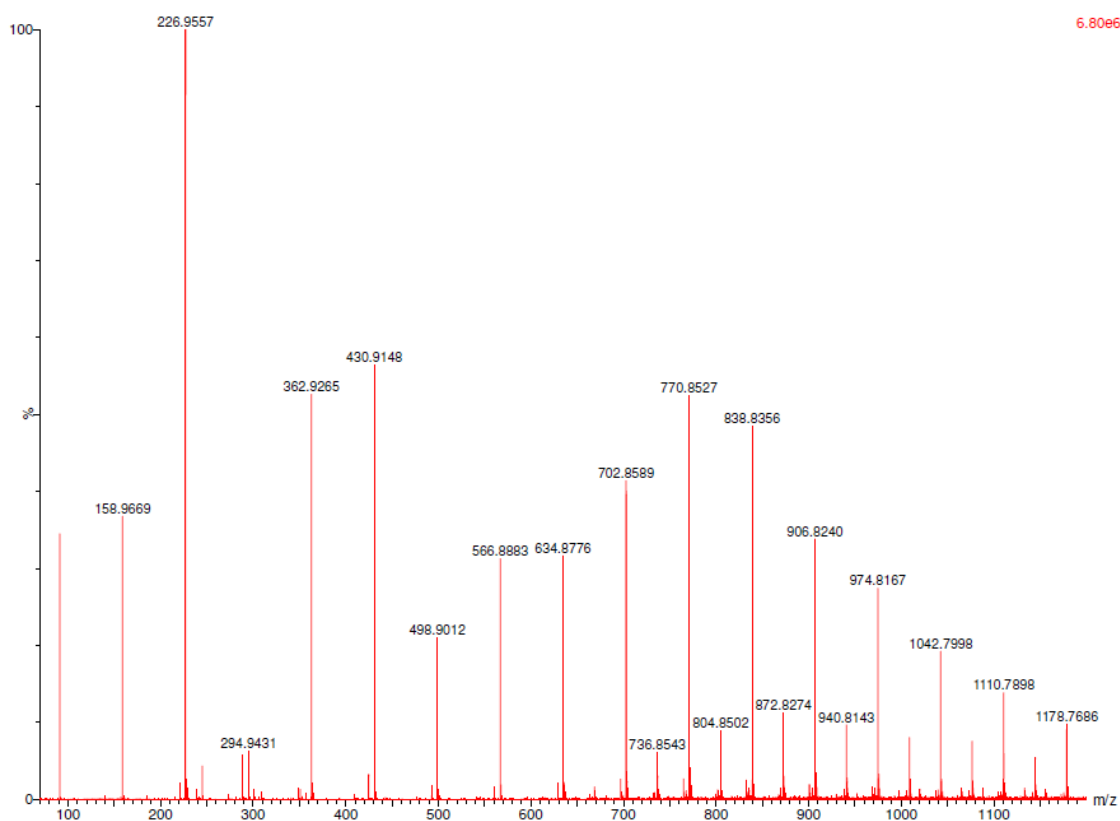


Fig 4.35: LC-MS spectrum of isolated PCL from HKUST-1

## Chapter 4: Characterisation and Analysis

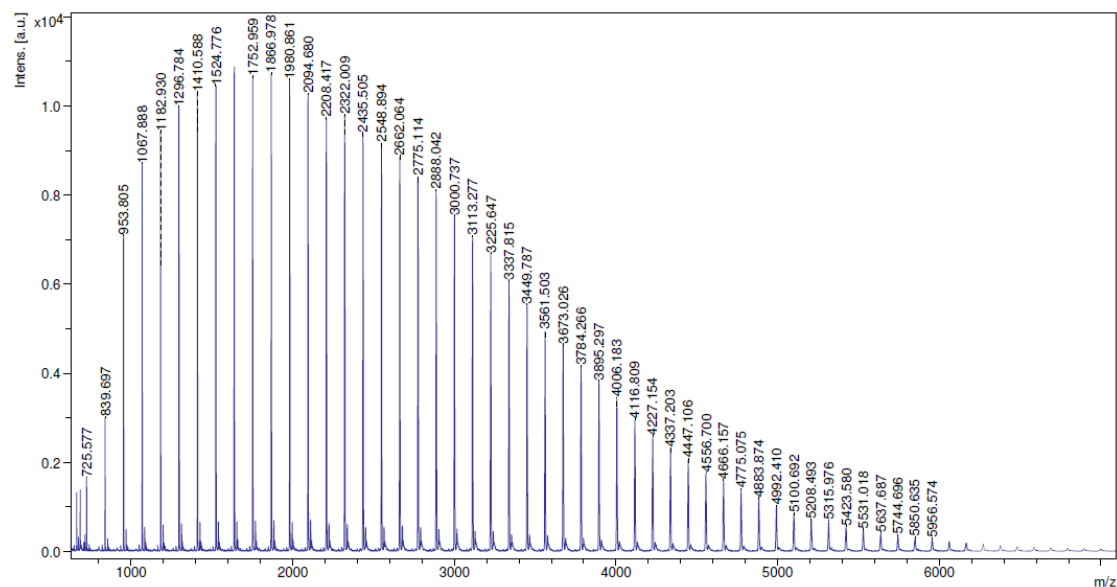


Fig 4.36: MALDI-TOF spectrum of isolated PCL from HKUST-1

PCL extracted from MOF-5 shows similar findings with molecular weight polymer as  $M_n = 1283.38$  and  $M_w = 1309.38$ , and a resulting PDI of 1.02. End group analysis also suggests presence of  $-OH$  groups on  $\alpha$  and  $\beta$  end group sites. LC-MS and MALDI-TOF spectrum are shown in Fig 4.37 and 4.38, respectively.

## Chapter 4: Characterisation and Analysis

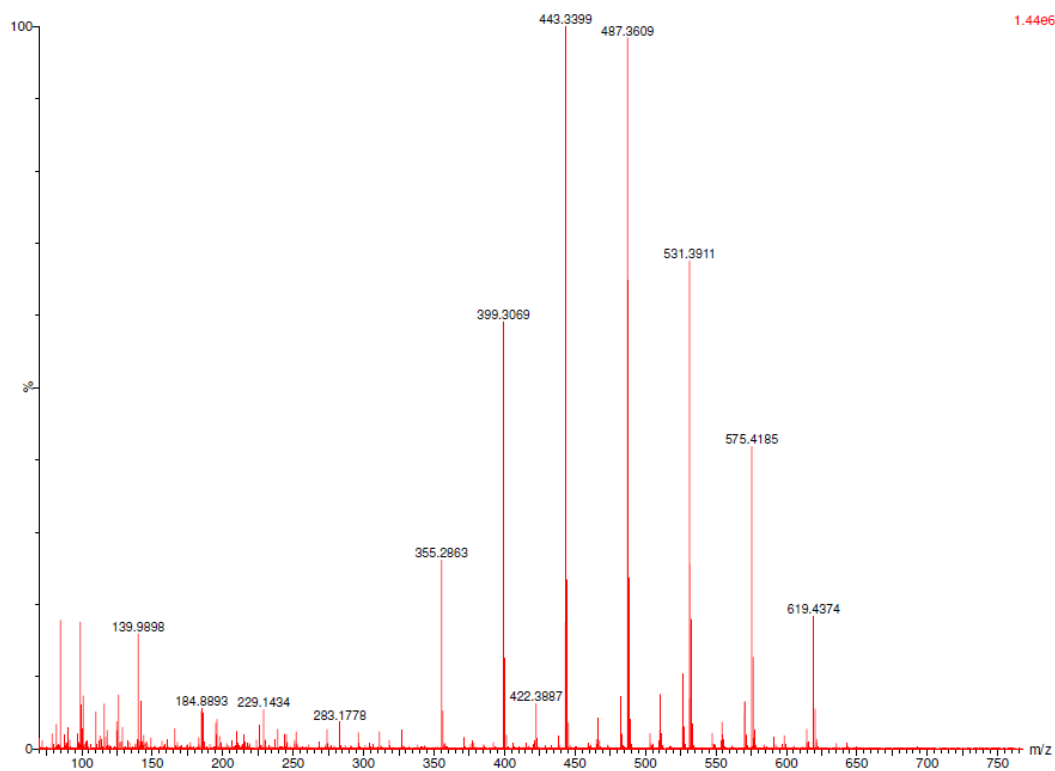


Fig 4.37: LC-MS spectrum of isolated PCL from MOF-5

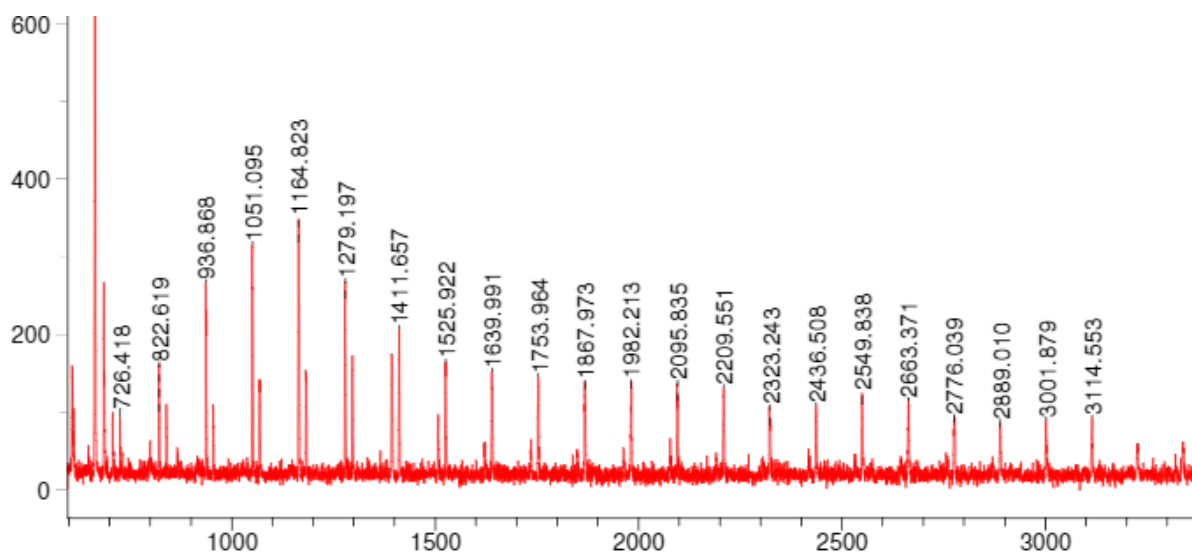


Fig 4.38: MALDI-TOF spectrum of isolated PCL from MOF-5

## Chapter 4: Characterisation and Analysis

### 4.7 Emission Spectroscopy: ICP-AES

Isolated polymers were characterised by ICP-AES to determine the amount of residual metal and to determine the amount of sodium ions due to –ONa present as the end groups on polymers, as suggested from fragmentation analysis of MS data. The measured values of sodium and metal ions are shown in Table 4.7. Measurement calibrations for isolated polymers from HKUST-1 and MOF-5 are presented in Appendix Table A4.28 and A4.29

Polymer	Host MOF	Concentration ( $\pm 0.5$ mg/g)	
		Na	M
Poly(vinyl acetate)	HKUST-1	115.1	8.8
	MOF-5	110.1	9.1
Poly( $\epsilon$ -Caprolactone)	HKUST-1	116.5	8.7
	MOF-5	116.7	50.7

Table 4.7: Measured concentrations of sodium (Na) and metal ions (M = Cu<sup>2+</sup> for HKUST-1; Zn<sup>2+</sup> for MOF-5) by ICP-AES.

### 4.8 Adsorption Isotherms and BET Surface Area Analysis

HKUST-1 and MOF-5 are highly porous material with a wide BET surface area range reported in the literature from 700–3400 m<sup>2</sup>/g and 680–1900 m<sup>2</sup>/g, respectively.<sup>29,41–44</sup> Most HKUST-1 studies however, report values between 700-1000 m<sup>2</sup>/g, whereas MOF-5 is commonly reported with a surface area between 700–950 m<sup>2</sup>/g.<sup>3</sup> N<sub>2</sub> adsorption isotherms were recorded at 77 K to determine pore volume and BET surface area. The pore volume and surface area values for as synthesised MOFs were compared with polymer@MOF samples to determine change in gas sorption and confirm pore occupancy following in-situ polymerisation.

Due to restrictions on lab access with the instrument during COVID-19 pandemic, all isotherm measurements were taken and recorded by Dr Greg Shaw (Cardiff Catalysis Institute, Cardiff School of Chemistry).

## Chapter 4: Characterisation and Analysis

### 4.8.1 MOF-5

N<sub>2</sub> adsorption experiments on MOF-5, PVAc@MOF-5, and PCL@MOF-5 show a reversible type I adsorption isotherm with a steep increase in at low pressures that are characteristic of microporous materials with high surface area (Fig 4.39).

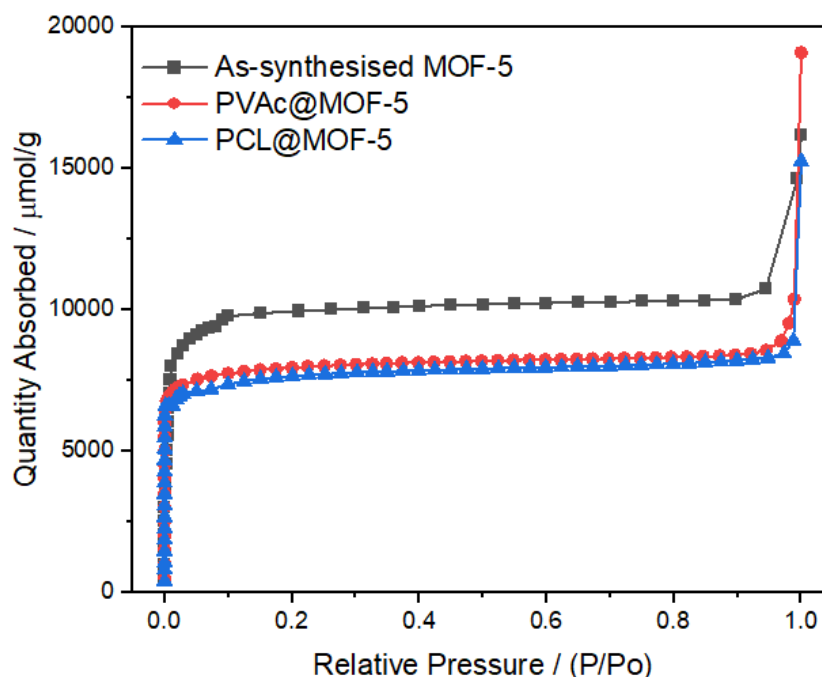


Fig 4.39: N<sub>2</sub> adsorption isotherm for MOF-5 (black), PVAc@MOF-5 (red), and PCL@MOF-5 (blue) recorded at 77 K.

The dimensionality of the MOF depends on the synthesis temperature with the pore dimensions and distribution of MOF-5 increasing as the reaction temperature is raised, a property which can explain the gas adsorption property of MOF-5 varying widely due to differences in crystal morphology or exposed surface of the crystals. Therefore, decreasing the crystal size results in a direct increase in the crystal surface area and leads to a larger amount of N<sub>2</sub> adsorption in the relatively high-pressure region of the isotherm. This suggests that synthesis with higher reaction temperatures may benefit to form multidimensional framework with larger voids. Based on these findings, the synthesis was altered from the earlier used synthesis in the research group resulting in an increase in surface area with the modified synthesis at 120 °C.

## Chapter 4: Characterisation and Analysis

---

The as synthesised MOF-5 shows a BET surface area of  $1027 \pm 2 \text{ m}^2/\text{g}$  and pore volume of  $0.41 \text{ cm}^3/\text{g}$ . As expected, upon in-situ polymerisation of monomers in MOF-5, there is a decrease in maximum available pore volume and BET surface area values as the polymers chains now occupy the pores of the MOF. The calculated values are shown in Table 4.8.

Table 4.8: Calculated BET surface area and maximum pore volume values for MOF-5.

<b>Sample</b>	<b>S<sub>BET</sub> (m<sup>2</sup>/g)</b>	<b>V<sub>Pore</sub> (cm<sup>3</sup>/g)</b>
MOF-5	1027	0.41
PVAc@MOF-5	688	0.27
PCL@MOF-5	771	0.29

From gas sorption isotherms, there are 34% and 29% reduction pore volumes between desolvated MOF and polymer@MOF-5 composites for PVAc@MOF-5 and PCL@MOF-5, respectively. These values are consistent to those calculated from TGA for the case of PVAc@MOF-5. However, in the case of PCL@MOF-5, measured values from N<sub>2</sub> adsorption isotherms are not. A possible explanation of this may be that during the sample preparation for N<sub>2</sub> adsorption experiments, the samples were dried under vacuum that may evacuate any residual moisture, unbound monomer, and/or surface monomer, prior to porosity measurements. The sample preparation prior to TGA measurements did not involve such procedure and due to the overlapping regions of monomer and polymer thermal degradation, it is not possible to conclude whether this is the reason without further investigation.

## Chapter 4: Characterisation and Analysis

### 4.8.2 HKUST-1

Due to instrument failures and travel restrictions during COVID-19 pandemic for maintenance to be carried out on the instrument by Micrometrics engineering team, measurements for PVAc@HKUST-1 was not possible.

N<sub>2</sub> adsorption isotherms for HKUST-1, PVAc@HKUST-1, and PCL@HKUST-1 in Fig 4.40 show a typical type I isotherm for all samples. The high N<sub>2</sub> adsorption capacity at low pressures for HKUST-1 indicates that the sample is micropore dominant.

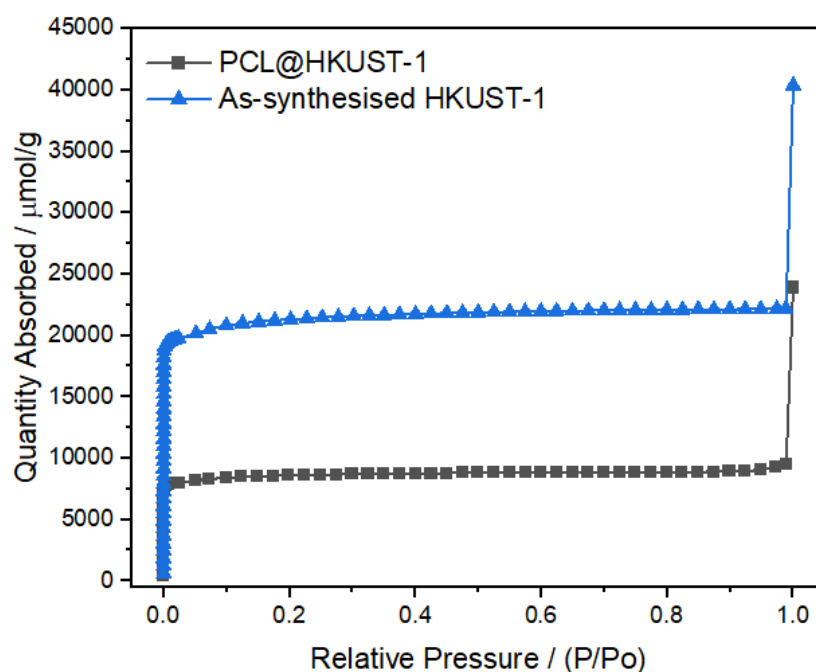


Fig 4.40: N<sub>2</sub> adsorption isotherm for HKUST-1 (black) and PCL@HKUST-1 (blue).

As synthesised HKUST-1 has a BET surface area of  $1895 \pm 1 \text{ m}^2/\text{g}$  that is consistent with the reported values for HKUST-1 with higher surface area.<sup>45</sup> In-situ polymerisation of polymers in HKUST-1 leads to an observable decrease in BET surface area and maximum available pore volume as the pores are blocked by the intrinsic polymer present in the crystal.

## Chapter 4: Characterisation and Analysis

---

Table 4.9: Calculated BET surface area and maximum pore volume values for HKUST-1.

Sample	S <sub>BET</sub> (m <sup>2</sup> /g)	V <sub>Pore</sub> (cm <sup>3</sup> /g)
HKUST-1	1895	0.71
PVAc@HKUST-1	N/A	N/A
PCL@HKUST-1	768	0.29

From adsorption isotherm data there is 59% reduction pore volume between desolvated HKUST-1 and PCL@HKUST-1 composites (Table 4.9). The reduction in pore volume is unexpected and contradicts observations from TGA. Repeat measurements are necessary to ascertain the validity of the of measured values. However, due to instrument failures and travel restrictions during COVID-19 pandemic for maintenance to be carried out on the instrument by Micrometrics engineering team only two samples for PCL@HKUST-1 were measured.

## Chapter 4: Characterisation and Analysis

### 4.9 Scanning Electron Microscopy (SEM)

All materials were dried in vacuum oven overnight at 60 °C before using SEM to capture images. Isolated polymers were dried without vacuum in an oven for 24 h at 60 °C.

#### 4.9.1 MOF-5

Fig 4.41 shows SEM images of crystalline MOF-5 and comparison against the morphology of MOF-2.

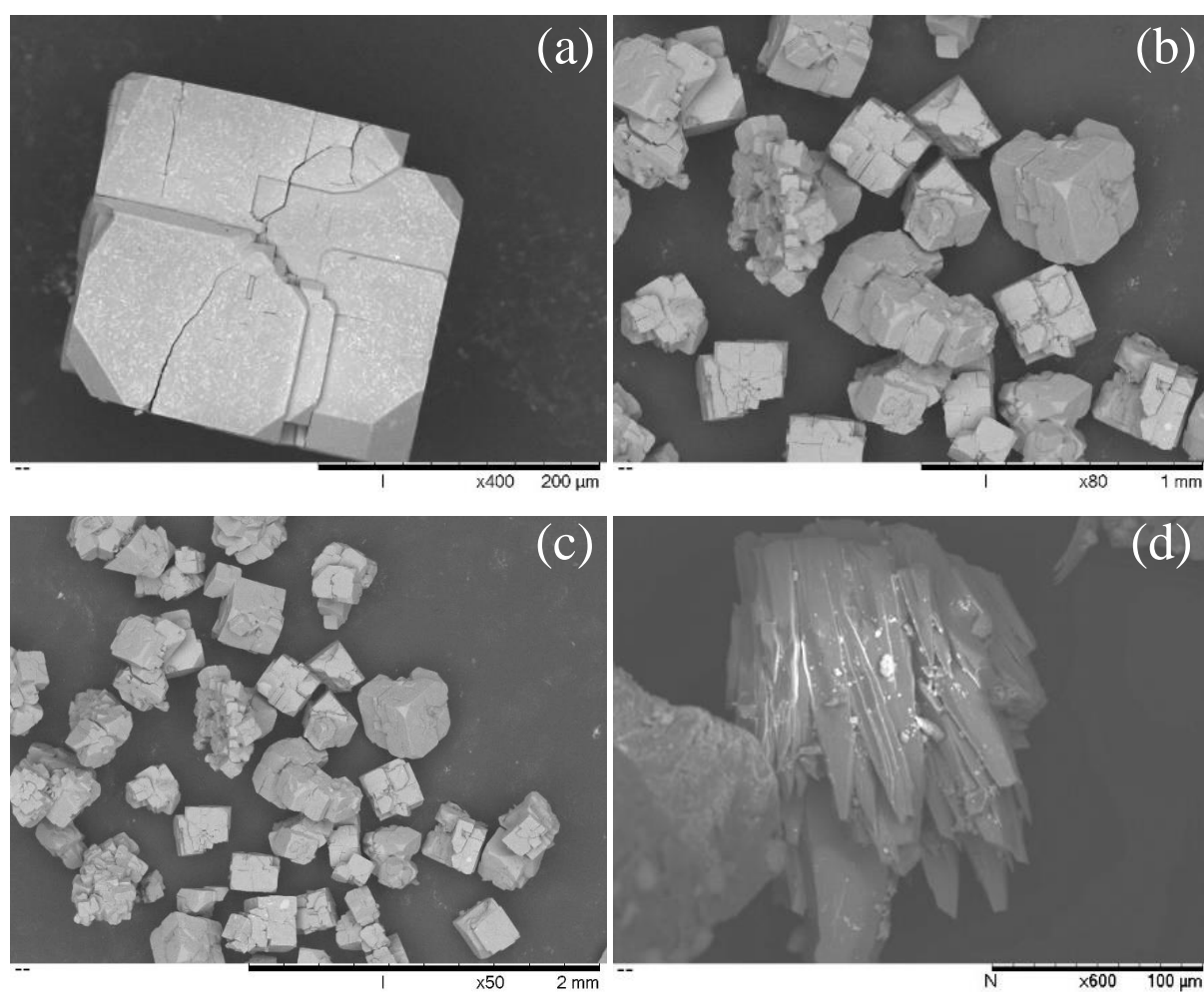


Fig 4.41: SEM images of crystalline MOF-5. (a) cubic shaped crystals of MOF-5, (b,c) agglomerates of cubic MOF-5 (d) sheet-like morphology of MOF-2 before synthesis optimisation.

## Chapter 4: Characterisation and Analysis

---

MOF-5 is a crystalline white powder with an average crystallite size ranging from 0.2–0.4  $\mu\text{m}$ . Fig 4.41 illustrates SEM images of MOF-5. The morphology of the crystals is typically cubic with average size of MOF-5 estimated to be around 0.2  $\mu\text{m}$ . During the process of optimising the literature reported synthesis, it was found that the zinc nitrate and  $\text{H}_2\text{BDC}$  molar ratio played an important part in the ultimate crystal size and morphology on increasing the zinc nitrate and  $\text{H}_2\text{BDC}$  ratio, the crystal morphology changes from having sheet-like crystals or rough cubic crystals to cubes with defined edges and a larger crystal size. It has been now reported that the higher molar ratio of the metal ions to ligand may cause MOF-5 into a self-confinement effect that results in regular cubic shaped crystals with a larger overall crystal size.<sup>3</sup>

## Chapter 4: Characterisation and Analysis

### 4.9.2 Monomer@MOF-5 composite

MOF-5 with adsorbed VAc and  $\epsilon$ CL monomer at experimental loading of 0.4 g/g of MOF was imaged to provide a visual comparison to the diffraction data that suggested expansion of the framework (Fig 4.42).

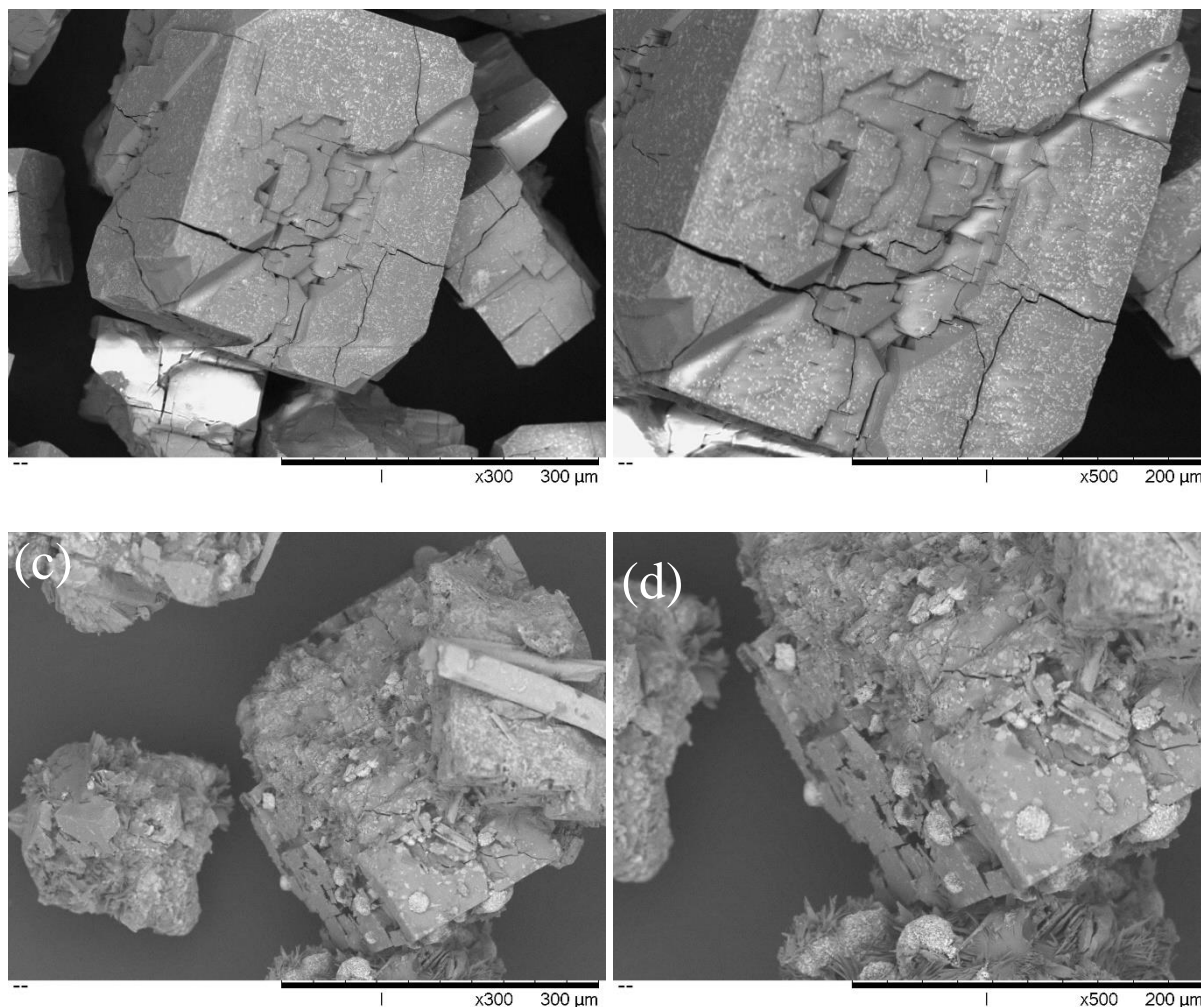


Fig 4.42: SEM images of monomer@MOF-5. (a,b) VAc@MOF-5 and (c,d)  $\epsilon$ CL@MOF-5.

As with all hard crystalline materials, MOFs tend to crack and deform under stress.<sup>48</sup> MOF-5 with adsorbed monomer shows visible appearance of cracks and fissures appearing on the MOF crystals. These cracks were consistent with all the monomer adsorbed and pre-polymerised samples indicating that upon adsorption of the monomer, the crystal is forced to expand as the micropores of the MOF are saturated with monomer and results in formation of cracks on the crystal. In the case of  $\epsilon$ CL@MOF-5, there is presence of surface species on the MOF crystal.  $\epsilon$ CL having a higher boiling point (b.p = 240 °C) and viscosity compared to

## **Chapter 4: Characterisation and Analysis**

---

VAc, does not vaporise at vacuum conditions and when electron beam is incident on the sample. As a result, surface species of extrinsic monomer can be observed on the crystal surface.

Additionally, white spots on the surface of the crystals appear that are otherwise not present in the MOF-5 without adsorbed monomer present. These are usually present because of organic molecules present on the surface of the material and appear due to desorption from the pores of the MOF upon excitation by the electron beam of the SEM.

## Chapter 4: Characterisation and Analysis

### 4.9.3 Polymer@MOF-5 composite

Polymer@MOF-5 samples were characterised by SEM as a composite with experimental loading of 0.4 g/g of MOF as a direct comparison to the monomer@MOF-5 samples and with an excess loading of 0.6 g/g of MOF to see the influence of excess monomer addition and polymerisation within the micropores of the MOF. (Fig 4.43)

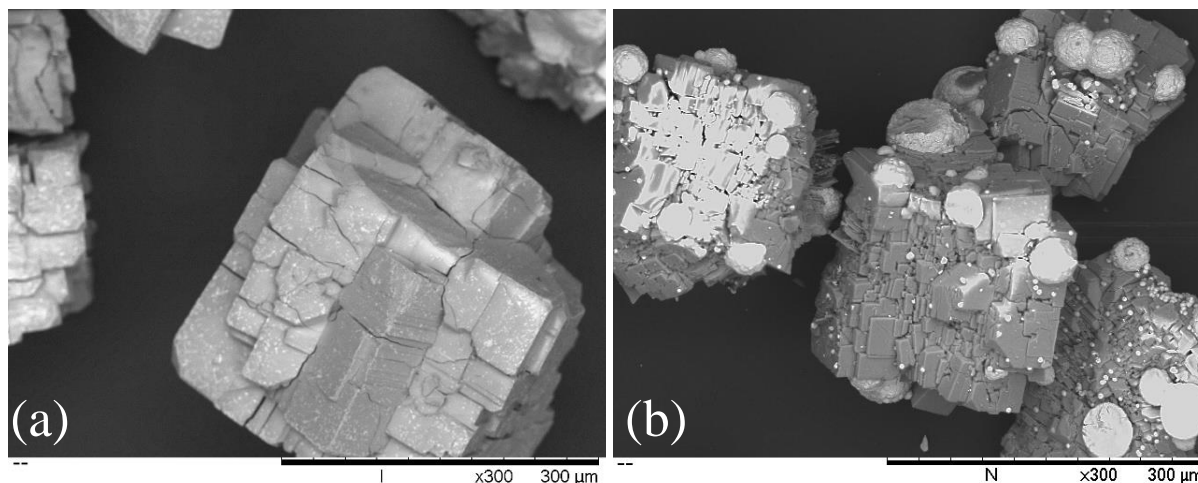


Fig 4.43: SEM images of polymer@MOF-5. (a) PVAc@MOF-5 at 0.4 g/g MOF loading, (b) PVAc@MOF-5 at an excess loading of 0.6g/g MOF.

For PVAc@MOF, Fig 4.43 shows that the samples have cracks and fissures that are seen in VAc@MOF-5 samples but the crevasse tend to have compressed as the structure of the MOF-5 retained its cubic shape with defined edges and surface. Visual representation of the MOF-5 crystals provides support to the experimental diffraction data that shows an increase in  $d$ -spacing for monomer@MOF, and the observations that the MOF structure contracts following polymerisation after it undergoes expansion as the monomer saturates the pores of MOF by a decrease in  $d$ -spacing compared to monomer@MOF. The contraction of the crystals is likely because of the polymer chains developing in the micropores of the MOF and reinforcing the crystalline structure.

## Chapter 4: Characterisation and Analysis

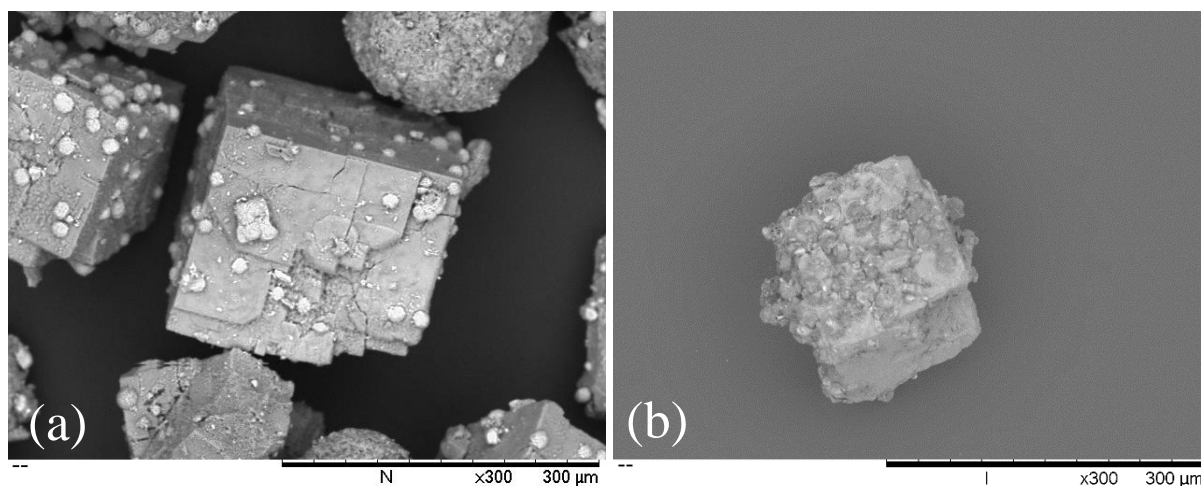


Fig 4.44: SEM images of polymer@MOF-5. (a) PCL@MOF-5 at 0.4 g/g MOF loading, (b) PCL@MOF-5 at an excess loading of 0.6g/g MOF

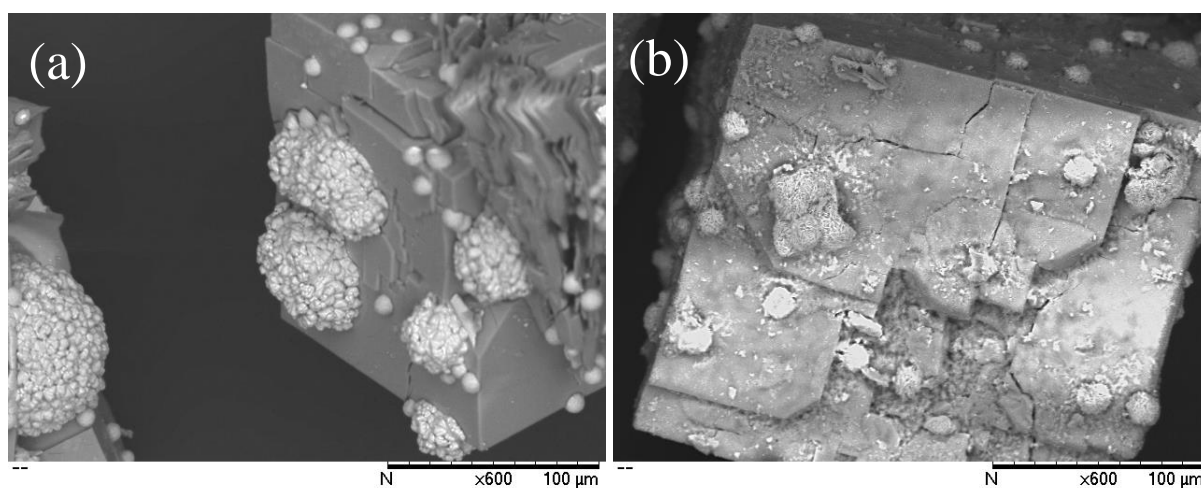


Fig 4.45: SEM images of polymer@MOF-5 protrusions on. (a) PVAc@MOF-5 and (b) PCL@MOF-5 at an excess loading of 0.6g/g MOF (Magnification – x600).

In the case of PCL@MOF-5, the shrinking of the crack width is also observed as with PVAc@MOF-5. The surface species seen with  $\epsilon$ CL@PCL are replaced by species with a bushy appearance that is likely due to polymer protruding out of the framework as the polymer chains grow and fill the pores of the MOF that eventually saturates the micropores and are forced out of the framework. (Fig 4.44)

## Chapter 4: Characterisation and Analysis

For structures with an excess loading of 0.6 g/g, the effect of polymer protrusions on the crystal surface are more prevalent than the experimental loading in the case of both PCL and PVAc (Fig 4.43, 4.44 and 4.45). PCL@MOF-5 composite protrusions resemble a bushy appearance that are fibrous in nature. On the other hand, the protrusions on PVAc@MOF-5 resemble globules of polymer with a smoother surface when compared to the fibrous nature of PCL@MOF-5. It is important to consider that nature of polymer synthesised from ex-situ polymerisation and reported morphology matches that observed with polymer protrusions.

### 4.9.4 HKUST-1

SEM images of HKUST-1 shows that the MOF has an octahedral shape with crystal diameter ranging from 8 to 10 nm (Fig 4.46).

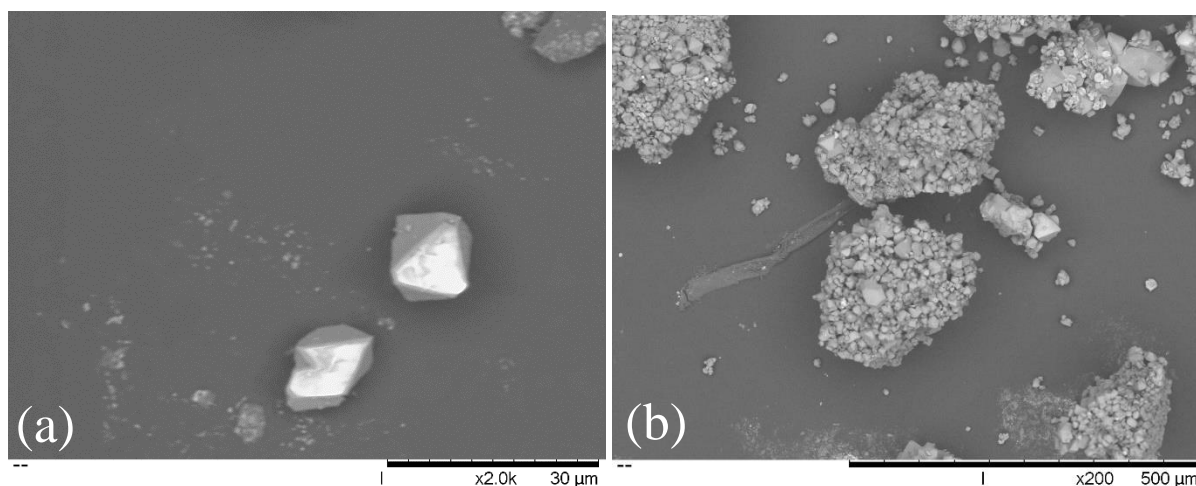


Fig 4.46: SEM images of crystalline HKUST-1. (a) Octahedral crystals of HKUST-1 (b) aggregated crystallites of HKUST-1 upon excess moisture adsorption.

The dimensions of the crystals are similar in size to reported in examples.<sup>37,46</sup> It was found that solvothermal synthesis at 100 °C with ethanol as reaction solvent gave the highest yield (83 %) and led to formation of octahedral crystals with defined edges whereas, earlier synthesis at 120 °C resulted in a more spherical shaped crystal with rounded edges. This observation is consistent with literature reported crystal morphology at elevated temperatures.<sup>47</sup>

## Chapter 4: Characterisation and Analysis

HKUST-1 is usually present as clusters of aggregated individual crystals. Adsorption of water molecules from ambient air causes crystal agglomeration.<sup>51</sup>

### 4.9.5 Monomer@HKUST-1 composite

SEM images were captured for monomer@MOF composites with the experimental loading of monomer equal to 0.45 g/g MOF. It can be observed that the aggregation of crystals is exaggerated than what was observed with as synthesised HKUST-1 crystals. This may be a result of electrostatic attraction between the individual crystals due to the presence of adsorbed monomer in the micropores of the MOF or wetting. (Fig 4.47)

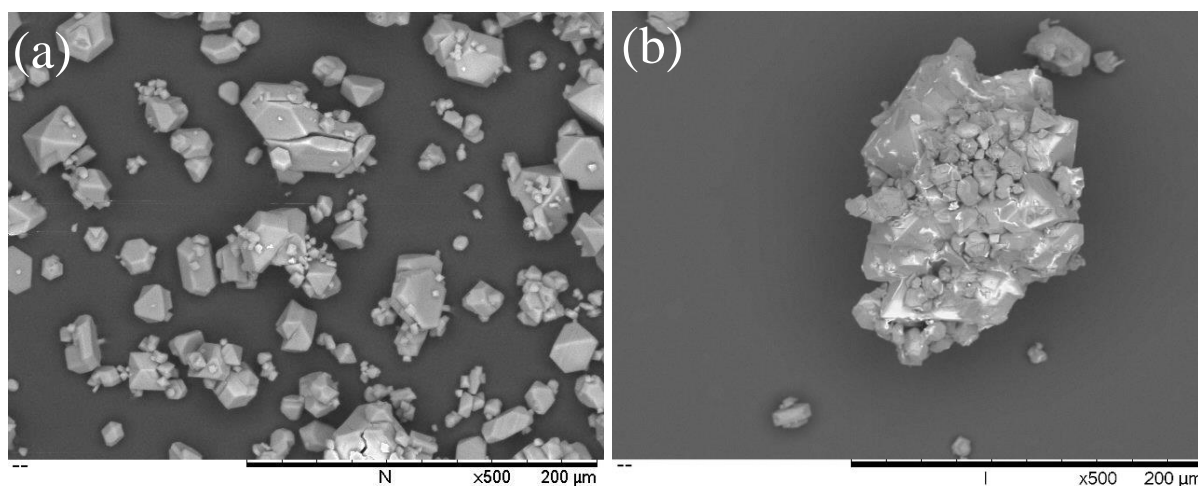


Fig 4.47: SEM images of monomer@HKUST-1. (a) VAc@HKUST-1, (b)  $\epsilon$ CL@HKUST-1.

As with the case of monomer@MOF-5 composites, white spots on the surface of the crystals appear that are otherwise not present on the as synthesised MOF due to the presence of organic molecules present on the surface of the material that appear due to desorption upon excitation by the electron beam of the SEM and the vacuum in the SEM chamber.

## Chapter 4: Characterisation and Analysis

### 4.9.6 Polymer@HKUST-1 composite

Fig 4.48 show SEM images of monomer@HKUST-1 composites. With polymer@MOF samples, the level of aggregation is lost and there are more individual crystals to be found in both PVAc@HKUST-1 and PCL@HKUST-1.

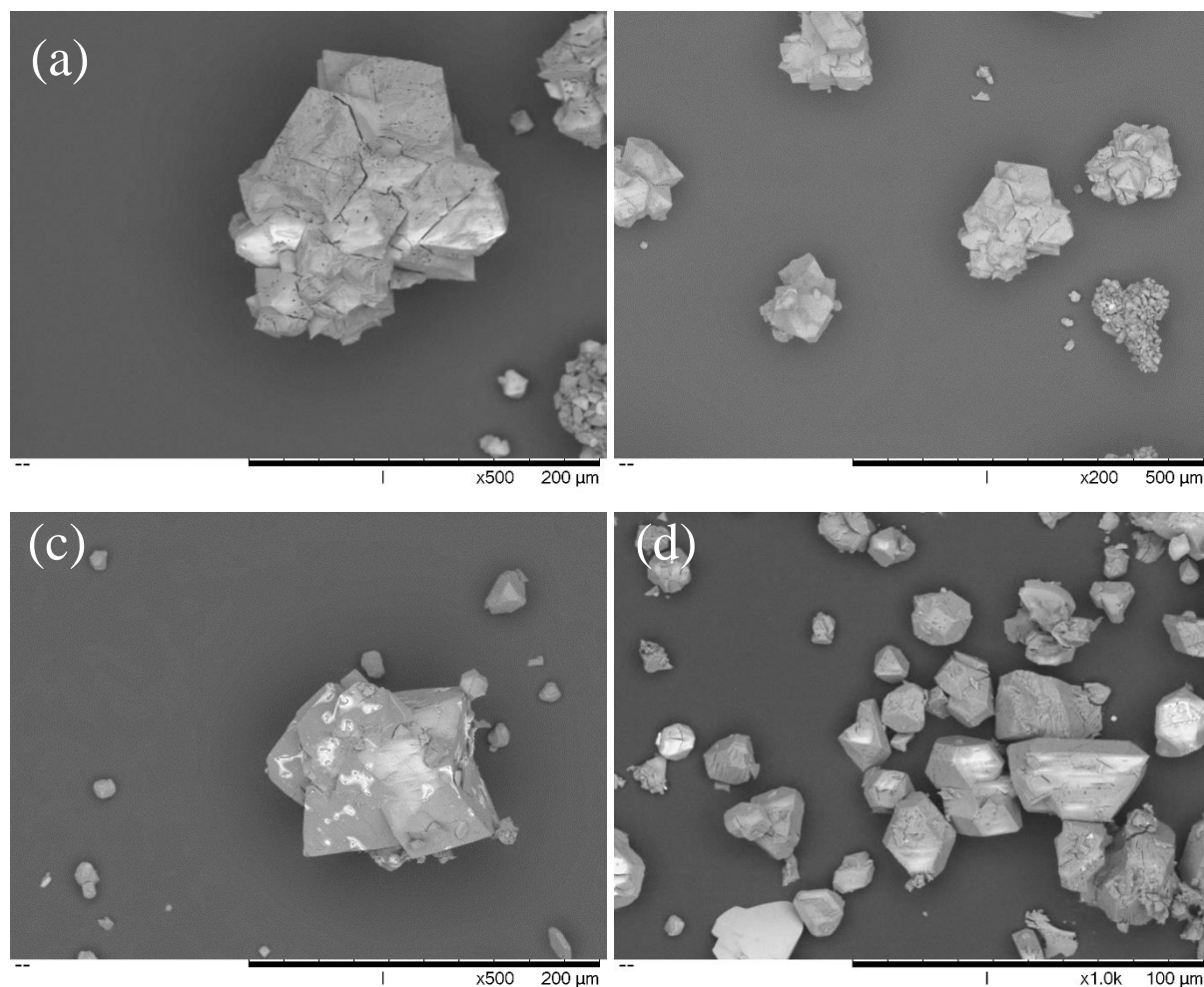


Fig 4.48: SEM images of in-situ polymerised monomer@HKUST-1. (a,b) PVAc@MOF-5 and (c,d) PCL@HKUST-1 at 0.4 g/g MOF loading.

The surface morphology of the HKUST-1 does not appear uniform in the SEM images and has lost its sharp and flat surfaces that were earlier observed with as synthesised HKUST-1. A likely cause for this change may be the in-situ polymerisation causing distortion in the crystal structure of the MOF, as seen in MOF-5. This effect is consistent with polymerisation of both VAc and  $\epsilon$ CL. It is to be noted that the structural changes in the MOF for HKUST-1 is observed in monomer@MOF and polymer@MOF samples through powder diffraction too.

## Chapter 4: Characterisation and Analysis

### 4.9.7 Isolated polymer

Polymer isolated by methods described in section 3.4, from MOF-5 and HKUST-1 were imaged under SEM to provide visual representation of isolated polymer by *in-situ* template polymerisation process (Fig 4.9). Literature reports polymers isolated from MOFs that were polymerised by the template approach to have a mesh-like network structure with large surface area that was otherwise difficult to achieve by solution polymerisation and other commonly used ex-situ polymerisation approaches.<sup>48-55</sup> However, there is a lack of evidence presented in the literature without surface area or imaging studies for homopolymers that have been isolated from MOF.

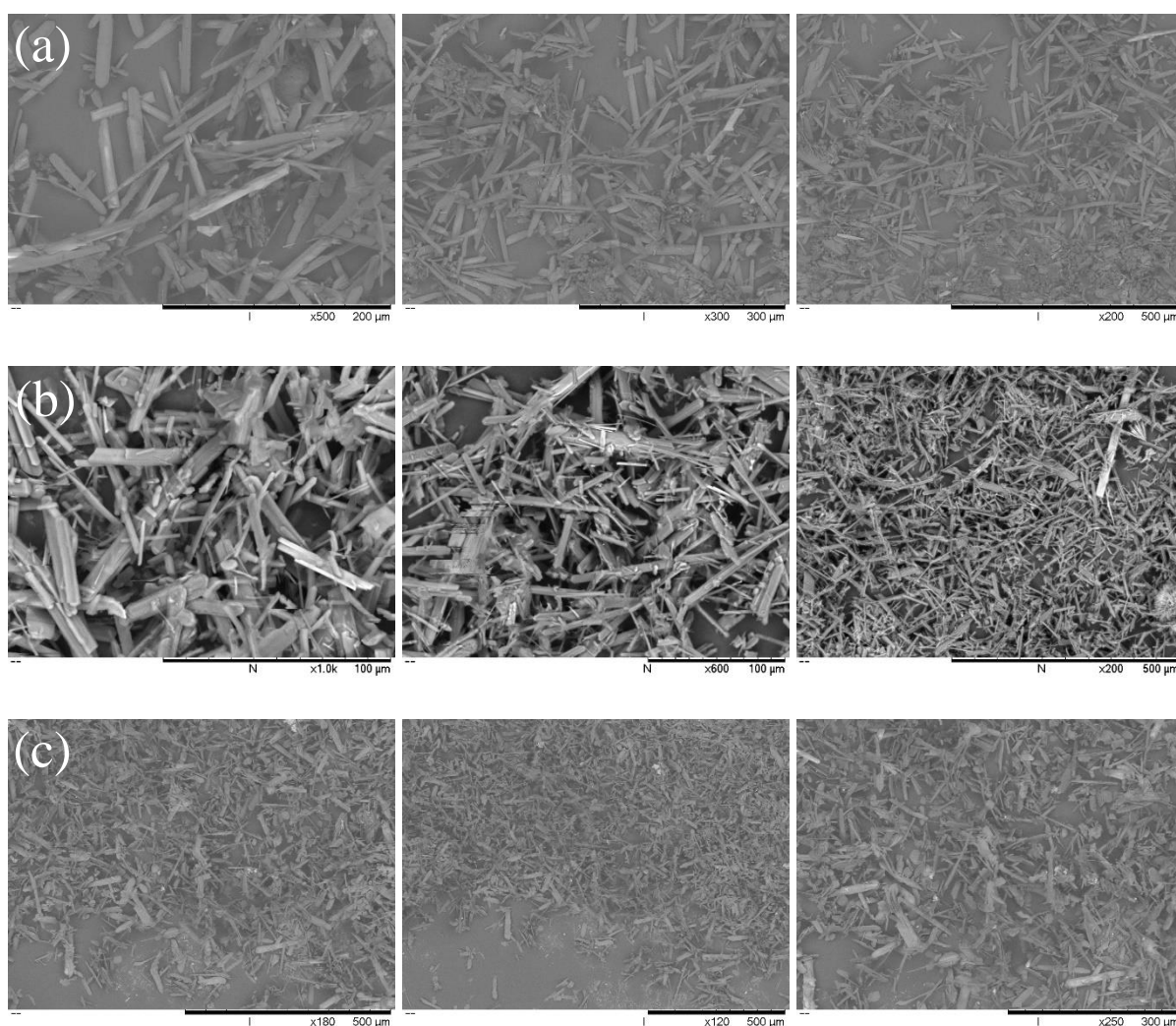


Fig 4.49: SEM images of (a) isolated PVAc from MOF-5, (b) isolated PCL from HKUST-1, (c) isolated PLAC from HKUST-1.

## Chapter 4: Characterisation and Analysis

---

SEM images of isolated polymer in our research conflicts this theory. Polymers isolated from the MOFs show a lack of definitive network-like structure. Instead, the isolated polymers represent miniature rods or sheets when seen under magnification of SEM. Dimensional analysis of the polymer reveals that the size distribution of the isolated polymer is similar to the size of MOF crystals (Fig 4.49). Whereas the polymerisation does successfully take place within the MOF pores replicating the shapes of the channels, it fails to form an intertwined or mesh-like structure as it has been reported.

It should be noted that dimensions of the isolated polymer rods are not an indication of pore dimensions. Upon isolation of the polymers, the polymer chains aggregate following drying and as a result, the dimension of different polymer 'rods' in the SEM images (Fig 4.49) appear non-uniform in size and dimensions.

Isolated PVAc from HKUST-1 and MOF-5 appears as sheets of polymers that collapse on top of each other upon isolation from the MOF. The isolated PCL does not form sheets as observed in the case of PVAc but resembles rod like fibres. PCL as a polymer is crystalline and ordered in nature and thus results in formation of such rod-like crystalline structures. The crystalline nature of isolated PCL is supported by PXRD analysis. As the polymerisation occurs, the polymers form with a rod-like like morphology of isolated polymers, as opposed to a mesh-like structure hypothesised in the literature.<sup>55</sup> This suggests a possibility that polymers form through the pores of the MOFs as rods, with each pore-channel having individual polymer propagation, but do not intertwine due to lack of chemical bonding between homopolymer chains that in other branching polymers could result in a covalently bonded mesh-like structure.

## Chapter 4: Characterisation and Analysis

---

### 4.10 Conclusions

In conclusion for characterisations performed on MOF and guest@MOF composites, we were able to determine structural changes on the host framework structure upon guest sorption and in-situ polymerisation of guest monomers. By comparing PXRD patterns of an-synthesised MOF with the monomer@MOF and polymer@MOF composites, we see the framework experiences stress effects in the presence of guests. Upon monomer adsorption, the framework experiences expansion of lattice, seen by an increase in  $d$ -spacing in the diffraction patterns. An opposite effect of decrease in  $d$ -spacing due to framework contraction is observed in the polymer@MOF composites following polymerisation of monomer. While this effect is consistent with both guest@HKUST-1 and guest@MOF-5, this effect is more prevalent in the case of guest@MOF-5, suggesting that the robust rigidity of MOF-5 widely reported in the literature may not be true.<sup>60,61</sup> Furthermore, in our PXRD studies with VAc@MOF-5, we see appearance of additional peak at  $2\theta = 8.9^\circ$  which may be due to guest coordination with the metal-node of MOF-5. It is possible that guest co-ordination also results in changes in framework lattice that results in framework distortion. To investigate the possible causes further, we performed neutron scattering experiments that will be discussed in the next chapter (Chapter 5).

Successful monomer conversion through in-situ polymerisation was determined by a range of characterisation methods. ATR-FTIR spectroscopy was used to determine the polymer conversion by observing characteristic monomer absorption band changes in the IR spectra. Changes in absorption bands of monomer upon polymerisation in MOF pores was consistent with both HKUST-1 and MOF-5. Furthermore, crystalline nature of PCL observed with PXRD patterns, was confirmed with FTIR by observing features unique to heterogeneous PCL with higher crystalline than amorphous nature.<sup>62</sup>

The amount of monomer adsorption was also determined by TG and DTG analysis. In the case of MOF-5, guest monomer uptake was found to be greater for  $\epsilon$ -CL ( $35 \pm 1$  % weight increase) compared to VAc ( $32 \pm 1$  % weight increase). This is possibly due to smaller molecular radius of  $\epsilon$ -CL compared to VAc. However, due to overlapping temperature regions for guest and framework decomposition, it is difficult to conclusively determine guest sorption in the case of  $\epsilon$ -CL composites. Presence of solvent DMF and atmospheric moisture

## Chapter 4: Characterisation and Analysis

---

was quantified in the case of MOF-5. Results suggest that even after activation of MOF to remove unbound solvent in the framework, the framework consists of an estimated  $3 (\pm 1)$  molecules of DMF and  $30 (\pm 5)$  molecules of water per unit cell that is not removed due to possible solvent interaction with the framework.

The monomer conversion to polymer was determined by  $^1\text{H}$  and  $^{13}\text{C}$  NMR spectroscopy. Structural properties and end-group analysis was also performed on the isolated polymers from the MOF. Characteristic PVAc polymer peaks were identified, and  $68 \pm 2\%$  and  $64 \pm 2\%$  of the loaded monomer was converted to polymer in MOF-5 and HKUST-1, respectively. In the case of PCL, the percentage conversion was determined to be  $59 \pm 2\%$  and  $65 \pm 2\%$  for PCL in MOF-5 and HKUST-1, respectively. TGA calculations for PCL@MOF-5 suggest a higher conversion. However, TGA is less reliable in the case of  $\epsilon$ -CL and PCL due to overlapping thermal degradation regions of host and guest. Consequently, further experiments to determine polymer conversion by solid-state NMR (Chapter 5) were performed and confirm the reliability of  $^1\text{H}$  NMR over TGA.  $^{13}\text{C}$ -NMR experiments were not performed on isolated polymer from MOF-5 due to insolubility in common NMR solvents. Ex-situ polymerised PCL was soluble, and used to provide reference data. We found by ICP-AES analysis that the reason for this is possibly due to high presence of metal complex in the polymer.

With SEM images of guest@MOF composites, we were able to visualise the structural deformation upon monomer adsorption for monomer@MOF composites, and contraction of the framework following polymerisation in polymer@MOF composites as the polymer chains in the pores of the MOF reinforce the structure. Images of isolated polymers from MOFs have not been previously reported, and to our best knowledge, this is the first-time polymers synthesised by templated approach have been visualised with SEM. It is hypothesised in the literature that with templated polymerisation approach, control over polymer morphology can be achieved and a three-dimensional polymer network is achievable. However, our observations suggest that the polymer chains form one dimensional structures, as opposed to a three dimensional polymer network hypothesised in reported studies for other linear polymers.<sup>63,64</sup>

## **Chapter 4: Characterisation and Analysis**

---

In conclusion, we have determined structural changes on MOF in presence of guests in MOF pores by PXRD and SEM. Additionally, monomer conversion and polymerisation has been quantified through complementary technique. Work presented in this chapter provides a basis for further studies for guest interactions and influence of guest on host structure that is presented in the next chapter.

## Chapter 4: Characterisation and Analysis

---

### 4.11 References

- 1 Y. Ming, J. Purewal, J. Yang, C. Xu, R. Soltis, J. Warner, M. Veenstra, M. Gaab, U. Müller and D. J. Siegel, *Langmuir*, 2015, **31**, 4988–4995.
- 2 T. Mueller and G. Ceder, *Journ. of Phys. Chem. B*, 2005, **109**, 17974–17983.
- 3 J. Hafizovic, M. Bjørgen, U. Olsbye, P. D. C. Dietzel, S. Bordiga, C. Prestipino, C. Lamberti and K. P. Lillerud, *J. Am. Chem. Soc.*, 2007, **129**, 3612–3620.
- 4 C. K. Brozek, V. K. Michaelis, T. C. Ong, L. Bellarosa, N. López, R. G. Griffin and M. Dincă, *ACS Cent. Sci.*, 2015, **1**, 252–260.
- 5 B. Chen, X. Wang, Q. Zhang, X. Xi, J. Cai, H. Qi, S. Shi, J. Wang, D. Yuan and M. Fang, *J. Mat. Chem.*, 2010, **20**, 3758–3767.
- 6 M. Eddaoudi, J. Kim, N. Rosi, D. Vodak, J. Wachter, M. O. Keefe, O. M. Yaghi, M. Eddaoudi, J. Kimrn, N. Rosi and O. M. Yaghil, *Science*, 2002, **295**, 469–472.
- 7 M. D. Allendorf, M. E. Foster, F. Léonard, V. Stavila, P. L. Feng, F. P. Doty, K. Leong, E. Y. Ma, S. R. Johnston and A. A. Talin, *J. Phys. Chem. Lett.*, 2015, **6**, 1182–1195.
- 8 T. Uemura, Y. Ono, K. Kitagawa and S. Kitagawa, *Macromolecules*, 2008, **41**, 87–94.
- 9 Z. Jian and W. Hejing, *Chin. J. Geochem.*, 2003, **22**, 38–44.
- 10 C. Baptista, A. Azagury, H. Shin, C. M. Baker, E. Ly, R. Lee and E. Mathiowitz, *Polymer*, 2020, **191**, 122227.
- 11 T. Ab. Saleh and V. K. Gupta, *Nanomaterial and Polymer Membranes - 1st Edition*, Elsevier, 2016, vol. 1.
- 12 Z. Q. Li, L. G. Qiu, T. Xu, Y. Wu, W. Wang, Z. Y. Wu and X. Jiang, *Mater. Lett.*, 2009, **63**, 78–80.
- 13 Y. Feng, H. Jiang, S. Li, J. Wang, X. Jing, Y. Wang and M. Chen, *Colloids Surf, A. Physicochem. Eng. Asp.*, 2013, **431**, 87–92.
- 14 K. Schlichte, T. Kratzke and S. Kaskel, *Micro. Meso. Mat.*, 2004, **73**, 81–88.
- 15 N. Iswarya, M. G. Kumar, K. S. Rajan and R. J. B. Balaguru, *A. Journ. Sci. Res.*, 2012, **5**, 247–254.
- 16 Y. Ming, N. Kumar and D. J. Siegel, *ACS Omega*, 2017, **2**, 4921–4928.
- 17 O. M. Yaghi, M. J. Kalmutzki and C. S. Diercks, *Introduction to Reticular Chemistry*, 2019.
- 18 J. Lee, O. K. Farha, J. Roberts, K. A. Scheidt, S. T. Nguyen and J. T. Hupp, *Chem. Soc. Rev.*, 2009, **38**, 1450–1459.
- 19 R. Sabouni, H. Kazemian and S. Rohani, *Chem. Eng. J.*, 2010, **165**, 966–973.
- 20 G. Socrates, *Infrared and Raman Characteristic Group Frequencies: Tables and Charts, 3rd Edition / Wiley*, Wiley, 3rd edn., 2004.
- 21 F. Rindfleisch, T. P. DiNoia and M. A. McHugh, *J. Phys. Chem.*, 1996, **100**, 15581–15587.
- 22 A. Kaoukabi, F. Guillen, H. Qayouh, A. Bouyahya, S. Balieu, L. Belachemi, G. Gouhier and M. Lahcini, *Ind. Crops. Prod.*, 2015, **72**, 16–23.

## Chapter 4: Characterisation and Analysis

---

- 23 M. Labet and W. Thielemans, *Chem. Soc. Rev.*, 2009, **38**, 3484–3504.
- 24 K. Phillipson, J. N. Hay and M. J. Jenkins, *Thermochim. Acta*, 2014, **595**, 74–82.
- 25 K. S. Lin, A. K. Adhikari, C. N. Ku, C. L. Chiang and H. Kuo, *Int. J. Hydrog. Energy*, 2012, **37**, 13865–13871.
- 26 W. W. Lestari, M. Adreane, C. Purnawan, H. Fansuri, N. Widiastuti and S. B. Rahardjo, *Mater. Sci. Eng.*, 2015, **107**, 012030.
- 27 C. M. Brown, Y. Liu, T. Yildirim, V. K. Peterson and C. J. Kepert, *Nanotechnology*, 2009, **20**, 204025.
- 28 S. Bordiga, L. Regli, F. Bonino, E. Groppo, C. Lamberti, B. Xiao, P. S. Wheatley, R. E. Morris and A. Zecchina, *Phys. Chem. Chem. Phys.*, 2007, **9**, 2676–2685.
- 29 R. P. D’Amelia, S. Gentile, W. F. Nirode and L. Huang, *W. Journ. Chem. Edu.*, Vol. 4, 2016, Pages 25-31, 2016, **4**, 25–31.
- 30 S. Wang, X. Xie, W. Xia, J. Cui, S. Zhang and X. Du, *High Temp. Mater. Process.*, 2020, **39**, 171–177.
- 31 G. Srinivas, V. Krungleviciute, Z. X. Guo and T. Yildirim, *Energy Environ. Sci.*, 2014, **7**, 335–342.
- 32 S. J. Yang, T. Kim, J. H. Im, Y. S. Kim, K. Lee, H. Jung and C. R. Park, *Chem. Mat.*, 2012, **24**, 464–470.
- 33 A. B. Davis, F. R. Fronczek and K. J. Wallace, *Acta Crystallographica Section E: Cryst. Comm.*, 2016, **72**, 1032–1036.
- 34 D. J. Tranchemontagne, J. L. Tranchemontagne, M. O’Keeffe and O. M. Yaghi, *Chem. Soc. Rev.*, 2009, **38**, 1257–1283.
- 35 W. Zhou, H. Wu, T. Yildirim, J. R. Simpson and A. R. H. Walker, *Phys. Rev. B Condens. Matter*, 2008, **78**, 054114.
- 36 Y. H. Hu and L. Zhang, *Phys. Rev. B Condens. Matter*, 2010, **81**, 174103.
- 37 H. W. B. Teo, A. Chakraborty and S. Kayal, *Appl. Therm. Eng.*, 2017, **110**, 891–900.
- 38 K.-S. Lin, A. K. Adhikari, C.-N. Ku, C.-L. Chiang and H. Kuo, *Int. J. Hydrog. Energy*, 2012, **37**, 13865–13871.
- 39 S. S. Y. Chui, S. M. F. Lo, J. P. H. Charmant, a G. Orpen and I. D. Williams, *Science*, 1999, **283**, 1148–1150.
- 40 S. L. Campello, G. Gentil, S. A. Júnior, W. M. de Azevedo, Q. Min Wang, D. Shen, M. Bulow, M. Ling Lau, S. Deng, F. R. Fitch, N. O. Lemcoff, J. Semanscin, P. Chowdhury, C. Bikkina, D. Meister, F. Dreisbach, S. Gumma, M. R. Armstrong, S. Senthilnathan, C. J. Balzer, B. Shan, L. Chen, B. Mu, F. Wang, H. Guo, Y. Chai, Y. Li and C. Liu, *Micro. Meso. Mat.*, 2002, **117**, 365–370.
- 41 K. Schlichte, T. Kratzke and S. Kaskel, *Micro. Meso. Mat.*, 2004, **73**, 81–88.
- 42 F. Gul-E-Noor, M. Mendt, D. Michel, A. Pöppel, H. Krautscheid, J. Haase and M. Bertmer, *J. Phys. Chem. C.*, 2013, **117**, 7703–7712.
- 43 L. Han, M. Budge and P. Alex Greaney, *Comput. Matter. Sci.*, 2014, **94**, 292–297.

## Chapter 4: Characterisation and Analysis

---

- 44 Y. Chen, X. Mu, E. Lester and T. Wu, *Prog. Nat. Sci.*, 2018, **28**, 584-589.
- 45 S. S. Nadar, L. Vaidya, S. Maurya and V. K. Rathod, *Coord. Chem. Rev.*, 2019, **396**, 1–21.
- 46 K. K. Gangu, S. Maddila, S. B. Mukkamala and S. B. Jonnalagadda, *Inorg. Chim. Acta*, 2016, **446**, 61–74.
- 47 Z. Wang, L. Ge, M. Li, R. Lin, H. Wang and Z. Zhu, *Chem. Eng. J.*, 2019, **357**, 320–327.
- 48 J. T. Hughes and A. Navrotsky, *J. Am. Chem. Soc.*, 2011, **133**, 9184–9187.
- 49 Q. Chen, Q. W. Chen, C. Zhuang, P. P. Tang, N. Lin and L. Q. Wei, *Inorg. Chem. Commun.*, 2017, **79**, 78–81.
- 50 E. Biemmi, S. Christian, N. Stock and T. Bein, *Micro. Meso. Matt.*, 2009, **117**, 111–117.
- 51 T. Wang, H. Zhu, Q. Zeng and D. Liu, *Adv. Mater. Interfaces*, 2019, **6**, 1900423.
- 52 T. Uemura, T. Kaseda, Y. Sasaki, M. Inukai, T. Toriyama, A. Takahara, H. Jinnai and S. Kitagawa, *Nature Comm.*, 2015, **6**, 1–8.
- 53 M.-L. Hu, M. Y. Masoomi and A. Morsali, *Coord. Chem. Rev.*, 2019, **387**, 415–435.
- 54 T. Uemura, Y. Kadowaki, N. Yanai and S. Kitagawa, *Chem. Mater.*, 2009, **21**, 4096–4098.
- 55 N. Hosono, S. Mochizuki, Y. Hayashi and T. Uemura, *Nature Comm.*, 2020, **11**, 3573.
- 56 X. Guo, S. Geng, M. Zhuo, Y. Chen, M. J. Zaworotko, P. Cheng and Z. Zhang, *Coord. Chem. Rev.*, 2019, **391**, 44–68.
- 57 T. Uemura, T. Kaseda and S. Kitagawa, *Chem. Mater.*, 2013, **25**, 3772–3776.
- 58 S. Begum, Z. Hassan, S. Bräse, C. Wöll and M. Tsotsalas, *Acc. Chem. Res.* 2019, **52**, **6**, 1598–1610.
- 59 Y. Kobayashi, K. Honjo, S. Kitagawa and T. Uemura, *ACS Appl. Mat. Int.*, 2017, **9**, 11373–11379.
- 60 D. N. Dybtsev, H. Chun and K. Kim, *Angew. Chem. Int. Ed.*, 2004, **43**, 5033–5036.
- 61 A. Bajpai, P. Chandrasekhar, S. Govardhan, R. Banerjee and J. N. Moorthy, *Chem. Eur.*, 2015, **21**, 2759–2765.
- 62 Q. Lv, D. Wu, H. Xie, S. Peng, Y. Chen and C. Xu, *RSC Advances*, 2016, **6**, 37721–37730.
- 63 T. Kitao and T. Uemura, *Chem. Lett.*, 2020, **49**, 624–632.
- 64 B. Le Ouay and T. Uemura, *Isr. J. Chem.*, 2018, **58**, 995–1009.
- 65 L. Qin, Y. Zhou, D. Li, L. Zhang, Z. Zhao, Z. Zuhra, and C. Mu, *Ind. Eng. Chem. Res.*, 2016, **55**, **27**, 7249–725
- 66 R. D’Amelia, S. Gentile, W.. F. Nirode, and L. Huang, *World J. Chem. Educ.*, 2016, **4**, **2**, 25-31.

# Chapter 5

---

Characterisation of Guest  
Interactions in VAc@MOF-5

## Chapter 5: Characterisation of Guest interactions in VAc@MOF-5

---

### Introduction

This chapter will briefly discuss the theory and characterisation results of the MOF and guest@MOF composites by means of neutron scattering experiments conducted at the ISIS Neutron and Muon Source facility at Rutherford Appleton Laboratories, Harwell on the Near and InterMediate Range Order Diffractometer (NIMROD) instrument and the IRIS spectrometer at ISIS Neutron and Muon Source (Oxfordshire, UK). *Solid-state* NMR spectroscopy and *single-crystal* XRD results are also discussed in the chapter.

NIMROD utilises small and wide-angle arrays of ZnS-based neutron scintillation detectors covering a wide range of solid angle from  $2\theta = 0.5$  to  $40^\circ$ . The instrument is designed to measure the differential scattering cross-section and total structure factor  $F(Q)$  of a liquid or structurally disordered system. The primary aim of the instrument is to correlate the short-range structure on interatomic and intermolecular length scales with nanoscale structures as the radial distribution function  $g(r)$  is usually not the most ideal function to illustrate the  $r$ -space correlation. It is expressed instead in terms of the pair correlation function  $G(r)$ .<sup>1</sup> This function considers long range correlation based on the length scale on which they occur, without masking the short-range structure. The total scattering structure factor  $F(Q)$  and pair distribution function  $G(r)$  are described as:

$$F(Q) = \sum_{i,j=1}^n c_i c_j b_i b_j [A_{ij}(Q) - 1] \quad (5.1)$$

And

$$G(r) = \sum_{i,j=1}^n c_i c_j b_i b_j [g_{ij}(r) - 1] \quad (5.2)$$

Where  $c$  is the proportion of species  $i$  and  $j$  in the material,  $b$  is the coherent bound neutron scattering length of species  $i$  and  $j$ , averaged over their nuclear spin states.  $A_{ij}(Q)$  and  $g_{ij}(r)$  are the Faber-Ziman partial structure factor and partial radial distribution function, respectively.<sup>2</sup> Consequently,  $F(Q)$  and  $G(r)$  are related to each other by Eq. 5.3 and Eq 5.4.

## Chapter 5: Characterisation of Guest interactions in VAc@MOF-5

---

$$F(Q) = \rho_0 \int_0^\infty 4\pi r^2 G(r) \frac{\sin Qr}{Qr} dr \quad (5.3)$$

$$G(r) = \frac{1}{(2\pi)^3 \rho_0} \int_0^\infty 4\pi r Q^2 F(Q) \frac{\sin Qr}{Qr} dQ \quad (5.4)$$

The NIMROD instrument has been used to study the structure of liquids and disordered solids on a continuous length scale, correlating interatomic and intermolecular length scales. There have been studies investigating liquids,<sup>3</sup> surfactant micelles,<sup>4</sup> biomolecules in solution where the intrinsic size of small proteins is matched into nanoscale capabilities of the instrument.<sup>5</sup> Confined liquid in crystalline substances such as monomer in crystalline microporous MOF in our case have also been studied.<sup>6,7</sup> Here, the phase behaviour of liquids can be modified to allow the investigation of structural changes that are induced by the guest in host crystal.

Investigations of guest sorbent molecules in MOFs by total neutron scattering (TNS) have been used to determine the MOF and guest–MOF lattice parameters and structures. The diffraction data of the empty framework can be analysed by Rietveld methods,<sup>8</sup> and compared with MD model developed to examine guest–MOF system with Fourier difference methods to produce nuclear-density maps that can directly identify the location of guest entities.<sup>9</sup> Furthermore, guest binding mechanisms can be obtained, and structural changes induced by the guest on MOF such as unit cell expansion or contraction can be investigated by total neutron scattering (TNS).<sup>10,11</sup>

TNS has been employed to investigate guest adsorption and binding sites and to visualise interactions between MOF and guest molecules but has been limited to small gas molecules such as CO<sub>2</sub>, O<sub>2</sub>, H<sub>2</sub>, and H<sub>2</sub>O.<sup>12–14</sup> Smaller hydrocarbons such as methane, acetylene, propane and propylene, and small organic molecules such as dimethylformamide have been investigated.<sup>15–17</sup> However, to the best of our knowledge investigations of larger liquid monomer molecules through TNS have not been reported in the literature. Our experiment at NIMROD investigating binding interactions of liquid monomer molecules confined within

## **Chapter 5: Characterisation of Guest interactions in VAc@MOF-5**

---

MOF pores, and guest induced structural effects on the MOF through total neutron scattering remains a standalone study at the time of writing this thesis.

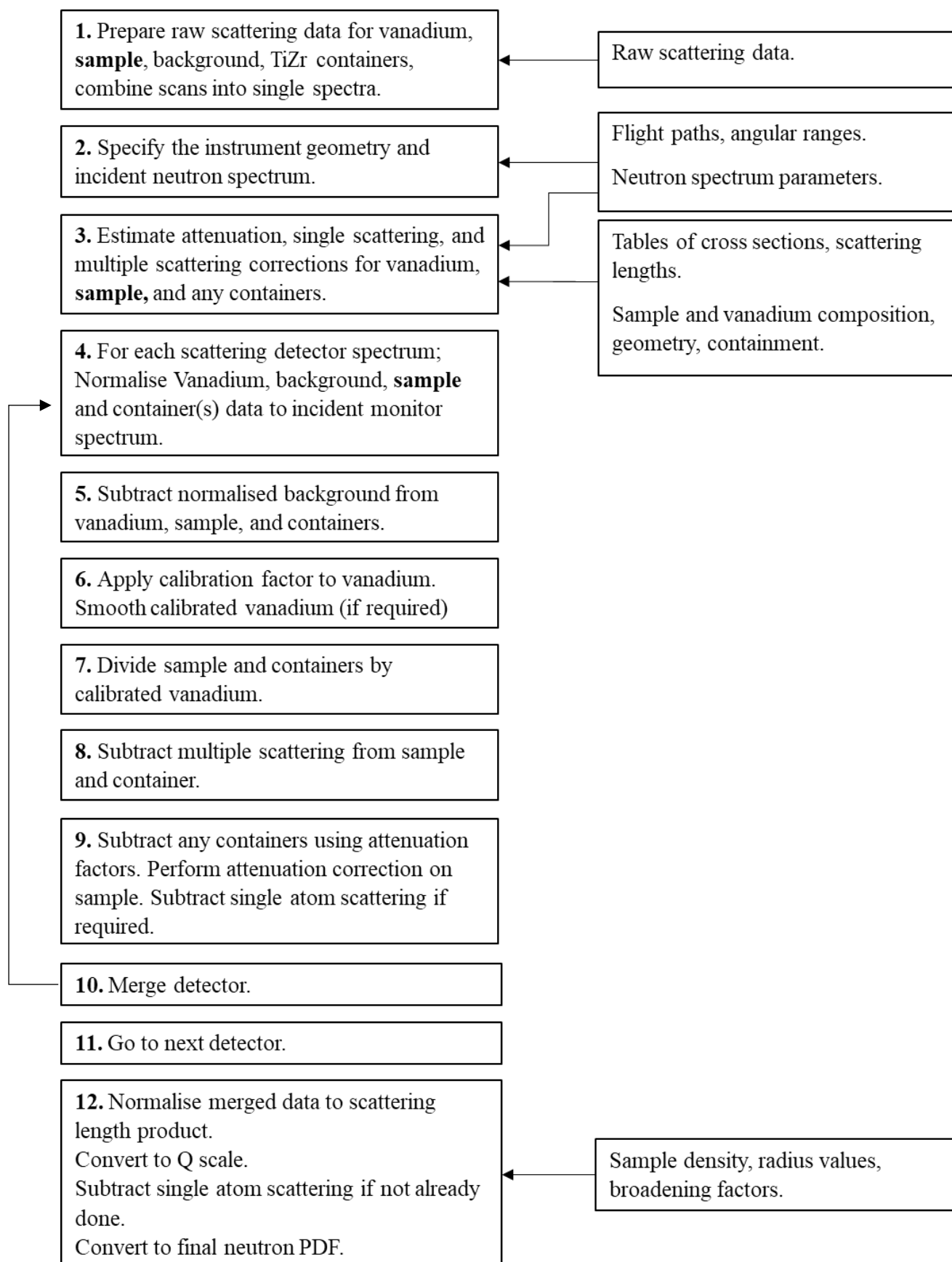
### **5.1 Total Neutron Scattering: Experimental Analysis (NIMROD)**

To process the data, the Gudrun package was employed for reducing total scattering data.<sup>18</sup> Gudrun removes instrument and sample backgrounds, performs sample attenuation and multiple scattering corrections, and places the data on an absolute scale by normalising it against a referencing sample, in this case a VNb alloy.<sup>19</sup> It also enables systematic reduction of inelasticity effects that arise from presence of light elements such as hydrogen.

#### **5.1.1 Diffraction Data Analysis**

The basic method and steps in data analysis followed are illustrated in Scheme 5.1 and described in detail in Appendix A5.1. The primary aim of data collection is to extract the scattering cross-section of the sample. Further details with steps involved in data processing can be found on the software packages website.<sup>18</sup>

## Chapter 5: Characterisation of Guest interactions in VAc@MOF-5



Scheme 5.1: Steps in scattering data analysis with Gudrun for reducing total scattering data.<sup>19</sup>

## Chapter 5: Characterisation of Guest interactions in VAc@MOF-5

### 5.1.2 Calculations on MOF-5 Crystallographic Unit.

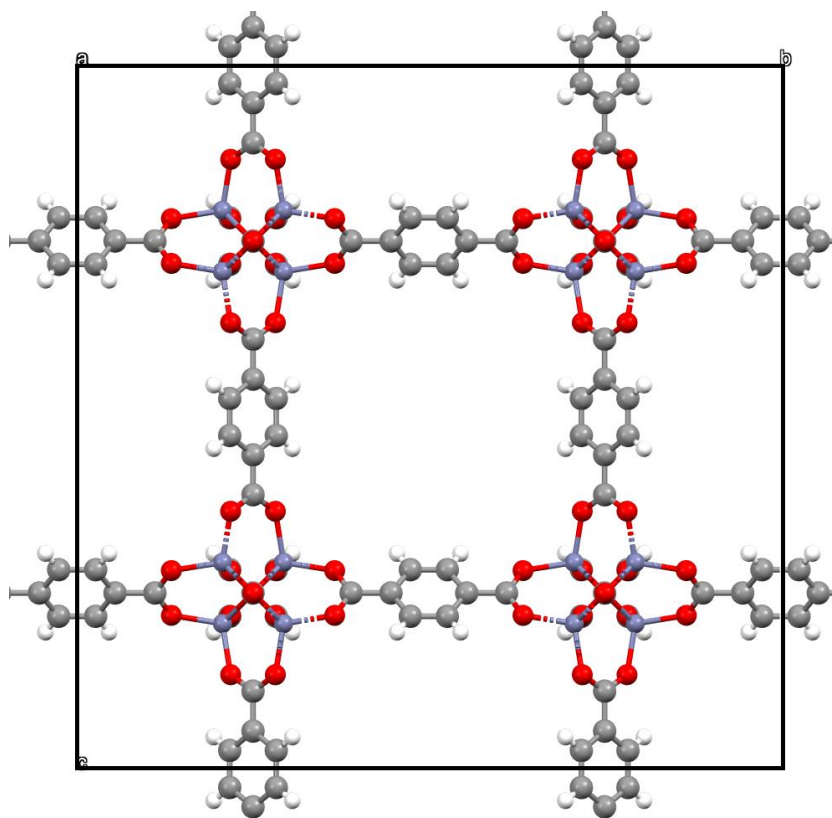


Fig 5.1: Crystallographic MOF-5 unit cell. Only the atoms within the dotted blue line have been shown and considered to be in the unit cell, full linkers have been shown to aid visual representation.

All calculations in Gudrun were performed on a MOF-5 crystallographic unit cell of an atomic composition consisting of 424 framework atoms [ $\text{Zn}_{32}\text{O}_{104}\text{C}_{192}\text{H}_{96}$ ] and is shown in Fig 5.1. As MOF-5 is a crystalline powder rather than a liquid, the data was corrected for the packing fraction of the crystal, considering the porosity of the framework using the '*tweak factor*' feature in Gudrun (Appendix A5.1), which effectively is the inverse of packing fraction.

A secondary complication arising from the MOF sample is the presence of residual solvent and adsorbed atmospheric moisture. The addition of DMF and water as solvent into the expected composition was performed to match the expected scattering levels determined with Gudrun to the mass of MOF-5 present in sample container, considering the packing fraction.

## Chapter 5: Characterisation of Guest interactions in VAc@MOF-5

---

The calculations consider presence of 30 water molecules [ $\text{H}_{60}\text{O}_{30}$ ] and 3 DMF molecules [ $\text{C}_9\text{H}_{21}\text{N}_3\text{O}_3$ ] based on calculations from the TGA data (Section 4.4.1). The density of the unit cell under consideration was calculated to be  $0.64049 \text{ g/cm}^3$  and  $0.0326 \text{ atoms/\AA}^3$ .

### 5.2 Investigation of Vinyl Acetate Binding and Interaction in MOF-5

Interaction and binding of vinyl acetate monomer molecules within MOF-5's crystal structure was investigated by TNS at Near and InterMediate Range Order Diffractometer (NIMROD) instrument at ISIS neutron and muon source, STFC. (*Experiment number RB1920428*)

#### 5.2.1 Materials and Sample Preparation

The synthesis for the MOF-5, H/D-MOF-5 and D-MOF-5 have been described in section 3.2.2. Deuterated  $d_4$ -vinyl acetate was sourced from QMX Laboratories Ltd, UK. Equimolar hydrogenated-deuterated vinyl acetate mixture was made by mixing equal volumes of vinyl acetate (Merck, 99%) and  $d_4$ -vinyl acetate.

Individual MOF samples were activated to remove residual solvent and minimise adsorbed moisture by heating in glass vials, in a vacuum oven at  $80 \text{ }^\circ\text{C}$  for 12 h. The vials containing the samples were sealed following activation of MOF to prevent moisture adsorption. The MOFs were loaded to flat-plate TiZr cell containers in a vacuum glove box under argon (Ar). Sample details are provided in Table 5.1.

## Chapter 5: Characterisation of Guest interactions in VAc@MOF-5

---

Table 5.1: Details of container and mass content of MOF in each container. (\* - H/D-MOF is 1:1 physical mixture of deuterated and hydrogenated reactants. Synthesis is described in section 3.2.2.3)

Container	MOF-5 Isotopologue	Container Path Length (mm)	Added Mass of MOF (g)
Cell A	H	2	1.492
Cell B	D	1	0.973
Cell C	D	1	1.197
Cell D	D	1	1.041
Cell E	H/D*	2	1.730
Cell H	H/D*	1	0.753
Cell G	H	2	1.493

## Chapter 5: Characterisation of Guest interactions in VAc@MOF-5

### 5.2.2 Monomer Addition

Vinyl acetate monomer was transferred into the cell container with MOF by vapour deposition (initial experiment) and liquid deposition (second experiment).

#### 5.2.2.1 Vapour Deposition Method

Vapour deposition method used the vacuum evaporation principle to transfer monomer onto the sample container with MOF-5. Monomer was transferred by generating vacuum in the transfer line, allowing monomer to vaporise by flash evaporation, which then is transferred to the sample container containing MOF. (Fig 5.2)

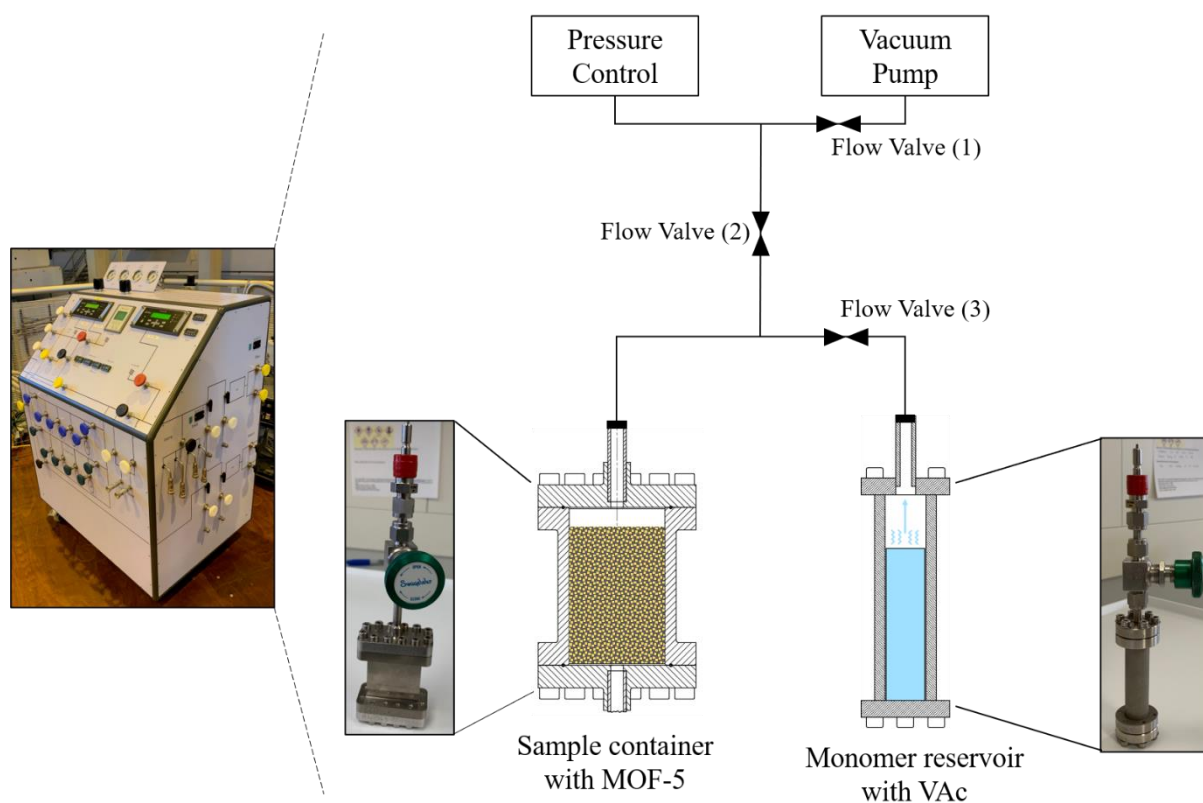


Fig 5.2: Schematic diagram of monomer addition by vapour deposition method. (Insets – Photographic image of cell container, monomer reservoir, and vacuum operated–vapour deposition system.)

## **Chapter 5: Characterisation of Guest interactions in VAc@MOF-5**

---

Negative pressure in the line is generated by a turbo vacuum pump which vaporises the monomer. When then the system is in vacuum state, the flow valve (2) is shut to the line and flow valve (3) is opened resulting in the vapourised monomer is transferred to the sample container with MOF-5 allowing dispersion of monomer over the MOF.

However, vapour deposition method resulted in majority of the monomer condensing at the top portion of the sample cell as the monomer vapours expanded from the inlet nozzle of the sample container and upon contact with the MOF. Consequently, the MOF crystals at the top were saturated with the monomer. On the other hand, crystals at a greater depth of the cell remained free of any interaction with monomer. This was evident on removing the samples which had been polymerised in-situ for potential experiment investigating binding and interaction of guests following polymerisation. Samples on removal from sample container were 'wet' and texturally resembling a paste at the top, possibly due to polymerisation of the monomer. MOF below  $\leq 1.5$  cm resembled dry MOF sample.

Additionally, this method gave evidence of some sample contamination from prior experiments and resulted in the loss of large quantities of monomer. As a result, the experiment was repeated using liquid adsorption method.

## Chapter 5: Characterisation of Guest interactions in VAc@MOF-5

### 5.2.2.2 Liquid Deposition Method – Monomer Addition

Monomer was transferred to the vacuum sealed container by using a syringe with outer diameter identical to the internal diameter of ‘port A’ (Fig 5.3). The syringe filled with predetermined volume of monomer was placed on the port A and ensure the syringe was sealed and locked in place. Once the tight seal was ensured, the Swagelok on the vacuum sealed container was opened such the vacuum pulled the monomer into the cell. Upon complete transfer of the monomer in the cell, the Swagelok was shut once again to allow the cell to remain under vacuum before removing the empty syringe from the top. The cell was then tested on the vacuum line to check for any leaks before running the deposition process.

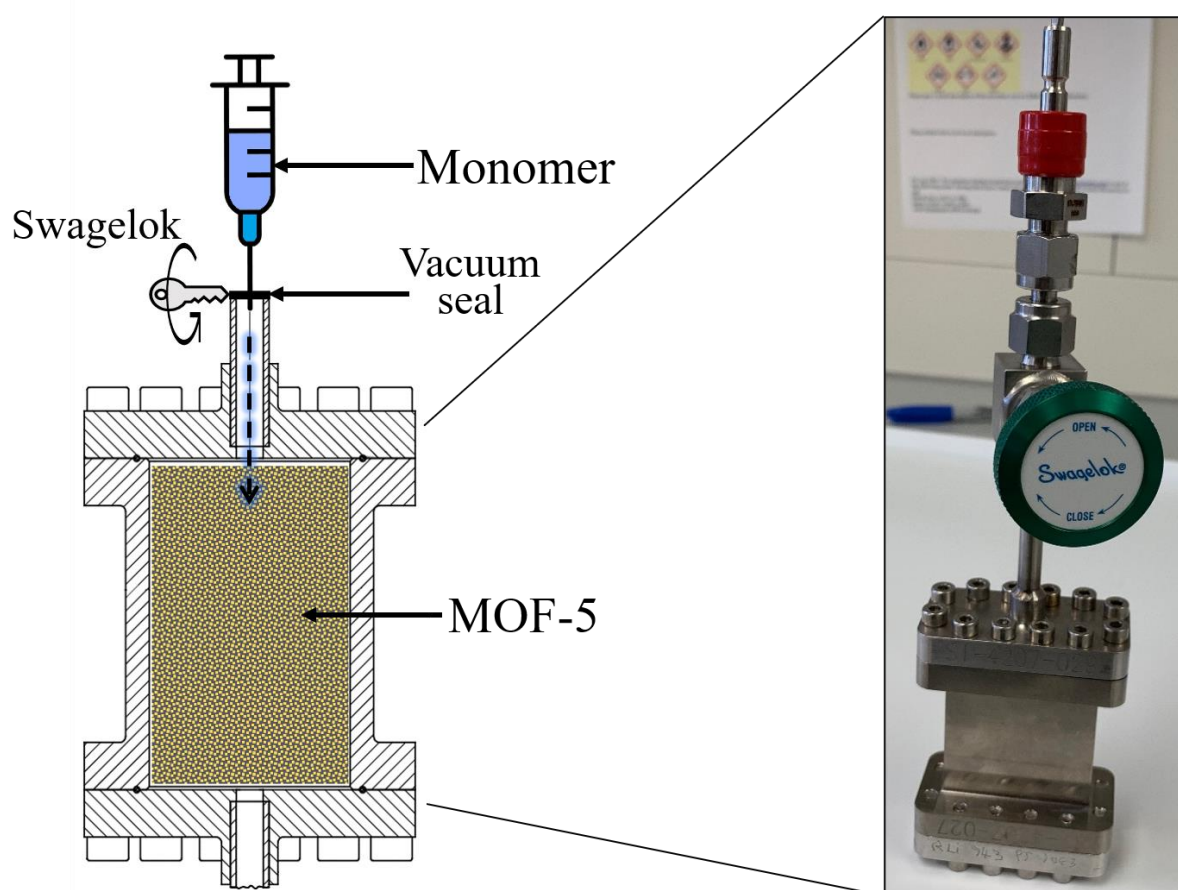


Fig 5.3: (a) Schematic diagram of monomer addition by liquid deposition method. (b) Photographic image of cell container with Swagelok and air-tight vacuum seal.

## **Chapter 5: Characterisation of Guest interactions in VAc@MOF-5**

---

The amount of monomer required was determined based on experiment at Cardiff University to determine optimum monomer adsorption by MOF-5 without excess extrinsic monomer present on the surface of MOF (Section 4.4.4.1). Following addition of monomer, it was allowed to equilibrate and the increment in mass of the cell was recorded to determine the exact mass of the monomer added.

## **Chapter 5: Characterisation of Guest interactions in VAc@MOF-5**

---

### **5.3 Results and Discussion**

The data analysis for total neutron scattering is a continuing work in progress. This is the first study attempting to interpret TNS data from NIMROD by simulation-based methods for confined fluids in MOFs. Due to time constraints and the lengthy process of simulating complex system, and delays caused by COVID-19 pandemic, the data analysis remains unfinished at the time of submission of thesis, but much has been learnt on how to deal with complex materials.

#### **5.3.1 Calculation of number of guest molecules.**

In order to calculate the number of guest molecules added to each sample container holding the sample MOF-5, two approaches were devised to calculate the appropriate amount of guest molecules. The first calculation approach was based on the physical mass of monomer added to the sample containing MOF taking the increase in weight upon monomer addition to calculate the number of monomers in the system. The second approach was based on approximation based on the expected scattering levels and packing fraction approximations from Gudrun. In this case, the number of monomer molecules calculated from the first approach were used as input parameter and matched with the expected calculations for scattering by Gudrun, and the number was increased or decreased appropriately.

## Chapter 5: Characterisation of Guest interactions in VAc@MOF-5

Table 5.2: Comparison of calculated number of molecules of monomer per unit cell of MOF-5 in each sample container. (50/50-Monomer is an equimolar sample of hydrogenated and deuterated monomer prepared by physical mixing)

Monomer Addition	Calculated based on isotopic mass.	Calculated from Gudrun.
Cell A (h-Monomer@H-MOF)	40	39
Cell B (d-Monomer@D-MOF)	28	27
Cell C (h-Monomer@D-MOF)	56	67
Cell D (50/50-Monomer@H-MOF)	32	38
Cell E (d-Monomer@H/D-MOF)	49	82
Cell G (50/50-Monomer@H/D-MOF)	49	59
Cell H (d-Monomer@H-MOF)	47	44

The number of molecules calculated from both approaches match within a tolerance of  $\pm 10$  molecules for sample containers A, B, C, D, H and G. However, cell E showed to have considerably large number based on Gudrun calculations compared to the isotopic mass calculations and it remained uncertain as to why this might be the case. However, considering a reasonable average DCS levels (br/atoms/sr) and tweak factor between empty MOF and monomer@MOF samples, the decision was made to accept the number of monomer molecules calculated from Gudrun as the basis for further calculations.

### 5.3.2 Modelling of Experimental Data

The simulations and modelling were performed using *Dissolve*, a software for simulation for total scattering data based on the refinement of structure by the generation of empirical potentials.<sup>20</sup> *Dissolve* allows investigation of microporous materials with variable pore size and partially filled porous systems, such as guest@MOF systems. Additionally, it is also possible to account for the additional solvent molecules embedded in the guest@MOF using *Dissolve*. The program also permits potential refinement on multiple compositions, or completely different systems that share common force field parameters.

## Chapter 5: Characterisation of Guest interactions in VAc@MOF-5

*Dissolve* software was developed by Dr Tristan Youngs at ISIS Pulsed Neutron and Muon Source, RAL (Oxfordshire, UK). Creation and implementation of MOF-5 simulation box, and structural refinement were performed by Calum Green (STFC Liquid Structure Simulation Placement Student, Imperial College London) under supervision of Dr Thomas Headen (ISIS Pulsed Neutron and Muon Source, RAL, Oxfordshire, UK).

### 5.3.2.1 Calculation of Bragg Peaks on *Dissolve*

*Dissolve* calculates the Bragg peak intensities separately from the local, diffuse scattering. The Bragg scattering amplitude is calculated using the Eq. 5.5:

$$B(hkl) = \sum_j b_j \exp[-2\pi i(hx_j + ky_j + lz_j)] \quad (5.5)$$

Where, the sum is over all the atoms in the simulation box,  $b_j$  is the scattering length of atom  $j$ ,  $(hkl)$  are the standard Miller indices and  $(x_j, y_j, z_j)$  are the fractional coordinates of the  $j$ th atom along the **a**, **b**, and **c** lattice vectors.<sup>21,22</sup>

Bragg reflections occur at discrete  $Q$  values:

$$Q_{hkl} = h\mathbf{a}^* + k\mathbf{b}^* + l\mathbf{c}^* \quad (5.6)$$

Where **a\***, **b\***, **c\*** are the reciprocal lattice vectors. Hence, to calculate Bragg intensities on the same scale as total scattering structure factor, *Dissolve* calculates the total structure factor by the following equation:

$$S_{Bragg,int}(Q) = \frac{\sum_{hkl} I_{tot}^P(Q, Q_{hkl}) - \sum_j b_j^2}{N_s (\sum_{\alpha} c_{\alpha} \langle b_{\alpha} \rangle)^2} \quad (5.7)$$

## Chapter 5: Characterisation of Guest interactions in VAc@MOF-5

---

Where  $N_s$  is the number of atoms in the simulation box,  $P$  is the three-dimensional Lorentzian broadening function, and  $I_{tot}$  is the total measured intensity. Each interaction between pairs of atoms in the sample is denoted to a partial structure factor  $S_{ij}(Q)$ , and these are weighted by the concentration  $c_i$ ,  $c_j$  and scattering lengths  $b_i$ ,  $b_j$  for atoms  $i$  and  $j$ . These are expressed as the sum of all correlations with Kronecker delta  $\delta_{nm}$  used to prevent double counting atomic pair terms.

$$F(Q) = \sum_{i,j \geq j} (2 - \delta_{ij}) c_i c_j b_i b_j S_{ij}(Q) \quad (5.8)$$

Eq. 5.8 details the total structure factor  $F(Q)$  obtained in the neutron scattering experiment. The differential cross section is measured as a function of magnitude of the momentum vector  $Q$ . This contains contributions from both single atom scattering and correlation between atom pairs

### 5.3.2.2 Calculations for $G(r)$

For monomer@MOF, a set of pair distribution functions were calculated as per the standard definition of  $G(r)$ , with limiting values  $g(r \rightarrow 0)$  and  $g(r \rightarrow \infty) = 1$ . For all distances above 6 Å, all PDF show a less intense peaks resembling liquid-like order. To compare the experimental neutron scattering data, the partial  $g(r)$  functions are combined to give a modification of Eq. 5.2 (Chapter 5 – Introduction) as:

$$G(r) = 4\pi\rho \sum_{m,n} c_m c_n b_m b_n d_{mn}(r) \quad (5.9)$$

In equation 5.9,  $m$  and  $n$  represent two atomic species,  $c_m$  is the atomic fraction of species  $m$ ,  $b_m$  is the coherent neutron scattering length for atomic species  $m$ . ( $b^H = -3.74$  barns,  $b^D = 6.67$  barns,  $b^C = 6.46$  barns). Calculated  $F(Q)$  and  $G(r)$  are related by Eq 5.3 and Eq 5.4 (Chapter 5 – Introduction).

## Chapter 5: Characterisation of Guest interactions in VAc@MOF-5

---

The oscillations at higher  $r$  are enhanced in the case of deuterated samples compared to the hydrogenated samples. This is because in the case of higher D concentrations, the C–H/D contribution in  $G(r)$  is similar in values to that of constant C–C contribution ( $b^D = 6.67$  barns,  $b^C = 6.46$  barns in Eq. 5.2). For higher H concentration, the contribution of C–H/D in total  $D(r)$  is the opposite to that of the C–C contribution ( $b^H = -3.74$  barns,  $b^C = 6.46$  barns in Eq. 5.2). In all cases, the H/D–H/D contribution is negligible for a perfect null composition. As the long-range  $r$  oscillations are present in each partial PDF, the effect of changing the H/D ratio is to go from the case where all three PDFs have positive weighting to the case where the C–H PDF has a negative weighting and in effect, the combination of the amplitude of the oscillations are diminished. This is a controlling factor when calculating the experimental scattering function and comparing experimental to simulated data.<sup>23</sup>

### 5.3.2.3 Implementing Forcefield on Dissolve.

Structural refinement of scattering data within the realms of a classical forcefield is performed on Dissolve with provision for common harmonic bond and angle potentials as well as several functions for torsional terms but with allowance for additional functions and inter-molecular terms.

For simulations for this experiment, a Universal ForceField (UFF) was implemented. The use of a general forcefield allows large and flexible monomer molecules to be accurately treated for molecular dynamics simulations in the structural refinement procedure. MOF-5 is classified under UFF4MOF atom types when implementing UFF and was used for all the simulations on Dissolve.<sup>24</sup> Forcefields for vinyl acetate monomer, water, and DMF were acquired and implemented from LigParGen OPLS/CM1A parameter generator for organic ligands database.<sup>25,26</sup>

## Chapter 5: Characterisation of Guest interactions in VAc@MOF-5

### 5.3.2.4 Building MOF-5 simulation box.

The configuration for MOF-5 used in this work contains 3,392 framework atoms (2x2x2 cubic cell). For empty MOF, simulations were carried out with solvent 3 DMF and 30 water molecules, contributing to additional 96 and 90 atoms, respectively. Fig 5.4 presents a snapshot of the simulation box for empty MOF and Fig 5.5 presents the equivalent for monomer@MOF.

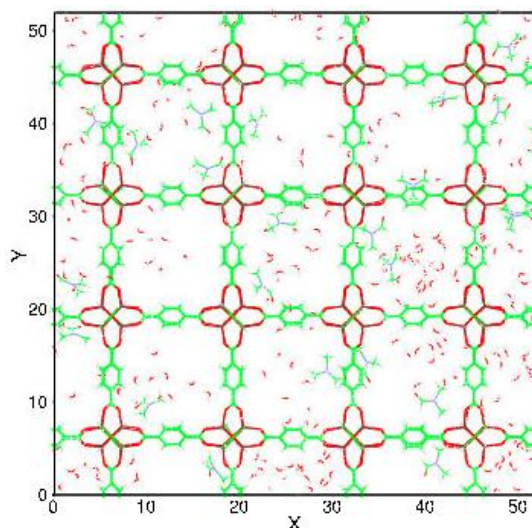


Fig 5.4: Atomic structure of crystalline MOF-5 from simulation environment in Dissolve for empty MOF with solvent DMF and water.

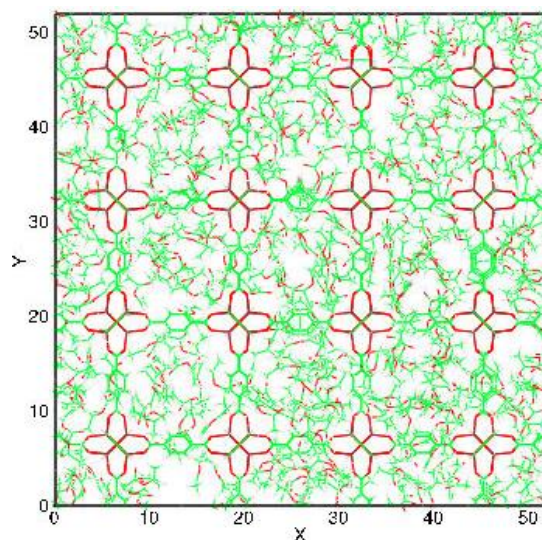


Fig 5.5: Atomic structure of crystalline MOF-5 from simulation environment in Dissolve for monomer@MOF without solvent (shown here is the h-monomer@H-MOF-5 sample with 414 monomer molecules per simulation box or 52 molecules/unit MOF cell loading before simulation)

## Chapter 5: Characterisation of Guest interactions in VAc@MOF-5

---

Simulations for monomer@MOF were performed with presence of the calculated monomer molecules for each sample contrast but in absence of guest molecules. This decision was made based on evidence from QENS (Section 5.5), solid-state NMR (Section 5.7) and SCXRD data (Section 5.9.2) which suggest that the monomer displaces DMF and water molecules from the MOF pores. The simulations were performed at a temperature of 300 K, mean configuration edge length was 51.95 Å, and the number average density of 0.0314 atoms/Å<sup>3</sup>.

### 5.3.2.5 General Atomistic Simulations

The atomistic simulations were performed with the help of core modules on Dissolve. MolShake performs whole-molecule Monte Carlo (MC) simulations and attempts a random MC translational and/or rotational move on every vinyl acetate molecule in the system. *MD* module performs NVT molecular dynamics on the specified species which are restricted to MOF and vinyl acetate for every 5 steps of molecular dynamics. *RDF* module calculates the inter- and intramolecular radial distribution function,  $G(r)$  and total  $G(r)$  out of the cubic box length. *Energy* module calculates the total system energy that arises from interatomic and intermolecular terms.<sup>27</sup>

## Chapter 5: Characterisation of Guest interactions in VAc@MOF-5

### 5.3.3 H- and D-MOF-5

The diffraction patterns for H-MOF-5 and D-MOF-5 were obtained from experimental samples as an output from Dissolve. The patterns are consistent with the space group cubic,  $Fm-3m$ , observed with powder XRD (Section 4.2).

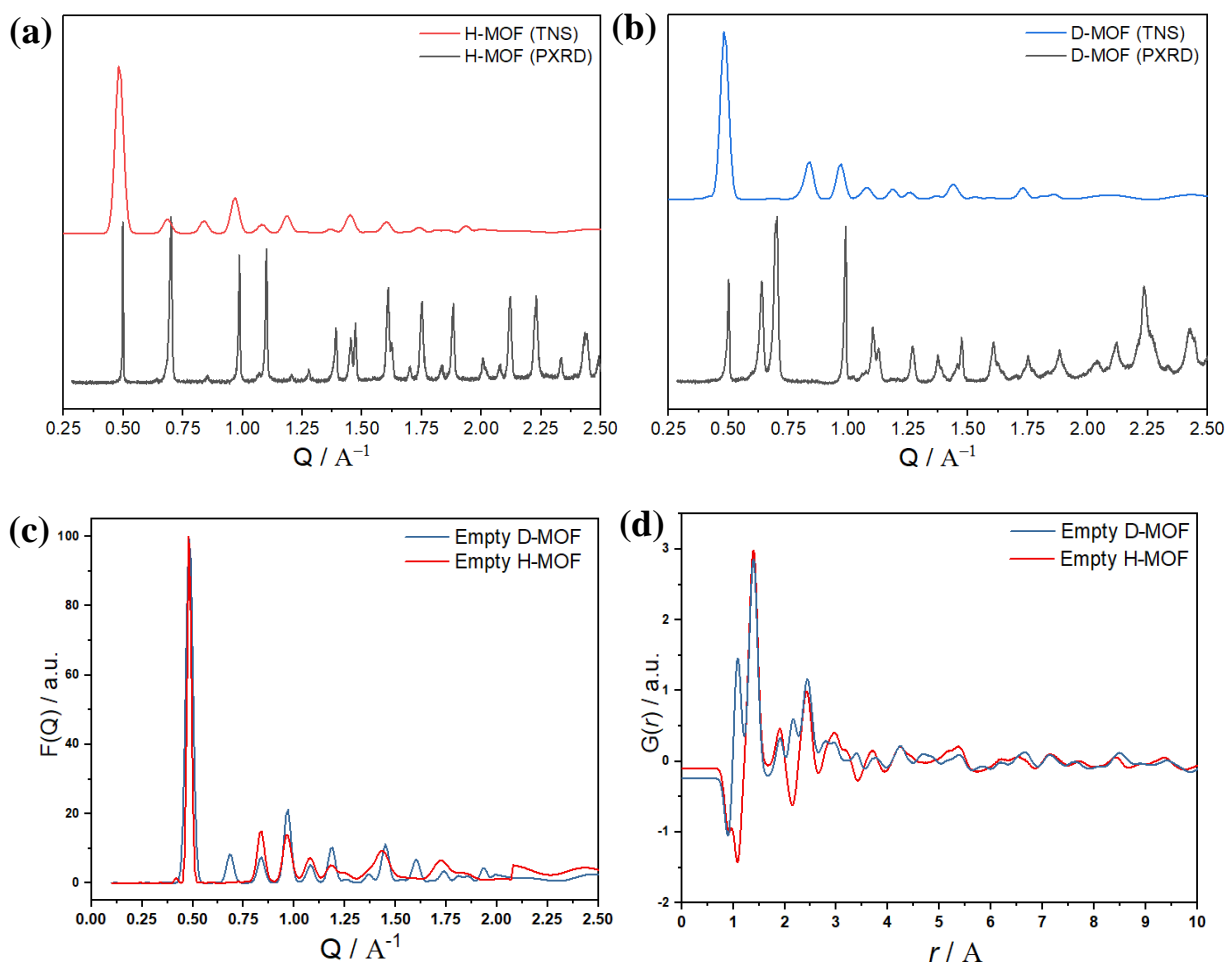


Fig 5.6: Comparison of powder XRD and TNS patterns for (a) H-MOF-5 and (b) D-MOF-5. (c) total structure factor  $F(Q)$  and (d) total pair distribution function  $G(r)$  for H- and D-MOF.

Fig 5.6 shows a comparison between powder XRD patterns and TNS (TNS) patterns from the scattering data from H- and D-MOF-5. As expected,  $F(Q)$  show sharp and well-defined peaks at lower  $Q$  from the crystalline MOF (Fig 5.4 (a)). The peaks can be associated with Bragg reflections observed by powder XRD to reciprocal space (Table 5.3).

## Chapter 5: Characterisation of Guest interactions in VAc@MOF-5

Table 5.3: Comparison of Bragg reflections observed through PXRD and TNS.

Bragg reflection observed in TNS ( $Q = \text{\AA}^{-1}$ )	Corresponding diffraction peak observed in PXRD ( $2\theta = ^\circ$ )	Miller Plane (hkl)
0.46	6.9	(200)
0.68	9.8	(220)
0.83	-	-
0.95	13.67	(400)
1.07	15.50	(420)
1.18	16.81	(440)
1.36	19.48	(531)
1.44	20.49	(442)
1.60	22.83	(533)

Fig 5.4(a) shows the characteristic Bragg peaks in the powder XRD data also appear as peaks in TNS (TNS) data for H-MOF-5. Fig 5.4 (b) shows a comparison between powder XRD and TNS patterns for the D-MOF. It is seen from both Fig (b) and (c), that of the D-MOF there is an additional peak in the  $F(Q)$  scattering data at  $Q = 0.42 \text{ \AA}^{-1}$  ( $2\theta = 5.9^\circ$ ) that does not appear in powder XRD data of H-MOF. Subsequent SCXRD analysis suggests that a peak at such diffraction angle may appear due to co-ordination from guest species present in the guest@MOF composites. As there is no guest monomer species present in the empty D-MOF, our working assumption during data analysis was that the peak at  $Q = 0.42 \text{ \AA}^{-1}$  ( $2\theta = 5.9^\circ$ ) is present due to solvent DMF coordination within the framework. A possible reason for this peak appearing only in D-MOF may be due to amplified coherent scattering effects from deuterium. Deuterium has a larger scattering cross-section ( $\sigma_{\text{coh}} = 5.56$  barns) compared to hydrogen ( $\sigma_{\text{coh}} = 1.76$  barns), and as a result, the relative intensity of the peak for hydrogenated DMF@D-MOF may be greater than the intensity observed with hydrogenated DMF@H-MOF.

In the  $G(r)$  comparison in Fig 5.5 (d) for H- and D-MOF, the first negative peak in both MOFs is observed at  $r = 0.88 \text{ \AA}$ . This peak may possibly be due to the presence of O–H from water or DMF interactions within the MOF framework. This is consistent with the earlier observed presence in the neutron diffraction samples from Gudrun (Section 5.1.2) and in

## Chapter 5: Characterisation of Guest interactions in VAc@MOF-5

---

$F(Q)$ . The next peak is observed at  $r = 1.09 \text{ \AA}$  as a negative peak for H-MOF and a positive peak for D-MOF, as expected to be from respective C–H and C–D due to a negative coherent scattering length of hydrogen ( $^H\sigma_{\text{coh}} = -3.74$ ,  $^D\sigma_{\text{coh}} = 6.67$ ). Another characteristic MOF-5 feature is observed at  $1.91 \text{ \AA}$  from framework Zn–O at distances  $> 2.0 \text{ \AA}$ .

### 5.3.4 Data Analysis: Monomer@MOF

Creation and implementation of monomer@MOF-5 simulation box, and structural refinement were performed on the empty MOF-5 simulation box created by Calum Green (STFC Liquid Structure Simulation Placement Student, Imperial College London) on Dissolve. Monomer molecules were added to the simulation box from calculations from Gudrun described in Section 5.3.1. All processing and changes with the simulation box were made with guidance from Dr Tristan Youngs and Dr Thomas Headen (Disordered Materials Group, ISIS Pulsed Neutron and Muon Source, RAL, Oxfordshire, UK).

All calculations shown here are performed in absence of DMF and water molecules as guest, and only vinyl acetate as guest species, unless stated otherwise. Forcefields parameters for vinyl acetate were acquired and implemented from LigParGen OPLS/CM1 and imported in Dissolve.<sup>25</sup> Depending on the number of monomers calculated for each sample (Section 3.5.1), appropriate number of monomers for the simulation box were added to determine  $F(Q)$  and  $G(r)$ . A separate simulation for each sample was performed and the results and observations are described below.

## Chapter 5: Characterisation of Guest interactions in VAc@MOF-5

### Hydrogenated monomer@MOF

The following section will discuss observations from total structure factor  $F(Q)$  and total pair distribution function  $G(r)$  for h-VAc@H-MOF and h-VAc@D-MOF.

#### 5.3.4.1 h-VAc@H-MOF

The calculated experimental and simulated  $F(Q)$  and  $G(r)$  for h-VAc@H-MOF are shown in Fig 5.7.

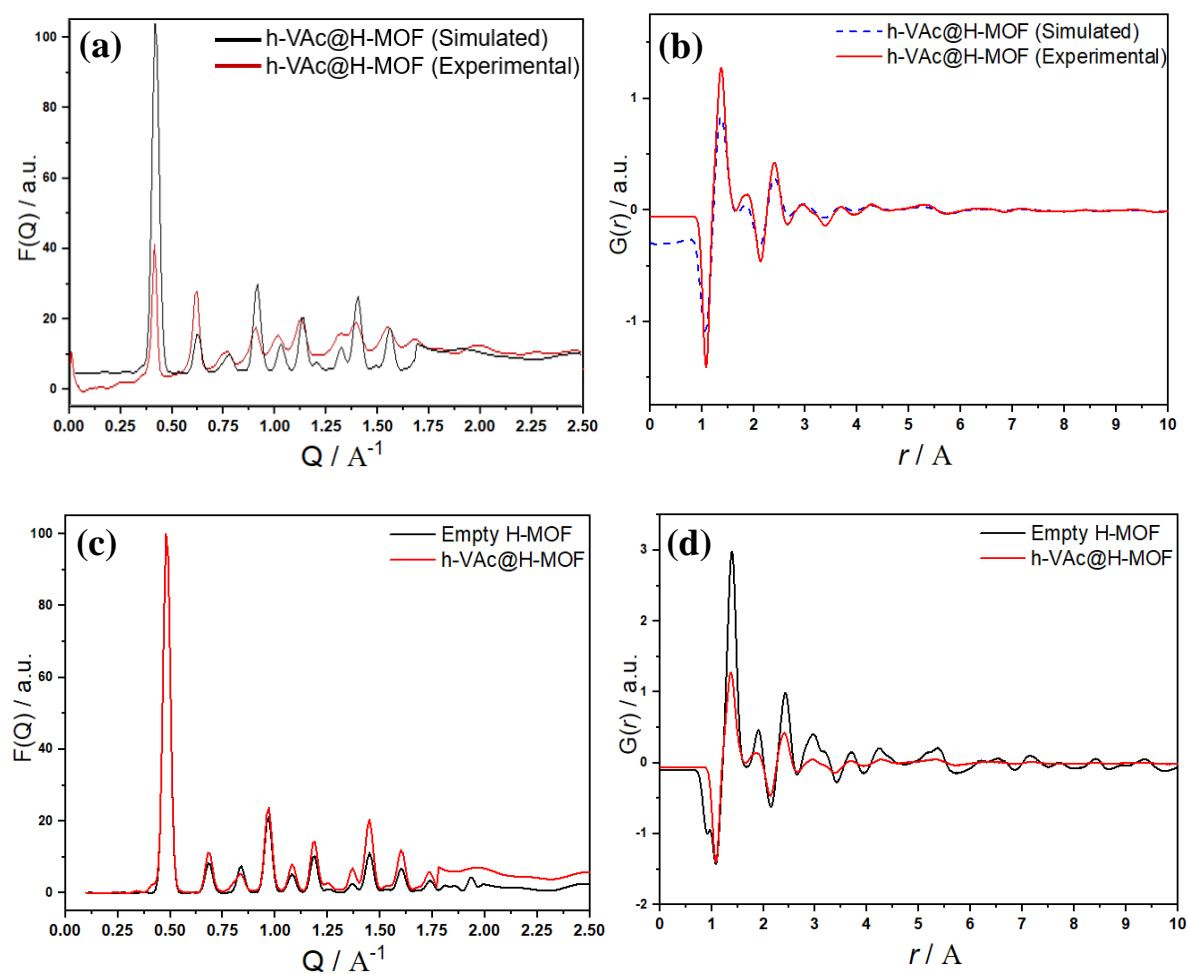


Fig 5.7: The experimental and calculated (a) total structure factor  $F(Q)$  and (b) total pair distribution function  $G(r)$  for h-VAc@H-MOF. Comparison between empty H-MOF and h-VAc@H-MOF (c) total structure factor  $F(Q)$  and (d) total pair distribution function  $G(r)$ .

## Chapter 5: Characterisation of Guest interactions in VAc@MOF-5

---

The experimental  $F(Q)$  for h-VAc@H-MOF are similar in peak positions to those simulated by Dissolve from the simulation ensemble. The peaks can be associated with Bragg reflections observed by powder XRD to reciprocal space (Table 5.3 in Section 5.3.3.1).

There is an additional peak seen in the  $Q = 0.83 \text{ \AA}^{-1}$  that is not seen in the powder XRD data for VAc@MOF-5 and TNS data for empty H-MOF. This new peak is possibly a result of solvent contribution on the framework as it appears following addition of guest monomer for all four samples. Comparing  $F(Q)$  for empty H-MOF and d-VAc@H-MOF show no clear peak shifts or changes in  $Q$  (Fig 5.7 (c)). Diffuse scattering over higher  $Q$  ( $Q > 1.75 \text{ \AA}^{-1}$ ) can be observed possibly from long range disorder imposed by monomer.

**$G(r)$ :** The pair distribution function  $G(r)$  gives the distribution of relative interatomic distances with respect to average atom at the origin. The overall intensity in the mismatch between atomic pairs may be due to the initial simulation models containing a higher order and crystallinity compared to experimental samples (Fig 5.7 (b)), but most features present in the data are well reproduced. Peaks at longer distances decrease much faster than those observed at shorter distances ( $< 3 \text{ \AA}$ ). The liquid like behaviour and loss of ordering at longer distances in overall  $G(r)$  suggest that the monomer is in a liquid state within the pores of the MOF. It is seen from Fig 5.7 (b) that the experimental (calculated) data matched well with the simulated data from the ensemble and suggests short-range order with sharp features. The expected interatomic distances as peaks from the MOF structure are present at the Zn–O peak ( $1.92 \text{ \AA}$ ) shows no change between empty H-MOF and h-VAc@H-MOF. However, there is an increase with monomer loaded sample by a magnitude of  $+ 0.2 \text{ \AA}$  for the peak at C–O ( $1.32 \text{ \AA}$ ) which merges in the C–C ( $1.38 \text{ \AA}$ ) peak (Fig 5.7 (d)). As there is no evidence of a formal change in coordination number around Zn, this suggests a possibility of framework expansion that results in an increase in bond length of the framework C–O bond connecting the metal node and the phenyl ring. It is expected that any framework expansion and structural changes occur at this bond based on observations from powder XRD (Section 4.2). In powder XRD, diffraction associated with (400) and (420) plane show a decrease in  $2\theta$  at  $13.7^\circ$  and  $15.5^\circ$  peaks (Appendix Fig A5.2).

## Chapter 5: Characterisation of Guest interactions in VAc@MOF-5

To mitigate the mismatch between  $F(Q)$  and  $G(r)$  between the experimental and simulated data for peak widths, the Bragg features were fitted to an omega-dependent Gaussian convolution for Bragg peaks (FWHM = 0.05) from independent Gaussian convolution (FWHM = 0.02). The results of this analysis are shown in the Fig 5.7 above.

### 5.3.4.2 h-VAc@D-MOF

The calculated experimental and simulated  $F(Q)$  and  $G(r)$  for h-VAc@D-MOF, and comparison of experimental  $F(Q)$  and  $G(r)$  against empty D-MOF are shown in Fig 5.8.

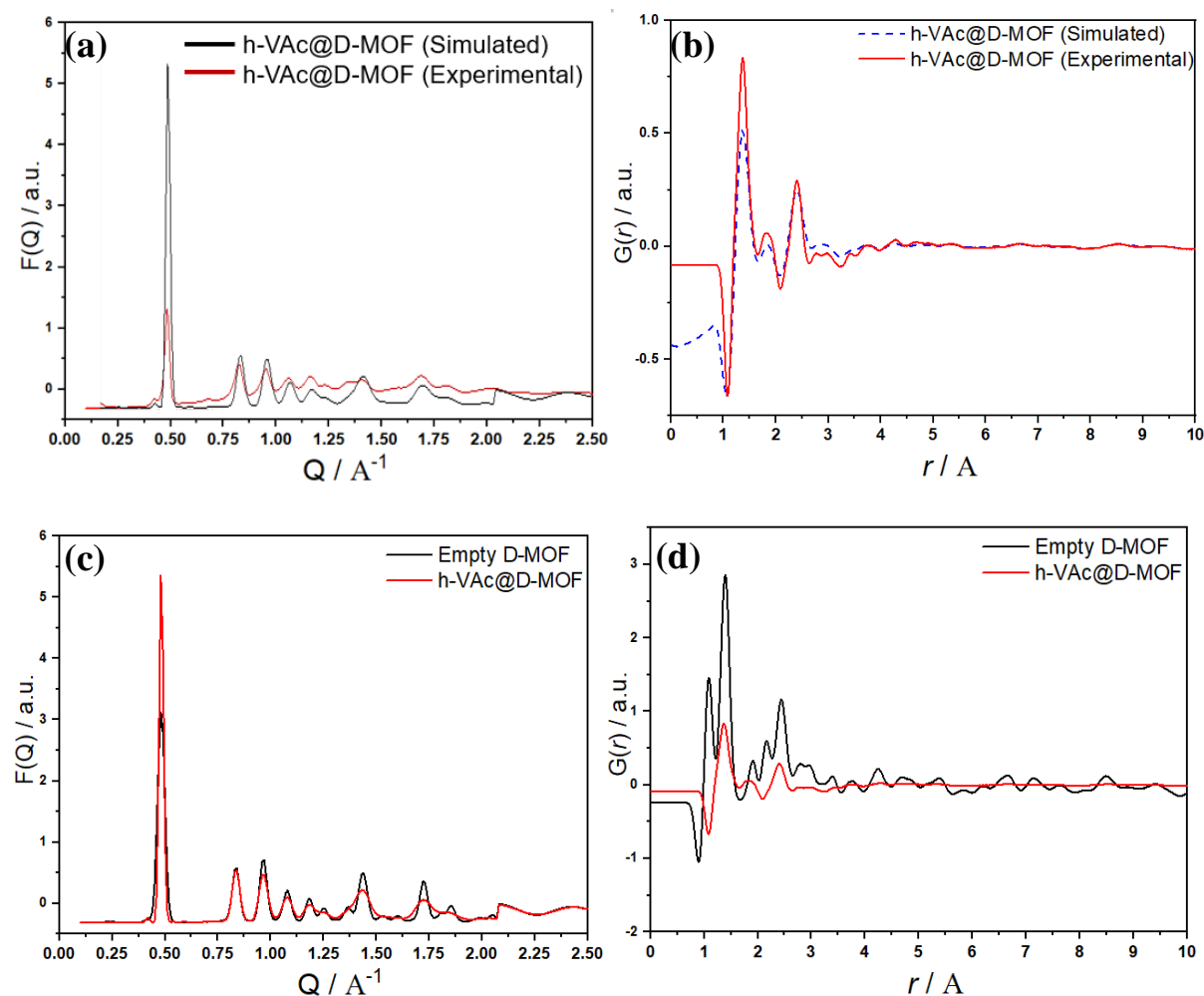


Fig 5.8: The experimental and calculated (a) total structure factor  $F(Q)$  and (b) total pair distribution function  $G(r)$  for h-VAc@D-MOF. Comparison between empty H-MOF and h-VAc@H-MOF (c) total structure factor  $F(Q)$  and (b) total pair distribution function  $G(r)$ .

## Chapter 5: Characterisation of Guest interactions in VAc@MOF-5

---

Simulated and experimental  $F(Q)$  data for h-VAc@D-MOF show a good match with all peak present in both sets of data. Observations from h-VAc@H-MOF also apply to h-VAc@D-MOF wherein the simulated data shows a greater crystallinity when compared to experimental data as observable diffuse scattering at higher  $Q$  (Fig 5.8 (a)). There is an additional peak in the h-VAc@D-MOF sample compared to the previous sample at  $Q = 0.83 \text{ \AA}^{-1}$  that is present which may be a contribution from solvent coordination with the framework (as described in Section 5.3.3.1). The peak is of a higher intensity in the case of h-VAc@D-MOF because the total coherent scattering contribution from h@D is expected to be greater than h@H. The relative intensity of this peak is expected to be highest in the case of d@D (shown later in Section 5.3.4.3).

$G(r)$ : Fig 5.8 (b) shows a moderate match between experimental and simulated data. Positions of the first peak ( $r = 1.09 \text{ \AA}$ ) is a negative peak in the D-MOF which is possibly due to greater atomic density of hydrogenated monomer C–H (486 bonds/unit cell) compared to framework C–D (92 bonds/unit cell) atoms. The peak is shifted towards lower distance compared to h-VAc@H-MOF by  $r = -0.01 \text{ \AA}$ . This is may be because of shorter C–D bond length compared to C–H of h-VAc@H-MOF but it is not possible to conclude the same as it is outside the resolution of instrument. However, due to the artifact between 0–0.8  $\text{\AA}$  in the simulated data for all monomer loaded samples, it is unclear if this is a real feature in the data. Most features beyond this region are well produced in the simulated data, and can be used for further analysis.

## Chapter 5: Characterisation of Guest interactions in VAc@MOF-5

---

### 5.3.4.3 Conclusions from h-VAc@MOF samples

The experimental  $F(Q)$  and  $G(r)$  for MOF-5 isotopologues with h-monomer is reasonably well reproduced in the simulated data following iterative corrections. Bragg features were fitted to an omega-dependent Gaussian convolution for Bragg peaks (FWHM = 0.05) from independent Gaussian convolution (FWHM = 0.02) to mitigate broadening mismatch. Partial  $g(r)$  showed features at low  $r$  distances ( $r > 0.5 \text{ \AA}$ ) suggested possibility of guest monomer penetration in the metal node which is physically not possible. Consequently, the tolerance values for MD/MC simulation ensemble were increased ( $0.2 \rightarrow 0.4$ ) to inhibit very short-range interactions between framework and guest species. QMax input in the Bragg layer module on *Dissolve* sets the width of the Bragg peak and the maximum  $Q$  to which Bragg peaks are calculated. These input values were changed to match the high  $Q$  range Bragg features to improve the gradient of the baseline in the experimental data by matching like Bragg features.

### Deuterated monomer@MOF

Iterative correction performed on h-monomer@MOF were also performed on d-monomer@MOF to reproduce improvements on the data. The following section will discuss observations from total structure factor  $F(Q)$  and total pair distribution function  $G(r)$  for d-VAc@D-MOF and d-VAc@H-MOF.

## Chapter 5: Characterisation of Guest interactions in VAc@MOF-5

### 5.3.4.4 d-VAc@D-MOF

Fig 5.9 shows the calculated experimental and simulated  $F(Q)$  and  $G(r)$  for h-VAc@D-MOF, and comparison of experimental  $F(Q)$  and  $G(r)$  against empty D-MOF.

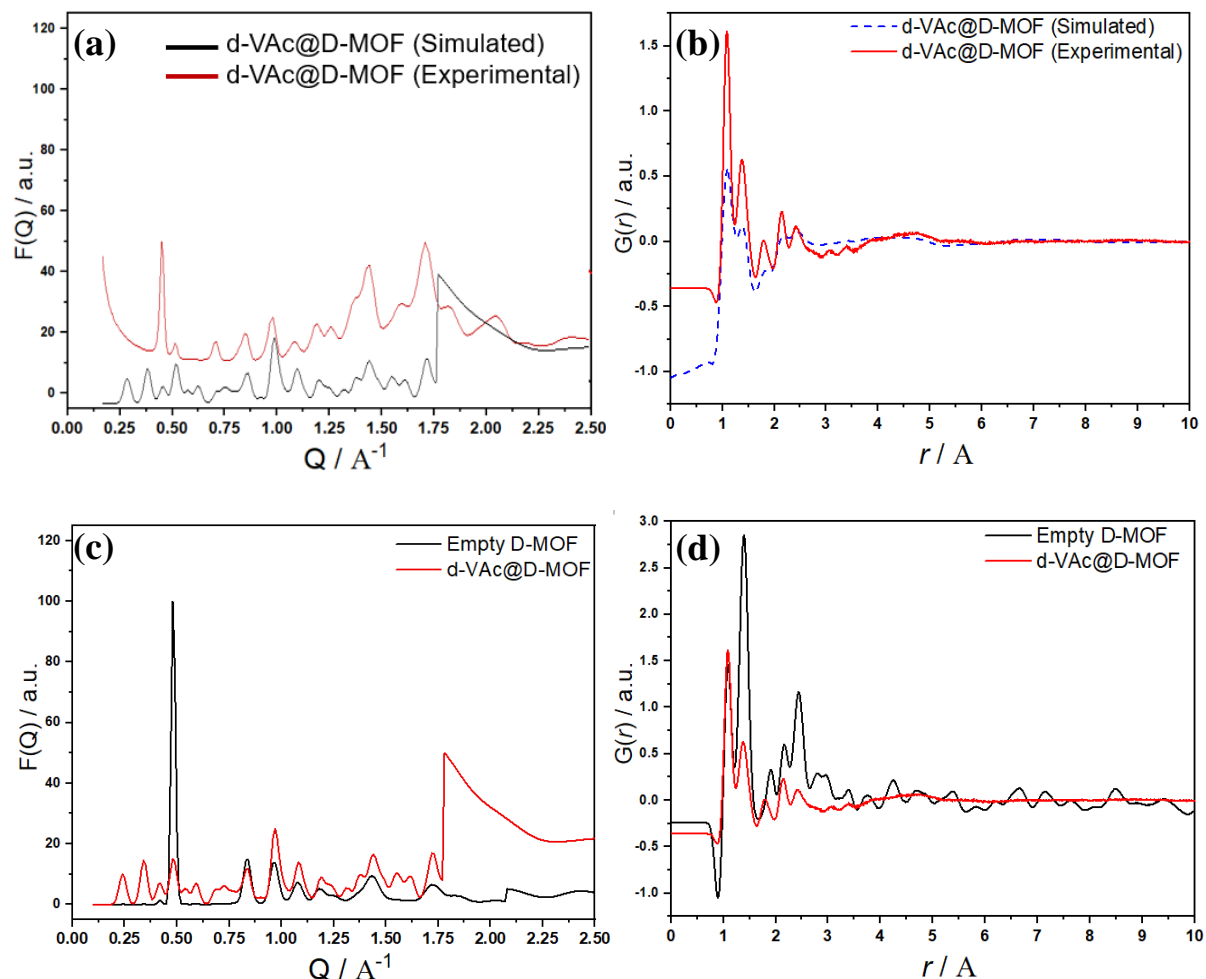


Fig 5.9: The experimental and calculated (a) total structure factor  $F(Q)$  and (b) total pair distribution function  $G(r)$  for d-VAc@D-MOF. Comparison between empty D-MOF and d-VAc@D-MOF (c) total structure factor  $F(Q)$  and (d) total pair distribution function  $G(r)$ .

The mismatch between experimental and simulated data, and the large spike in data at  $Q \approx 1.75 \text{\AA}^{-1}$  in Fig 5.9 (a) is a result of crossover between direct (Bragg) and diffuse (Fourier-transformed) parts of the structure factor calculations (further discussion in Section 5.4). Currently, *Dissolve* is unable to address this error, but work is being carried out to find a solution to this problem.

## Chapter 5: Characterisation of Guest interactions in VAc@MOF-5

---

The Bragg peaks observed on the  $F(Q)$  of the experimental pattern are reproduced in the simulated patterns for d-VAc@D-MOF. There is considerable mismatch between scattering level baseline experimental and simulated data. The most likely cause of this may be overcalculation of average differential scattering cross-section levels in Gudrun resulting in under subtraction scattering intensities. Hence, total scattering data reductions and iterative corrections for d-VAc@D-MOF were repeated on Gudrun. Following no improvement with recalculation of data, alternate approaches to mitigate this effect are under consideration.

A more significant discrepancy between experimental and simulated data is the appearance of additional peaks at low  $Q$  ( $Q = 0.24$  and  $0.34 \text{ \AA}^{-1}$ ). The source of these peaks is unclear at present. Several possible hypotheses were explored, and necessary measures were attempted to understand the presence of these peaks. Simulations on the ensemble for h-VAc@MOF were performed using the appropriate number of monomer molecules calculated from Gudrun. For d-VAc@D-MOF a possibility of DMF and water being present was investigated as a small feature in the  $G(r)$  is observed at  $r = 0.87 \text{ \AA}$  may be present due to O–H bond interactions in water or from DMF (Fig 5.9 (b)). From updated input reference files following recalculations on Gudrun, simulations were run again with halved the number of monomers, and in the presence of both water and DMF (160 water and 16 DMF/ensemble). However, upon doing so, improvements were not made, and the low  $Q$  peaks were still present. The possibility of interpenetrating networks of MOF-5 was considered and ruled out following *solid-state* NMR and SCXRD experiments (Section 5.7 and 5.8).

Another approach implemented was of introducing disorder in the empty MOF ensemble before addition of guest species. For the experiment, the empty MOF samples were activated prior to addition of monomer guests to remove excess solvent within the MOF pores at 443 K (170 °C). This was replicated on the ensemble by performing atomistic simulations at 443 K till a stable energy was achieved. Following this step, monomer, water, and DMF species were added in the ensemble and simulations were performed. Although this resulted in no significant improvement, it is decided that for all future simulations, disorder will be introduced in the empty MOF prior to adding guest species to better replicate the experimental environment. Further analysis of the data cannot be carried out without identifying the source of the error. The peak intensity will be most prominent on d@D

## Chapter 5: Characterisation of Guest interactions in VAc@MOF-5

samples due to highest average coherent scattering and all attempts to find possible solutions are being made on this sample at the time thesis submission.

### 5.3.4.5 d-VAc@H-MOF

The experimental and calculated total structure factor  $F(Q)$  and total pair distribution function  $G(r)$  for h- and d-VAc@D-MOF are shown in Fig 5.10.

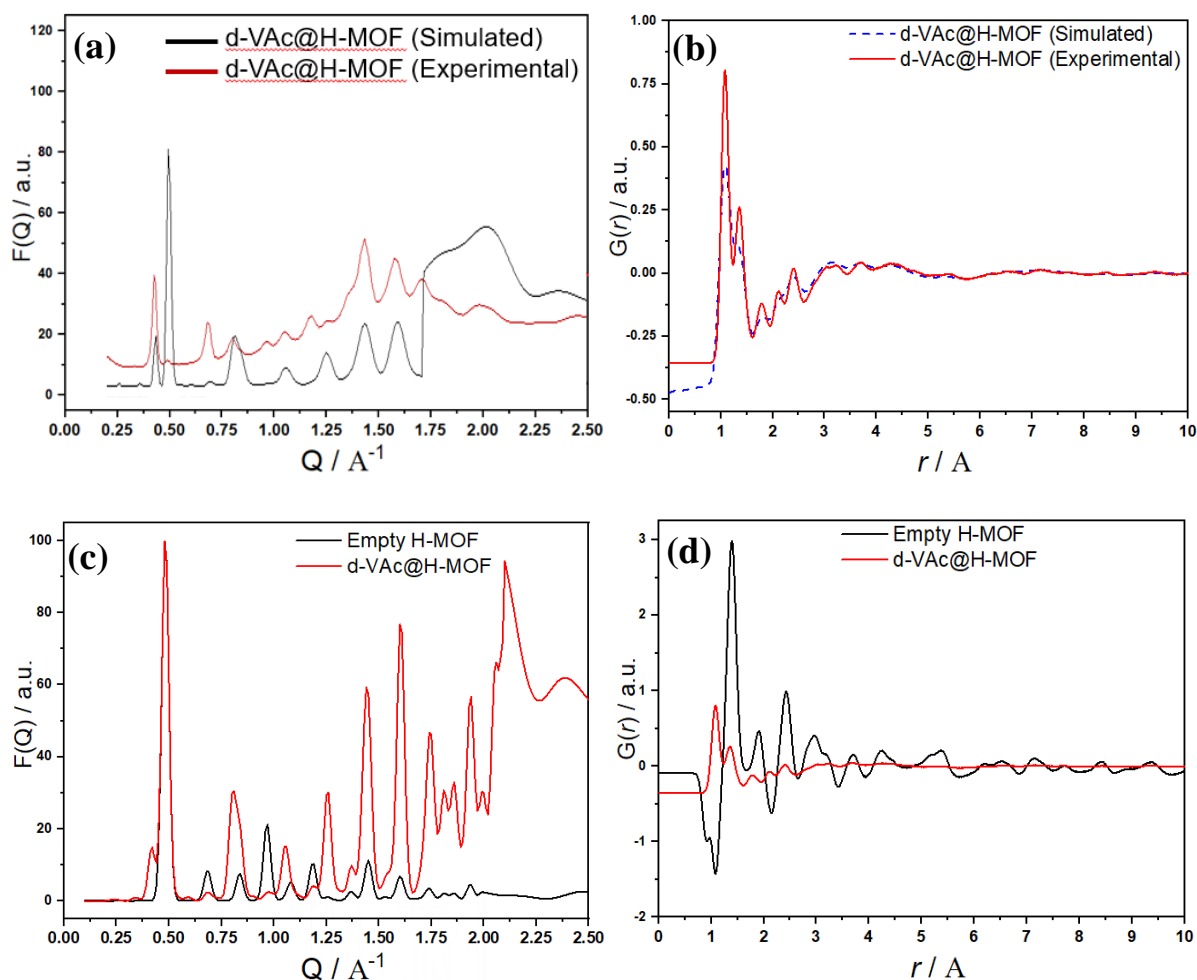


Fig 5.10: The experimental and calculated (a) total structure factor  $F(Q)$  and (b) total pair distribution function  $G(r)$  for d-VAc@D-MOF. Comparison between empty D-MOF and d-VAc@D-MOF (c) total structure factor  $F(Q)$  and (b) total pair distribution function  $G(r)$ .

The d-VAc@H-MOF presents the same disparity between simulated and experimental  $F(Q)$  vs.  $Q$  data as observed with d-VAc@D-MOF samples (Fig 5.10 (a)). The low  $Q$  peaks at 0.24 and  $0.34 \text{\AA}^{-1}$  are present but are less intense due to presence of less coherently scattering

## Chapter 5: Characterisation of Guest interactions in VAc@MOF-5

---

hydrogen. Fig 5.10 (c) shows a comparison between empty H-MOF and d-VAc@H-MOF. All Bragg peaks observed in empty MOF are present in d-VAc@H-MOF. However, at this point of time, conclusions cannot be derived due to aforementioned problems with disparities between simulated and experimental d-VAc@H-MOF data.

Fig 5.10 (b) shows pair distribution function for d-VAc@D-MOF. Features present in the simulated data are well reproduced in the experimental data, but without a match between intensities. Possible reasons for this may be due to simulations assuming a lesser crystalline order of the composite or due to iterative errors in simulating data that also results in low  $G(r)$  values at distances at  $r > 0.5$ . The overall match between peak positions is acceptable.

### 5.3.4.6 Conclusions from d-VAc@MOF

It remains unclear at present as to why the problems in matching experimental and simulated data is exacerbated in the case of deuterated monomer. Changes implemented in the case of h-VAc@MOF described in section 5.3.4.5 have been applied to d-VAc@MOF composites without improvement in Bragg calculation discrepancies at  $Q > 0.5 \text{ \AA}^{-1}$ . The reason for the presence of peaks at  $0.24$  and  $0.34 \text{ \AA}^{-1}$  remains uncertain and possible causes and subsequent steps to improve reproducibility will be discussed in the following section (Section 5.4)

## 5.4 Present Hypotheses and Future Outlook

The aim of the neutron diffraction experiment was to investigate monomer interactions in host MOF at atomic level. Through analysis of diffraction data, we are *en route* to conclusively identify the binding interactions and sites of monomer species in the framework, and the effect sorbent monomer has on the crystal structure of the host MOF. The data modelling and analysis is presently ongoing and continuous efforts are being made to draw conclusions towards the aim of the experiment. The results of some trial investigation are described below.

## Chapter 5: Characterisation of Guest interactions in VAc@MOF-5

### Future Simulations on *Dissolve*

Experimental samples, prior to monomer loading, are activated at 443 K under vacuum to remove any unbound moisture and solvent molecules present in the framework. It is expected that this introduces disorder in the host MOF due to thermal effects on the framework atoms. To mimic this, empty MOF ensemble will be '*heated*' to introduce disorder in the system by performing simulation at high temperature prior to adding monomer.

Fig 5.11 shows differences between two simulation ensembles before and after introducing disorder. There is noticeable lattice distortion seen in Fig 5.9 (b) as a result of simulated heating resulting and differences in individual pore dimensions.

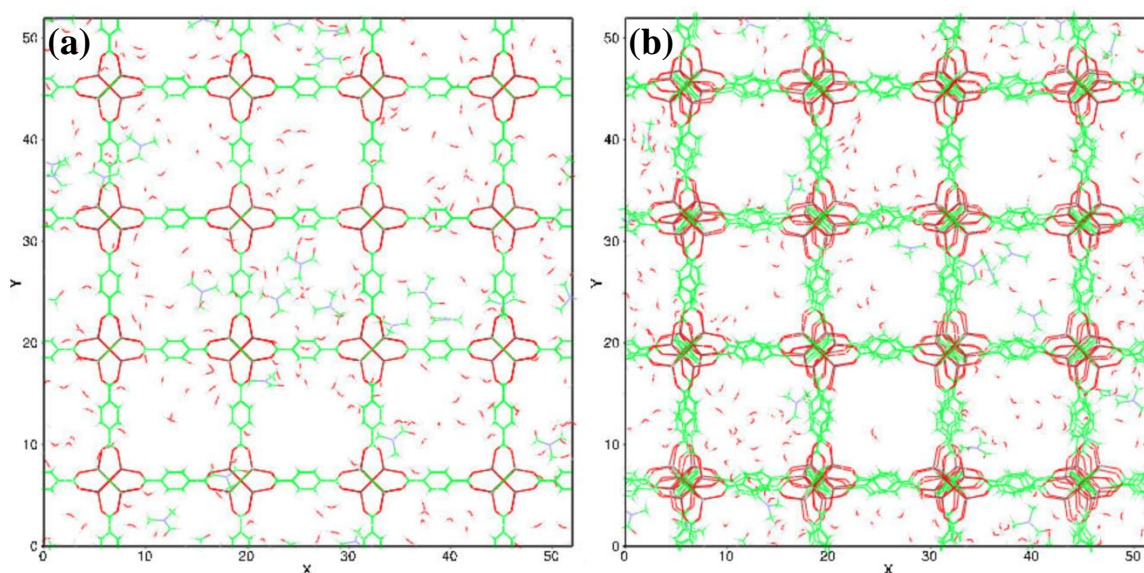


Fig 5.11: A comparison between simulation ensemble used during (a) preliminary simulations and (b) after introduction of disorder following simulated heating at 443 K.

Current calculations for monomer addition content are based on isotopic mass calculations that assume uniform distribution of monomer in the sample container in beam path. The inhomogeneity in pore filling by monomer is a possibility and thus, calculations will be attempted to alter monomer content to achieve desirable scattering and match average differential scattering cross-section by data processing on Gudrun. Pair distribution function analysis suggest that upon monomer loading, not all guest solvent and water molecules may

## Chapter 5: Characterisation of Guest interactions in VAc@MOF-5

---

be evacuated from the framework as there are peaks observed at shorter distances of  $r = 0.88$  Å, possibly from O–H bonds on water molecules.

There have been considerable improvements made to reproduce Bragg features on simulated data to experimental calculated data through fitting to an omega-dependent Gaussian convolution for Bragg peaks (FWHM = 0.05) and altering QMax for setting an appropriate width of the Bragg peak and the maximum Q to which Bragg peaks are calculated. Further investigation for setting these values will be made to improve match between simulated and experimental data.

H and D contrast variations are unique to neutron scattering and enables visualisation of structures within an intact system, providing information that is otherwise not accessible by other structure characterisation methods. Contrast variation by selective deuteration composites has been employed to differentiate between component in the complex monomer@MOF composites. However, we have found that there are some structural differences between the H-MOF and the D-MOF making data analysis and interpretation more complex as the contrast must be treated as individual samples for atomistic simulation. Therefore, next simulations will be performed on four different MOF ensembles.

Currently, our hypothesis with the appearance of intense low Q peaks ( $Q = 0.24$  and  $0.34$  Å<sup>-1</sup>) in the case of d-VAc@MOF is that they are a contribution from monomer interactions with the framework Zn–O metal node. Due to the simulation ensemble currently being a 2x2x2 supercell of MOF unit cell, this effect is amplified, and interactions appear as Bragg features in the F(Q) vs. Q plots. It is proposed that simulations with a larger ensemble (8x8x8 supercell) and through introduction of disorder in the system prior to monomer addition, this effect may be mitigated.

Simulations with standalone ensemble for each sample and a larger simulation box will enable us to reason and conclude whether isotopic effects contribute towards distinct Bragg features in the monomer@MOF composites.

## Chapter 5: Characterisation of Guest interactions in VAc@MOF-5

---

### Present Hypothesis and Conclusion

In conclusion from available data, the differences between the hydrogenated and deuterated MOF-5 structure are revealed that cannot be concluded by PXRD. For deuterated MOF-5, there is an additional peak observed at  $Q = 0.42 \text{ \AA}^{-1}$  ( $2\theta = 5.9^\circ$ ) that does not appear in PXRD data of D-MOF. Possible reasons for this may be from structural differences between H- and D-MOF. Subsequent SCXRD analysis suggests that a peak at such diffraction angle may appear due to co-ordination from guest species and interactions on the MOF that distorts the framework lattice from  $Fm-3m$  (cubic) to  $R-3m$  (rhombohedral or trigonal). This hypothesis is further supported with guest@MOF composite data where there is an increase in the scattering intensity of this peak. For the case of empty MOF, this peak may be present due to residual solvent DMF molecules in the framework. This result also questions the widely reported methodologies for MOF-5 activation to remove any intrinsic solvent molecules without structural distortion.<sup>28-30</sup>

From the preliminary analysis of the  $G(r)$ , we can sufficiently identify MOF contributions and differentiate short-range monomer interactions in the system. The long-range features observed in  $G(r)$  of all samples assumes that framework consists of an alternating open and closed pore structure with different pore diameters (discussed in detail in section 5.7.2) in the current ensemble, and the monomer filling infinitely translates into all directions to successive unit cells in the framework. It is possible that the simulation introduces an isotope effect to calculate scattering which is amplified through assumed homogenous filling, and current ensemble size. To allow for inhomogeneity in pore filling by guest species, a larger ensemble will provide a more accurate representation of experimental samples. Furthermore, control over individual pore filling in the simulation ensemble will aid identifying the source of features from scattering.

Through proposed changes on the simulation ensemble and Bragg corrections to match simulated and experimental data, from this experiment we will be able to conclude the effect of guest molecules on the host MOF that have previously not been studied or reported. Current research has been limited to transport behaviour and interactions of ions and small gaseous alkanes such as methane, butane, acetylene,  $\text{CO}_2$ ,  $\text{H}^+$  and  $\text{Li}^+$ .<sup>31-34</sup> Large molecules interactions such as vinyl acetate interactions in MOF-5 at the time of writing this thesis have

## Chapter 5: Characterisation of Guest interactions in VAc@MOF-5

---

not been reported. Furthermore, understanding structural effects of guest monomers on host MOF will correlate with observation from PXRD data (Section 4.2) will be confirmed by neutron scattering data simulated on Dissolve. Isotopic effects of monomer isotopologues on host framework have not been reported and conclusions from simulations will conclude our current hypothesis of short-range binding interactions of monomer on the host framework through observation of peaks at  $Q = 0.24$  and  $0.34 \text{ \AA}^{-1}$ .

Lastly, initial simulations of monomer@MOF on Dissolve have contributed towards determining avenues that can be applied on the code to understand complex systems such as confined liquids in crystals. Currently, it is not possible to introduce inhomogeneous pore filling on Dissolve simulations that result in correlating effects that are not present in the experimental samples. Identifying these changes provides a basis and direction to further improve simulations and development of *Dissolve*.

### **Progress following submission of thesis.**

The simulation ensemble was expanded to an  $8 \times 8 \times 8$  supercell, and disorder was introduced in the MOF by simulating the activation of the MOF. This was done by heating the simulation ensemble to 443 K and MD and MC simulations were performed till a stable energy was reached. Doing so resulted in an improved match on the Bragg peak positions on the experimental versus simulated data. The additional peak observed at low  $Q$  values ( $Q = 0.24$  and  $0.34 \text{ \AA}^{-1}$ ) in the case of D-MOF diminished upon expansion of the simulation ensemble too. This suggests that in the data earlier in the  $2 \times 2 \times 2$  ensemble, these peaks may be a result of homogeneous filling of the guest molecules within the pores of the MOF.

Another key factor that may have played a vital part in the appearance of these peaks may have been result of incorrect molecular charges implemented at the time of creating the MOF-5 unit cell ensemble. This has been realised and corrected by creating a new MOF-5 unit cell with correct molecular charge assignment and distribution. In our opinion, this may have been cause of many discrepancies with simulation of data.

## Chapter 5: Characterisation of Guest interactions in VAc@MOF-5

---

Furthermore, an envelope function was implemented that allows the Schrödinger equation to be simplified to refer only to the behaviour of the envelope by applying boundary conditions envelope function directly, rather than to the complete wavefunction.<sup>35</sup> This allowed a more accurate match between the simulated and experimental data. QMax was altered (QMax = 20) for setting an appropriate width of the Bragg peak and the maximum Q to which Bragg peaks are calculated.<sup>‡</sup> This change resulted in improvement of the baseline gradient in the experimental data by matching like Bragg features of the simulated data.

This proves to be a positive step forward in data analysis and interpretation by enlarging the simulation ensemble (8x8x8 from 2x2x2 unit cell), with incorporation of envelope function for scattered neutron wave and modified Bragg parameters. The subsequent steps will involve addition of monomer molecules and simulating the ensemble to determine if the improvements on empty MOF ensemble are translated in the monomer@MOF ensemble as well. Upon doing so, we will be able to precisely identify additional guest monomer peaks and/or structural changes on the MOF structure with greater certainty from F(Q) data and identify the binding sites and interactions of the guest species within the framework by investigation of G(r). Currently, the data analysis and interpretation will be carried forward by Dr Tristan Youngs and Dr Thomas Headen (Disordered Materials Group – ISIS Pulsed Neutron and Muon Source) with input from the candidate, Dr Alison Paul, and Dr Timothy Easun (Cardiff University).

---

<sup>‡</sup> - QMax input in the Bragg layer module on *Dissolve* sets the width of the Bragg peak and the maximum Q to which Bragg peaks are calculated. (Section 5.3.4.3)

## Chapter 5: Characterisation of Guest interactions in VAc@MOF-5

---

### 5.5 Quasi-Elastic Neutron Scattering (QENS) Experiment:

In order to investigate the dynamics, mobility rate, and length-scales of guest motion within the MOF framework QENS experiment was performed at IRIS spectrometer at Target Station-1 (TS1) of ISIS Pulsed Neutron and Muon Source facility at Rutherford Appleton Laboratories, Oxfordshire, UK (*Experiment RB2010536*). IRIS is a high resolution TOF instrument with indirect geometry QENS spectroscopy and long  $d$ -spacing window scan capability. In addition to guest mobility, it also provides analysis regarding the influence of guest species in MOF to further corroborate the framework contraction and expansion observed with neutron diffraction (NIMROD) and X-ray diffraction (Cardiff University).

We aimed to use elastic and inelastic window scans to determine how the motion of guest species in the framework evolves over time upon initiation of polymerisation. Additionally, interpreting the coherent and incoherent elastic and quasi-elastic contributions affected independent resolution of the guest and its motion within the framework. The extended Q-resolved capability of the IRIS spectrometer was exploited to determine the geometry of motion of two components as by interpretation of elastic incoherent structure factor (EISF). However, EISF did not provide any useful information for guest@MOF-5 system following the experiment (described in detail; Section 5.5.3.7).

#### 5.5.1 In-situ polymerisation of vinyl acetate monomer in MOF-5

##### 5.5.1.1 Materials and Methods

The synthesis for the H-MOF-5 and D-MOF-5 have been described in section 3.2.2 of Chapter 3 of this thesis. Deuterated  $d_4$ -vinyl acetate was sourced from QMX Laboratories Ltd, UK. Hydrogenated vinyl acetate ( $\geq 99\%$  purity) and AIBN (98%) were purchased from Merck KGaA.

Individual MOF samples were activated to remove residual solvent and minimise adsorbed moisture by heating glass vials containing MOFs in a vacuum oven at 80 °C for 12 h. The MOFs, upon activation were sealed in the reaction flask and transferred to the sample container in a vacuum glovebox with inert atmosphere.

## **Chapter 5: Characterisation of Guest interactions in VAc@MOF-5**

---

Monomer@MOF and oligomer@MOF samples were prepared by methods described in section 3.3. Upon preparation, samples were sealed in reaction flask and transferred to the sample container in a vacuum glovebox. Polymer@MOF sample was prepared by polymerising monomer@MOF samples for 48 h in an oven at 70 °C. Approximately 2 g of sample was transferred to cylindrical aluminium sample container in a glove box filled with nitrogen gas to prevent air exposure.

QENS experiments were carried out on time-of-flight IRIS spectrometer at ISIS Neutron and Muon Source, STFC, Harwell. The QENS spectra were recorded by the IRIS spectrometers, affording the FWHM of 17.5  $\mu\text{eV}$  energy resolution with momentum transfer range varying 0.5 to 1.8  $\text{\AA}^{-1}$ . QENS measurements were taken from 4 – 300 K at a heating rate of 10 K/min using PG002 pyrolytic graphite analyser bank on the IRIS spectrometer. The background contribution and experimental distortion were not corrected. All measurements were taken and recorded by Dr Ian Silverwood at ISIS Pulsed Neutron and Muon Source (Rutherford Appleton Laboratory, Oxfordshire, UK) due to restrictions on site access due to COVID-19 pandemic. Data processing and analysis were also performed by Dr Ian Silverwood with input from the candidate for system specific interpretation.

## Chapter 5: Characterisation of Guest interactions in VAc@MOF-5

### 5.5.1.2 Sample Containers

The sample containers for the experiment used were cylindrical sample cans made from aluminium, 55 mm in height and 22 mm in diameter (i.d.) (Fig 5.12)

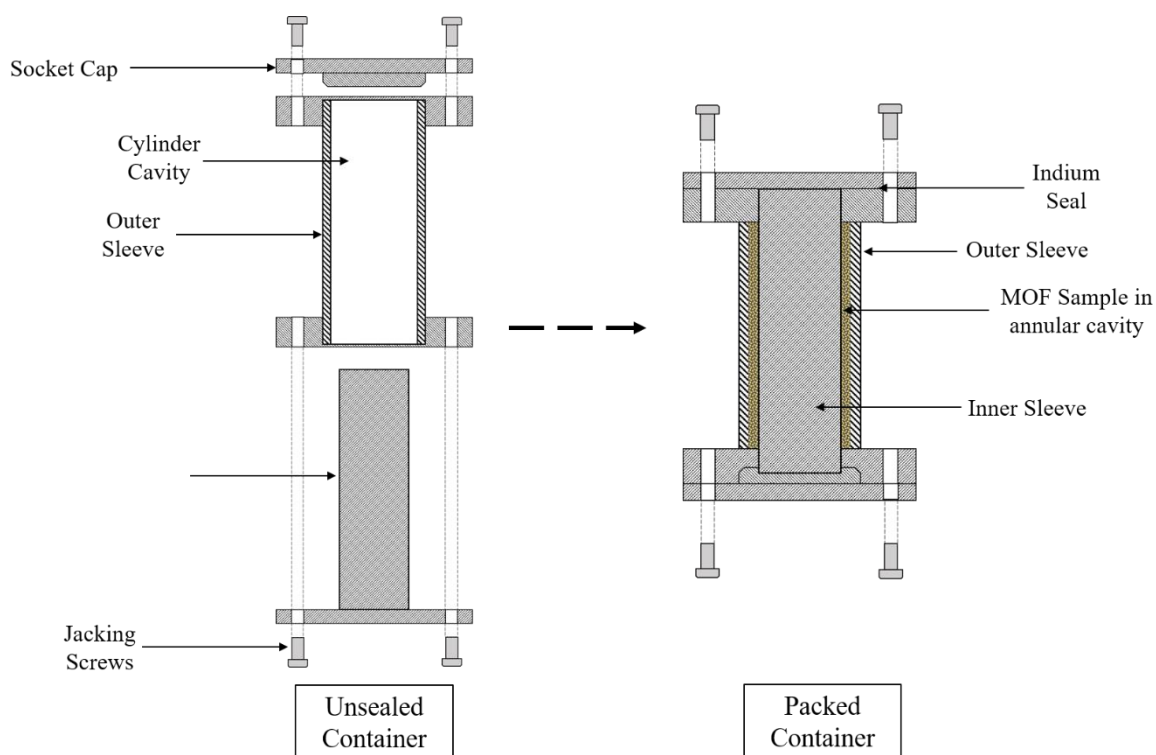


Fig 5.12: Schematic diagram of sample containers used for investigation of in-situ polymerisation of monomer@MOF-5 experiment by neutron spectroscopy on the IRIS instrument.

The sample cylinder contains a hollow insert resulting in an annular cross-section with 1 mm void space between the outer and inner cylinder. The overall volume of the void space is 3.97 cm<sup>3</sup> and serves as the volume in which the sample is deposited. The sample cylinder and the insert are sealed with an indium wire and sealed air-tight with screws on the circumference. The void space in the centre of the cell serves as the path length for incident neutrons.

## Chapter 5: Characterisation of Guest interactions in VAc@MOF-5

### 5.5.1.3 Experimental Samples

The samples used for experiments were a total of eight hydrogenated and deuterated variants of MOF and the guest (Table 5.4). Samples were in the sets of empty MOF-5 without adsorbed guest monomer, monomer adsorbed MOF-5 (VAc@MOF-5; monomer@MOF-5), MOF-5 wherein the adsorbed monomer partially polymerised sampled for a total time of 18 h (OVAc@MOF-5; oligomer@MOF-5), and monomer polymerised over complete polymerisation time of 48 h.

Table 5.4: Sample list and numbers for the neutron spectroscopy experiment.

No.	Sample	No.	Sample
1	H-MOF-5	5	D-MOF-5
2	d-VAc@H-MOF-5	6	h-VAc@D-MOF-5
3	d-OVAc@H-MOF-5	7	h-OVAc@D-MOF-5
4	d-PVAc@H-MOF-5	8	h-PVAc@D-MOF-5

The initial experimental plan involved having multiple samples for sample 3 and 7 at different polymerisation times to evaluate the onset and the mechanism of polymerisation in the MOF. The oligomer@MOF-5 samples would be divided into samples with polymerisation times of 3 h intervals starting from 12 h, until 48 h. The basis for the first oligomer sample was supported by laboratory PXRD and FTIR experiments observed on the monomer@MOF and partially polymerised samples (Section 4.2.1.1). However, due to experimental time limitations and site accessibility restrictions imposed by the COVID-19 pandemic, only one sample at an intermediate polymerisation time of 18 h was selected as the intermediate, oligomer@MOF-5 sample.

## Chapter 5: Characterisation of Guest interactions in VAc@MOF-5

---

### 5.5.2 QENS Data Analysis – Underlying Theory

During a normal QENS experiment, the measurements are taken from motions in  $Q-\omega$  space, where  $\omega$  is the angular velocity, which occur in real space and time.<sup>36</sup> The intensity of elastic, coherent neutron scattering is proportional to the spatial Fourier transform of the pair correlation function,  $G(r)$  i.e., the probability of finding a particle at position  $r$  when there is simultaneously, a particle at origin ( $r = 0$ ). The intensity of inelastic coherent neutron scattering is proportional to the space and time, and Fourier transform of the time dependent pair correlation function  $G(r,t)$  i.e., the probability of finding a particle at a position  $r$ , at time  $t$  when there is a particle at  $r = 0$  and  $t = 0$ . As for inelastic incoherent scattering, the intensity is proportional to the space and time Fourier transform of the self-correlation function  $G_s(r,t)$  i.e., the probability of finding a particle at position  $r$  at time  $t$  when the particle was as  $r = 0$  and  $t = 0$ . Thus,  $S_{\text{coh}}(\mathbf{Q}, \omega)$  is proportional to the two dimensional Fourier transform of time-dependent pair correlation function  $G(r, t)$ . Whereas,  $S_{\text{inc}}(\mathbf{Q}, \omega)$  is proportional to the two dimensional Fourier transform of time-dependent self-correlation function,  $G_{\text{self}}(r, t)$ . The total structure factor is a sum of coherent and incoherent structure factors. The scattering functions are from the van Hove correlation function  $G(\mathbf{r}, t)$  given by equation 5.10 and denoted the probability of finding the particle at a distance  $d\mathbf{r}$  at a position  $\mathbf{r}$  at a time  $t$ :

$$S(\mathbf{Q}, \omega) = \frac{1}{2\pi} \int dt \exp(-i\omega t) \int d\mathbf{r} \exp(i\mathbf{Q} \cdot \mathbf{r}) G(\mathbf{r}, t) \quad (5.10)$$

This equation can be described in the form of intermediate scattering function,  $I(\mathbf{Q}, t)$  as:

$$I(\mathbf{Q}, t) = \int d\mathbf{r} \exp(i\mathbf{Q} \cdot \mathbf{r}) G(\mathbf{r}, t) \quad (5.11)$$

## Chapter 5: Characterisation of Guest interactions in VAc@MOF-5

---

From the equation Eq 5.11, the scattering function and the inverse Fourier transform gives another expression for the intermediate scattering function result in:

$$S(\mathbf{Q}, \omega) = \frac{1}{2\pi} \int dt \exp(-i\omega t) I(\mathbf{Q}, t) \quad (5.12)$$

$$I(\mathbf{Q}, t) = \int d\omega \exp(i\omega t) S(\mathbf{Q}, \omega) \quad (5.13)$$

The incoherent and coherent scattering functions are related to the self and pair correlation function by:

$$S_{inc}(\mathbf{Q}, \omega) = \frac{1}{2\pi} \int dt \exp(-i\omega t) \int d\mathbf{r} \exp(i\mathbf{Q} \cdot \mathbf{r}) G(\mathbf{r}, t) \quad (5.14)$$

$$S_{coh}(\mathbf{Q}, \omega) = \frac{1}{2\pi} \int dt \exp(-i\omega t) \int d\mathbf{r} \exp(i\mathbf{Q} \cdot \mathbf{r}) G(\mathbf{r}, t) \quad (5.15)$$

$\mathbf{Q}$  and  $\omega$  are the Fourier transform variables of  $\mathbf{r}$  and  $t$ .  $\mathbf{Q}$  has the dimension of reciprocal distance, and  $\omega$  of angular frequency. Hence, larger distances will correspond to low  $\mathbf{Q}$  values and small energy changes will correspond to longer times in  $G(\mathbf{r}, t)$ .<sup>37</sup> Broadening of the elastic peak is observed when the characteristic time of a dynamical process measured is shorter than the inverse of resolution offered by the instrument,  $\Delta\omega$ . Hence, to observe true broadening of the elastic peak, it is essential to consider that the scattering function is convoluted by the instrumental energy resolution.<sup>36,37</sup> Analysis mainly focusses on  $S_{inc}(\mathbf{Q}, \omega)$  and the intermediate scattering function  $I_s(\mathbf{Q}, t)$  due to exceptionally high incoherent cross-section of hydrogen.. Analysing  $S(\mathbf{Q}, \omega)$  is comprised of two parts, the analysis of elastic region where energy transfer is zero being the first, and the broadening of the spectrum beyond the elastic region being the second. The analyses are described for the systems of study in Section 5.3.3.

## Chapter 5: Characterisation of Guest interactions in VAc@MOF-5

---

### 5.5.3 Results and Discussion

#### 5.5.3.1 Elastic Fixed Window Scan (EFWS)

The elastic fixed window scan (EFWS,  $k_i = k_f$ ,  $\Delta\hbar\omega = 0$ ) measurement observes temperature dependent changes in elastic intensity of scattered neutrons from the sample as a function of  $Q$ .<sup>38</sup> EFWS allow measurements of transition temperatures of the guest, molecular rigidity of the MOF framework, and Debye-Waller information ( $d\langle u^2 \rangle/dT$ ) that determines the thermally-averaged atomic positions. In addition, further analysis may potentially yield useful information such as activation energies ( $E_a$ ), mobile fractions ( $p_m$ ) and associated geometry of motion ( $A_o(Q)$ ) through detailed fitting of the quasi-elastic peak. For the IRIS spectrometer, the elastic scattering intensity is determined by integrating  $S(\mathbf{Q}, \omega)$  between  $\Delta\hbar\omega_{\min} = -\Gamma_{\text{res}}/2$  and between  $\Delta\hbar\omega_{\max} = +\Gamma_{\text{res}}/2$ . Where, the  $\Gamma_{\text{res}}$  is the energy resolution of the instrument. This is experimentally determined by measuring the full-width at half maximum (FWHM) of elastic peak in a sample with minimal inelastic scattering.

#### 5.5.3.2 EFWS: Observing MOF Dynamics

The signal in the QENS measurement is likely to be a contribution from both incoherent and coherent scattering weighted in accordance with isotopic contributions. MOF and guest are primarily formed of carbon, oxygen, zinc, and hydrogen. Hydrogen will have a sizable incoherent scattering contribution compared to other nuclei and any measurement from protonated material will be dominated by the incoherent dynamic structure factor  $S_i(\mathbf{Q}, \omega)$  arising from scattering of  $^1\text{H}$  nuclei. Therefore, the information that is extracted is dominated by the mobility or self-motion of the  $^1\text{H}$  species. Deuterium ( $^2\text{H}$ ) on the other hand is a coherent scatterer and has a weak incoherent cross-section relative to hydrogen ( $\sigma_i^{\text{D}} = 2.05$  barns) and is not ‘seen’ in EFWS. Therefore, EFWS for hydrogenated MOF and deuterated guest provides information regarding structural dynamics of the MOF in the presence of deuterated guest molecules. EFWS of empty H-MOF and d-guest@H-MOF are shown in Fig 5.13.

## Chapter 5: Characterisation of Guest interactions in VAc@MOF-5

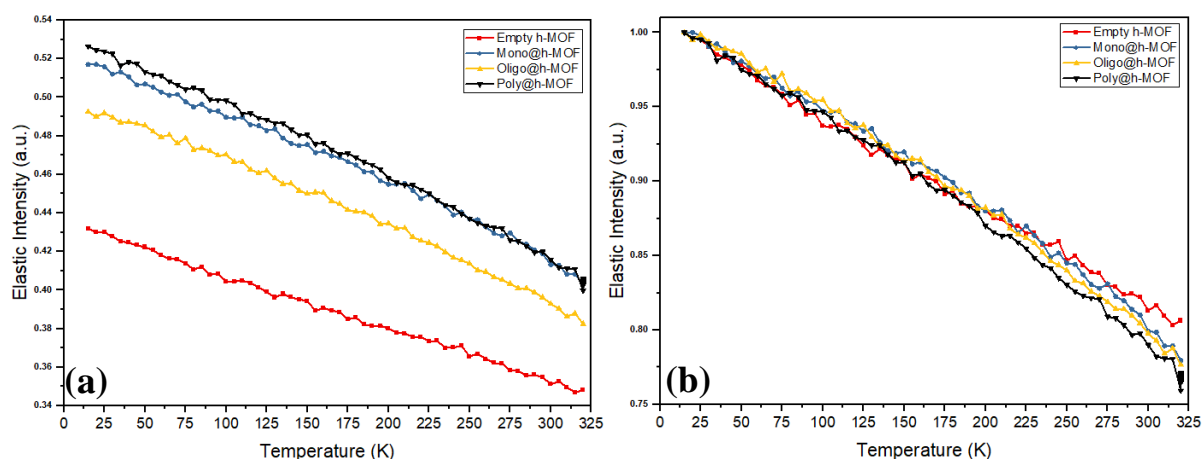


Fig 5.13: EFWS of empty H-MOF and d-guest@H-MOF plotted as (a) absolute elastic intensity versus temperature, and as (b) normalised to elastic intensity measurement at 15 K versus temperature.

To measure the extent of changes, benchmark measurements were carried out with hydrogenated MOF-5 in absence of deuterated guest. Fig 5.13 (a) shows elastic intensity as a function of temperature. Introduction of guest species in the framework causes an increase in the elastic intensity of the framework, which may arise from framework stiffening. This would be consistent with studies by high pressure crystallography which have shown framework stiffening at high guest loadings.<sup>62,63</sup> To confirm this premise, it is useful to normalise the data to the first data point of the lowest temperature to account for any variation in the amount of sample in the containers which may likely cause and increased or decreased elastic scattering as a proportion to relative amount of sample present.

Fig 5.13 (b) shows the elastic intensity versus temperature plots that have been normalised to the first measurement point at  $15 \pm 0.01$  K. This case assumes that there is no discernible motion visible at lower temperatures. Small differences are observed amongst samples with localised framework motion restricting upon guest inclusion. Empty H-MOF shows a shallower gradient when compared to the H-MOF with deuterated guest present in the pores of the MOF. This may suggest that the framework flexibility is decreases upon guest inclusion and increases slightly upon subsequent polymerisation. The motion observed in the empty H-MOF sample may be a result of the elastic contribution from the  $^1\text{H}$  of residual solvent DMF and water. This observation furthers the conclusion derived from neutron

## **Chapter 5: Characterisation of Guest interactions in VAc@MOF-5**

---

diffraction data (Section 5.1.2), powder XRD, and other characterisation methods presented in chapter 4. A change in slope of the elastic scattering intensity for empty MOF at 205-210 K is observed suggesting a slight increase in framework mobility at the higher temperature. This may be due to coordinated solvent DMF changing phase from solid to liquid that allow for greater framework flexibility (DMFm.p. = 212 K). Further, as elastic scattering is dominated by localised motion, translational or long-range motion of liquid DMF may not be observed.

The difference in gradient between monomer@MOF, oligomer@MOF, and polymer@MOF is negligible and it is therefore not possible to quantify the differences between each without further data analysis with higher instrumental resolution. However, it cannot be made certain that experiments using higher resolution can yield the desired information.

### **5.5.3.3 EFWS: Observing Guest Dynamics**

The absolute and normalised data for EFWS as a function of temperature are shown in Fig 5.14. Fig 5.14 (a) shows a noticeable increase in elastic scattering for the h-guest loaded D-MOF which is as expected due to an increased cross-section of  $^1\text{H}$  atoms on hydrogenated guests.

## Chapter 5: Characterisation of Guest interactions in VAc@MOF-5

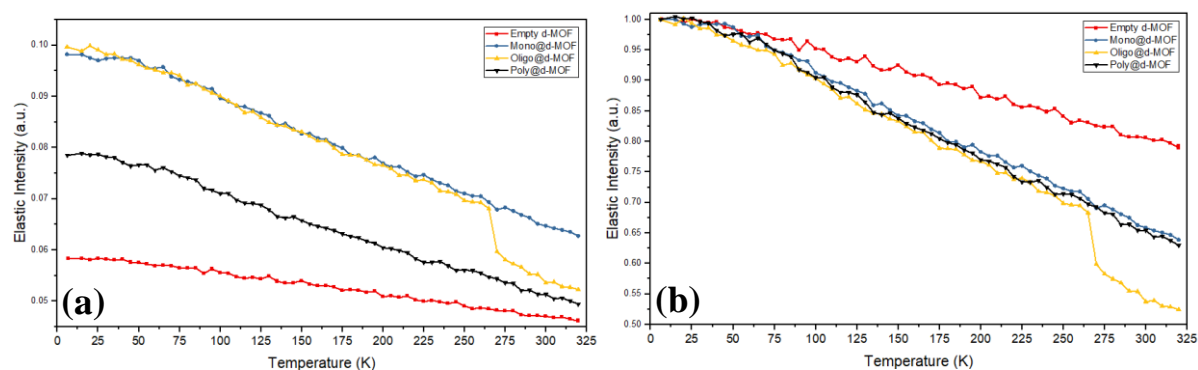


Fig 5.14: EFWS of empty D-MOF and h-guest@D-MOF plotted as (a) absolute elastic intensity versus temperature, and as (b) normalised to elastic intensity measurement at 15 K versus temperature. (The discrepancy between two data points at 260 K for oligomer@MOF-5 sample is due to recording measurements in two different times. Measurements at temperature 0–260 K were recorded two months prior to final 260–320 K measurements due to scheduled maintenance of the IRIS instrument)

EFWS for hydrogenated guest confined in deuterated MOF provides information regarding observable localised motion from elastic signal contributions from the H-guests. Benchmark measurements were carried out with deuterated MOF-5 in absence of hydrogenated guest.

The quasi-elastic peak may contain elastic contributions associated with localised dynamic contributions from the hydrogenated guests. A diffusive species that is no longer free to move without constraint, and is geometrically anchored, may show an increased elastic scattering compared to an unbound species present in the framework. We hypothesise that this is the case when considering the decreased elastic scattering intensity with polymer@MOF compared to monomer@MOF and oligomer@MOF samples. A possible reason for this effect is that monomer molecules and short oligomer chains remain bound to the structure of the MOF enhancing the probability of elastic scattering through localised motions. This would explain the stiffening of the framework that is observed in the case of EFWS with d-guest@H-MOF. Polymer@MOF the other hand, remains ‘free’ and is not geometrically bound to the framework. It therefore exhibits a higher degree of translational motion, being unbound, resulting in a lower intensity of the observable elastic scattering. There can be an argument made regarding the polymer chains diffusing out of the framework based on the above hypothesis. We can, however, successfully eliminate the likelihood of this based on

## Chapter 5: Characterisation of Guest interactions in VAc@MOF-5

---

evidence from EFWS of d-polymer@H-MOF which shows that the polymer@MOF sample shows much higher elastic scattering intensity compared to the empty MOF and relatively similar to other guest@MOF samples, that is likely only if the framework stiffness (compared to the empty MOF) is maintained due to the presence of deuterated guest species present in the framework. Furthermore, complimentary characterisation methods such as solid-state NMR (Section 5.7), powder XRD, FTIR, SEM (Chapter 4) and show no evidence of polymer diffusion out of the MOF crystals.

### 5.5.3.4 Quasi-elastic Peak Fitting

#### Translational Diffusion

Guests, especially monomers, are expected to undergo long range isotropic translational diffusion.<sup>38</sup> For translational diffusion, the particles are considered to be unconstrained and move through the pores of the MOF. Particle fluctuations in this case are governed by Fick's law,<sup>39</sup> with the incoherent structure factor  $S_{\text{inc}}(Q, \omega)$  being described by the Lorentzian or exponential, respectively. The  $Q$  dependence of the quasi-elastic broadening at a given temperature can be related to the diffusion coefficient of the guest given by:

$$\Gamma(\text{HWHM}) = D_s Q^2 \quad (5.16)$$

Where  $\Gamma$  is the line broadening at half-width at half maximum (HWHM) and  $D_s$  is the self-diffusion coefficient. Hence, a continuous diffusion is a linear trace if  $\Gamma$  is plotted as a function of  $Q^2$ , with the gradient being equal to  $D_s$ .

Data from QENS spectrum and  $S(Q, \omega)$  are divided into two part analysis, that of the elastic region and broadening of the spectrum beyond the elastic region.<sup>40</sup> The integral of the spectrum within the dynamic range is instrument resolution depends on  $Q$  and is an approximation to the dynamic structure factor of the elastic scattering.

## Chapter 5: Characterisation of Guest interactions in VAc@MOF-5

---

The data analysis included fitting of a scattering function consisting of the convolution of instrumental resolution with a delta function and a Lorentzian function. The Q dependence of the width and intensities of these peaks showed systematic trends suggesting faster process with rotational character and slower process which were dominated primarily by translational character. For our data, fitting of the elastic peak was performed with DAVE.<sup>41</sup> DAVE (Data Analysis and Visualization Environment) is a software package for the reduction, visualization, and analysis of neutron spectroscopic data as well as providing experiment planning tools. Mantid software platform was used for reduction, and other analysis for neutron scattering and muon spectroscopy data.<sup>42,43</sup> Delta function was used to represent the elastic scattering and the Lorentzian function to represent the inelastic peaks. Further information about the theory of fitting convolution of resolution with theoretical function is given in Appendix A5.1. It is worth mentioning that for some samples, the data was sufficiently fitted without a Lorentzian contribution. This may suggest that any motion present in the sample is outside the dynamic range of the instrument and only the elastic scattering contribution is observed as a result.

### 5.5.3.5 Lorentzian Peak Area

Lorentzian peak height represents the quantity of inelastic scattering from the sample under observation. For the case of h-guest@D-MOF systems, this would elucidate the modes of molecular motion by the guest molecules. Coherent scattering dominated by <sup>2</sup>H nuclei results from interference between scattered neutron waves and different atoms to give information relating to the relative position of the atoms. In terms of  $G(r, t)$ , coherent scattering will give information regarding interactions between atoms within the framework, and correlated inelastic events. Incoherent scattering that is dominated by the presence of <sup>1</sup>H nuclei, gives the probability  $G(r, t)$  of finding an atom at a given position ( $r$ ) at a time ( $t$ ) when the same atom is present at the origin and gives information regarding diffusion-like motion. Fig 5.15 shows a plot of area of the Lorentzian peak v Q.

## Chapter 5: Characterisation of Guest interactions in VAc@MOF-5

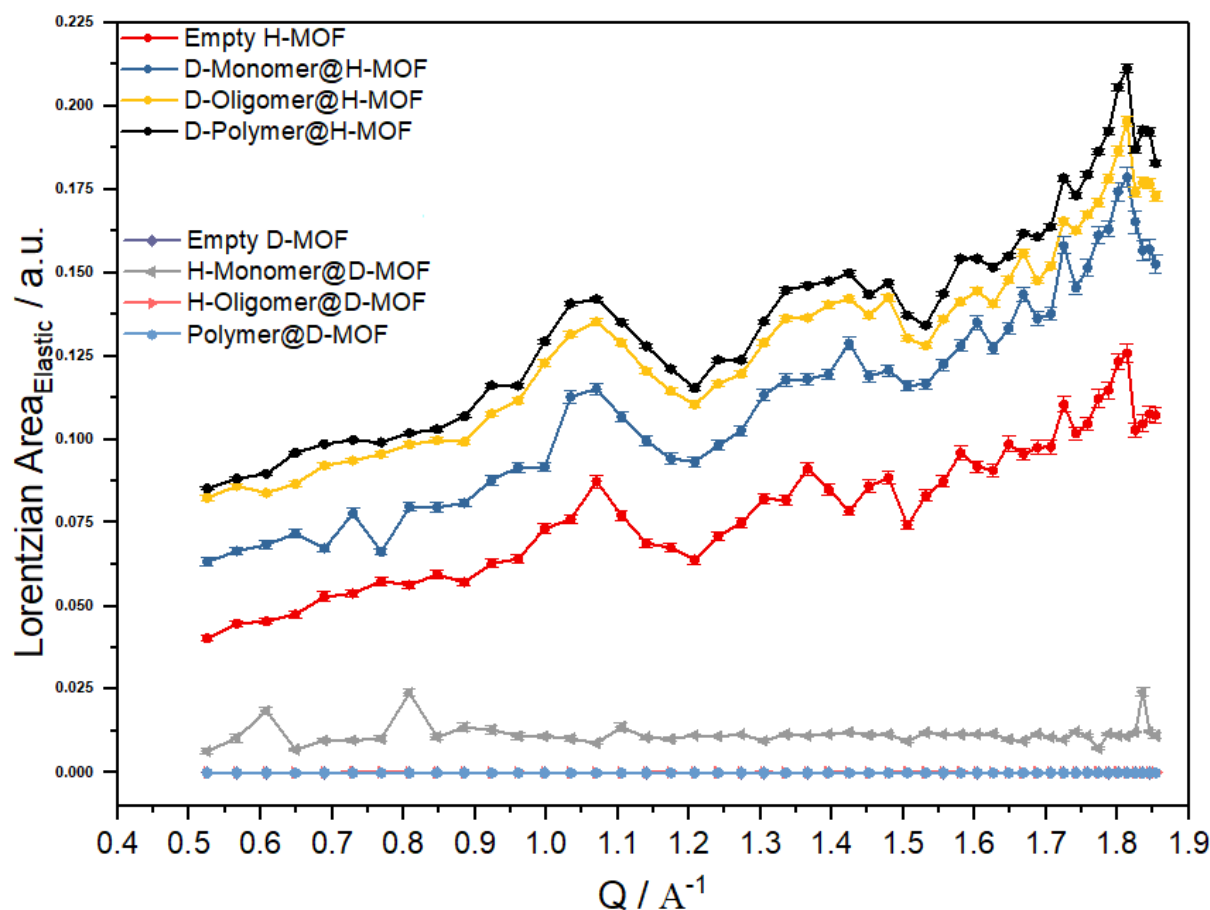


Fig 5.15: Height of Lorentzian peak vs  $Q$  for guest@MOF. (The  $Q$  dependence of scattering intensity for D-MOF, H-Monomer@D-MOF and H-Oligomer@D-MOF have not been fitted to Lorentzian model, shown here as a reference only).

For H-MOF systems, there is an increase in intensity of inelastic scattering with the d-guest loaded H-MOF compared to the empty MOF. The inelastic intensity increases with the monomer loaded sample, and further with oligomer@MOF. Polymer@MOF shows the highest intensity of inelastic scattering. The increase in elastic scattering with guest inclusion suggests that there is an increase in diffusional motion. It is seen from the EFWS observing MOF structure that it is most rigid in the presence of monomer guest suggesting that the monomer is bound within the pores of the framework. The lack of long-range Fickian diffusion resulting from Brownian motion observed on the monomer@MOF sample further supports the conclusion regarding binding of the monomer. Further studies to confirm this with solid state NMR will be discussed in Section 5.7 of this chapter.

## Chapter 5: Characterisation of Guest interactions in VAc@MOF-5

---

The oligomer and polymer@MOF show a further increase in inelastic scattering. This observation suggests that as the monomer polymerises, there is an increase in diffusion going from oligomer to polymer. The intensity of the polymer also supports the earlier observation from EWFS for h-guest@D-MOF that the polymer remains unbound to the framework in comparison to monomer and oligomer that remain bound, resulting in an increased framework stiffness.

To identify the kinetics and length scale of motion, we investigated the FWHM variation of the inelastic peak with  $Q$ .

### 5.5.3.6 Full Width at Half Maximum (FWHM)

In QENS experiment for samples that follow Fickian diffusion, the solution of the diffusion equation shows that the single-particle intermediate scattering function in  $(Q, \omega)$  space decays exponentially with time [ $I(Q, \omega) = \text{Exp}(-DQ^2\omega)$ , where  $D$  is the translational diffusion coefficient].<sup>38</sup> A Delta function is used to elastic contribution from hydrogens that do not show motion during the experimental time window and length scale. A Lorentzian is used to describe the quasi-elastic broadening (dynamics), and a linear function is included to represent the background signal and dynamics that are much faster than the time window. The corresponding scattering function in  $(Q, E)$  space is a Lorentzian with FWHM represented by Eq 5.10, can be modified to:

$$\Gamma(\text{FWHM}) = \hbar D Q^2 \quad (5.17)$$

Here,  $\hbar$  is the modified Plank's constant. Diffusion in such systems that follow Brownian motion, is described by Fick's Law. Several models can be used to understand the geometry of motion such as translational diffusion (TD) model based on Fick's law of diffusion, for particles when they experience very high energy barriers for diffusion where the guest motion is no longer continuous, but stepwise. Chudley-Elliot (CE) model is applicable for confined guests that undergo jump diffusion on a lattice, Singwi-Sjölander (SS) model for molecules is suited for guests that show oscillatory and directional motions, and Hall-Ross (HR) Model

## Chapter 5: Characterisation of Guest interactions in VAc@MOF-5

that shows jump diffusion of guest molecules within a restricted volume.<sup>44</sup> In the case for guest@MOF, the extracted Q-dependence of the Lorentzian function parameters can be fitted to a jump diffusion model in a restricted volume, Hall-Ross model, to extract information such as jump length, residence time, and diffusion constant. The parameters obtained from the fits are the width and intensities of the Lorentzian peaks, and the intensity of elastic line. The Q dependence of the widths (FWHM) of the Lorentzian peaks are shown in Fig 5.16.

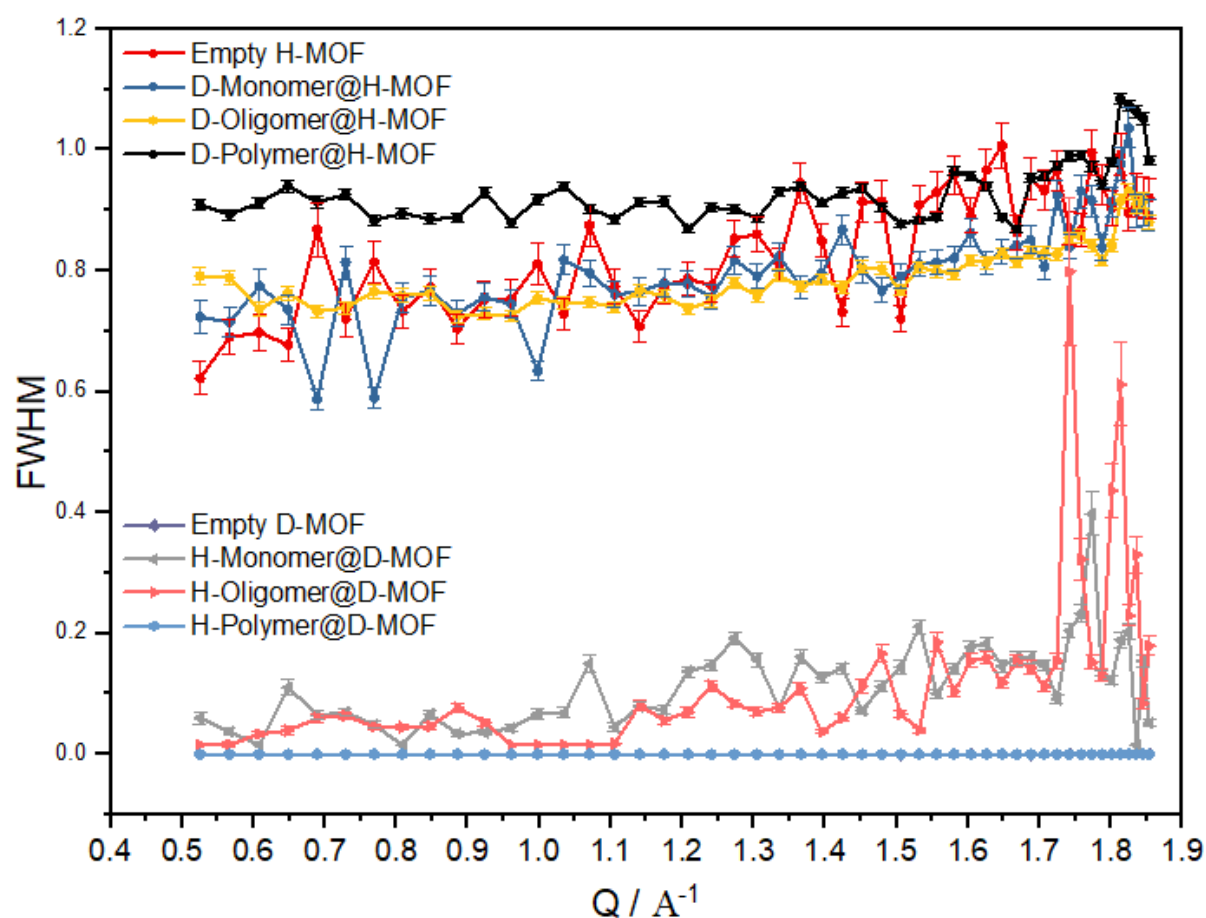


Fig 5.16: The Q dependence of the widths (FWHM) of the Lorentzian peaks for empty MOF and guest@MOF. (The inconsistency in data beyond  $Q = 1.7 \text{ \AA}^{-1}$  is due to weak signal at higher Q derived from the instrument detector for H-Monomer@D-MOF and H-Oligomer@D-MOF).

For the specific samples of empty D-MOF and h-polymer@D-MOF, the data was better fitted to a single Delta model due to elastic scattering dominating in case of these samples. Much of the scattering observed in the case of empty MOF is expected to be by framework deuterium

## Chapter 5: Characterisation of Guest interactions in VAc@MOF-5

---

atoms and data from this sample is expected to be dominated by elastic scattering. This may be because coherent elastic scattering from deuterium is greatly emphasised for empty D-MOF and h-polymer@D-MOF relative to monomer and oligomer@D-MOF due to lack of guest diffusional motion. This in turn, may suggest that in the case of D-MOF with hydrogenated monomer and oligomer guest species, there is translational motion observed but upon polymerisation, the diffusional motion is reduced resulting in decrease in inelastic signal from the polymer hydrogens.

Loss in elastic scattering intensity is accompanied by a gain in inelastic scattering intensity. Thus, quasi-elastic broadening increases linearly with  $Q^2$ , and indicates diffusive motion where the slope is related to the diffusion coefficient. Variation in quasi-elastic peak width (FWHM) over  $Q$  can help understand the length scale and degree of motion for guest species (h-guest@D-MOF) or framework hydrogen atoms (d-guest@H-MOF). Changes in quasi-elastic peak FWHM over  $Q$  shows that the motion of BDC linker protons on empty H-MOF and d-guest@H-MOF composites are confined over the measured length-scales. The variations in the absolute values of scattering due to this loss of elastic intensity and gain in inelastic intensity for d-polymer@H-MOF is lesser compared to empty H-MOF, monomer@MOF-5 and oligomer@MOF. This suggests that there is degree of motion seen on the H-MOF linkers in the case of d-polymer@H-MOF is greater than that seen from monomer@MOF and oligomer@MOF. This supports earlier observed stiffening of the framework in EWFS of d-guest@H-MOF that suggests a greater degree of stiffening with monomer@MOF and oligomer@MOF, compared to the polymer@MOF. Furthermore, observations from EFWS of h-guest@D-MOF also suggest that the h-polymer@D-MOF remains free and less bound to the framework showing a greater degree of motion compared to monomer@MOF and oligomer@MOF. Overall absolute values for d-polymer@H-MOF show greater FWHM of quasi-elastic peak in comparison to empty H-MOF confirms presence of guest species within the framework and provides further support against possibility of polymer chain diffusion out of the framework.

## Chapter 5: Characterisation of Guest interactions in VAc@MOF-5

---

### 5.5.3.7 Elastic Incoherent Structure Factor (EISF)

An important parameter to consider when analysing particle motion in restricted space as in guest@MOF system, is the elastic incoherent structure factor (EISF), that describes the geometry of underlying motions defined by:

$$EISF = \frac{S_0(Q,0)}{S(Q)} = \frac{I_{el}}{I_{el}+I_{qel}} \quad (5.18)$$

The EISF, relative integrated intensities of the incoherent elastic  $I^{el}(Q)$  and quasi-elastic  $I^{qe}(Q)$  components, is indicative of the specific type of motion in localised space. In principle, this can be used to identify changes in guest motion as the monomer polymerised can be compared to each other to observe the changes. Analysis in time-domain  $A_0(Q)$  can be evaluated by considering the Q dependence of the long-time asymptote reached by  $I_s(Q,t) \rightarrow \infty$ . EISF can reveal important information such as geometry of motion in a confined system. However, analysis of EISF was not useful in case of guest@MOF samples due to poor signal from complex samples and detection limitations of the IRIS instrument. Further experiments would also provide data difficult to interpret and there would be no guarantee for successful measurements even with higher performance instruments with greater detection limits, such as LET (ISIS Pulsed Neutron and Muon Source, UK) or IN6B (Institut Laue-Langevin, France).

### 5.6 Conclusion of QENS Experiment.

In conclusion we investigated from QENS experiment and available data, the diffusion of guest molecules in the MOF-5 framework and their influence on the structure. We observe that the guest species are bound to the MOF's framework that result in stiffening of the MOF structure. We examined elastic scattering from the materials through elastic fixed window scan of the elastic peak (EFWS) and analysed shape of Lorentzian curve through inelastic intensity and broadening of elastic peak. Our observations suggest that vinyl acetate monomer remains bound to the MOF framework resulting in greater rigidity of the framework compared to oligomer species and polymer species. This observation supports conclusions derived from total neutron scattering experiment (Section 5.1) that identifies that

## **Chapter 5: Characterisation of Guest interactions in VAc@MOF-5**

---

the monomer primarily remains bound to the framework atoms of the MOF, resulting in framework expansion after guest loading. Observations that a lower proportion of unbound and freely diffusive intrinsic monomer is supported here through lack of evident motion seen from the monomer, and greater elastic scattering observed with monomer@MOF samples relative to polymer@MOF. In contrast, the framework is less constrained in the case of polymer@MOF suggesting that the polymer remains relatively less bound geometrically to the framework atoms. This is supported by the Q dependent changes observed from FWHM of quasi-elastic peak for d-polymer@H-MOF which shows a greater degree of diffusional motion for linker hydrogen atoms. Furthermore, the presence of polymer guest in framework can be confirmed by comparing the absolute values on the FWHM versus Q plot of d-polymer@H-MOF and empty H-MOF. The possibility of polymer chains diffusing out of the framework therefore can be satisfactorily ruled out through evidence from PXRD (Section 4.2), ATR-FTIR (Section 4.3), TGA (Section 4.4), and SEM (Section 4.9) which shows, at this degree of monomer loading, that polymer chains remain within the framework following polymerisation.

## Chapter 5: Characterisation of Guest interactions in VAc@MOF-5

---

### 5.7 $^{13}\text{C}$ solid-state NMR analysis of VAc@MOF-5 Polymerisation

Solid-state NMR (ssNMR) is a powerful characterisation tool that can provide element-specific atomic-resolution insight into materials and is well-established as a technique of various porous materials.<sup>45</sup> As ssNMR yields information about the local structure of the material, it is complementary to diffraction techniques that rely on the existence of long-range order and probe an average crystal structure.<sup>46</sup> As a result, ssNMR provides support to characterisation of the monomer@MOF composite structure and reveals structural changes that may occur during monomer adsorption and polymerisation of the monomer.

Additionally, it can be used to follow the conversion of monomer to polymer, and to locate and quantify the molecules present to support data from neutron scattering experiments.

Therefore, employing ssNMR spectroscopy is crucial for supporting the conclusion of host-guest relationship of MOF.<sup>47</sup>

NMR in solid-state faces two major hurdles. One of achieving a readable NMR signal from the species and the other of precisely quantifying species. The Cross-polarisation – Magic angle spinning (CP-MAS) technique based on orientation averaging produces solution NMR like resolution for solid samples by removing the chemical anisotropy. To achieve a stronger signal, a routinely employed technique is that of cross polarisation (CP), where the signal of a selected atomic nuclei is enhanced via the transfer of spin polarisation from atomic nuclei with larger magnetic moments.<sup>48</sup> CP method is most suitable for atomic nuclei having spin quantum number of  $\frac{1}{2}$  and if the nuclei are coupled with a strong dipolar coupling.  $^1\text{H}$  nuclei have 4 to 10 times larger magnetic moment than  $^{13}\text{C}$ , thus the application of  $^1\text{H}$ - $^{13}\text{C}$  CP approach can greatly enhance the  $^{13}\text{C}$  NMR signals. Both  $^1\text{H}$  and  $^{13}\text{C}$  nuclei are primary constituents of vinyl acetate and BDC linkers on MOF-5, we employed CP MAS method to study VAc polymerisation in MOF-5. Cross-polarisation also circumvents problems with inherently long relaxation times for carbon nuclei. The intensity of the CP signals depends on the so-called contact time; when  $^1\text{H}$  and  $^{13}\text{C}$  are brought in contact and magnetisation is transferred from the former to the latter. As a result, it is possible to infer the chemical nature of potentially mobile carbons associated with the monomer and its influence on the structure of the MOF as strongly bound guest molecules will have a greater contact time, resulting in a greater signal enhancement to  $^{13}\text{C}$  MOF signals compared to the non-interacting guests.

## Chapter 5: Characterisation of Guest interactions in VAc@MOF-5

---

High power  $^1\text{H}$  decoupling (HPDEC) is a technique that can substantially reduce line-broadening by isolating  $^{13}\text{C}$  and  $^1\text{H}$  spin systems during detection. Furthermore, HDEC can be used to quantify the species by isolating  $^1\text{H}$  and  $^{13}\text{C}$  signals of the monomer and polymer. In theory, when observing a dilute spin such as  $^{13}\text{C}$  (1.1% abundance), with  $^1\text{H}$  or other abundant spins nearby, heteronuclear dipolar coupling always causes broadening on a spectrum that is already weak. HPDEC removes the effect of heteronuclear coupling by applying a continuous irradiation of very high power (100-1000 W) at the frequency of proton resonance.<sup>49</sup> The required pulse sequence for the  $^{13}\text{C}$  nuclei is then applied, and the  $^{13}\text{C}$  free induction decay (FID) is measured while continuing the  $^1\text{H}$  irradiation. Hence, as the monomer polymerises the intensity of characteristic monomer signals are expected to decrease, with increments in signals from polymer carbons. The HPDEC spectra can also show the growth and precipitation of oligomers with time.

### 5.7.1 Sample Preparation

Three samples were analysed for referencing and studying the polymerisation process: MOF-5, VAc@MOF-5, and PVAc@MOF-5. MOF-5 and PVAc@MOF-5 were prepared using the methods described in sections 3.2.3 and 3.3.1, respectively. VAc@MOF-5 was prepared by adding a mixture of VAc and AIBN to dried and activated MOF-5 and allowed to soak for 24 h. PVAc@MOF-5 was prepared as VAc@MOF-5, and subsequently polymerised for 72 h at 70 °C under nitrogen.

All measurements were taken and recorded by Dr Nia Richards (Cardiff University) due to restrictions on site access due to COVID-19 pandemic. Data processing and analysis were performed by Dr Colan Hughes (Cardiff University) with input from the candidate for system specific interpretation.

## Chapter 5: Characterisation of Guest interactions in VAc@MOF-5

---

### 5.7.2 $^{13}\text{C}$ MAS NMR Experimental Method

$^{13}\text{C}$  solid-state MAS NMR spectra were recorded at 400 MHz (9.4 T) on a Bruker AVANCE III spectrometer with a 4 mm Bruker MAS NMR probe.  $^{13}\text{C}$  cross-polarised (CP) MAS NMR spectra were performed with a contact time of 5 ms and repetition time of 5 s.  $^{13}\text{C}$  high-power decoupling (HPDEC) MAS NMR spectra were recorded after an excitation with a  $\pi/2$  pulse with a repetition time of 5 s. For  $^{13}\text{C}$  spin-counting experiments, a repetition time of 30 s was performed. The sample spinning rates of ca. 3.5 to 4.5 kHz were applied. All  $^{13}\text{C}$  MAS NMR spectra were referenced to glycine ( $\text{C}_2\text{H}_5\text{NO}_2$ ; CAS: 56-40-06).

Crystalline empty MOF-5, VAc@MOF-5, and PVAc@MOF-5 samples were packed in separate 4 mm Bruker MAS NMR  $\text{ZrO}_2$  rotor with a Vespel (SP1) caps and in a rotor with  $\text{ZrO}_2$  cap for polymerisation experiment. The  $^1\text{H}$ - $^{13}\text{C}$  CP and  $^{13}\text{C}$  HPDEC spectrum for MOF-5, VAc@MOF-5 and PVAc@MOF-5 were collected for reference spectrum at room temperature. For the polymerisation experiment, measurements were taken at temperatures below the polymerisation temperature at 4, 10, 20, 30 and 40 °C to observe any changes in mobility of the linkers on the host and/or guest monomer. Spectral acquisitions were taken at polymerisation temperature of 70 °C from the onset, alternating between CP and HPDEC for an extended polymerisation time of 72 h. Acquisition time for each measurement was 21.5 minutes, accounting to total time of 43 min for a cycle of CP and HPDEC measurement.

## Chapter 5: Characterisation of Guest interactions in VAc@MOF-5

### 5.7.3 $^1\text{H}$ - $^{13}\text{C}$ MAS NMR of MOF-5

$^{13}\text{C}$  CP and HPDEC MAS NMR spectrum of MOF-5 recorded are shown in Fig 5.17.

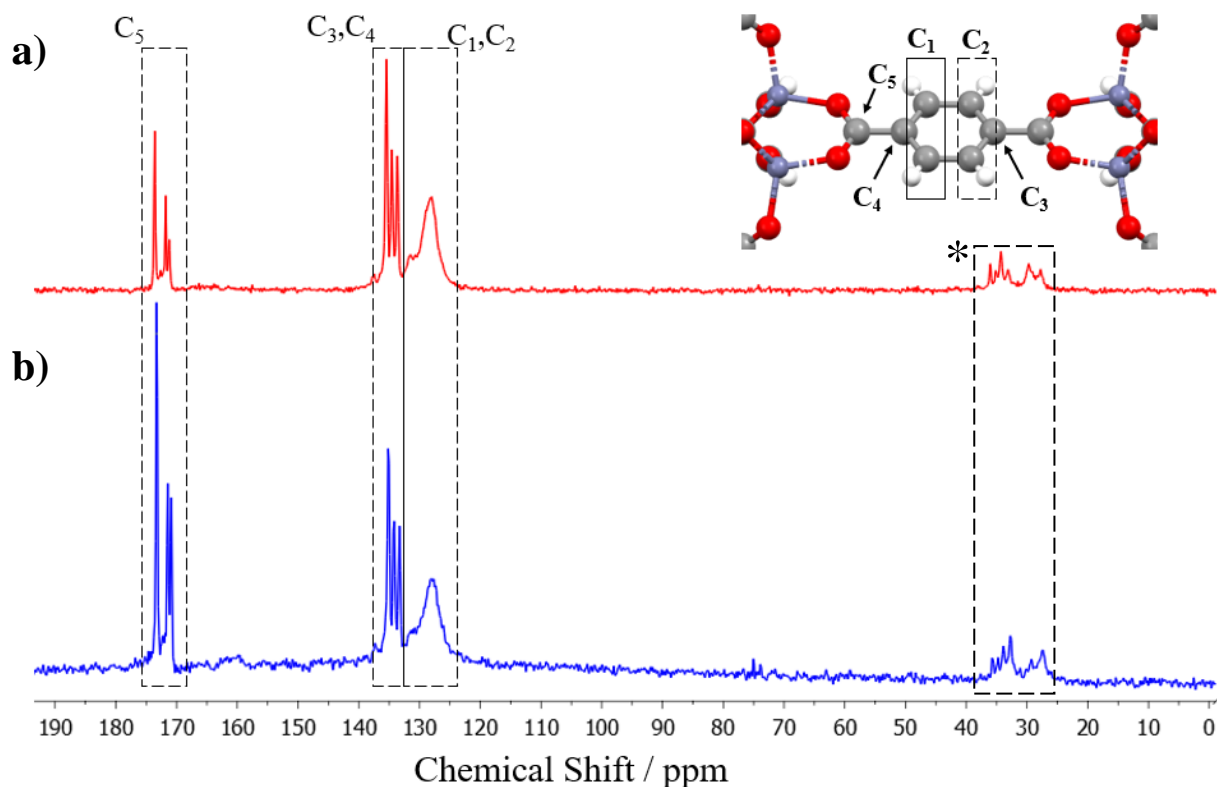


Fig 5.17:  $^1\text{H}$ - $^{13}\text{C}$  MAS NMR spectrum of MOF-5 (a) CP and (b) HPDEC. Expansion of the range 120 – 180 ppm is shown in Appendix A5.1.

MOF-5 forms crystals with density of  $0.59 \text{ g/cm}^3$  and a porosity ranging from 50-55% for hydrogenated MOF-5. The phenyl ring on the BDC is the source of  $\text{C}_1$  and  $\text{C}_2$  signal in the carbon spectrum at 128 and 132 ppm. Additional carbon signals ( $\text{C}_{3,4}$ ) are a contribution from the carbon linking the phenyl ring to the carbon ( $\text{C}_5$ ) linking to  $\text{Zn}_4\text{O}$  tetrahedra and appears at around 138 ppm. The BDC linkers and the nodes formed by the  $\text{Zn}_4\text{O}$  clusters are easily identified in the  $^{13}\text{C}$  NMR by the peak corresponding to  $\text{C}_5$  at 171 ppm.<sup>45</sup>

## Chapter 5: Characterisation of Guest interactions in VAc@MOF-5

The MOF-5 unit cell consists of two different types of alternating cavities that differ slightly in terms of void spaces (Fig 5.18).

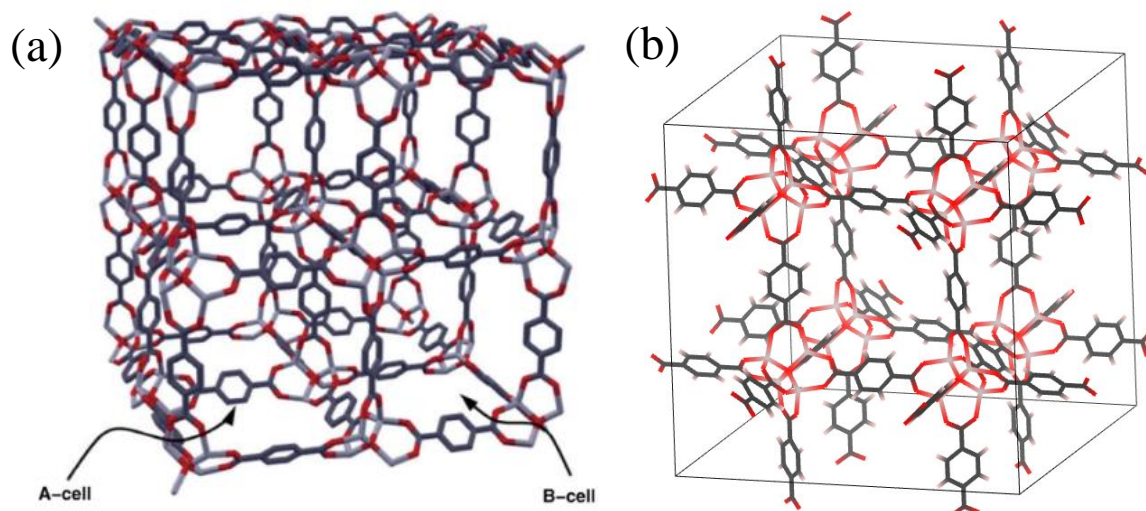


Fig 5.18: (a) The 2x2x2 unit cell of MOF-5 formed by four A- and four B-subcells. (b) single crystallographic unit cell of MOF-5.<sup>50</sup>

The larger sub cell A has a diameter equalling 1.5 nm and the smaller sub cell B with a diameter of 1.1 nm. As a result, the resonances from C<sub>3</sub> and C<sub>4</sub> are present at two adjacent peaks, due to a different chemical environment around respective carbons. The same is true for C<sub>5</sub> peak. From the data obtained, a preliminary analysis of 171 ppm peak from the C<sub>5</sub> carbon showed the least observable changes over the course of the experiment and was therefore used as a reference for quantifying and observing the mobility of the monomer.

MOF-5 unit cell formed by four A- and four B-sub cells determines the accessibility of the metal centres for adsorbed molecules.<sup>30,51</sup> In general, inside the microporous solids adsorbed guest molecules are constantly interacting within the pore walls and as a result, thermally activated motion inside microporous materials can be considered as an activated process.<sup>52</sup>

The <sup>13</sup>C CP NMR spectrum of the VAc@MOF-5 sample is shown in Fig 5.19.

## Chapter 5: Characterisation of Guest interactions in VAc@MOF-5

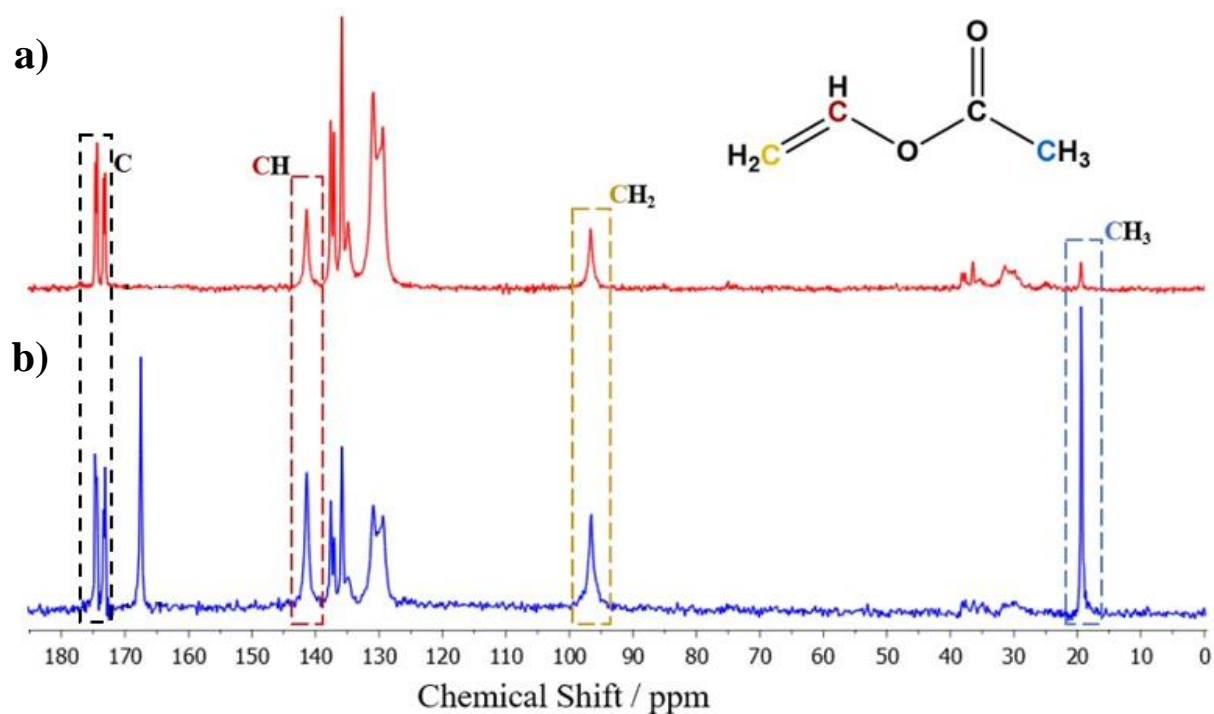


Fig 5.19:  $^1\text{H}$ - $^{13}\text{C}$  MAS NMR spectrum of VAc@MOF-5 (a) CP and (b) HPDEC. The box (dotted lines) indicate key regions of the spectra, as described in the text.

A sharp singlet at 19 ppm originates from the methyl carbon associated to the acetyl group on the monomer molecule. No compositional nor configurational splitting is observed on the peak and is in line with the literature reported and solution NMR results of the monomer. The methylene carbon resonance lines appear at 97 ppm. The methine carbon peaks of the acetate give rise to a single peak adjacent to the MOF-5 resonance peaks in the range of 128 – 134 ppm, at 141 ppm. The carbonyl carbon from the acetyl group appears as a peak at 168 ppm.

The  $^{13}\text{C}$  CP NMR spectrum of PVAc@MOF-5(L) sample is shown in Fig 5.20.

## Chapter 5: Characterisation of Guest interactions in VAc@MOF-5

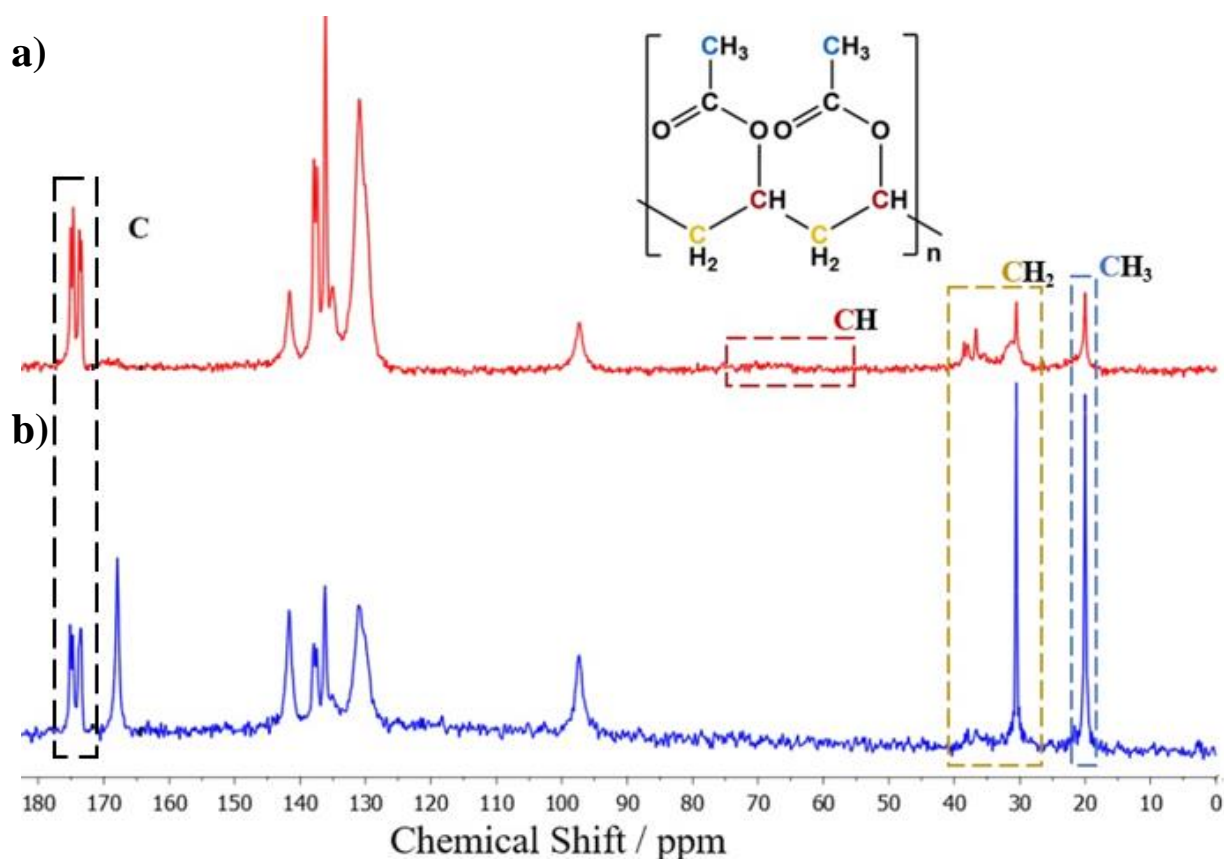


Fig 5.20:  $^1\text{H}$ - $^{13}\text{C}$  MAS NMR spectrum of PVAc@MOF-5 (a) CP and (b) HPDEC. The box (dotted lines) indicate key regions of the spectra, as described in the text.

The methyl carbon associated with the branching acetyl group on the polymer backbone remains in the region of 19 ppm. The methyl resonance signal overlaps with the residual monomer peak in the same region, however, the base of the peak increasing in width. The methylene carbon peaks appear in the region between 28 and 38 ppm as broad signals, rising highest at 32 ppm and 38 ppm respectively. The methine carbons substituted by the acetate group give rise to a complicated spectrum at 60 – 65 ppm due to different configurational and compositional splitting (red dotted box in Fig 5.18). The carbonyl carbons from acetyl side group resonates at 168 ppm. Recording the C=O region with sufficient data points gives rise to two well resolved lines at 174.4 and 176.8 ppm (black box in Fig 5.20).

## Chapter 5: Characterisation of Guest interactions in VAc@MOF-5

---

### 5.7.4 Data Analysis and Fitting

To analyse changes in the peak intensities, peak shape, and the appearance of new peaks plus the changes in integrations of monomer, polymer, and MOF-5 signals were calculated using MestReNova NMR (Mestrelab Research, S.L.) and Wolfram Mathematica software.<sup>53,54</sup> The integral values were fitted to an exponential decay curve (Eq. 5.19) and least squared fitting by the Levenberg–Marquardt algorithm to avoid local minima in finding the best fit for experimental data of the integrals. Analysis was initiated from first two starting points and the fit with the lowest  $\chi^2$  was chosen.<sup>§</sup>

$$y = y_0 + A_1 e^{\frac{-x}{t_1}} \quad (5.19)$$

$$\text{And } k = \frac{1}{t_1} \quad (5.20)$$

(Where;  $y_0$  is the intercept,  $A_1$  is the pre-exponential factor, and  $t_1$  is the time constant for the reaction, and  $k$  = rate constant for the reaction)

Estimated amplitude and decay constants were determined from Eq 5.20 by fitting the integrations using the Levenberg–Marquardt non-linear least squared algorithm fitting function in OriginPro 2020b (OriginLab, USA) which is an iterative procedure which combines the Gauss-Newton method and the steepest descent method to give estimated amplitudes and decay constants with associated standard errors for the exponential components.<sup>55</sup> No allowance was made for gradient nonuniformity and pure exponential decay as a function of gradient square was assumed. Integrals belonging to MOF-5 signals in the <sup>13</sup>C HPDEC spectrum were fitted as a linear fit (with gradient zero) because it was not expected that the quantity of MOF changes during the NMR experiment.

Polymerisation kinetics can be analysed with several models. The rate of solid-state isothermal reactions is usually shown by Eq 5.21

---

<sup>§</sup> Integrals for polymerisation reaction were fitted to first-order kinetics. Rate of vinyl acetate conversion depends only on the decay rate constant and the concentration of the initiator. Reaction initiation and chain propagation are expected to decrease exponentially as VAc is converted into PVAc polymer.

## Chapter 5: Characterisation of Guest interactions in VAc@MOF-5

---

$$\frac{d\alpha}{dt} = kf(\alpha) \quad (5.21)$$

And, 
$$f(\alpha) = n(1 - \alpha)[- \ln(1 - \alpha)]^{(m-1)/m} \quad (5.22)$$

Here,  $k$  is the reaction rate constant,  $f(\alpha)$  is the reaction model and  $\alpha$  is the conversion fraction. The results from the  $^{13}\text{C}$  HPDEC data was used to calculate the monomer to polymer conversion by observing well resolved peaks at 97 ppm and 141 ppm, using the exponential decay fitted integrals from the polymerisation experiment. The dynamics and monomer conversion were calculated using the Avrami-Erofeev model (Eq. 5.23).

$$- \ln(1 - \alpha) = (k_i t)^m \quad (5.23)$$

Where  $\alpha$  is the fraction of reacted monomer,  $k_i$  is the overall reaction rate constant of the polymerisation reaction,  $t$  is the decay time of the exponential, and  $m$  is the Avrami constant of dimensional growth ( $m = 1$  for one-dimensional growth).

A major limitation of the Avrami-Erofeev model is that it does not distinguish between nucleation and a growth process.<sup>56</sup> The model assumes that the material growth occurs by stepwise addition of individual molecules at a constant rate. In theory, the Avrami constant consists of information regarding the dimensionality and mechanism of growth. Three regimes are often described as diffusion mechanism ( $m = 0.5-0.6$ ), one-dimensional or point growth ( $m = 1.0$ ), two-dimensional or spherical growth in more than one direction ( $m = 2, 3, 4$ ). We expect polymerisation to be a one-dimensional or point growth where oligomers are formed by successive addition of monomer molecules in the chain propagation step. We have also considered two-dimensional growth ( $m = 2$ ) to determine its probability of a two-dimensional growth occurring and to directly relate values to one-dimensional growth. However,  $m = 2$  yields a negative value of  $\alpha = -1.7$ , thus ruling out the possibility of a two-dimensional growth. Considering  $m = 3$ , the values for  $\alpha$  are like those obtained considering one-dimensional growth ( $\alpha = 0.63$ ). Vinyl acetate forms an unbranched homopolymer from

## Chapter 5: Characterisation of Guest interactions in VAc@MOF-5

---

in a chain growth progressive addition of monomer molecules during chain propagation step of the polymerisation. It is likely that the assumption of three-dimensional growth ( $m = 3$ ) gives reasonable values due to the inability of Avrami-Erofeev model to discern between nucleation and growth processes. Development of local exothermic ‘hot-spots’ within the MOF framework initiates polymerisation at different locations resulting in chain propagation to commence and increasing monomer diffusivity within the framework.

### 5.7.5 Results and Discussion

#### 5.7.5.1 Temperature Ramp Experiment.

A temperature ramp experiment prior to initiation of polymerisation at 70 °C was performed on VAc@MOF-5 sample to observe changes in the mobility of the monomer and phenyl rings of MOF-5’s linker.

The experiment involved acquiring CP spectrum of the VAc@MOF-5 sample at 4, 10, 20, 30, 40 °C and initiating polymerisation at 70 °C. The heating on the instrument is by hot gas stream where a variable temperature gas stream which flows towards the centre of the spinning rotor containing the sample to accomplish VT. The bearing and drive gas streams that spins the rotor remain at room temperature. As a result, a temperature gradient is established from the centre of the sample towards the end of the rotor. Hence, to mitigate this effect, the instrument was allowed to reach the set temperature and allowed to equilibrate for 30 minutes before commencing  $^{13}\text{C}$  CP spectral acquisition. (Fig 5.21)

## Chapter 5: Characterisation of Guest interactions in VAc@MOF-5

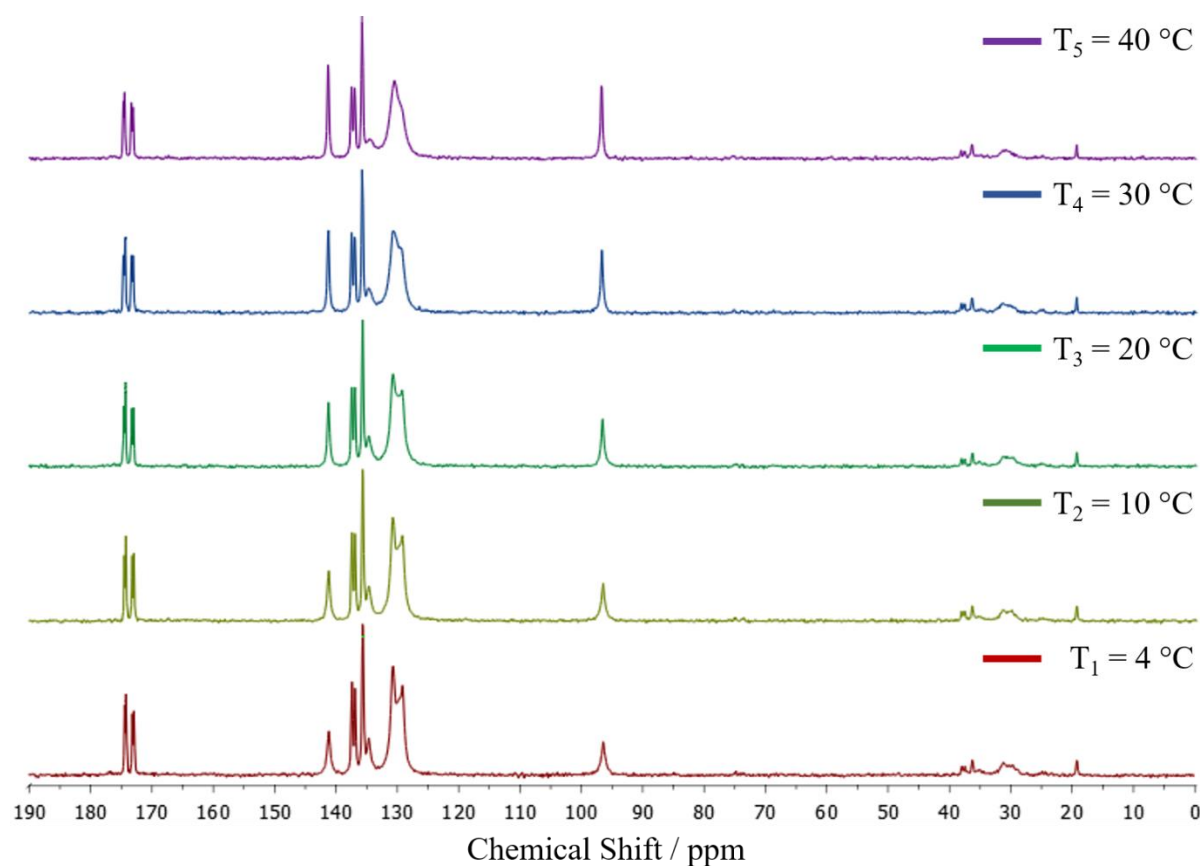


Fig 5.21:  $^{13}\text{C}$  CP MAS NMR spectrum of VAc@MOF-5 at set temperatures during the temperature ramp step. Monomer and expected (if present) polymer peaks positions:  $^{13}\text{C}$  NMR:  $\delta = 19$  ppm ( $\text{CH}_3$  – Monomer/Polymer), 31 and 38 ppm ( $\text{CH}_2$  – Polymer), 97 ppm ( $\text{CH}_2$  – Monomer), 128 ppm ( $\text{C}_1, \text{C}_2$  – MOF), 136 ppm ( $\text{C}_3$  – MOF), 138 ppm ( $\text{C}_4$  – MOF), 141 ppm ( $\text{CH}$  – Monomer), 168-170 ppm ( $\text{C}_5$  – MOF).

As seen in Fig 5.21, all monomer and MOF-5 characteristic peaks can be identified in the temperature ramp experiment from 4  $^\circ\text{C}$ . There is an increase in integral of the monomer peaks at 19, 97, 141 and 168 ppm as the temperature increases consistent with the monomer becoming more mobile as the sample temperature increases. No additional polymer peaks can be observed developing in the characteristic chemical shift regions and no broadening in the  $\text{CH}_3$  region of monomer and polymer overlapping region at 19 ppm is observed, suggesting that no significant polymerisation occurs during the experiment.

## Chapter 5: Characterisation of Guest interactions in VAc@MOF-5

---

Characteristic peaks associated with the phenyl ring of the linker on the other hand, show a decrease in mobility with the increase in temperature. Based on interpretation of data from the 70 °C, it is reasonable to assume that this effect is likely due to the steric hindrance imposed by mobile monomer molecules that saturate the MOF pores. As the temperature increased, mobility of the monomer increases within the microporous MOF and increase in steric effects and dynamic binding to restrict the free rotation of the phenyl ring. In addition, at T<sub>1</sub> the CH peaks from MOF-5's phenyl linker at 128 ppm is in form of a *pake* doublet pattern which begins to merge into a broad single peak as the temperature increases. This feature is characteristic of phenyl ring rotation observed in MOFs where the increase in flip-rotation around C<sub>2</sub> principal axis.<sup>57,58</sup>

The region 134 to 138 ppm features two sets of double peaks (assigned as C<sub>3</sub> and C<sub>4</sub>) that arise from identical carbons on that phenyl ring that bridges with C<sub>5</sub> carbon. The peak at lower chemical shift is a sharp single peak with an accompanying shoulder that diminishes as the temperature increases as the sharp single peak is relatively unchanged. This is a temperature effect of change in linker mobility as observed with CH peaks at 128 ppm. On the other hand, signals downfield show a decrease in intensity with the increase in temperature the C<sub>5</sub> peaks at 168–171 ppm. These effects suggest that upon increasing the temperature from 4 to 40 °C while the phenyl ring rotation increases along its axis, the MOF itself becomes rigid in presence of guest molecules in the framework.

### 5.7.5.2 Polymerisation Experiment

Considering parameters for individual peak changes for VAc@MOF-5 during polymerisation allowed us to identify changes in mobility (through <sup>13</sup>C-<sup>1</sup>H CP NMR) and quantify monomer conversion (<sup>13</sup>C-<sup>1</sup>H HPDEC NMR) by observing peak integrations. The results of Avrami-Erofeev model analysis for VAc@MOF-5 are collated and tabulated as Table 5.5, Table 5.6, and shown in Fig 5.22. (Shown on the next page)

## Chapter 5: Characterisation of Guest interactions in VAc@MOF-5

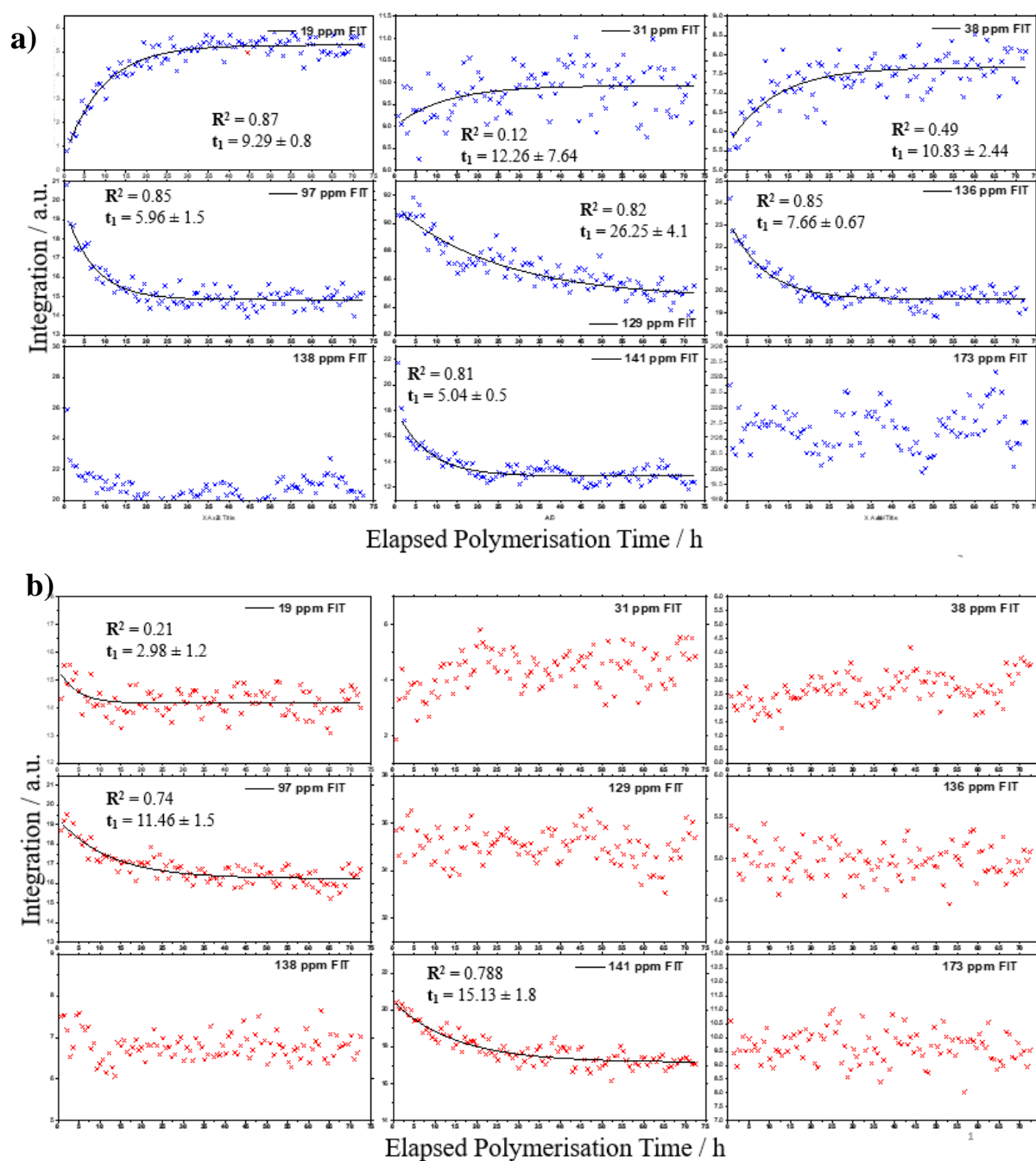


Fig 5.22:  $^{13}\text{C}$  (a) CP and (b) HPDEC exponential fits of peak integral values for all resonance peaks. (Blue and red crosses indicate the integral values and black lines indicate the fit. Plots without black fit line could not meaningfully be fitted to linear or exponential kinetics.)

## Chapter 5: Characterisation of Guest interactions in VAc@MOF-5

Table 5.5:  $^{13}\text{C}$  CP MAS NMR exponential fit  $R^2$  values with corresponding decay time and rate constants.

$^{13}\text{C}$ CP NMR Signal	Source	$R^2$	Time Constant ( $t_1$ )		Rate Constant (k)	
			Value	Error ( $\pm$ )	Value	Error ( $\pm$ )
19 ppm	Mono/Poly ( $\text{CH}_3$ )	0.87	9.3	0.3	0.11	0.01
31 ppm	Polymer ( $\text{CH}_2$ )	0.12	12.3	7.6	0.09	0.05
38 ppm	Polymer ( $\text{CH}_2$ )	0.50	10.8	2.4	0.09	0.02
97 ppm	Monomer ( $\text{CH}_2$ )	0.85	5.9	0.5	0.14	0.01
128 ppm	$\text{CH}_{(\text{Phenyl})} - \text{MOF}$ ( $\text{C}_1, \text{C}_2$ )	0.82	26.2	4.1	0.04	0.01
136 ppm	$\text{C}=\text{C} - \text{MOF}$ ( $\text{C}_3$ )	0.85	7.7	0.7	0.12	0.01
138 ppm	$\text{C}=\text{C} - \text{MOF}$ ( $\text{C}_4$ )	0.45	2.6	0.6	0.20	0.07
141 ppm	$\text{CH} - \text{Monomer}$	0.81	5.1	0.5	0.13	0.01
173 ppm	$\text{O}-\text{C}-\text{O} - \text{MOF}$ ( $\text{C}_5$ )	0.01	-	-	-	-

Table 5.6:  $^{13}\text{C}$  HPDEC MAS NMR exponential fit  $R^2$  values with corresponding decay time and rate constants.

$^{13}\text{C}$ HPDEC NMR Signal	Source	$R^2$	Time Constant ( $t_1$ )		Rate Constant (k)	
			Value	Error ( $\pm$ )	Value	Error ( $\pm$ )
19 ppm	Mono/Poly. ( $\text{CH}_3$ )	0.21	2.9	0.3	0.34	0.13
97 ppm	Monomer ( $\text{CH}_2$ )	0.74	11.46	1.5	0.09	0.01
141 ppm	$\text{CH} - \text{Mono}$	0.79	15.13	1.8	0.07	0.01

Figures 5.23, 5.24, 5.26, 5.27, 5.28 and 5.29 show the components of figure 5.22. The assignments and behaviour of each set of signals are discussed below.

## Chapter 5: Characterisation of Guest interactions in VAc@MOF-5

### 19 ppm: CH<sub>3</sub> Monomer-Polymer Overlapping Methyl Signal

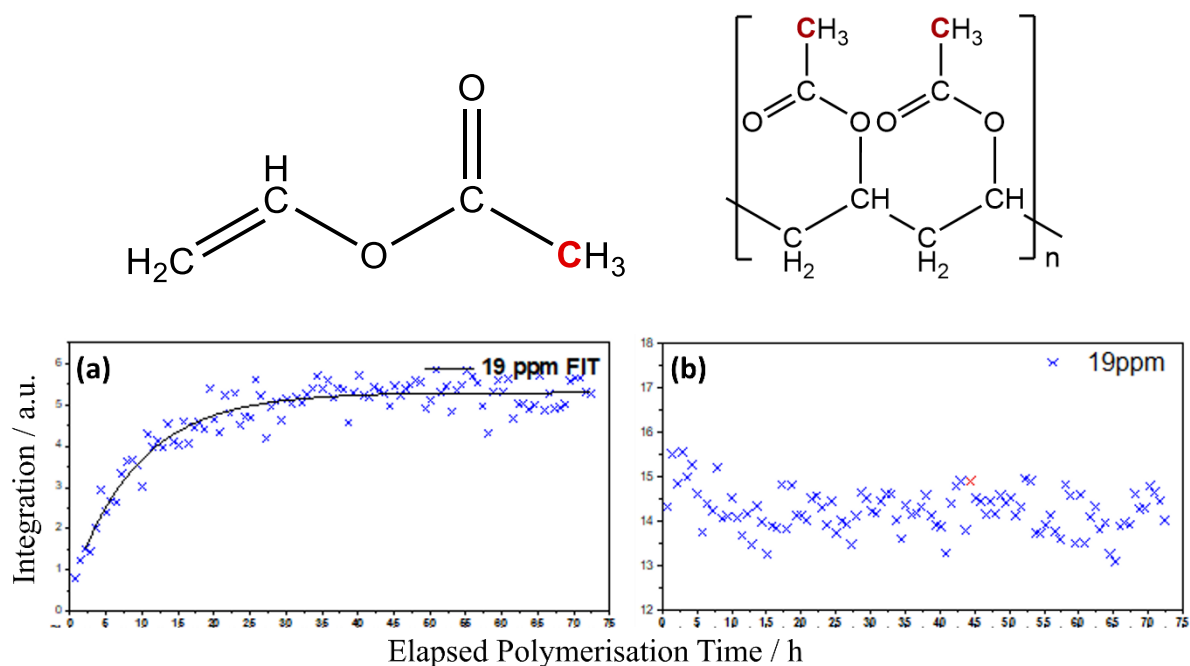


Fig 5.23: <sup>13</sup>C (a) CP and (b) HPDEC exponential fits of peak integral values for resonance peak at 19 ppm. (Blue crosses indicate the integral values fit to exponential fit – black lines)

Fig 5.23 shows exponential fits for integration values of CP spectra show a steady increase in mobility of the monomer and polymer species with a steady and steep increase up to 15 h, followed by a gradual increase beyond 15 h up to 45 h. Overall, an exponential fit to these data was good with a  $R^2 = 0.87$  and  $t_1 = 9.3 \pm 0.8$  h. The peak behaviour suggests an increase in mobility of this carbon as the polymerisation time progresses as more monomers are converted to polymer. Since the contact time coupling parameter are sensitive to dynamic averaging, it is possible to measure local mobility by CP MAS. The polymerisation can be monitored by observing changes in integration area of monomer peaks, as it is expected that the overall mobility of monomer will decrease as it is converted into polymer. The 19 ppm peak begins as a sharp singlet for the monomer and widens at the base (19 – 20 ppm) as overlapping polymer peaks grow during the experiment.

As the monomer and polymer peaks overlap, it is not possible to differentiate between, and quantify the possible increase in polymer species and decrease in monomer species in the

## Chapter 5: Characterisation of Guest interactions in VAc@MOF-5

HPDEC data. Additionally, the initial peak is very intense, making quantification impossible. Consequently, these peaks were not used for further analysis.

### 30-40 ppm: CH<sub>2</sub> Polymer Methylene Signal

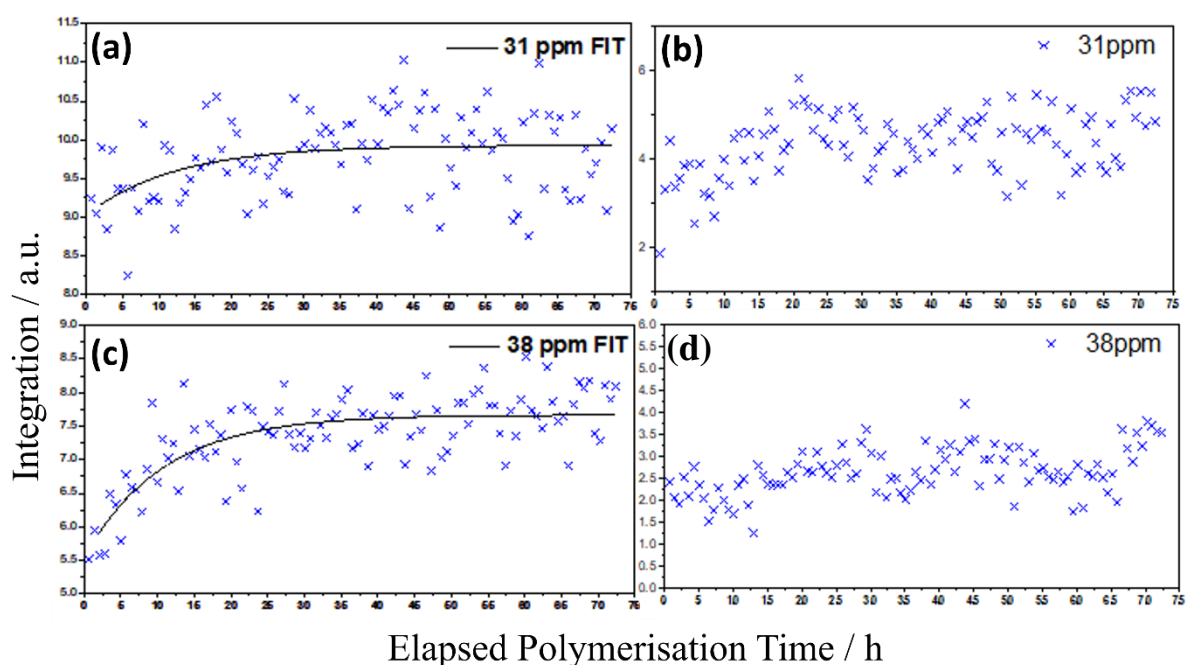
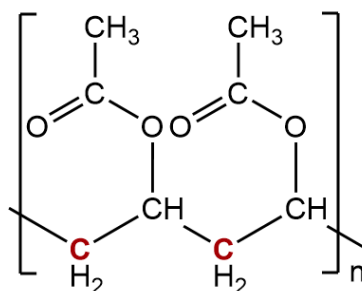


Fig 5.24: <sup>13</sup>C (a, c) CP and (b, d) HPDEC exponential fits of peak integral values for resonance peak at 31 and 38 ppm. (Blue crosses indicate the integral values fit to exponential fit – black lines)

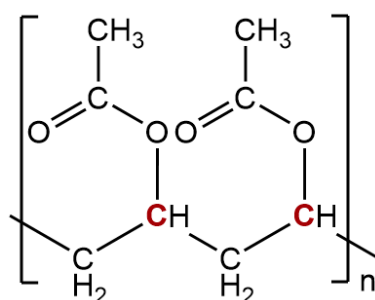
Integration changes over the course of the experiment were small, and as a result, exponential fits for both CP and HPDEC experiment were poor (Fig 5.22). The peaks were fitted to a Gaussian curve and the integration values was calculated based on the curve. However, due

## Chapter 5: Characterisation of Guest interactions in VAc@MOF-5

to large signal-to-noise, the integrations were inconsistent. The methylene peaks in the HPDEC spectra were poorly resolved and difficult to separate from the noise.

The polymer gives rise to two characteristic broad signals at 31 and 38 ppm. This indicates that two different chemical interaction environments are experienced by the polymer backbone. One possibility is one peak appears from interaction with the metal node and the second from unbound polymer experiencing weak interaction with the phenyl ring on the linker. Another possibility is that we are observing the difference between bound and unbound polymer in the framework whereby the latter is occupying the void spaces within the MOF, and the former interacting with the framework atoms. It is also possible that the combination of these two effects is occurring.

### 60-75 ppm: CH Polymer Methine Signal



A broad signal corresponding to methine peak develops in the region between 60 – 75 ppm as the polymerisation progresses. However, due to the low intensity of the signals, it was not possible to quantify and extract integration values or fit the change in integral over time. As a result, no analysis was carried on this peak. Fig 5.25 shows 2D contour plots of <sup>13</sup>C CP and HPDEC NMR spectrum over the experiment time of 72 h.

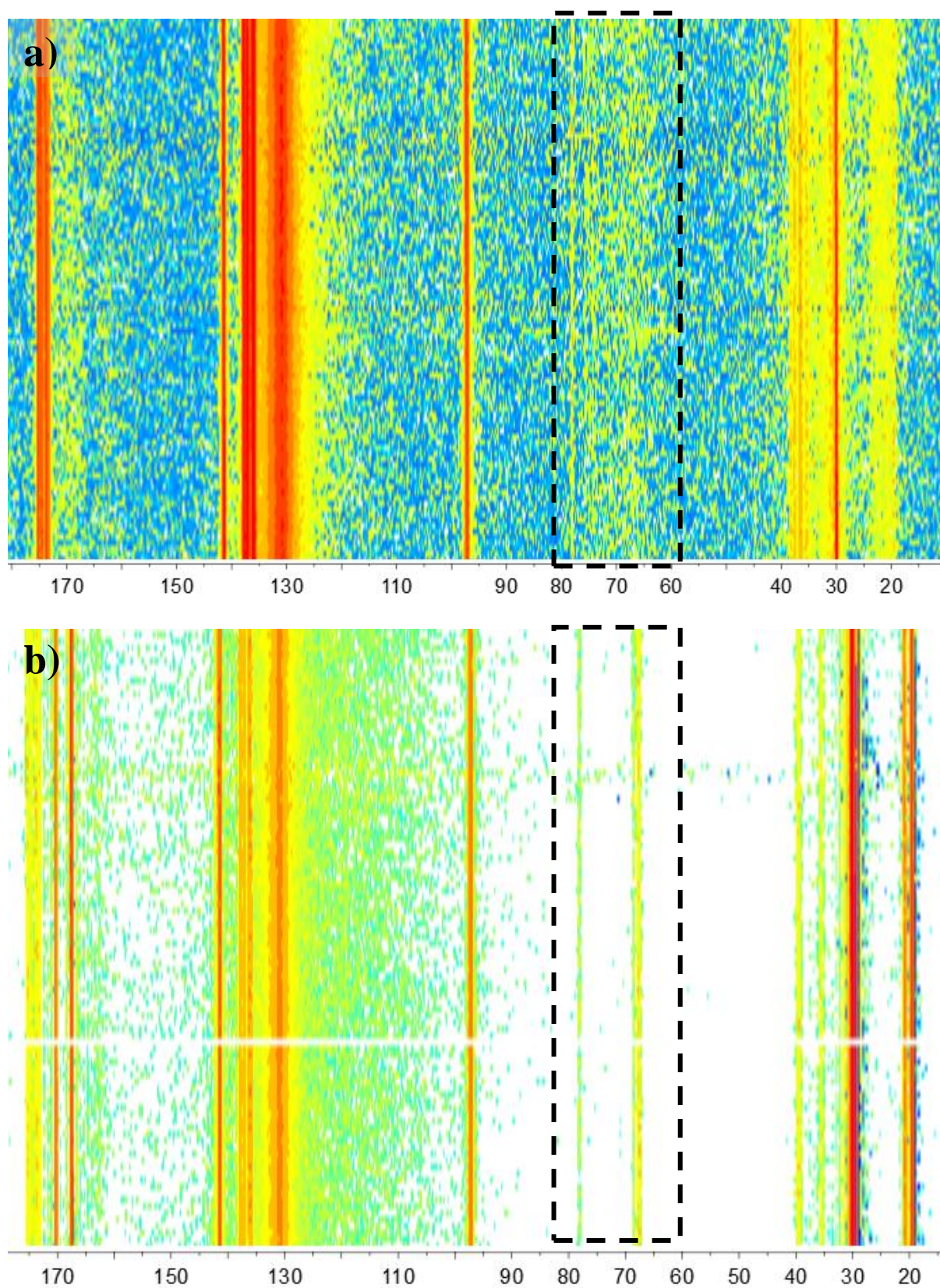


Fig 5.25: 2D contour plots of  $^{13}\text{C}$  (a) CP and (b) HPDEC spectrum over the experiment time of 72 h. Black box with dotted line shows the region of development of methine signal from the polymer over time.

## Chapter 5: Characterisation of Guest interactions in VAc@MOF-5

### 97 ppm: CH<sub>2</sub> Monomer Methylene Signal

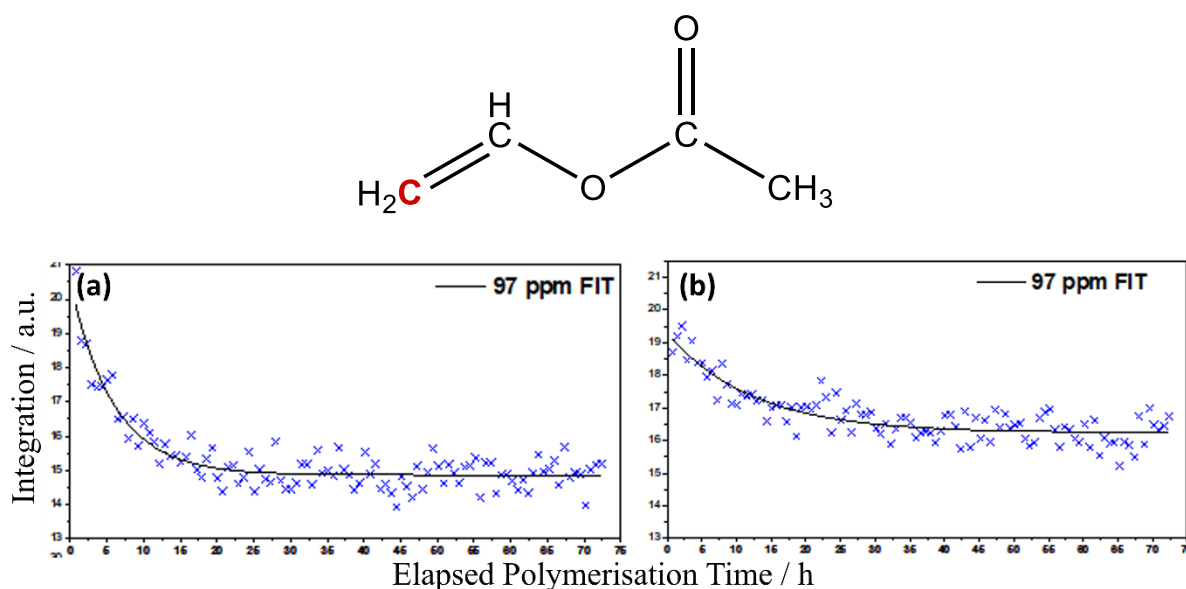


Fig 5.26: <sup>13</sup>C (a) CP and (b) HPDEC exponential fits of peak integral values for resonance peak at 19 ppm. (Blue crosses indicate the integral values fit to exponential fit – black lines)

In Fig 5.26, the CH<sub>2</sub> monomer peaks in the CP spectrum shows an evident decrease over time, and integrals and can be fitted exponentially with  $R^2 = 0.81$  and  $t_1 = 6.8 \pm 0.7$  h. This decrease suggests that the mobility of the methylene group of the monomer decreases during polymerisation but does not reach zero. This is suggestive of incomplete polymerisation, possibly due to saturation of MOF pores with polymer chains.

HPDEC data could be fitted to an exponential decay with a  $R^2 = 0.75$  and  $t_1 = 12.3 \pm 1.6$  h. This decrease in observable monomer signal in the HPDEC data is due to a reduction in the monomer amount as it is converted to polymer. At the end of the experiment, the methylene signal is still present and consistent with incomplete conversion. These fit parameters were used to calculate conversion through Avrami-Erofeev equation resulting in  $\alpha = 0.632$  or 63.2 % monomer conversion to polymer. (Section 5.5.4 and Table 5.7)

## Chapter 5: Characterisation of Guest interactions in VAc@MOF-5

Table 5.7: Estimated percentage conversion from Avrami-Erofeev equation compared to conversion values calculated from TGA and  $^1\text{H}$  NMR.

$^{13}\text{C}$ HPDEC peak assignment	Avrami-Erofeev Conversion ( $\alpha$ ).	TGA Calculated Deg. of Polym.	Estimated $^1\text{H}$ NMR Conversion
97 ppm – Monomer ( $\text{CH}_2$ )	0.63	$0.8 \pm 0.05$	0.68

### 141 ppm: CH Monomer Methine Signal

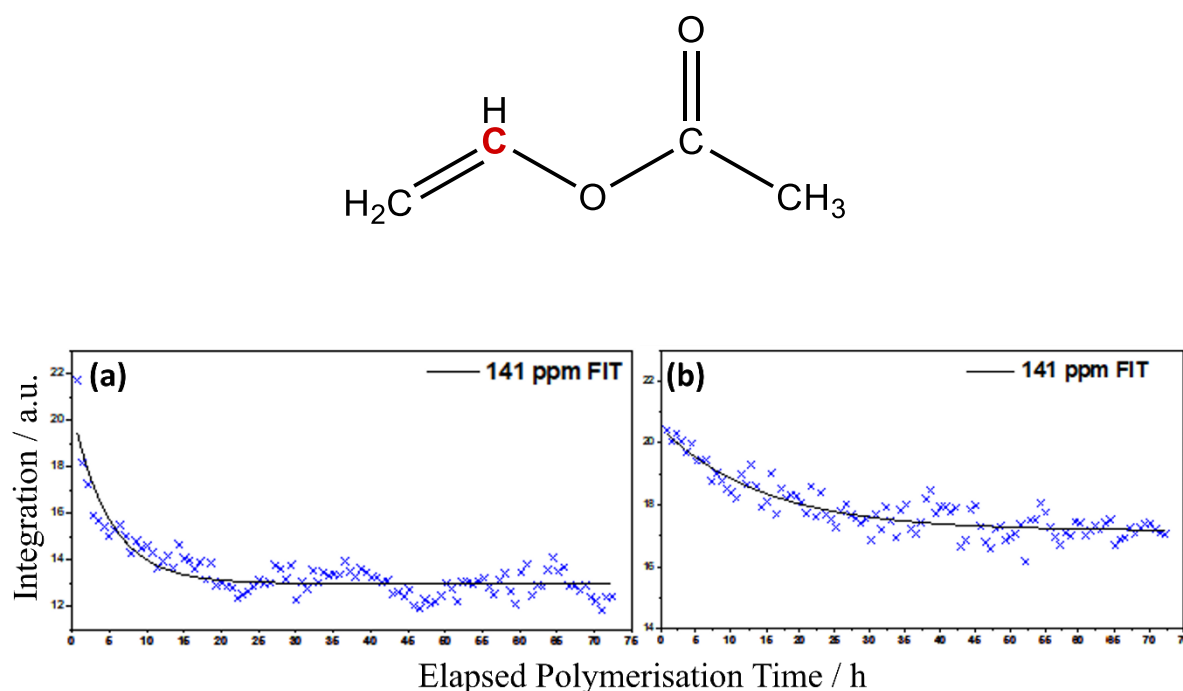


Fig 5.27:  $^{13}\text{C}$  (a) CP and (b) HPDEC exponential fits of peak integral values for resonance peak at 141 ppm. (Blue crosses indicate the integral values fit to exponential fit – black lines)

Like the methylene signal of the monomer, the methine signal shows similar exponential decay with acceptable exponential fits ( $R^2 = 0.81$  and  $t_1 = 5.04 \pm 0.5$  h) (Fig 5.27). The methine signal is present after the experiment suggesting incomplete monomer conversion. The presence of methine and methylene peaks on CP data after the experiment suggest that the carbons associated with CH and  $\text{CH}_2$  on the monomer have unrestricted and free motion, unlike the vinylic C and methyl carbon (that interact with the framework) that have inhibited its motion are indicative of the interactions within the framework.

## Chapter 5: Characterisation of Guest interactions in VAc@MOF-5

---

Integrations from HPDEC data results in an acceptable fit with a  $R^2 = 0.8$  and  $t_1 = 14.9 \pm 1.8$  h. In the HPDEC experiment, there is a constant decrease in integral values of the monomer signal, but it is still present after the end of experiment, supporting the changes observed in the  $\text{CH}_2$  monomer peak at 97 ppm. Exponential fit on the HPDEC integration data ( $R^2 = 0.8$  and  $t_1 = 14.9 \pm 1.8$  h) was used to calculate conversion through Avrami-Erofeev equation resulting in  $\alpha = 0.631$  or 63.1 % monomer conversion to polymer. The conversion values observed here are closely similar to the values earlier obtained from  $\text{CH}_2$  monomer (97 ppm) peak ( $\alpha = 0.632$  or 63.2 %) and calculated from  $^1\text{H}$  NMR and TGA. (Table 5.8)

Table 5.8: Estimated percentage conversion from Avrami-Erofeev equation compared to conversion values calculated from TGA (Section 4.4) and  $^1\text{H}$  NMR (Section 4.5).

$^{13}\text{C}$ HPDEC peak assignment	Avrami-Erofeev Conversion ( $\alpha$ ).	TGA Calculated Deg. of Polym.	Estimated $^1\text{H}$ NMR Conversion
141 ppm – Monomer ( $\text{CH}_2$ )	0.63	$0.8 \pm 0.05$	0.68

## Chapter 5: Characterisation of Guest interactions in VAc@MOF-5

### 168-171 ppm: C Monomer-Polymer Overlapping Carbon Signal

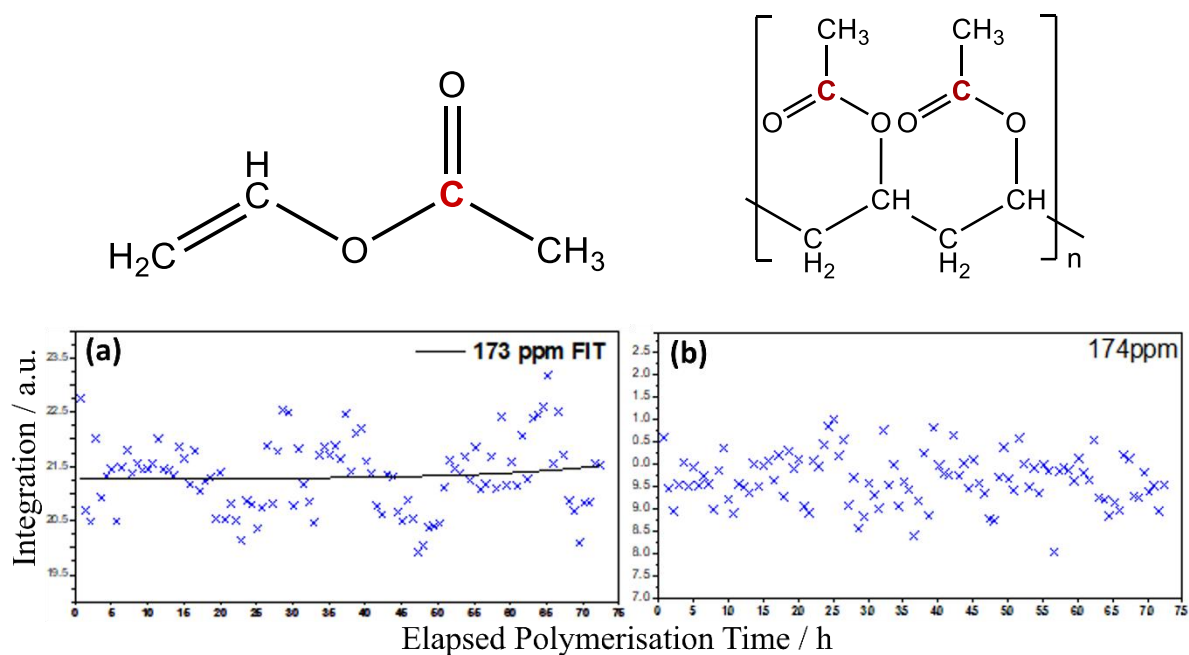


Fig 5.28:  $^{13}\text{C}$  (a) CP and (b) HPDEC exponential fits of peak integral values for resonance peak at 168-171 ppm. (Blue crosses indicate the integral values fit to exponential fit – black lines)

The acetate carbon signal arises from the polymer and monomer at 168 ppm in CP and at 171 ppm in HPDEC spectrum and is overlapped with MOF signal arising from C=O bond (Fig 5.28). As a result of this multiple overlapping signals, the integration values are could not be accurately determined to extract useful information. Exponential fitting was poor due to large fluctuations in the integral values.

### 5.8 Summary and Conclusion for Polymerisation.

Monomer mobility changes in the integration values for the resolved CH and CH<sub>2</sub> monomer peaks in the  $^{13}\text{C}$  CP spectra show a steep decrease in mobility of the monomer for 15 h, followed by a gradual decrease from 15 – 45 h. This suggests that the monomer becomes less mobile during the initial phase and then remains mobile at the end of the experiment. It is most likely that this is a result of incomplete conversion of the monomer to polymer. This is supported by calculations for monomer conversion by Avrami-Erofeev equation ( $\alpha = 0.63$ ).

## Chapter 5: Characterisation of Guest interactions in VAc@MOF-5

---

Due to overlapping signals of monomer and polymer at 19 ppm and 168/171 ppm, it is difficult to observe the monomer mobility for the CH<sub>3</sub> and C signals and extract useful information. However, as the carbons associated with CH<sub>2</sub> and CH groups show little change in the signal intensity on the <sup>13</sup>C CP spectrum, it is reasonable to assume that the associated carbons have unrestricted and free motion. On the other hand, although the vinylic C and methyl signals cannot be integrated to extract reasonably accurate integral values, the monomer signal intensity can be seen to visibly decrease. This may suggest that their motion is restricted due to interaction with the framework atoms. Further investigation of identifying binding sites through SCXRD further support this hypothesis (Section 5.9.2).

<sup>13</sup>C HPDEC spectrum quantifies the number of mobile species present in the sample under investigation.<sup>59</sup> The characteristic monomer peaks show a continuous decrease up to 15 h of polymerisation time and levels beyond 15 h to the end of the experiment (72 h). The monomer peaks remain appreciably present in the HPDEC spectrum after the experiment, confirming incomplete polymerisation. Calculations for monomer conversion through Avrami-Erofeev equation with Avrami constant ( $m$ ) = 1, 3 suggest a 63 % conversion ( $\alpha$  = 0.63) of monomer to polymer which agree with the conversion calculated by other characterisation methods such as <sup>1</sup>H NMR, TGA and MALDI. Integration values derived from the HPDEC spectra of the methine (141 ppm) and methylene (97 ppm) groups on the monomer does not show a drop of 60–65 %. Due to the alternating CP and HPDEC experiments, the first HPDEC spectrum was acquired at  $t$  = 1 h after reaching 70 °C, and the prior spectrum at 40 °C. Therefore, during this period there may have been some polymerisation at 70 °C, prior to reaching the first HPDEC spectrum and possibly at lower temperatures as well which would explain an observable drop less than 60%. To confirm that  $\alpha$  = 0.63 was a reasonably accurate value for monomer conversion, reverse calculations to estimate the amount of elapsed time required to achieve this resulted in  $t$  = 14 h.

This suggests that initiation of polymerisation is rapid, and possibly occurs earlier at temperatures lower than 70 °C. Unfortunately, the polymer characteristic peaks and the comparable decrease in monomer peaks observed due to the poor signal-to-noise ratio. Due to the complexity of the three-component system and present of liquid monomer (directionality), this cannot be avoided.

## Chapter 5: Characterisation of Guest interactions in VAc@MOF-5

### 5.8.1 MOF Dynamics during Polymerisation.

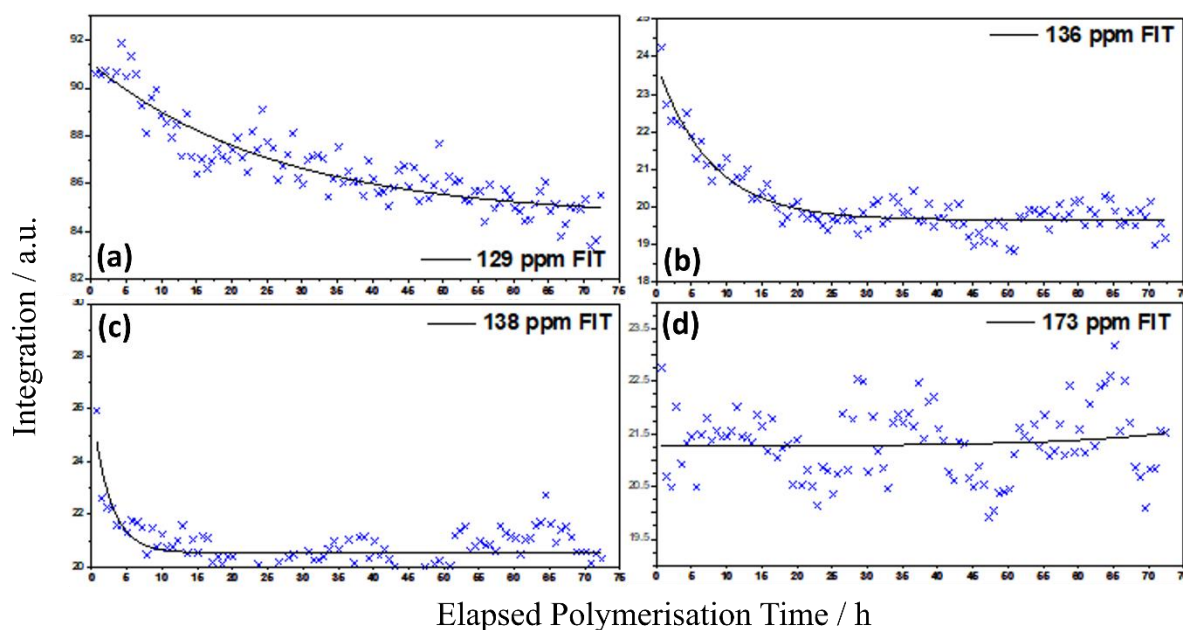


Fig 5.29:  $^{13}\text{C}$  (a) CP and (b) HPDEC exponential fits of peak integral values for MOF peaks at 168-171 ppm ( $\text{C}_4$ ). (Blue crosses indicate the integral values fit to exponential fit – black lines)

Characteristic MOF peaks at 129 ( $\text{C}_1$ ), 136 ( $\text{C}_2$ ), 138 ( $\text{C}_3$ ), and 171 ( $\text{C}_4$ ) ppm in  $^{13}\text{C}$  CP NMR spectra acquired during polymerisation was used as a basis to gather understanding of guest species influence on the phenyl rings on the linker and structural changes resulting from increase or decrease in the mobility of the associated carbons. (Fig 5.29)

$\text{C}_1$  and  $\text{C}_2$  carbon peaks associated with the phenyl ring methine carbons show a continuous decrease in mobility through the polymerisation process over 72 h. This decrease in mobility of the phenyl is likely a result of two contributing factors. Firstly, the polymer chains develop and grow within the micropores of the MOF, it restricts the motion of the phenyl ring is restricted by steric hindrance induced by the polymer chains. Secondly, polymer chains grow to saturate the micropores of the MOF, and reinforce the structure without causing long-range disorder and restrict the motion of the phenyl rings. This conclusion supports earlier observable changes of lattice expansion on monomer inclusion and subsequent contraction upon polymerisation seen by powder XRD ( $d = \pm 1 \text{ \AA}$ ) and SEM.

## Chapter 5: Characterisation of Guest interactions in VAc@MOF-5

---

C<sub>3</sub> (C=C) peak at 138 ppm, shows an early decrease in mobility up to 15 h and small fluctuations in the later times of polymerisation as observed with all characteristic MOF peaks. This may be a result of polymer chains influencing the expansion-contraction of the framework or from external instrumental effects. C<sub>4</sub> carbon connects the linker to oxygens on Zn<sub>4</sub>O metal node and is expected to show least displacement being more strongly bound than the C–C bonds.

### 5.9 X-ray Structure Analysis.

The MOF-5 crystal structure used in the NMR study was verified by PXRD and SCXRD. The first PXRD were measured with the crystals as obtained from synthesis, suffix (1). The second PXRD pattern was taken after the NMR study and upon polymerisation of VAc@MOF-5 sample on the instrument, suffix (2). SCXRD patterns were measured on VAc@MOF-5 samples to determine the structure and obtain an electron density map of the guest in MOF-5 structure.

#### 5.9.1 Powder XRD of *solid-state* NMR Samples

PXRD samples were prepared by opening the NMR sample rotor tube and removing the powder with a screw packer tool and transferring sample to silicon zero-background wafer for PXRD. Powder XRD was performed on X'Pert PRO PANalytical Chiller 59 diffractometer using Ni-filtered CuK $\alpha$  radiation source ( $\lambda = 1.5418 \text{ \AA}$ ) at room temperature.

### Result and Discussion

PXRD patterns obtained for VAc@MOF-5 are shown in Fig 5.30 (shown on next page). Both pre- and post-ssNMR experiment samples show no splitting. The ratio of relative peak intensities for (200) and (220) reflection ( $I_{6.9^\circ}/I_{9.7^\circ} \approx 2.1$ ) and positions ( $2\theta = 6.9^\circ$  and  $9.7^\circ$ ) were in good agreement with all synthesised samples for earlier experiments. Any peak splitting and intensity ratio between peaks at  $6.9^\circ$  (200) and  $9.7^\circ$  (220) would indicate zinc hydroxide inclusion ( $I_{6.9^\circ}/I_{9.7^\circ} < 1$ ) and an interpenetrated MOF-5 crystal structure would give ( $I_{6.9^\circ}/I_{9.7^\circ} \approx 1.33$ ). The observed peak ratio  $I_{6.9^\circ}/I_{9.7^\circ} > 2$  and the absence of peak splitting of  $6.9^\circ$  (200) and  $9.7^\circ$  (220) indicates presence of cubic MOF-5 structure. However, upon closer

## Chapter 5: Characterisation of Guest interactions in VAc@MOF-5

inspection of the  $9.7^\circ$  peak for VAc@MOF-5 sample, slight broadening can be observed which could arise from either a change in electron density of the material due to the presence of mobile VAc monomer molecules in the crystal structure or perhaps degradation of the sample to form nanocrystallites. To investigate this, SCXRD analysis was carried out, as this provides more detailed electron density mapping than is possible from PXRD.

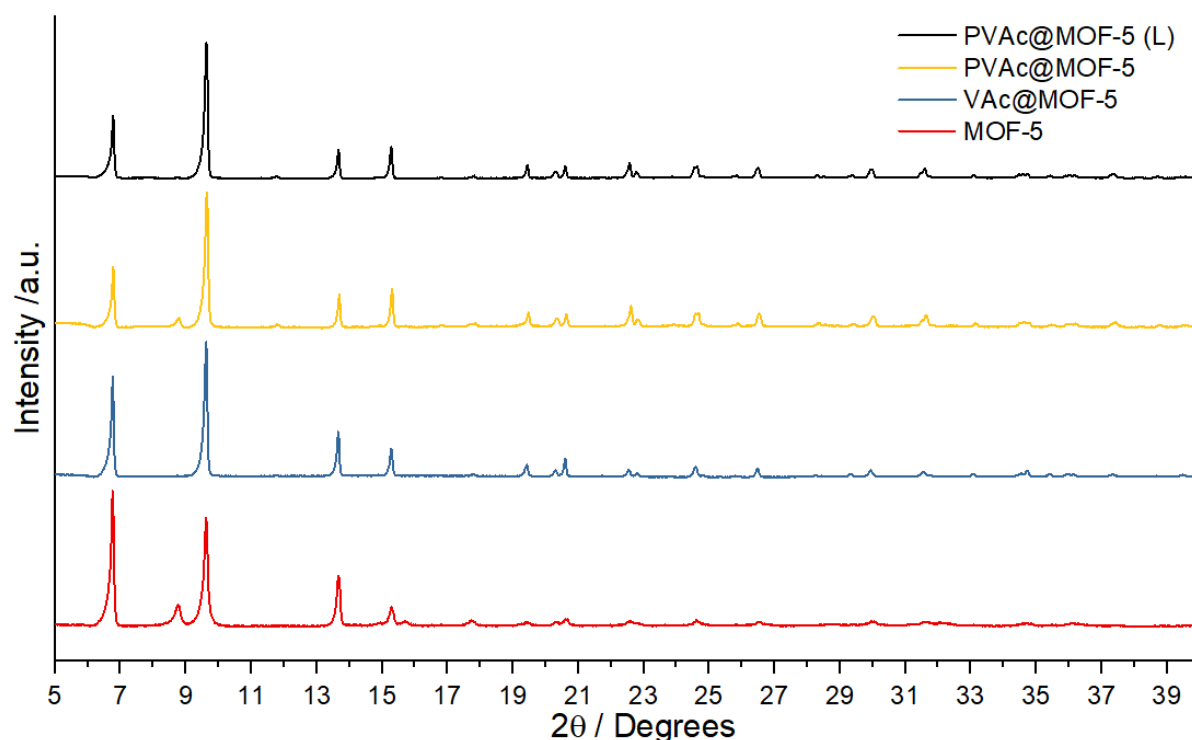


Fig 5.30: PXRD pattern for (a) MOF-5, VAc@MOF-5, PVAc@MOF-5 and PVAc@MOF-5 (L). Here PVAc@MOF-5 (L) is the sample polymerised during the solid-state NMR experiment.

### 5.9.2 Single-crystal XRD (SCXRD)

SCXRD was performed on VAc@MOF-5 samples to obtain an electron density map and localised interaction on the structure of the MOF. SCXRD data was collected on a Rigaku Oxford Diffraction dual source Gemini A Ultra diffractometer equipped with an Atlas CCD area detector and an Oxford Cryosystems CryojetXL liquid nitrogen flow device for temperature control.

## Chapter 5: Characterisation of Guest interactions in VAc@MOF-5

The data were collected using MoK $\alpha$  radiation ( $\lambda = 0.71073 \text{ \AA}$ ). The crystal was mounted in fomblin oil on a MiTeGen micromount and flash cooled to 150 K for data collection.

Data collection, indexing and integration procedures were completed with CrysAlisPro version 41.107. The structure was solved via dual-space methods using ShelXT and refined by full-matrix least squares on  $F^2$  using ShelXL-2014. The relevant portion of the structure is shown in Fig 5.32.

All measurements were taken and recorded by Dr Lauren Hatcher (Royal Society University Research Fellow, Cardiff University) due to restrictions on site access due to COVID-19 pandemic. Data processing and analysis was also performed by Dr Lauren Hatcher with input from the candidate for system specific interpretation.

### Result and Discussion

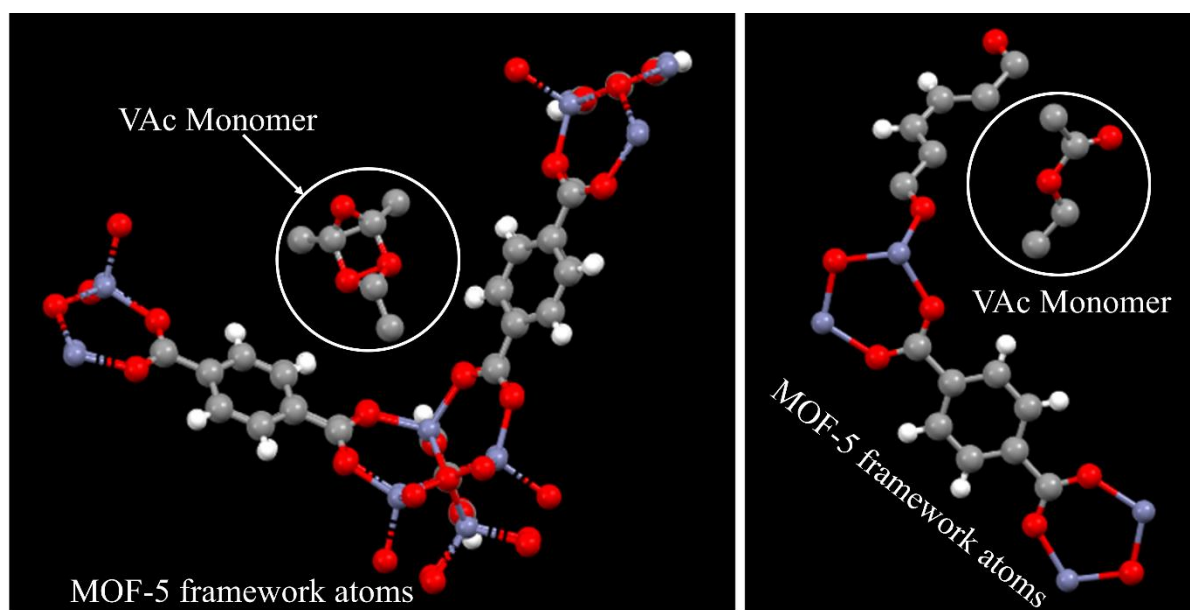


Fig 5.31: Crystal structure of VAc@MOF-5 determined by SCXRD. The network atoms are depicted by solid sticks, whereas guest monomer molecules are represented by red (oxygen) and grey (carbon) stick/solid surfaces. Only partial MOF-5 framework has been shown for clarity.

## Chapter 5: Characterisation of Guest interactions in VAc@MOF-5

---

The crystal structure of VAc@MOF-5 determined by single-crystal X-ray diffraction (SCXRD) suggested the crystals are isomorphic and crystallise in  $R\bar{3}m$  space group of the rhombohedral or trigonal crystal system. Initially, the fitted structure of VAc@MOF-5 suggested a network with two interpenetrated nets of cubic MOF-5 with the phenyl rings oriented such that they are laterally inverted compared to the opposite linker ring at any given time. Each net would consist of cubic channels with virtual diameter  $\sim 11 \text{ \AA}$ , where the secondary MOF-5 net is interpenetrated and a vinyl acetate molecule coordinates with each  $\text{Zn}_4\text{O}$  node. However, following further structure determination this was ruled out on the basis of systematic absences of monomer causing a higher order symmetry fit. Furthermore, the MOF-5 structure prior to monomer loading is not interpenetrated and there is no rational mechanism by which monomer loading could generate a second net.

The orientation of vinyl acetate molecule is such that the methyl group on the vinyl acetate is closest to the metal node. All monomer molecules reside in the pores and shows hydrogen bond interactions mediated by the methyl groups, with the acetate group on the monomer facing away. This supports our initial conclusion from the  $^{13}\text{C}$  CP NMR spectra of the monomer in the polymerisation experiment that methylene (97 ppm) and methine (141 ppm) group on the vinyl acetate monomer remain mobile through the experimental time. It should be noted that the arrangement of adsorbate monomer molecules strictly depends on the nature and the size of guest molecules and are possibly responsible for different degree of loadings.

### 5.9.3 Conclusions from X-Ray Diffraction.

The aim of the system investigated through SCXRD was to replicate samples studied by *solid-state* NMR and neutron diffraction and spectroscopy experiments to support the hypothesis derived from their data analysis.

In Fig 5.32, a comparison of simulated powder XRD pattern from the SCXRD data shows additional peaks at  $2\theta = 5.9^\circ$  that is possible due to vinyl acetate coordinating within the framework near the metal SBU which does not appear in the powder XRD patterns of VAc@MOF-5 prepared by method described in section 3.3.1. This peak is also observed in neutron diffraction data for d-monomer@D-MOF ( $Q = 0.42 \text{ \AA}^{-1}$ ). The presence of VAc

## Chapter 5: Characterisation of Guest interactions in VAc@MOF-5

monomer in MOF-5 changes the symmetry of the MOF from cubic ( $Fm-3m$ ) to trigonal/rhombohedral ( $R-3m$ ) and may explain widening of the peak at  $2\theta = 9.7^\circ$  observed in the powder patterns. However, through only powder XRD pattern, it is not possible to conclude the symmetry of MOF-5 as the powder XRD patterns only show framework expansion and peak widening but changes in symmetry cannot be concluded without additional diffraction data through SCXRD and neutron diffraction.

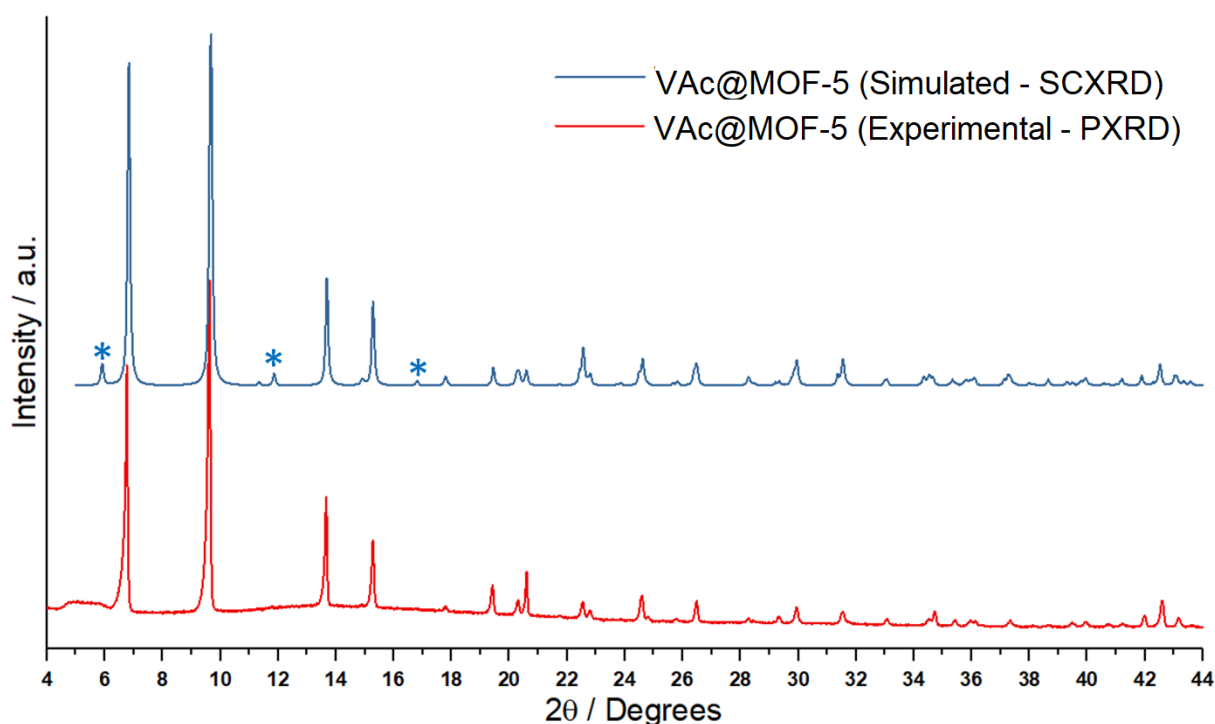


Fig 5.32: Comparison of PXRd pattern of synthesised VAc@MOF-5 versus simulated powder pattern of VAc@MOF-5 following SCXRD analysis on the same sample. (Blue asterisks show additional peaks on the simulated pattern below  $2\theta = 20^\circ$  that is otherwise not present in the experimental PXRd).

## Chapter 5: Characterisation of Guest interactions in VAc@MOF-5

---

### Future Work

Further work studying guest@MOF-5 is planned and will be performed after the submission of the thesis. First measure will be to determine if the current rhombohedral model for the disorder of VAc monomer across the mirror plane. This will be performed by checking the Crystallographic Information File (CIF) by structure validation software in PLATON software to confirm rhombohedral space group for VAc@MOF-5 composite.<sup>60</sup> Following this conformation, a second model for the data will be generated for an empty MOF-5. This model will be used to create a Fourier electron density difference map to show the precise location of VAc molecules. This will allow us to analyse a structure model for MOF-5, before and after loading the guest VAc molecules and compare the changes in diffraction patterns. Additionally, SQUEEZE procedure will be performed which takes in account the contribution of a heavily disordered solvent and/or monomer to the calculated structure factors by back-Fourier transformation of the continuous density found in a masked region of the difference map. The masked region is defined as the solvent accessible region left by the ordered part of the structure.<sup>61</sup> These steps will allow us to directly compare the guest interaction and binding sites in the MOF to the data obtained from neutron scattering experiments.

### 5.10 Conclusions

We performed total neutron scattering experiment to investigate monomer interaction, identify monomer binding sites, and to study the influence of guest species on the structure of the MOF-5 framework. The data analysis and interpretation are still in its early stages despite considerable work and progress having been made. The data shows a difference between the hydrogenated and deuterated MOF-5 structure that cannot be concluded by means of powder X-ray diffraction. Additional peaks are observed at  $Q = 0.42 \text{ \AA}^{-1}$  ( $2\theta = 5.9^\circ$ ) that does not appear in PXRD data of D-MOF suggesting a difference in structure of the H- and D-MOF isotopologues. Guest@MOF composite data show that there is an increase in intensity of the peak, and we think that this may be present due to guest specie interactions with the zinc metal-node on the MOF-5. This conclusion is further supported by SCXRD data that identifies similar interaction site of the guest monomer in MOF by mapping the electron density of the monomer@MOF composite. For the case of empty MOF, this peak may be present due to residual solvent DMF molecules in the framework. This result also questions

## Chapter 5: Characterisation of Guest interactions in VAc@MOF-5

---

the widely reported methodologies for MOF-5 activation to remove any intrinsic solvent molecules without structural distortion.<sup>28–30</sup>

We have identified steps to move forward with further analysis of the data. From the preliminary analysis of the  $G(r)$ , we can sufficiently identify MOF contributions and differentiate short-range monomer interactions in the system. The long-range features observed in  $G(r)$  of all samples assumes that framework consists of an alternating open and closed pore structure with different pore diameters (discussed in detail in section 5.7.2) in the current ensemble, and the monomer filling infinitely translates into all directions to successive unit cells in the framework. It is possible that the simulation introduces an isotope effect to calculate scattering which is amplified through assumed homogenous filling, and current ensemble size. To allow for inhomogeneity in pore filling by guest species, a larger ensemble will provide a more accurate representation of experimental samples. Furthermore, control over individual pore filling in the simulation ensemble will aid identifying the source of features from scattering.

Through proposed changes on the simulation ensemble and Bragg corrections to match simulated and experimental data, from this experiment we will be able to conclude the effect of guest molecules on the host MOF that have previously not been studied or reported. Current research has been limited to transport behaviour and interactions of ions and small gaseous alkanes such as methane, butane, acetylene,  $\text{CO}_2$ ,  $\text{H}^+$  and  $\text{Li}^+$ .<sup>31–34</sup> Large molecules interactions such as vinyl acetate interactions in MOF-5 at the time of writing this thesis have not been reported. Furthermore, understanding structural effects of guest monomers on host MOF will correlate with observation from PXRD data (Section 4.2) will be confirmed by neutron scattering data simulated on Dissolve. Isotopic effects of monomer isotopologues on host framework have not been reported and conclusions from simulations will help affirm our current hypothesis of short-range binding interactions of monomer on the host framework through observation of peaks at  $Q = 0.24$  and  $0.34 \text{ \AA}^{-1}$ .

Lastly, initial simulations of monomer@MOF on Dissolve have contributed towards determining avenues that can be applied on the code to understand complex systems such as

## Chapter 5: Characterisation of Guest interactions in VAc@MOF-5

---

those of confined liquids in crystalline solids. Currently, it is not possible to introduce inhomogeneous pore filling on Dissolve simulations that result in correlating effects that are not present in the experimental samples. Identifying these changes provides a basis and direction to further improve simulations and development of *Dissolve*.

Changes in monomer mobility and quantity during the polymerisation of vinyl acetate in MOF-5 was investigated by means of  $^{13}\text{C}$  CP and HPDEC MAS NMR spectroscopy, respectively. This was done by calculating integration values for characteristic monomer peaks present in the  $^{13}\text{C}$  CP and HPDEC NMR spectra and plotting the changes over elapsed polymerisation time. We see that the CH and  $\text{CH}_2$  monomer peaks show a steep decrease in mobility up to 15 h, followed by a gradual and steady decrease from 15 – 45 h, and little to no changes beyond 45 h. This suggests that the polymer becomes less mobile as polymerisation is initiated and the monomer begins to polymerise. Much of the changes and conversion occurs to ~ 15 h, and the characteristic NMR peaks remain present at the end of the experiment due to monomer species remaining present within the MOF pores due to incomplete conversion of the monomer into polymer. Investigation of  $^{13}\text{C}$  HPDEC NMR confirms this hypothesis as we observe monomer peaks at the end of the experiment. To calculate the conversion of the monomer, we have used Avrami-Erofeev equation, considering Avrami constant ( $m$ ) as 1 and 3-dimensional growth. Calculations suggest a 63 % conversion ( $\alpha = 0.63$ ) of monomer to polymer which agree with the conversion calculated by other characterisation methods such as  $^1\text{H}$  NMR spectroscopy and TGA. As the carbons associated with  $\text{CH}_2$  and CH groups show little change in the signal intensity on the  $^{13}\text{C}$  CP spectrum, it is possible to suggest that the associated carbons associated to these peaks have unrestricted and free motion. However, it should be noted that the vinylic C and  $\text{CH}_3$  methyl signals cannot be integrated to reasonably accurate integral values due to overlap of the monomer and polymer  $\text{CH}_3$  signals in the  $^{13}\text{C}$  CP and HPDEC NMR spectroscopy data. the monomer signal intensity can be seen to visibly decrease.

We studied changes in the characteristic MOF-5 peaks associated with the phenyl ring of the linker that shows a decrease in mobility with the increase in temperature from 4 to 70 °C. Based on interpretation of data from the 70 °C, it is reasonable to assume that this effect is likely due to the steric hindrance imposed by mobile monomer molecules on the MOF-5

## Chapter 5: Characterisation of Guest interactions in VAc@MOF-5

---

phenyl linkers. Additionally, at lower temperatures, the CH peaks from MOF-5's phenyl linker at 128 ppm is in form of a *pake* doublet pattern which begins to merge into a broad single peak as the temperature increases. This feature is characteristic of phenyl ring rotation observed in MOFs where the increase in flip-rotation around  $C_2$  principal axis. Polymer peaks were not observed during the temperature ramp experiment or any broadening in the  $CH_3$  region of monomer and polymer overlapping region at 19 ppm is observed, suggesting that no significant polymerisation occurs during the experiment. However, due to the complexity of the three-component system and present of liquid monomer and poor resolution, this cannot be confirmed using *solid-state* NMR spectroscopy.

We used *single crystal* XRD to analyse the crystal structure of VAc@MOF-5 and to confirm monomer interaction and binding sites within the pores of MOF-5 by modelling and creating electron density maps to further support results seen from ssNMR, TNS and QENS experiments. SCXRD suggested the crystals are isomorphic and crystallise in  $R-3m$  space group of the rhombohedral or trigonal crystal system in presence of guest species. Our data suggests that in the presence of VAc monomer in MOF-5 changes the symmetry of the MOF from cubic ( $Fm-3m$ ) to trigonal/rhombohedral ( $R-3m$ ). An important conclusion is that powder XRD as a stand-alone method, is unable to conclude the symmetry of MOF-5 as the powder XRD patterns only show framework expansion and peak widening but changes in symmetry cannot be concluded without additional diffraction data through SCXRD and neutron diffraction.

## Chapter 5: Characterisation of Guest interactions in VAc@MOF-5

---

### 5.10 References:

- 1 D. A. Keen, *J. Appl. Crystallogr.*, 2001, **34**, 172–177.
- 2 T. E. Faber and J. M. Ziman, *J. Theor. Appl. Phys.*, 2006, **11**, 153–173.
- 3 V. Tudisca, F. Bruni, E. Scoppola, R. Angelini, B. Ruzicka, L. Zulian, A. K. Soper and M. A. Ricci, *Phys. Rev. E*, 2014, **90**, 032301.
- 4 K. J. Edler and D. T. Bowron, *Curr. Opin. Colloid Interface Sci.*, 2015, **20**, 227–234.
- 5 D. T. Bowron, A. K. Soper, K. Jones, S. Ansell, S. Birch, J. Norris, L. Perrott, D. Riedel, N. J. Rhodes, S. R. Wakefield, A. Botti, M.-A. Ricci, F. Grazzi and M. Zoppi, *Rev. Sci. Instrum.*, 2010, **81**, 033905.
- 6 D. T. Bowron and A. K. Soper, *Neutron News*, 2011, **22**, 12–14.
- 7 D. T. Bowron, A. K. Soper, K. Jones, S. Ansell, S. Birch, J. Norris, L. Perrott, D. Riedel, N. J. Rhodes, S. R. Wakefield, A. Botti, M. A. Ricci, F. Grazzi and M. Zoppi, *Rev. Sci. Instrum*, 2011, **22**, 14-18.
- 8 R. B. von Dreele, J. D. Jorgensen, C. G. Windsor, *J. Appl. Cryst.*, 1982, **15**, 581–589.
- 9 H. Chevreau, S. G. Duyker, V. K. Peterson, *Acta Cryst.*, 2015, **71**, 648–660.
- 10 C. M. Brown, Y. Liu and D. A. Neumann, *Pramana*, 2008, **71**, 755–760.
- 11 N. L. Rosi, *Science*, 2003, **300**, 1127.
- 12 D. Saha, Z. Bao, F. Jia and S. Deng, *Environ. Sci. Technol.*, 2010, **44**, 1820–1826.
- 13 J. Li, S. Cheng, Q. Zhao, P. Long and J. Dong, *Int. J. Hydrog. Energy*, 2009, **34**, 1377–1382.
- 14 Y. Ming, N. Kumar and D. J. Siegel, *ACS Omega*, 2017, **2**, 4921–4928.
- 15 Y. Peng, V. Krungleviciute, I. Eryazici, J. T. Hupp, O. K. Farha and T. Yildirim, *J. Am. Chem. Soc.*, 2013, **135**, 11887–11894.
- 16 S. A. Prabhudesai, V. K. Sharma, S. Mitra and R. Mukhopadhyay, *Eur. Phys. J. B*, 2013, **86**, 22–27.
- 17 C. K. Brozek, V. K. Michaelis, T. C. Ong, L. Bellarosa, N. López, R. G. Griffin and M. Dincă, *ACS Cent. Sci.*, 2015, **1**, 252–260.
- 18 ISIS Gudrun - Routines for reducing total scattering data, <https://www.isis.stfc.ac.uk/Pages/Gudrun.aspx>, (accessed January 7, 2021).
- 19 A. K. Soper, *RAL Report RAL-TR-2011-013*.
- 20 T. Youngs, *Mol. Phys.*, 2019, **117**, 3464–3477.
- 21 C. Kittel, *Introduction to Solid State Physics, 8th Edition*, Wiley, New York, 1971.
- 22 A. K. Soper, K. Page and A. Llobet, *J. Condens. Matter Phys.*, 2013, **25**, 454219.
- 23 G. Cai, A. E. Phillips, T. F. Headen, T. G. A. Youngs, T. Ben and M. T. Dove, *J. Phys. Commun.*, 2020, **4**, 23001
- 24 M. A. Addicoat, N. Vankova, I. F. Akter and T. Heine, *J. Chem. Theory Comput.*, 2014, **10**, 880–891.

## Chapter 5: Characterisation of Guest interactions in VAc@MOF-5

---

- 25 L. S. Dodda, I. C. de Vaca, J. Tirado-Rives and W. L. Jorgensen, *Nucleic Acids Res.*, 2017, **45**, W331–W336.
- 26 LigParGen Server, <http://zarbi.chem.yale.edu/ligpargen/>, (accessed September 6, 2021).
- 27 T. Youngs, *Mol. Phys.*, 2019, 1–14.
- 28 D. J. Tranchemontagne, J. R. Hunt and O. M. Yaghi, *Tetrahedron Lett.*, 2008, **64**, 8553–8557.
- 29 S. Begum, Z. Hassan, S. Bräse and M. Tsotsalas, *Langmuir*, 2020, **36**, 10657–10673.
- 30 S. Amirjalayer and R. Schmid, *Micropor. Mesopor. Mat.*, 2009, **125**, 90–96.
- 31 S. A. Prabhudesai, V. K. Sharma, S. Mitra and R. Mukhopadhyay, *Eur. Phys. J. B*, 2013, **86**, 1–7.
- 32 F. Salles, H. Jobic, A. Ghoufi, P. L. Llewellyn, C. Serre, S. Bourrelly, G. Férey and G. Maurin, *Angew. Chem. Int. Ed.*, 2009, **48**, 8335–8339.
- 33 H. Jobic, N. Rosenbach, A. Ghoufi, D. I. Kolokolov, Pascal. G. Yot, T. Devic, C. Serre, G. Férey and G. Maurin, *Chem. Eur.*, 2010, **16**, 10337–10341.
- 34 S. Rives, H. Jobic, F. Ragon, T. Devic, C. Serre, G. Férey, J. Ollivier and G. Maurin, *Micropor. Mesopor. Mat.*, 2012, **164**, 259–265.
- 35 R. Krahne, G. Chilla, C. Schüller, L. Carbone, S. Kudera, G. Mannarini, L. Manna, D. Heitmann, R. Cingolani, *Nano Lett.* 2006, **6**, 3, 478–482.
- 36 M. Kruteva, *Adsorption*, 2021, **27**, 875–889.
- 37 H. Jobic, *Molecular Sieves - Science and Technology*, 2008, **7**. Springer, Berlin, Heidelberg.
- 38 M. T. F. Telling, *A Practical Guide to Quasi-elastic Neutron Scattering*, 2020.
- 39 Fick's Law | Statement & Diffusion | nuclear-power.com, <https://www.nuclear-power.com/nuclear-power/reactor-physics/neutron-diffusion-theory/ficks-law/>, (accessed September 22, 2021).
- 40 M. Ricco, L. Cristofolini, G. Viola and E. Dalcanale, *J. Phys. Chem. Solids*, 1993, **54**, 1487–1490.
- 41 R. T. Azuah, L. R. Kneller, Y. Qiu, P. L. W. Tregenna-Piggott, C. M. Brown, J. R. D. Copley and R. M. Dimeo, *J. Res. Natl. Inst. Stand. Technol.*, 2009, **114**, 341.
- 42 O. Arnold, J. C. Bilheux, J. M. Borreguero, A. Buts, S. I. Campbell, L. Chapon, M. Doucet, N. Draper, R. Ferraz Leal, M. A. Gigg, V. E. Lynch, A. Markvardsen, D. J. Mikkelsen, R. L. Mikkelsen, R. Miller, K. Palmén, P. Parker, G. Passos, T. G. Perring, P. F. Peterson, S. Ren, M. A. Reuter, A. T. Savici, J. W. Taylor, R. J. Taylor, R. Tolchenov, W. Zhou and J. Zikovsky, *Nucl. Instrum. Methods Phys. Res. A*, 2014, **764**, 156–166.
- 43 Mantid, [https://www.mantidproject.org/Main\\_Page.html](https://www.mantidproject.org/Main_Page.html), (accessed September 8, 2021).
- 44 E. Mamontov, R. W. Smith, J. J. Billings and A. J. Ramirez-Cuesta, *Physica B: Cond. Matter Phys.*, 2019, **566**, 50–54.
- 45 H. Hoffmann, M. Debowski, P. Müller, S. Paasch, I. Senkovska, S. Kaskel and E. Brunner, *Materials*, 2012, **5**, 2537–2572.
- 46 G. Mali, in *Metal-Organic Frameworks*, InTech, 2016.

## Chapter 5: Characterisation of Guest interactions in VAc@MOF-5

---

- 47 H. C. Hoffmann, M. Debowski, P. Müller, S. Paasch, I. Senkovska, S. Kaskel and E. Brunner, *Materials*, 2012, 5, 2537–2572.
- 48 M. K. Pandey, Z. Qadri and R. Ramachandran, *J. Chem. Phys.*, 2013, **138**, 114108.
- 49 Dr Melinda J. Duer, *Solid-State NMR: Principles and Applications*, Wiley-Blackwell, New York, Ed. 2, 2002.
- 50 S. Hertel, M. Wehring, S. Amirjalayer, M. Gratz, J. Lincke, H. Krautscheid, R. Schmid and F. Stallmach, *J. Appl. Phys.*, 2011, **55**, 20702.
- 51 H. Li, M. Eddaoudi, M. O’Keeffe and O. M. Yaghi, *Nature*, 1999, **402**, 276–279.
- 52 H. G. Karge, *Adsorption and Diffusion*, Springer Berlin, Heidelberg, vol. 1, 2008.
- 53 Wolfram Mathematica: Modern Technical Computing, <https://www.wolfram.com/mathematica/>, (accessed June 21, 2021).
- 54 Mnova NMR to visualize, process, analyze & report 1D and 2D NMR data, <https://mestrelab.com/software/mnova/nmr/>, (accessed June 21, 2021).
- 55 Help Online - Origin Help - Theory of Nonlinear Curve Fitting, <https://www.originlab.com/doc/origin-help/nlfit-theory>, (accessed September 16, 2021).
- 56 M. J. van Vleet, T. Weng, X. Li and J. R. Schmidt, *Chem. Rev.*, 2018, **118**, 3681–3721.
- 57 F. Moreau, D. I. Kolokolov, A. G. Stepanov, T. L. Easun, A. Dailly, W. Lewis, A. J. Blake, H. Nowell, M. J. Lennox, E. Besley, S. Yang and M. Schröder, *Proc. Natl. Acad. Sci. U. S. A.*, 2017, **114**, 3056–3061.
- 58 A. Gonzalez-Nelson, F. X. Coudert and M. A. van der Veen, *Nanomaterials*, 2019, 9, 330.
- 59 R. W. McDowell, L. M. Condrón, N. Mahieu, P. C. Brookes, P. R. Poulton and A. N. Sharpley, *J. Environ. Qual.*, 2002, **31**, 450–456.
- 60 THE PLATON HOMEPAGE, <http://www.platonsoft.nl/platon/>, (accessed January 3, 2022).
- 61 PLATON/SQUEEZE, <http://www.platonsoft.nl/platon/pl000303.html>, (accessed January 3, 2022).
- 62 P. Vervoorts, J. Stebani, A. S. J. Mendez, and G. Kieslich, *ACS Materials Lett.*, 2021, **3**, 12, 1635-1651.
- 63 C. L. Hobday, R. J. Marshall, C. F. Murphie, J. Sotelo, T. Richards, D. R. Allan, T. Duren, F. X. Coudert, R. S. Forgan, *Angew Chemie. Int. Ed.*, 55, 7, 2401-2405.

# Chapter 6

---

Conclusion

# Chapter 6: Conclusion

---

The conclusions and future work from Chapter 4 and 5 presented in the thesis are detailed in this chapter.

## 6.1 Conclusion

The use of powder X-ray diffraction (PXRD) enabled structural characterisation of MOF-5 and HKUST-1 for as-synthesised MOFs and guest@MOF composites using vinyl acetate,  $\epsilon$ -caprolactone, lactic acid, lactide, and their respective polymers. Structural changes upon guest sorption in both MOF were observed through positional changes in the  $2\theta$  of the characteristic MOF peaks in PXRD patterns. The result of these studies shows that upon monomer adsorption within the MOF pores, the MOF undergoes structural changes. However, further detailed analysis by indexing and structural refinement is necessary to quantify and confirm these changes using PXRD as a method. Conversely, when the monomer in the MOF pores is polymerised, an effect of framework expansion was observed with an increase in the  $d$ -spacing for PVAc@MOF-5 samples. It was determined from PXRD patterns of MOF-5 and guest@MOF-5 composites that an additional peak at  $2\theta = 8.9^\circ$  appears in presence of guest molecules in the host framework that coordinate with the metal node of MOF-5 framework. MOF-5 by  $\epsilon$ -CL monomer show similar changes in  $d$ -spacing upon guest adsorption and polymerisation, and peak broadening on powder pattern. These results provide support to the hypothesis that MOF lattice undergoes framework deformation upon guest adsorption. Guest@HKUST-1 composites were also investigated and showed similar changes in  $d$ -spacing to those observed with  $\epsilon$ -CL@MOF-5 upon guest adsorption with a shift towards a greater  $2\theta$  angle compared to as-synthesised MOF.

Results from SCXRD (Section 5.9) and neutron powder diffraction experiments (Section 5.1) suggest a possibility of structural disorder in guest@MOF-5 composites that is not observed through PXRD and were indicative of a transformation from a cubic ( $Fm-3m$ ) to rhombohedral ( $R-3m$ ) structure induced by monomer association at the nodes. PXRD studies are the basis for the neutron scattering experiments to accurately determine the structural changes in the MOF-5 in presence of VAc and PVAc guests. We also conclude that PXRD characterisation as a method

## Chapter 6: Conclusion

---

cannot be used by itself to determine the symmetry of MOF-5 and additional diffraction data through SCXRD and neutron diffraction is required to draw conclusions.

Monomer inclusion and conversion for composites prepared by in-situ polymerisation in host MOF has been studied and quantified through spectroscopic methods and thermal analysis. ATR-FTIR spectroscopy was performed on MOF and guest@MOF composites to confirm presence of adsorbed monomer through appearance of characteristic monomer absorption bands. Moreover, comparisons between the monomer@MOF and polymer@MOF spectra were made by observing band characteristics before and after polymerisation. Crystalline nature of isolated PCL observed with PXRD was also confirmed with FTIR by observing spectra for PCL which showed sharp features of asymmetric  $\nu(\text{C-H})$  band at  $2960\text{ cm}^{-1}$  with a shoulder developing on the same band, in addition to absorption bands shifted at higher wavenumbers ( $5 \pm 1\text{ cm}^{-1}$ ), which is typical of crystalline PCL. Presence of atmospheric water and DMF in MOF-5 was determined by FTIR, and subsequently quantified with TGA and total neutron scattering intensity via data reduction using Gudrun.

TGA analysis was conducted to study thermal stability of the materials and showed that under confinement, guest species degrade at a higher temperature compared to bulk polymers without confinement. Monomer loadings in the MOFs were estimated by the mass loss in the central region of the TGA plots (Region II). Monomer conversion could not be reliably determined from TGA but qualitatively appeared higher than the values obtained from solution ( $68 \pm 2\%$ ) and solid-state NMR ( $64 \pm 1\%$ ). This is likely due to overlapping thermal region of intrinsic polymer and framework-bound DMF molecules observed to be present through other characterisation methods and neutron scattering experiments.

## Chapter 6: Conclusion

---

### Overview in context of previous studies.

Guest interactions in MOF have been reported in the literature, mainly exploring transport behaviour of ions and covalent binding interaction of light gaseous hydrocarbons.<sup>1-15</sup> Interactions of large molecule such as VAc and  $\epsilon$ -CL monomer have not previously been reported, and the work in the thesis investigating interaction of VAc in MOF-5 by neutron scattering, to the best of our knowledge, is the first of its kind to merge neutron diffraction and neutron spectroscopic techniques to investigate behaviour of a confined liquid (monomer) in crystalline solids. This has identified the challenges of performing general atomistic, MC and MD simulations with such materials has been realised and substantial steps towards improving data analysis and simulation environment are being continuously explored, following recommendations from this work.

In current reports, research is based on the hypothesis that MOFs can be used as templates to achieve three-dimensional polymer matrices of homopolymers with control over stereoregularity, and polymerisation to create polymer structures. Despite the advantages resulting from templated polymerisation by MOFs, there is a lack in understanding of how to effectively control these reactions and polymerisation dynamics in the confinement of MOF pores.<sup>18</sup> Furthermore, little is known on how the guests interacts with the MOF framework during polymerisation. The first evidence of polymerisation in MOFs was from Uemura *et al.* on the radical polymerisation of styrene monomers within MOF pores.<sup>21</sup> Although polymerisation of vinyl acetate in MOF (not MOF-5 and HKUST-1) has been investigated,<sup>22</sup> studies to understand polymerisation dynamics, composite structure, and guest kinetics have not been explored in depth.

Dimensionality and porosity of such structures can be tailored can be tailored by taking advantage of the unique isorecticular property of certain MOFs. Polymers isolated from the MOF do not undergo recrystallisation but are isolated by disassembly of the MOF structure by chelating complexes. Such an approach should preserve the polymer architecture. Through SEM, we initially realised that this may not be the case in practice by observing isolated polymers as MOFs as one-dimensional rods or chains. SEM images show that although polymerisation of the monomer takes places within the MOF pores resulting in regular one-dimensional rods of length

## Chapter 6: Conclusion

---

symmetrical with the MOF crystal size, it is unable to form a multi-dimensional homopolymer matrices as has been previously reported.<sup>16-18</sup> To investigate the possible reasons regarding such an effect, we studied the composites at an atomic and molecular level by means of total neutron scattering (TNS) and quasi-elastic neutron spectroscopy (QENS).

The aim of total neutron scattering experiment at the NIMROD instrument (ISIS Pulsed Neutron and Muon Source, RAL, UK) was to understand guest behaviour and identify possible binding sites and interactions of VAc in MOF-5. Additionally, we studied the influence of guest species on the structure of the host MOF, to identify the sources from the differences in diffraction patterns of MOF and guest@MOF composites observed through PXRD. By means of the QENS experiment on the IRIS instrument (ISIS Pulsed Neutron and Muon Source, RAL, UK) we were able to use elastic and inelastic window scans to observe the dynamics of guest motion in the framework evolves over time with VAc@MOF-5 and PVAc@MOF-5 composite, and an intermediate partially polymerised OVAc@MOF-5 sample. We were able to identify and interpret coherent and incoherent elastic and quasi-elastic contributions that affected independent resolution of the guest and its motion within the framework which has not been reported in the literature for composites alike. From the available data, we can observe stiffening of MOF structure in presence of guest sorbent molecules at different points of polymerisation. Monomer species bind to the framework atoms that result in stiffening of the MOF structure, more so than oligomer and polymer species. As a result, the framework undergoes tension resulting in expansion at a greater degree for monomer guest compared to polymer guest. The shape analysis of Lorentzian contributions on the quasi-elastic peaks show that framework linker atoms are more restricted in the presence of monomer within MOF than what is observed in the case of polymer@MOF which show less restrictive motion, therefore, suggesting that the polymer chains remain free under confinement in the MOF pores. Observing these phenomena, supports the PXRD data showing that the framework undergoes contraction due to monomer adsorption and contraction upon polymerisation. Furthermore, initial data analysis from TNS experiments suggests that the monomer primarily remains bound to framework atoms of the MOF, resulting in the framework expansion following guest loading, providing support to our findings from other characterisation methods.

## Chapter 6: Conclusion

---

We performed solid-state NMR experiments using  $^1\text{H}$ - $^{13}\text{C}$  cross-polarisation and high-powered decoupling MAS NMR methods to extract information about the local structure of guest@MOF-5 and to understand the dynamics of polymerisation reaction within the MOF. From this experiment, we are able to provide additional support to our findings from complimentary methods and neutron scattering experiments. We observed monomer mobility from the  $^1\text{H}$ - $^{13}\text{C}$  CP MAS NMR method to find that the monomer remains mobile at the end of the extended polymerisation time (72 h) that suggests incomplete conversion earlier observed through solution  $^1\text{H}$  NMR and TG analyses. We quantified the monomer conversion by Avrami-Erofeev kinetic model using integration values of characteristic resonance peaks from the  $^1\text{H}$ - $^{13}\text{C}$  HPDEC MAS NMR. The resulting values of  $63 \pm 1 \%$  are in agreement with the conversion values obtained from solution  $^1\text{H}$  NMR. We also observed the mobility of phenyl rings on the BDC linker of MOF-5 to understand the influence of guest monomers on linker rotation and to identify binding interactions. The carbons associated with the phenyl rings show a continuous decrease in mobility during the early stages of polymerisation time followed by a gradual decrease. This supports the hypothesis that even after polymerisation, the linker rotation is restricted due to the presence of polymers to a degree. However, it is not possible to provide a direct comparison with experimental polymerisation time and polymerisation time during the *solid-state* NMR experiment as the reaction times are elongated due to slow diffusion in the system.<sup>19</sup>

To identify binding and interaction sites of the monomer guest in host MOF, we used *single-crystal* XRD to map electron densities in the monomer@MOF composite. Results support the suggestions from TNS data simulations and analysis of the possible binding sites. VAc interacts with the framework such that methyl group on the acetate group of the monomer is closest to the metal node. Monomers also show hydrogen bond interactions mediated by the methyl groups, supporting our initial conclusion from the  $^{13}\text{C}$  CP NMR spectra of the monomer in the polymerisation experiment that methylene (97 ppm) and methine (141 ppm) group on the vinyl acetate monomer remain mobile through the experimental time. We realise that for guest@MOF-5 composites, PXRD is unable to discern between structural changes due to introduced disorder.

## Chapter 6: Conclusion

---

We observe that upon guest monomer adsorption, MOF-5 undergoes structural changes from a cubic ( $Fm-3m$ ) structure to a rhombohedral ( $R-3m$ ) structure. This observation has not previously been reported in the literature as a contribution from the guest.

The neutron scattering studies of guest@MOF and similar confined liquids in crystalline solid materials is still in its infancy. Resources available for data analysis, processing, and simulations are yet in their development stage for such materials. Through our experiments, we have identified the specific areas for improvement of analysis of guest@MOF materials that we aim to address in our future work.

### 6.2 Future Work

Preliminary studies detailed in the work, such as the investigation and modelling of local structure of monomer@MOF-5 composites by total neutron scattering, dynamical studies to understanding in-situ polymerisation kinetics by QENS and *solid-state* NMR, present opportunities for this work to develop and expand in the future to other materials and guest@MOF composites.

The planned experiment proposal for total neutron scattering encompassed studying guest binding sites and interaction in MOF-5 by investigating monomer@MOF and polymer@MOF composites. However, due to experimental challenges leading to a repeat experiment, we were unable to analyse polymer@MOF composite due to restrictions on experimental time. Initial data analysis with monomer@MOF composites are unique in its novelty and the challenges encountered during data analysis with monomer@MOF composites has driven improvements on currently available resources for simulation and modelling complex materials alike. With a rescheduled experiment to investigate polymer@MOF composites, we will be able to push our findings forward and correlate with the data obtained from the QENS experiment at IRIS spectrometer.

## Chapter 6: Conclusion

---

In the short term with ongoing data analysis and simulation modelling on Dissolve to determine binding interactions of VAc monomer in MOF-5, we have identified the changes that will be implemented moving forward. Simulations will be performed by introducing disorder in the empty MOF framework prior to addition of monomer in the simulation ensemble to imitate experimental sample preparation that involves activation of MOF at 443 K. Furthermore, changes in the simulation Bragg parameters will be implemented to match experimental and simulated Bragg features for total structure factor  $F(Q)$  determination. Artificial features due to introduction of isotopic effects from the simulation that may not be present in experimental samples and other challenges may be addressed and mitigated by using a larger simulation ensemble.

Preliminary data analysis of QENS experiment with guest@MOF reveal findings and conclusions that have previously not been reported. The experiment on such materials was one of the first to look at structural changes on the MOF induces by guest molecules. Experimental plan to study real-time changes on the MOF structure and guest mobility as polymerisation takes place was unable to be performed due to restrictions on site access and cancellation of the experiment due to COVID-19 pandemic. However, it was possible to perform measurements on a partially polymerised sample in addition to monomer@MOF and polymer@MOF sample to determine guest interaction. Further experiments can be performed using the initial experimental plan which would also provide data from measurements that we were unable to perform. Using higher performance instruments with greater detection limits, such as LET (ISIS Pulsed Neutron and Muon Source, UK) or IN6B (Institut Laue-Langevin, France), we can achieve greater resolution for our samples that restricted analysis from measurements on IRIS.

In the longer term, these studies can be expanded to other guest@MOF composites to determine polymerisation kinetics and binding interactions of guest monomers in the MOF, and to complementary characterisation methods such as inelastic neutron scattering (INS), synchrotron X-Ray scattering and *solid-state* PFG-NMR. Composites such as  $\epsilon$ -CL@HKUST-1 has shown promising results through structural change observation and the ability to isolate polymer from

## Chapter 6: Conclusion

---

the host MOF with relative ease and minimum residual impurities (Chapter 4). Experimental studies with benzene diffusion in the pores of HKUST-1 has been previously performed on the NIMROD instrument and recently reported.<sup>20</sup> Hence, HKUST-1 is a good candidate to perform next experimental studies on and implement modelling and simulations using *Dissolve*.

Our results have shown promise in understanding polymerisation mechanism for guest monomer species under confinement of MOF through identifying possible binding interactions and determining the role of guest monomer and polymer materials on framework structure. Reported studies investigate possibility of polymerisation in MOFs using templated polymerisation approach but our studies have stretched to understanding the processes at an atomistic level. We have also demonstrated the possibility of studying such materials with methods such as total neutron scattering, quasi-elastic neutron scattering, single-crystal XRD, solid-state NMR and suitability for further studies using inelastic neutron scattering.

# Chapter 6: Conclusion

---

## 6.3 References

- 1 T. Uemura, R. Kitaura, Y. Ohta, M. Nagaoka and S. Kitagawa, *Angew. Chem. Int. Ed.*, 2006, **45**, 4112–4116.
- 2 S. A. Prabhudesai, V. K. Sharma, S. Mitra and R. Mukhopadhyay, *Eur. Phys. J. B.*, 2013, **86**, 1–7.
- 3 F. Salles, H. Jobic, A. Ghoufi, P. L. Llewellyn, C. Serre, S. Bourrelly, G. Férey and G. Maurin, *Angew. Chem. Int. Ed.*, 2009, **48**, 8335–8339.
- 4 F. Salles, H. Jobic, G. Maurin, M. M. Koza, P. L. Llewellyn, T. Devic, P. L. Llewellyn, K. C. Serre, *Phys. Rev. Lett.*, 2010, **4**, 143–152.
- 5 W. Gao, A. D. Cardenal, C. Wang and D. C. Powers, *Chem. Eur.*, 2019, **25**, 3465–3476.
- 6 S. Amirjalayer and R. Schmid, *Micropor. Mesopor. Matter*, 2009, **125**, 90–96.
- 7 S. Amirjalayer, M. Tafipolsky and R. Schmid, *Angew. Chem. Int. Ed.*, 2007, **46**, 463–466.
- 8 D. Colognesi, L. Ulivi, M. Zoppi, A. J. Ramirez-Cuesta, A. Orecchini, A. J. Karkamkar, M. Fichtner, E. Gil Bardají and Z. Zhao-Karger, *J. Alloys Compd.*, 2012, **538**, 91–99.
- 9 Q. Li and T. Thonhauser, *J. Condens. Matter. Phys*, 2017, **29**, 465901.
- 10 J. Li, S. Li, A. Zheng, X. Liu, N. Yu and F. Deng, *J. Phys. Chem. C*, 2017, **121**, 14261–14268.
- 11 D. Saha, Z. Bao, F. Jia and S. Deng, *Environ. Sci. Technol.*, 2010, **44**, 1820–1826.
- 12 M. Dincă and J. R. Long, *J. Am. Chem. Soc.*, 2005, **127**, 9376–9377.
- 13 T. L. Easun, F. Moreau, Y. Yan, S. Yang and M. Schröder, *Chem. Soc. Rev.*, 2017, **46**, 239–274.
- 14 T. D. Duong, S. A. Sapchenko, I. da Silva, H. G. W. Godfrey, Y. Cheng, L. L. Daemen, P. Manuel, M. D. Frogley, G. Cinque, A. J. Ramirez-Cuesta, S. Yang and M. Schröder, *Chem. Sci.*, 2020, **11**, 5339–5346.
- 15 S. Yang, A. J. Ramirez-Cuesta and M. Schröder, *Chem. Phys.*, 2014, **428**, 111–116.
- 16 T. Uemura, *Kinetic Control in Synthesis of Polymers Using Nanoporous Metal-Organic Frameworks*, Elsevier, 2018.
- 17 T. Kitao and T. Uemura, *Chem. Lett.*, 2020, **49**, 624–632.
- 18 B. Le Ouay and T. Uemura, *Isr. J. Chem.*, 2018, **58**, 995–1009.
- 19 C. L. Jones, PhD Thesis, Cardiff University, 2019.

## Chapter 6: Conclusion

---

- 20 M. Falkowska, D. T. Bowron, H. Manyar, T. G. A. Youngs and C. Hardacre, *Angew. Chem. Int. Ed.*, 2018, **57**, 4565–4570.
- 21 T. Uemura, K. Kitagawa, S. Horike, T. Kawamura, S. Kitagawa, M. Mizuno, and K. Endo, *Chem. Commun.*, 2005, **48**, 5968-5970.
- 22 T. Uemura, R. Nakanishi, S. Mochizuki, S. Kitagawa, and M. Mizuno, *Angew. Chem. Int. Ed.*, 2016, **55**, 6643–6447.

# Appendix

---

# Appendix

All appendices have been named with the following nomenclature:

**A<X>.<Y>**

Where, X = Chapter number, Y = Figure/Table number.

**Table A2.1: Properties of Poly(vinyl acetate)**

Summary of properties of poly(vinyl acetate). Data collected from Oxford Handbook of Polymers.<sup>1</sup>

Parameter	Unit	Value
<b>GENERAL</b>		
Common name	-	Poly(vinyl acetate)
IUPAC name	-	Poly(ethenyl ethanoate)
Acronym	-	PVAc
CAS number	-	9003-20-7
Empirical Formula	-	(C <sub>4</sub> H <sub>6</sub> O <sub>2</sub> ) <sub>n</sub>
<b>SYNTHESIS</b>		
Monomer	-	Vinyl Acetate
Molecular weight	g/mol	86.09
Synthesis method	-	Oxidative addition of acetic acid to ethylene.
Mass average molecular weight	g/mol	13,000 – 500,000
Polydispersity, M <sub>w</sub> /M <sub>n</sub>	-	2.0
Molar volume (298 K)	cm <sup>3</sup> /mol	74.25
Radius of gyration (R <sub>g</sub> )	nm	66
<b>PHYSICAL PROPERTIES</b>		
Density at 20 °C	g/cm <sup>3</sup>	1.18 – 1.20
Bulk density at 20 °C	g/cm <sup>3</sup>	0.7 – 0.85
Colour	-	Colourless
Odour	-	Odourless
Melting temperature	°C	152 – 180

# Appendix

Softening point	°C	> 190
Decomposition temperature	°C	> 250
Thermal expansion coefficient 23–80 °C	°C <sup>-1</sup>	2.8E-4
Thermal conductivity	W m <sup>-1</sup> K <sup>-1</sup>	0.16
Glass transition temperature	°C	24-32 (atactic); 26 (isotactic); 28-40 (commercial)
Hansen solubility parameter, $\delta_D$ , $\delta_P$ , $\delta_H$	MPa <sup>0.5</sup>	10.9, 11.3, 9.7
Surface tension	mN m <sup>-1</sup>	36.5
Surface free energy	mJ m <sup>-2</sup>	38.5
<b>CHEMICAL SOLUBILITY</b>		
Good solvent	-	Acetic acid, Acetone, Acetonitrile, Allyl alcohol, Chlorobenzene, Chloroform, DMF, DMSO, Methanol, THF, Toluene.
Non-solvent	-	Acids, Dilute alkali, Carbon disulfide, Cyclohexanol, ethylene, Glycol, Mesitylene.
<b>CHARACTERISTICS</b>		
<sup>1</sup> H NMR (chemical shifts)	ppm	COOH – 8.76; OH – 5.61, 5.58.
FTIR (wavenumber assignment)	cm <sup>-1</sup>	C=O – 1737; C-H – 1375; O-C – 1020
Raman (wavenumber assignment)	cm <sup>-1</sup>	C-C – 1132; C=C – 1525

# Appendix

**Table A2.2: Properties of Poly(lactic acid)**

Summary of properties of PLA. Data collected from Oxford Handbook of Polymers.<sup>1</sup>

Parameter	Unit	Value
<b>GENERAL</b>		
Common name	-	Poly(lactic acid)
IUPAC name	-	1,4-dioxane-2,5-dione
Acronym	-	PLA
CAS number	-	51063-13-9, 26680-10-4, 34346-01-5
Empirical Formula	-	(C <sub>3</sub> H <sub>4</sub> O <sub>2</sub> ) <sub>n</sub>
<b>SYNTHESIS</b>		
Monomer	-	Lactic acid, Lactide
Molecular weight	g/mol	144.13
Synthesis method	-	Lactic acid is heated to 150 °C to obtain oligomeric PLA. Oligomers are heated to 180 °C under vacuum for 5 h to give PLA.
Mass average molecular weight	g/mol	13,000 – 500,000
Polymerisation temperature	°C	150-180
Catalyst	-	Tin(II) ethylhexanoate
Polydispersity, M <sub>w</sub> /M <sub>n</sub>	-	1.5-3.8
Molar volume (298 K)	cm <sup>3</sup> /mol	74.25
Radius of gyration (R <sub>g</sub> )	nm	66
<b>PHYSICAL PROPERTIES</b>		
Density at 20 °C	g/cm <sup>3</sup>	1.21 – 1.29
Molar Volume	mL/mol	56.7-57.7
Colour	-	Colourless
Odour	-	Odourless
Melting temperature	°C	150 – 180
Decomposition temperature	°C	> 200
Thermal expansion coefficient 23–80 °C	°C <sup>-1</sup>	2.8E-4

# Appendix

Glass transition temperature	°C	55 – 75
Enthalpy of fusion	kJ mol <sup>-1</sup>	21.9 – 43.8
Specific heat capacity	J K <sup>-1</sup> kg <sup>-1</sup>	540 – 600
Hansen solubility parameter, $\delta_D$ , $\delta_P$ , $\delta_H$	MPa <sup>0.5</sup>	18.50, 9.7, 6.0
<b>CHEMICAL SOLUBILITY</b>		
Good solvent	-	Acetone, Benzene, Chloroform, m-Cresol, Dichloromethane, Dioxane, DMF, Ethyl acetate, Isoamyl alcohol, Toluene, Xylene..
Non-solvent	-	Methanol, Ethanol, Most alcohol, Ketones, Halogenated hydrocarbons
<b>CHARACTERISTICS</b>		
<sup>13</sup> C NMR (chemical shifts)	ppm	C=O – 170.8; –CH – 70.5, –CH <sub>3</sub> 5.58.
FTIR (wavenumber assignment)	cm <sup>-1</sup>	C=O – 1748; ref - 1451
Raman (wavenumber assignment)	cm <sup>-1</sup>	C-O – 1128; C-C – 1044

# Appendix

**Table A2.3: Properties of Poly( $\epsilon$ -caprolactone)**

Summary of properties of poly( $\epsilon$ -caprolactone). Data collected from Oxford Handbook of Polymers.<sup>1</sup>

Parameter	Unit	Value
<b>GENERAL</b>		
Common name	-	Poly( $\epsilon$ -caprolactone)
IUPAC name	-	2-oxepanone, homopolymer; Poly[oxy(1-oxo-1,6,hexanediyl)]
Acronym	-	PCL
CAS number	-	24980-41-4; 25248-42-4
Empirical Formula	-	(C <sub>6</sub> H <sub>10</sub> O <sub>2</sub> ) <sub>n</sub>
<b>SYNTHESIS</b>		
Monomer	-	$\epsilon$ -caprolactone
Molecular weight	g/mol	114.14
Synthesis method	-	Ring-opening addition polymerisation of $\epsilon$ -caprolactone at 70 °C under vacuum with Sn(II)Oct <sub>2</sub> as catalyst.
Mass average molecular weight	g/mol	13,000 – 500,000
Polymerisation temperature	°C	120
Catalyst	-	Tin(II) ethylhexanoate
Polydispersity, M <sub>w</sub> /M <sub>n</sub>	-	1.08-1.53
<b>PHYSICAL PROPERTIES</b>		
Density at 20 °C	g/cm <sup>3</sup>	1.07 – 1.2
Molar Volume	mL/mol	99.7 – 104.2
Colour	-	White
Odour	-	Odourless
Melting temperature	°C	58 – 63
Decomposition temperature	°C	200 – 220
Glass transition temperature	°C	-60 to -72
Ignition temperature	°C	275

# Appendix

Specific volume	$\text{cm}^3 \text{g}^{-1}$	0.83 – 1.01
Specific heat capacity	$\text{cal g}^{-1} \text{C}^{-1}$	1.5E-1 to 4.7E-1
Enthalpy of fusion	$\text{kJ mol}^{-1}$	24.4
Hansen solubility parameter, $\delta_D$ , $\delta_P$ , $\delta_H$	$\text{MPa}^{0.5}$	18.50, 9.7, 6.0
<b>CHEMICAL SOLUBILITY</b>		
Good solvent	-	Benzene, Chloroform, Dimethylacetamide, Dichloromethane, Carbon tetrachloride, Toluene, Cyclohexane, 2-nitropropane, THF
Non-solvent	-	Alcohols, Petroleum ether, Diethyl ether, and Water.
<b>CHARACTERISTICS</b>		
$^1\text{H}$ NMR (chemical shifts)	ppm	$\text{CH}_2$ – 1.6, 2.3, 3.63, 3.8, 4.0, 4.2.
FTIR (wavenumber assignment)	$\text{cm}^{-1}$	C=O – 1778; C=C – 1642; C-O – 1164, 1107.

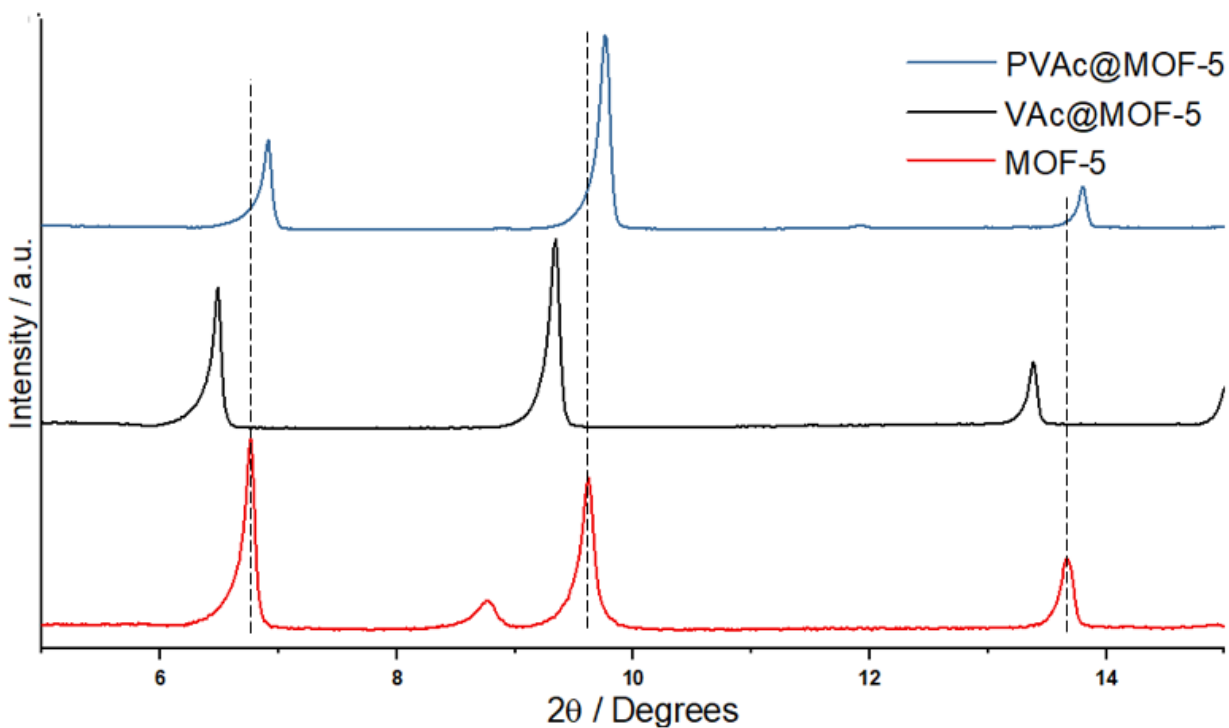


Fig A4.1: PXR D pattern with  $2\theta = 5\text{--}15^\circ$  range expansion for synthesised MOF-5, VAc@MOF-5, and PVAc@MOF-5. (The diffraction patterns shown are background subtracted)

# Appendix

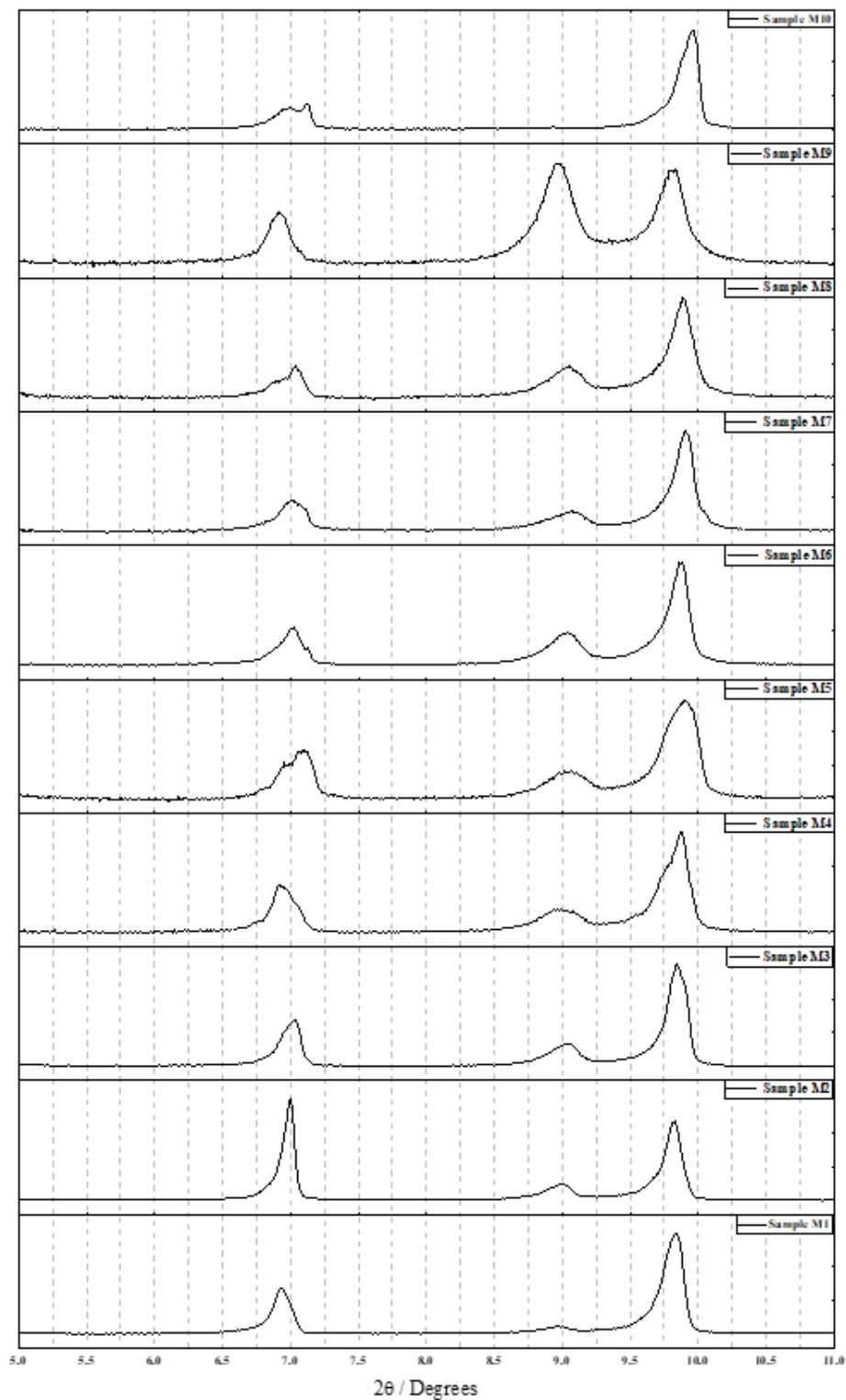


Fig A4.2: PXRD pattern with  $2\theta = 5\text{--}11^\circ$  range expansion for synthesised MOF-5, VAc@MOF-5, and PVAc@MOF-5.

# Appendix

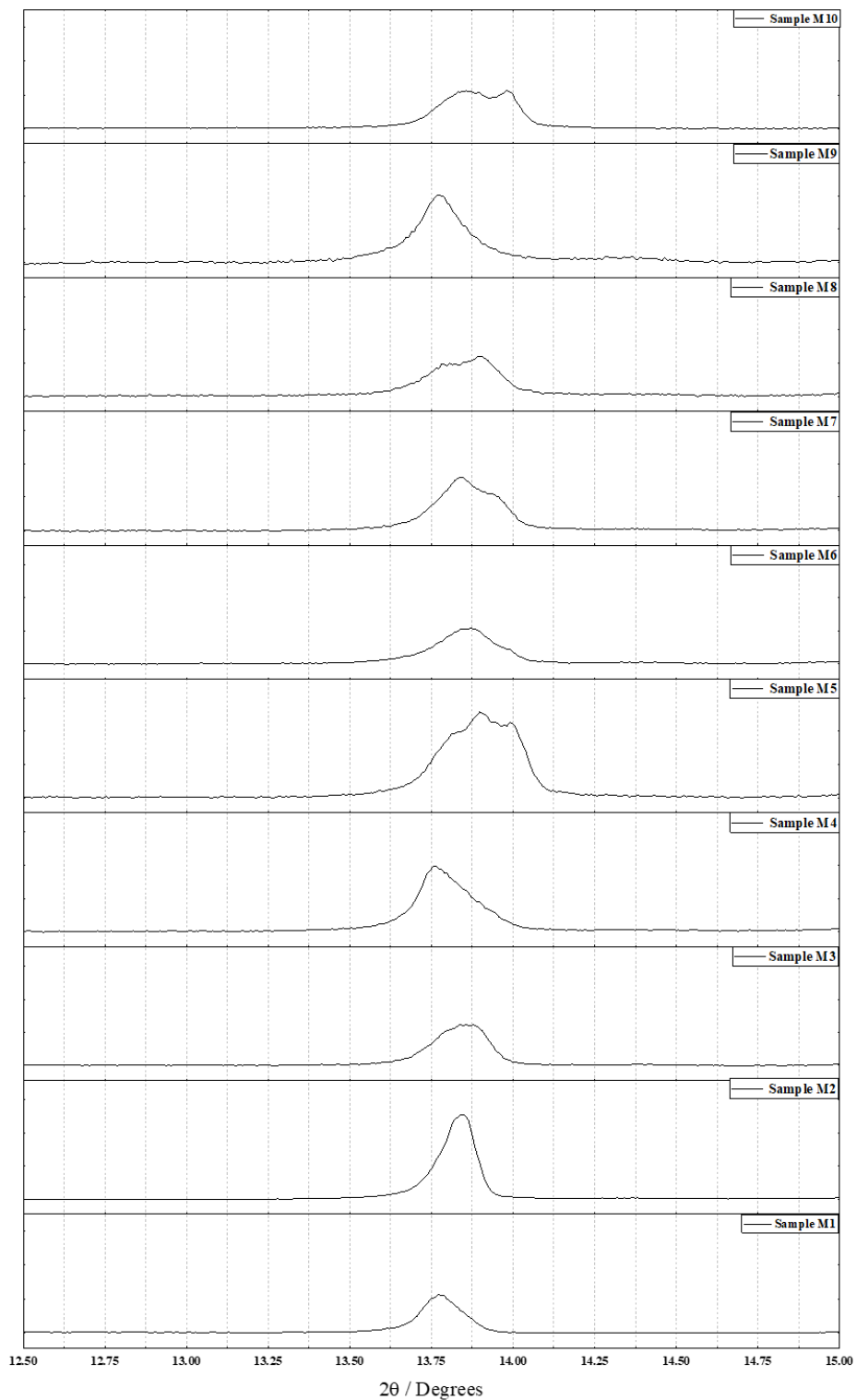


Fig A4.3: PXRD pattern with  $2\theta = 11\text{--}15^\circ$  range expansion for synthesised MOF-5, VAc@MOF-5, and PVAc@MOF-5.

# Appendix

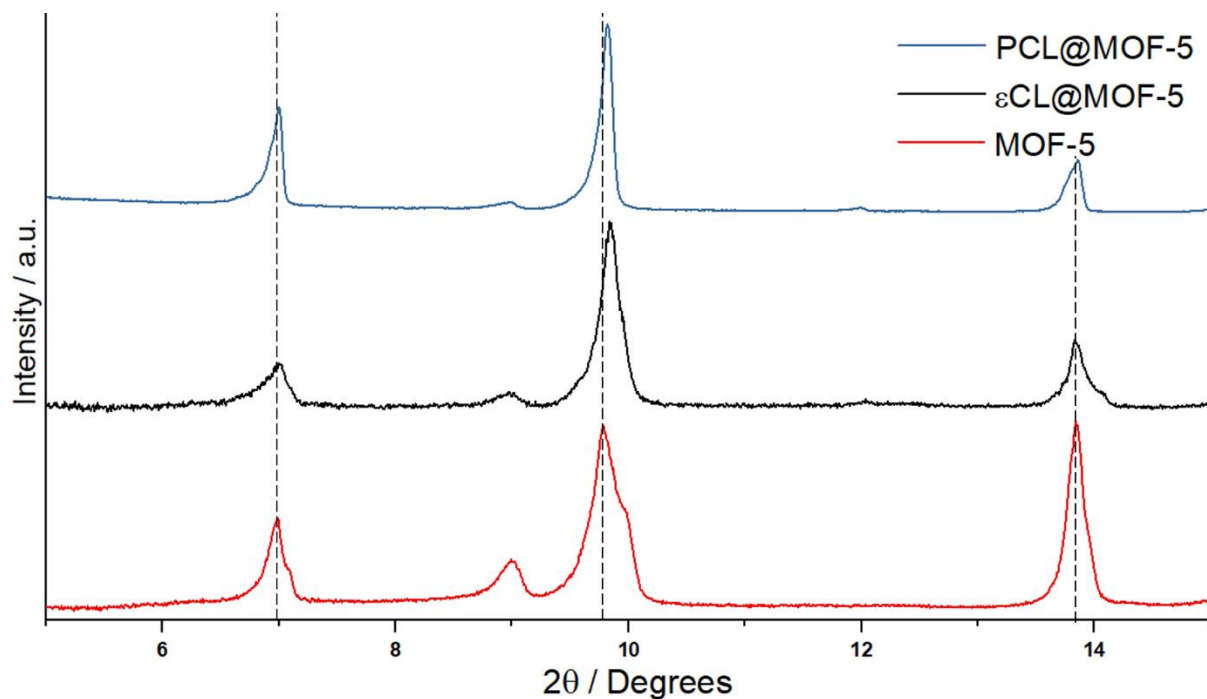


Fig A4.4: PXRD pattern with  $2\theta = 5\text{--}15^\circ$  range expansion for synthesised MOF-5,  $\epsilon\text{CL@MOF-5}$ , and PCL@MOF-5. (The diffraction patterns shown are background subtracted)

# Appendix

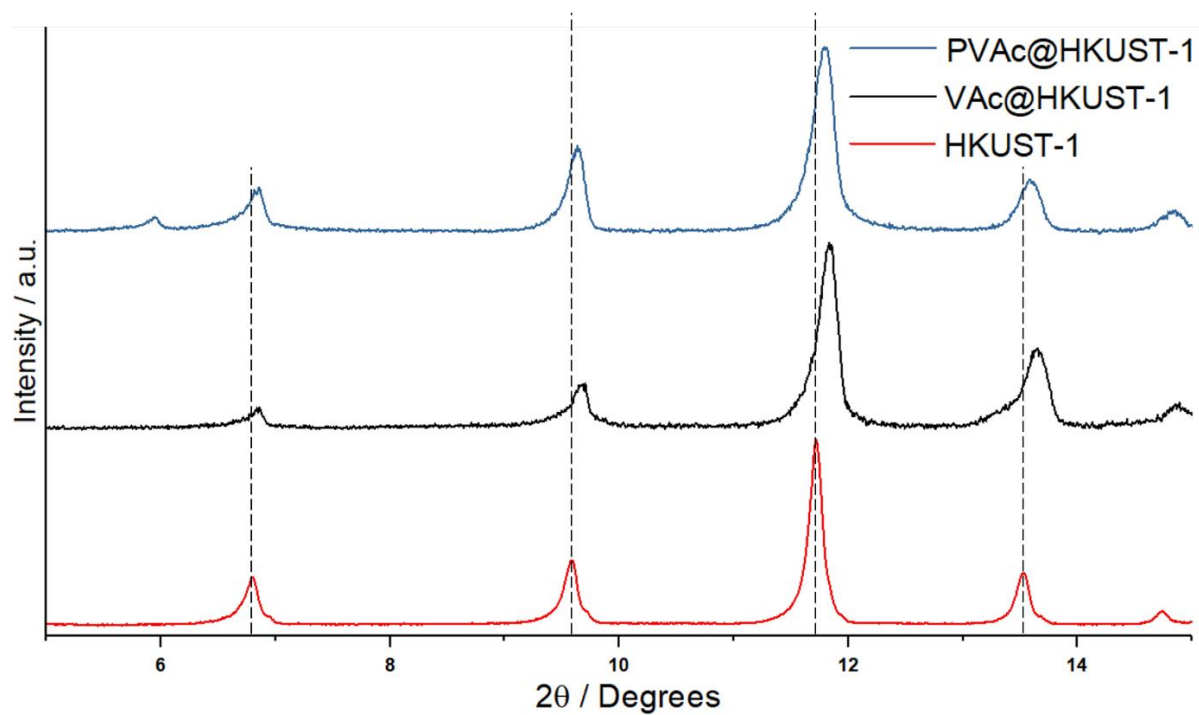


Fig A4.5: PXR D pattern with  $2\theta = 5\text{--}15^\circ$  range expansion for synthesised HKUST-1, VAc@HKUST-1, and PVAc@HKUST-1. (The diffraction patterns shown are background subtracted)

# Appendix

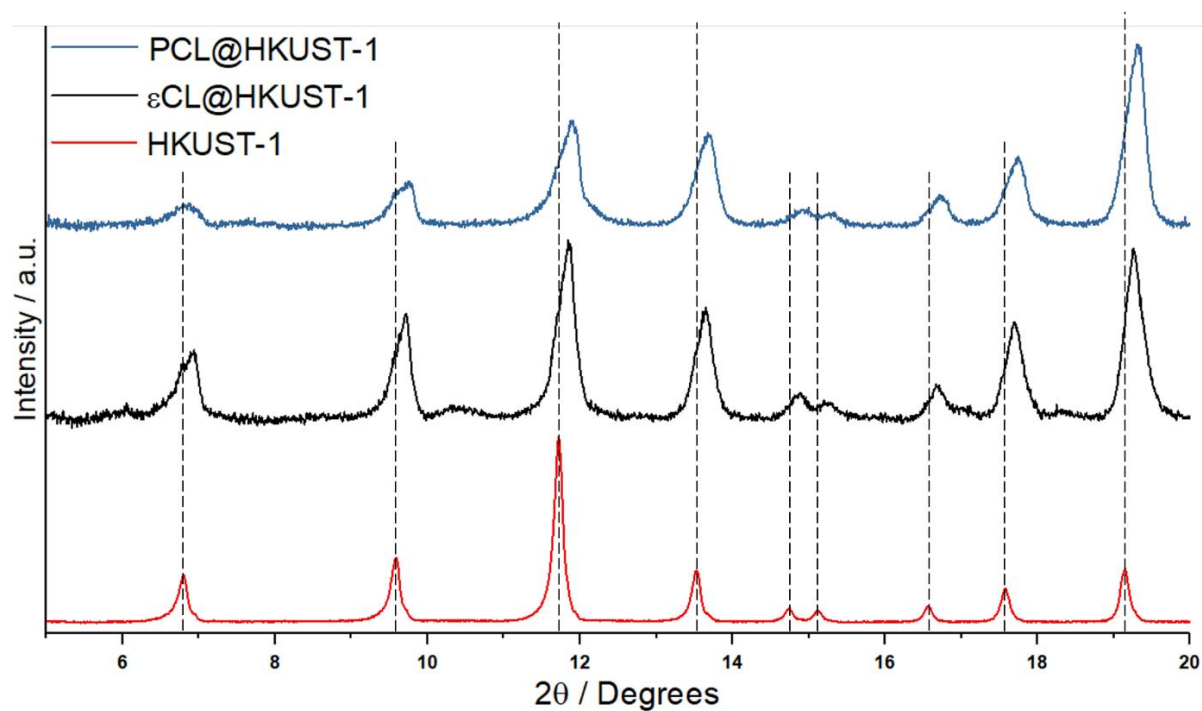


Fig A4.6: PXRD pattern with  $2\theta = 5\text{--}20^\circ$  range expansion for synthesised HKUST-1,  $\epsilon\text{CL@HKUST-1}$ , and PCL@HKUST-1. (The diffraction patterns shown are background subtracted)

# Appendix

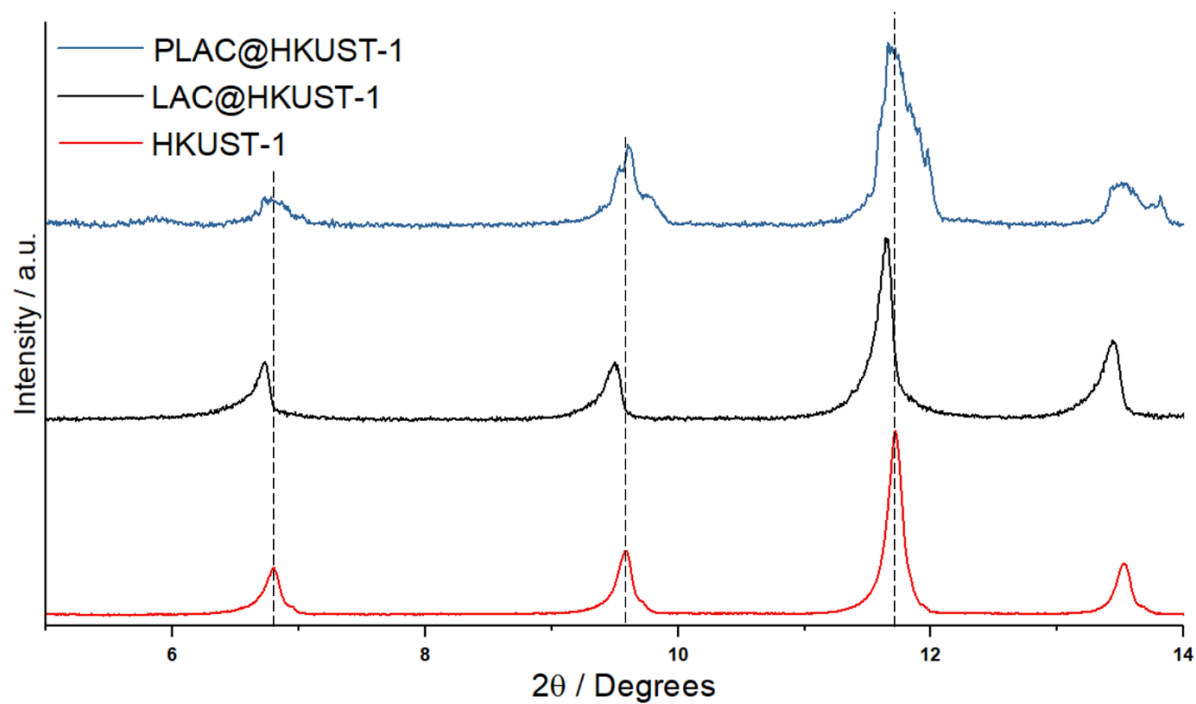


Fig A4.7: PXRD pattern with  $2\theta = 5\text{--}14^\circ$  range expansion for synthesised HKUST-1, LAC@HKUST-1, and PLAC@HKUST-1. (The diffraction patterns shown are background subtracted)

# Appendix

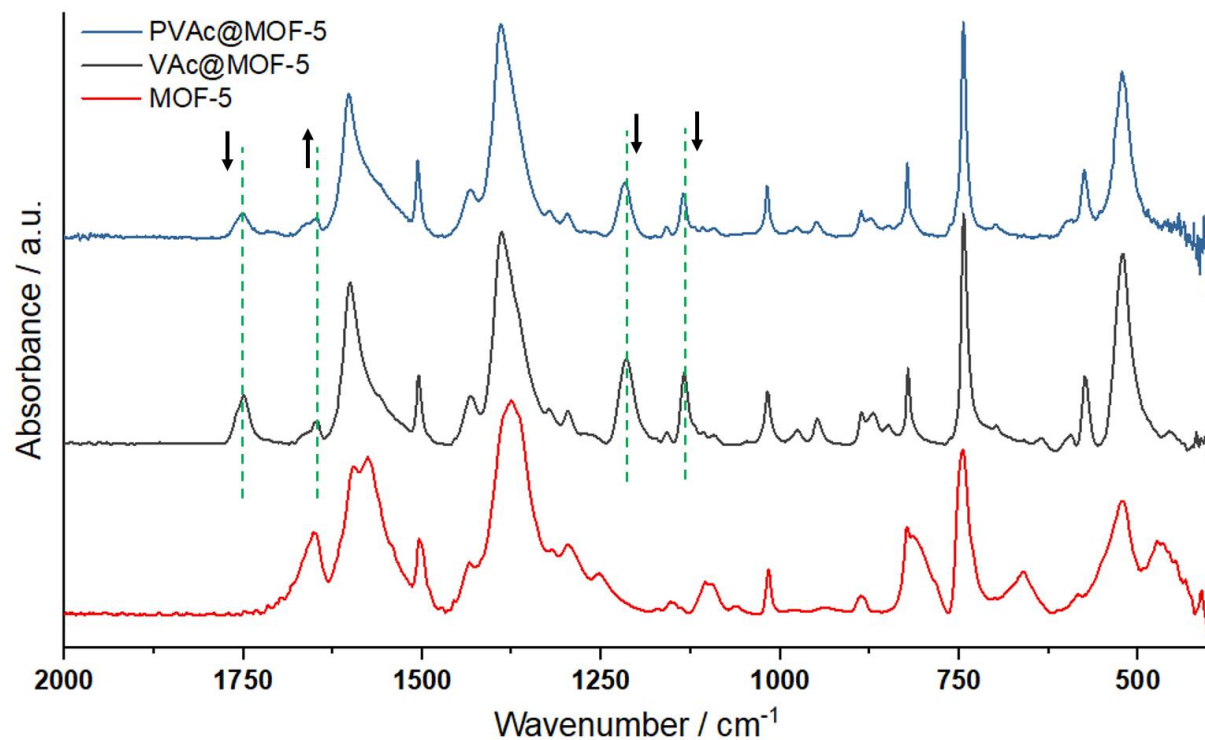


Fig A4.8: ATR-FTIR spectra of MOF-5, VAc@MOF-5 and PVAc@MOF-5. Region between 2000–450  $\text{cm}^{-1}$ . Dashed green lines and corresponding arrows indicate changes in absorbance intensity with polymerisation. (The spectra have been normalised to  $\nu(\text{C}=\text{O})$  1350  $\text{cm}^{-1}$  absorbance peak of the MOF.)

# Appendix

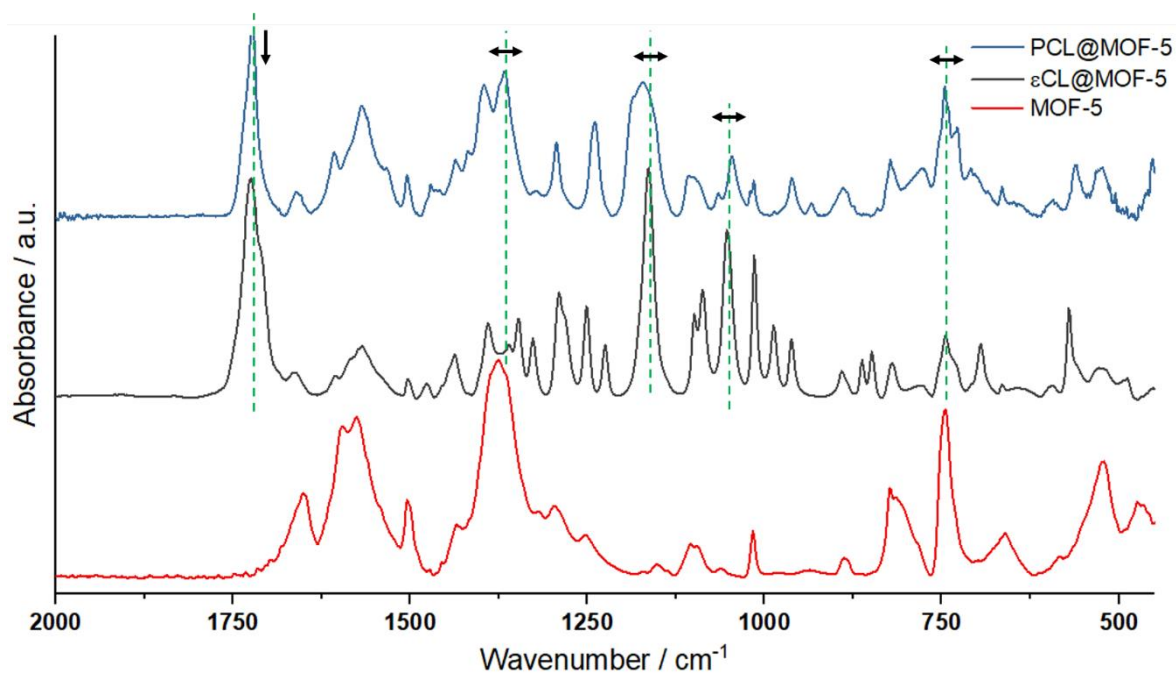


Fig A4.9: ATR-FTIR spectra of MOF-5,  $\epsilon$ CL@MOF-5 and PCL@MOF-5. Region between 2000–450  $\text{cm}^{-1}$ . Dashed green lines and corresponding arrows indicate changes in absorbance intensity with polymerisation. (The spectra have been normalised to  $\nu(\text{C}=\text{O})$  1350  $\text{cm}^{-1}$  absorbance peak of the MOF.)

# Appendix

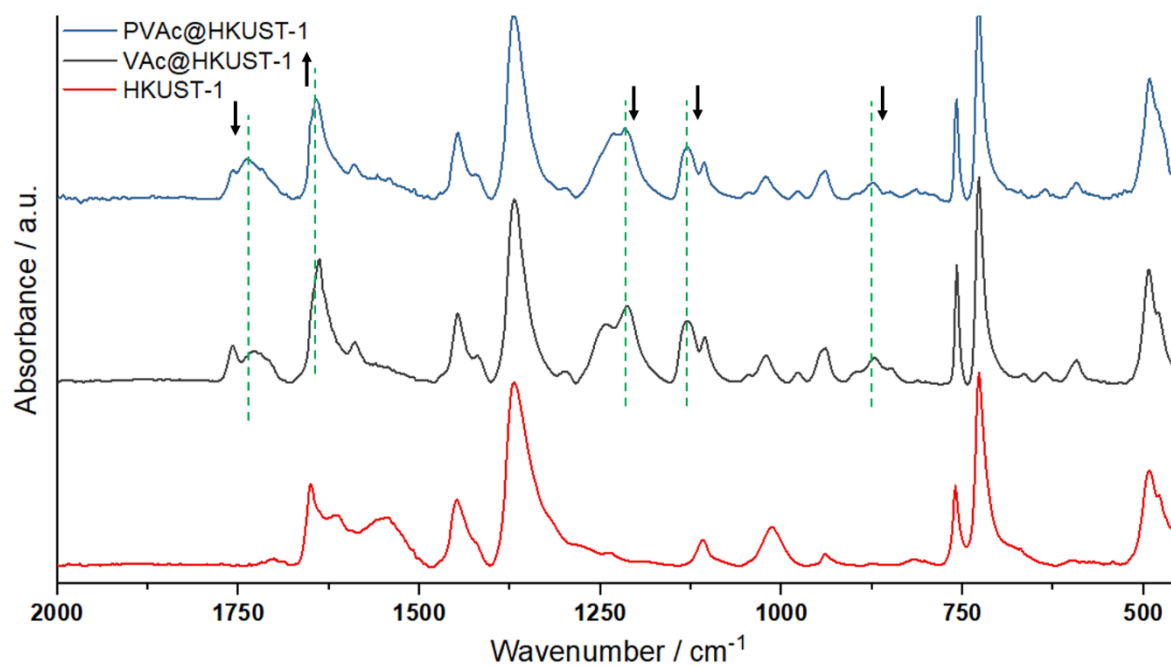


Fig A4.10: ATR-FTIR spectra of HKUST-1, VAc@HKUST-1 and PVAc@HKUST-1. Region between 2000–450  $\text{cm}^{-1}$ . Dashed green lines and corresponding arrows indicate changes in absorbance intensity with polymerisation. (The spectra have been normalised to  $\nu(\text{C}=\text{O})$  1350  $\text{cm}^{-1}$  absorbance peak of the MOF.)

# Appendix

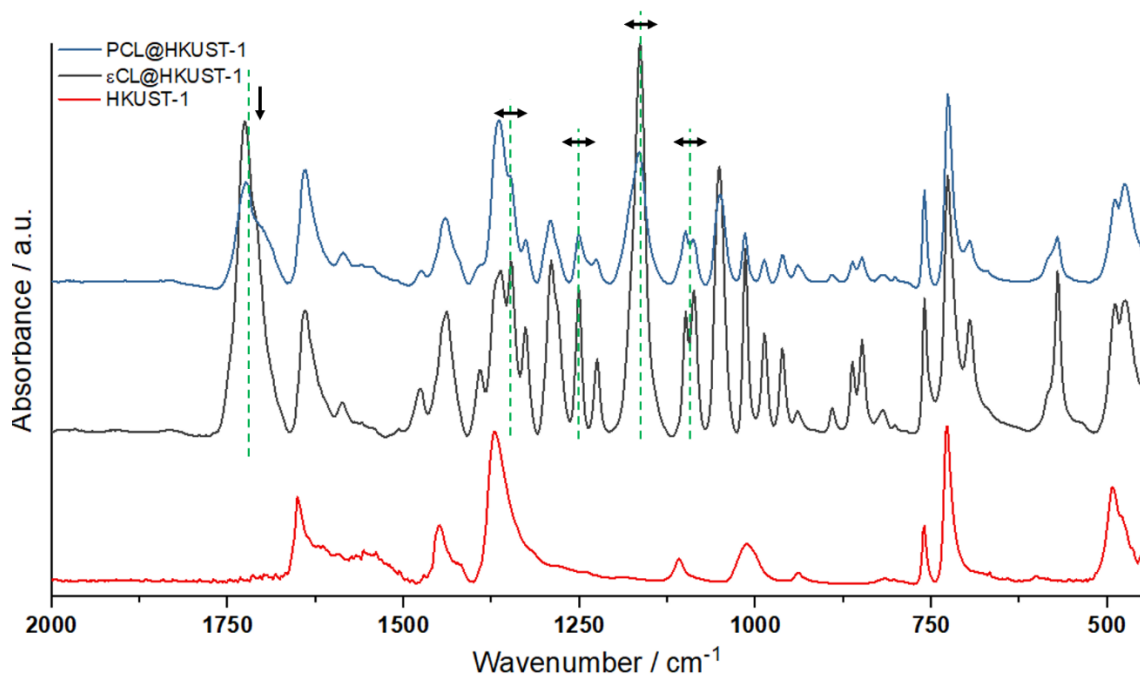


Fig A4.11: ATR-FTIR spectra of HKUST-1,  $\epsilon$ CL@HKUST-1 and PCL@HKUST-1. Region between 2000–450  $\text{cm}^{-1}$ . Dashed green lines and corresponding arrows indicate changes in absorbance intensity with polymerisation. (The spectra have been normalised to  $\nu(\text{C}=\text{O})$  1350  $\text{cm}^{-1}$  absorbance peak of the MOF.)

# Appendix

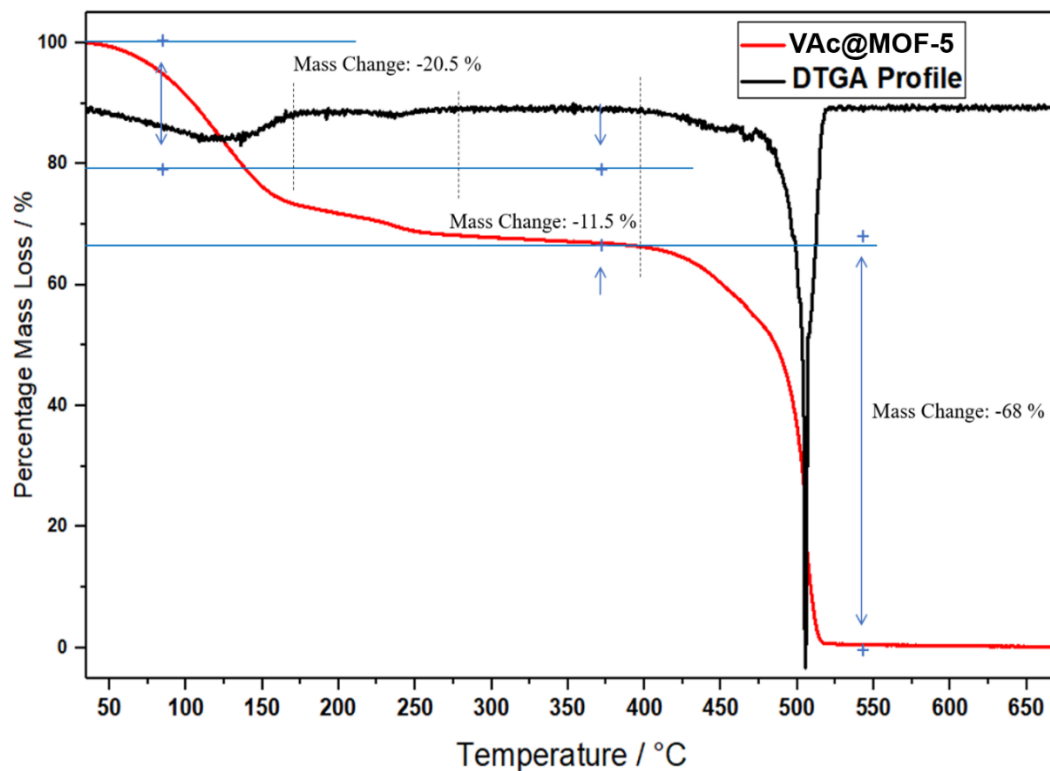


Fig A4.12: TGA and DTGA profile of VAc@MOF-5 under air flow. (The 1<sup>st</sup> order DTGA profile is smoothed to weighted average of 10 points equivalent to 0.01 °C).

# Appendix

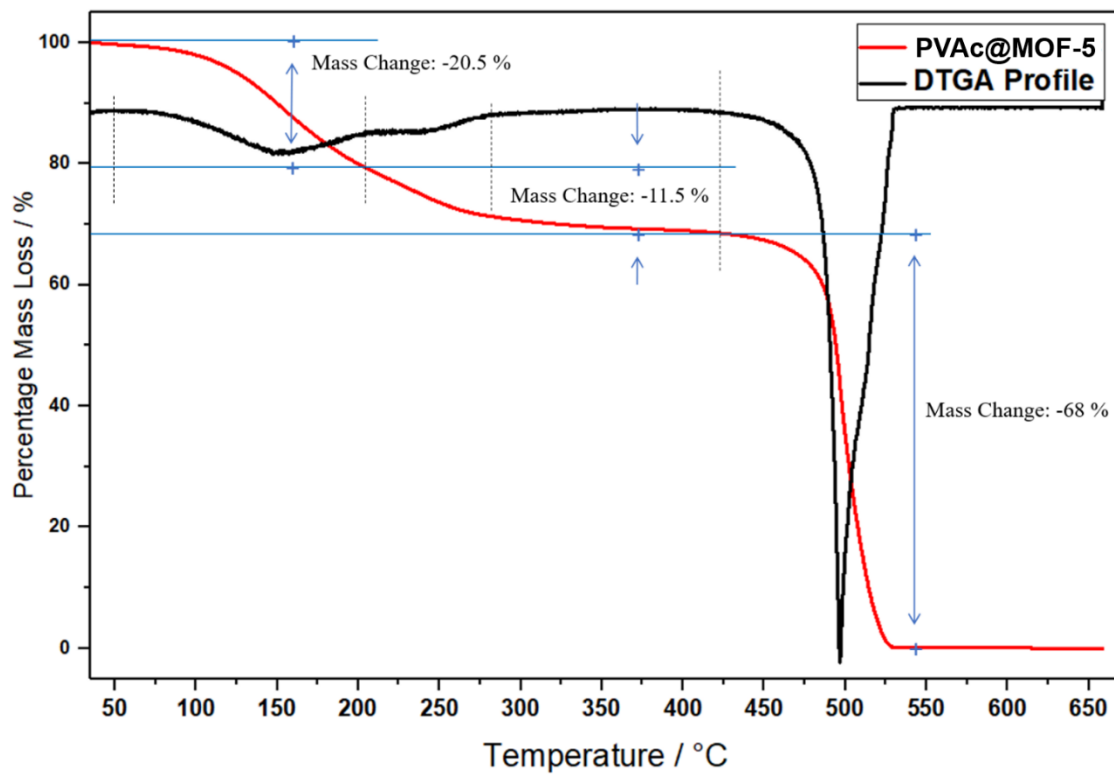


Fig A4.13: TGA and DTGA profile of PVAc@MOF-5 under air flow. (The 1<sup>st</sup> order DTGA profile is smoothened to weighted average of 10 points equivalent to 0.01 °C).

# Appendix

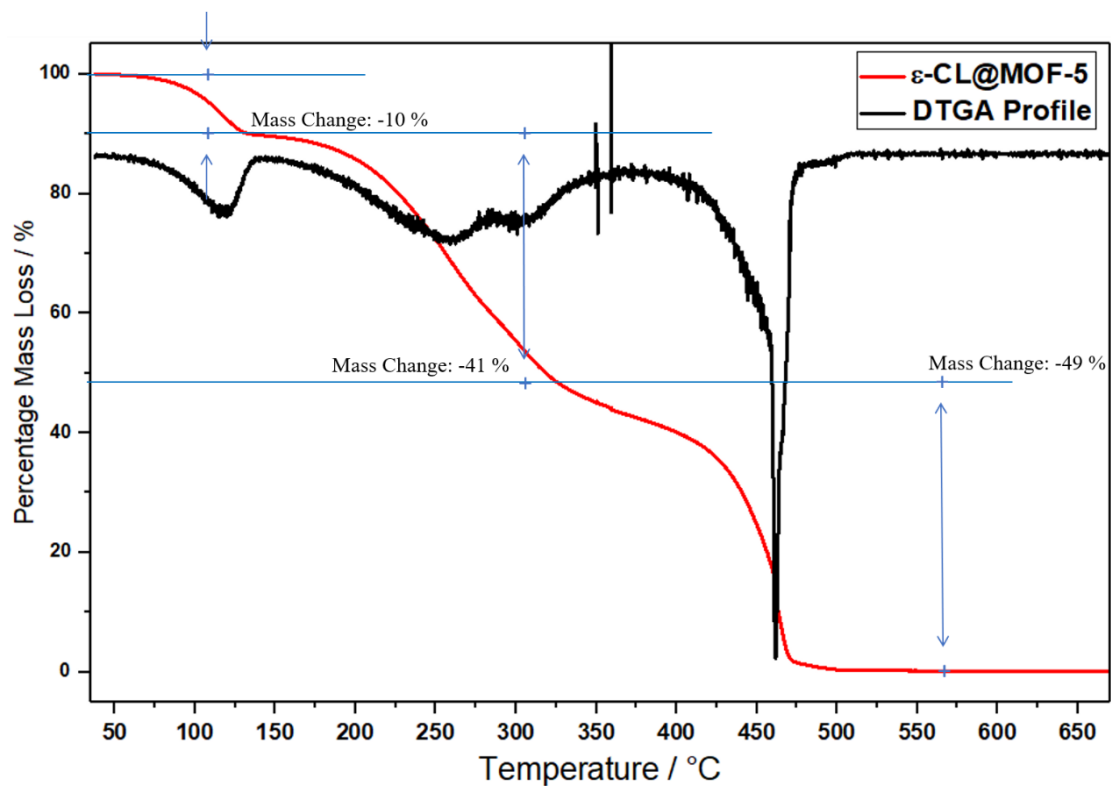


Fig A4.14: TGA and DTGA profile of  $\epsilon$ CL@MOF-5 under air flow. (The 1<sup>st</sup> order DTGA profile is smoothed to weighted average of 10 points equivalent to 0.01 °C).

# Appendix

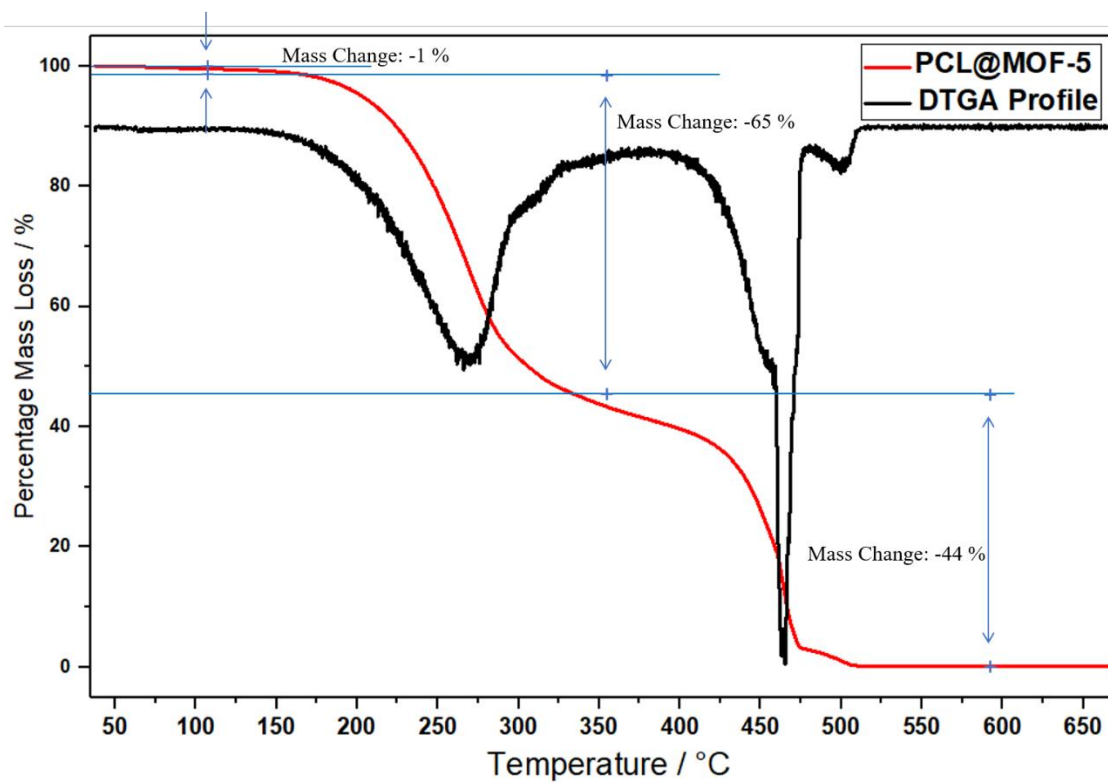


Fig A4.15: TGA and DTGA profile of PCL@MOF-5 under air flow. (The 1<sup>st</sup> order DTGA profile is smoothed to weighted average of 10 points equivalent to 0.01 °C).

# Appendix

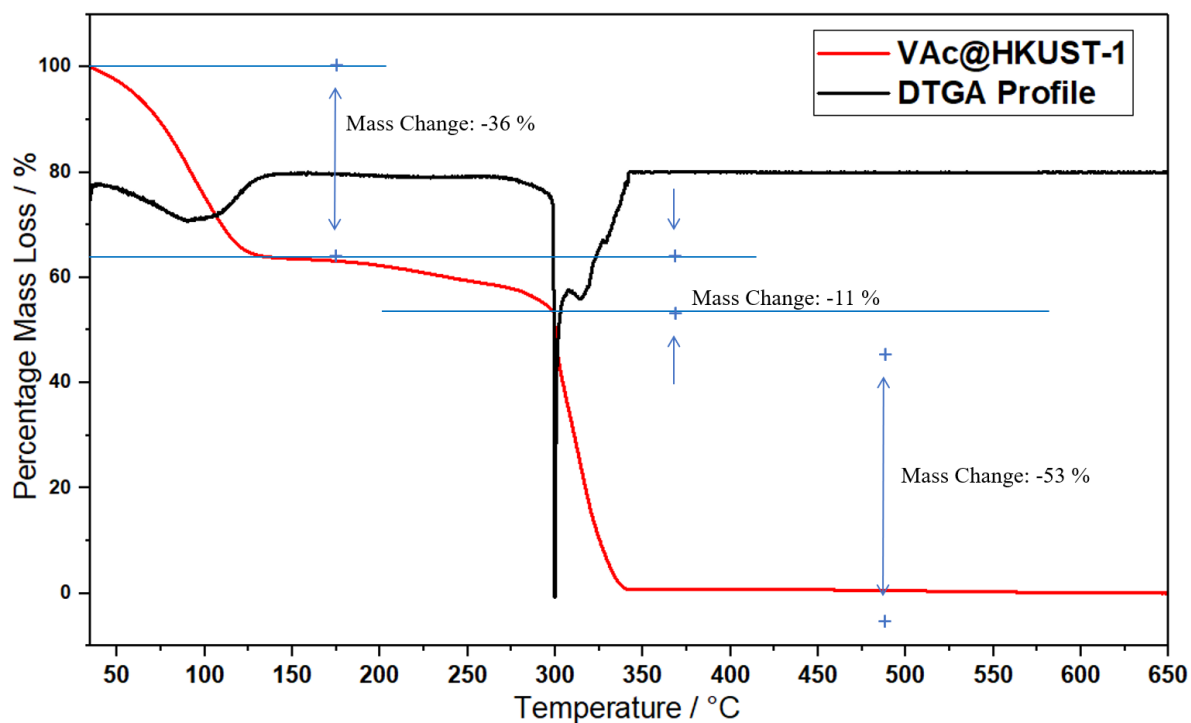


Fig A4.16: TGA and DTGA profile of VAc@HKUST-1 under air flow. (The 1<sup>st</sup> order DTGA profile is smoothed to weighted average of 10 points equivalent to 0.01 °C).

# Appendix

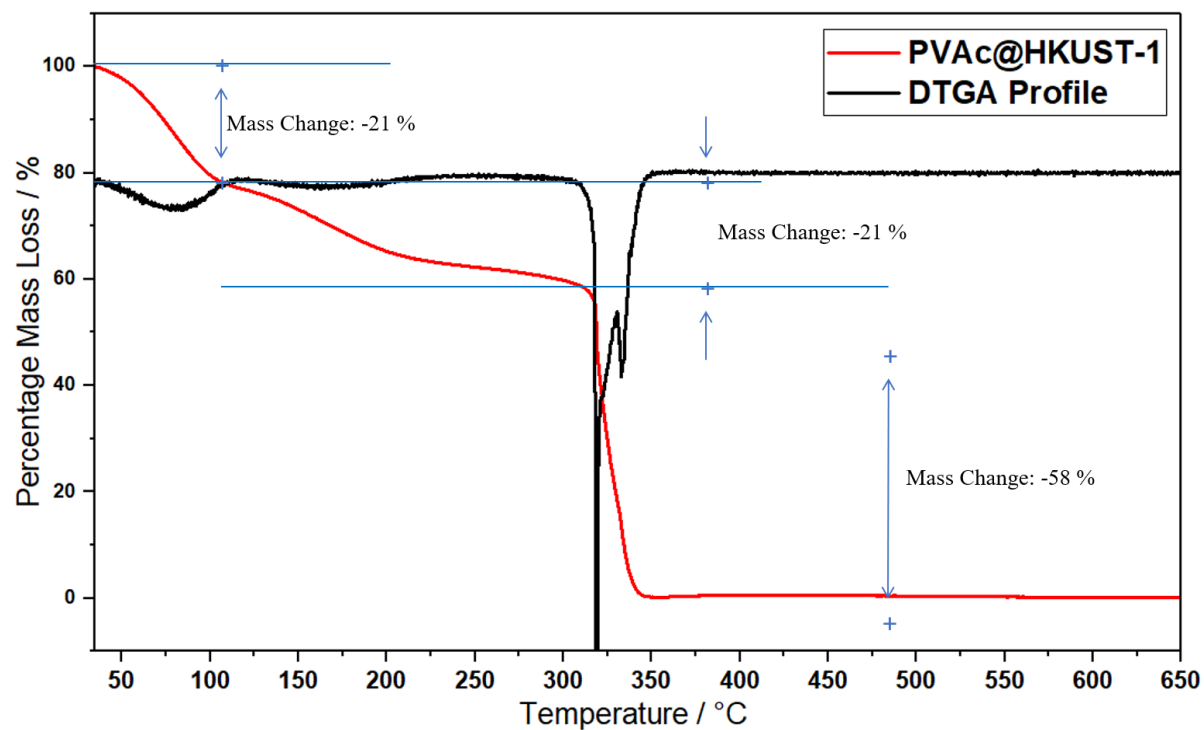


Fig A4.17: TGA and DTGA profile of PVAc@HKUST-1 under air flow. (The 1<sup>st</sup> order DTGA profile is smoothened to weighted average of 10 points equivalent to 0.01 °C).

# Appendix

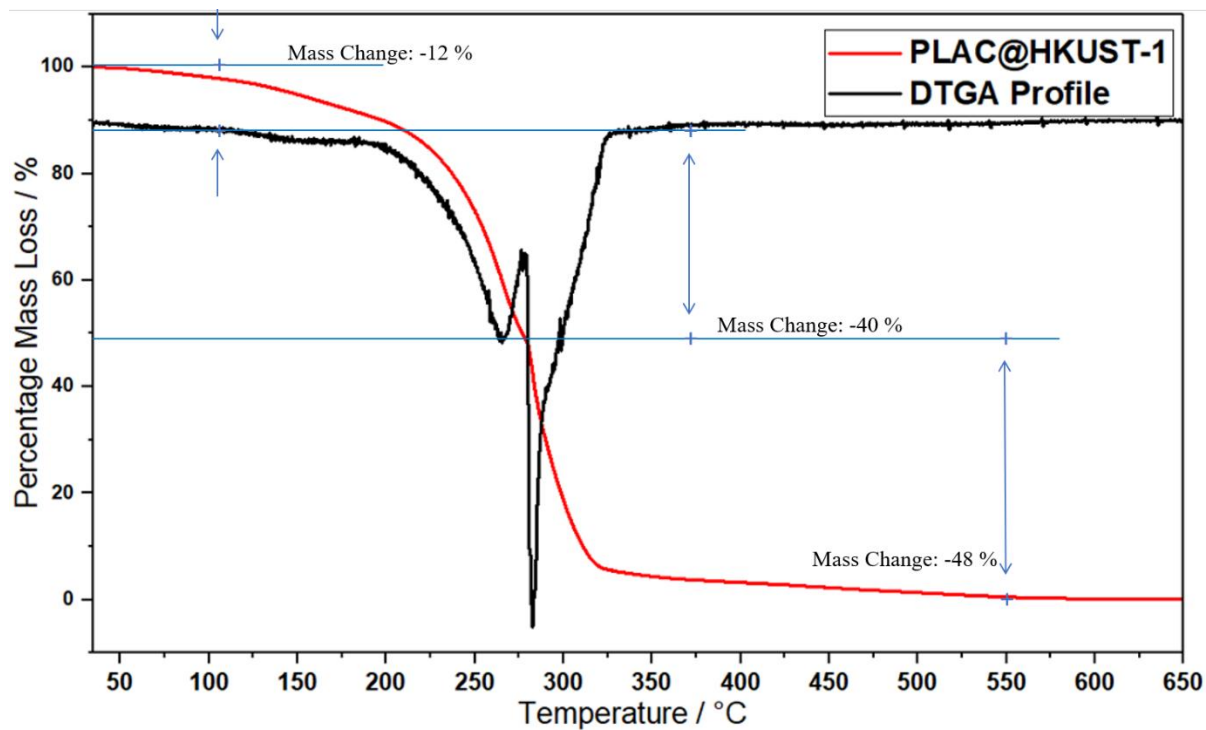


Fig A4.18: TGA and DTGA profile of PLAC@HKUST-1 under air flow. (*The 1<sup>st</sup> order DTGA profile is smoothened to weighted average of 10 points equivalent to 0.01 °C.*)

# Appendix

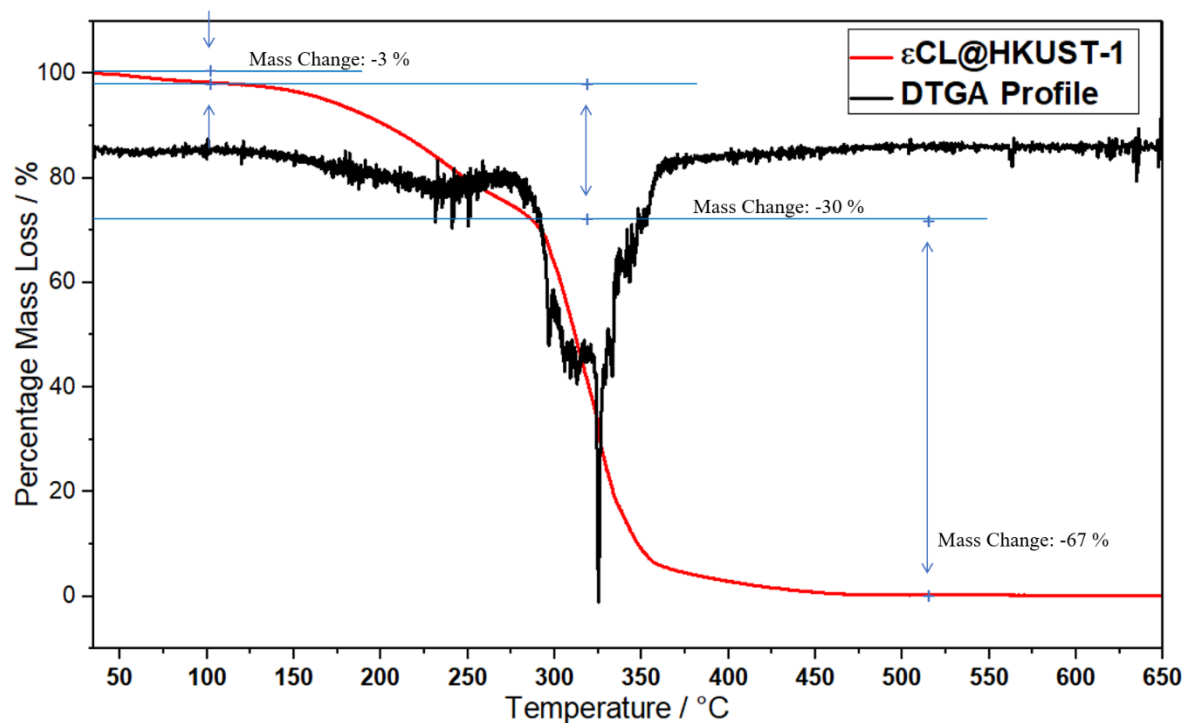


Fig A4.19: TGA and DTGA profile of  $\epsilon\text{CL@HKUST-1}$  under air flow. (The 1<sup>st</sup> order DTGA profile is smoothed to weighted average of 10 points equivalent to 0.01 °C).

# Appendix

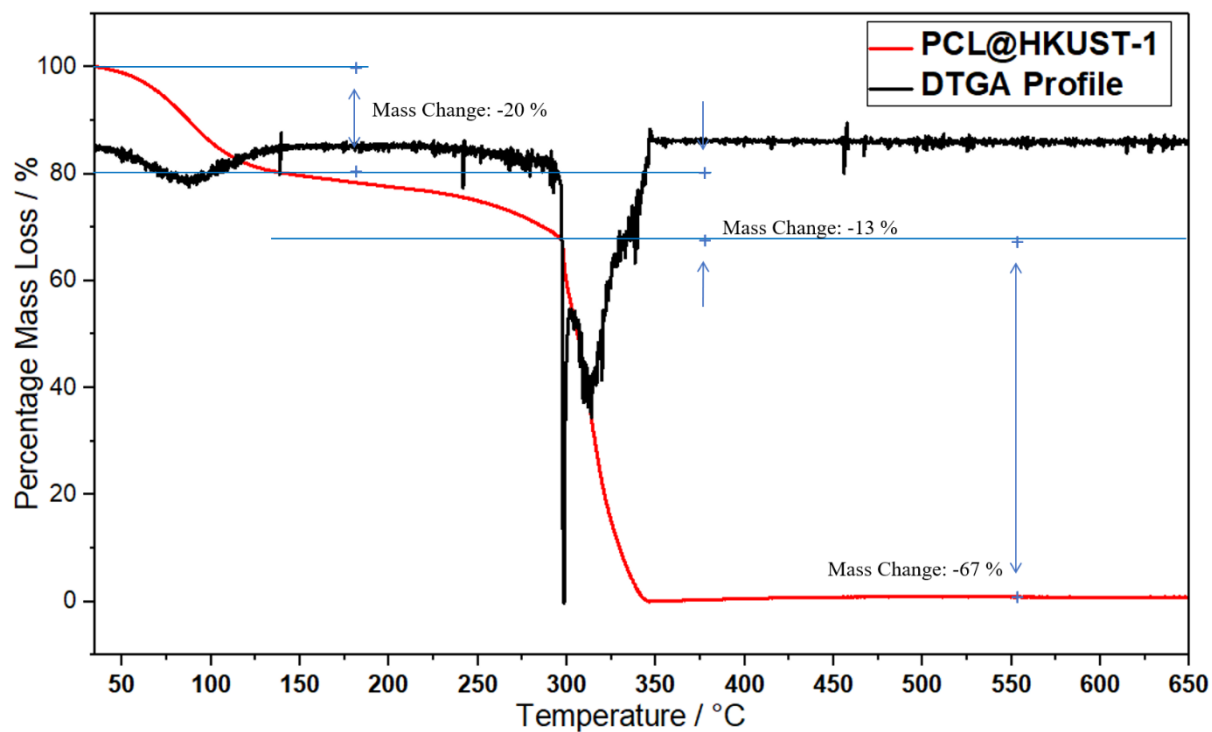


Fig A4.20: TGA and DTGA profile of PCL@HKUST-1 under air flow. (The 1<sup>st</sup> order DTGA profile is smoothened to weighted average of 10 points equivalent to 0.01 °C).

# Appendix

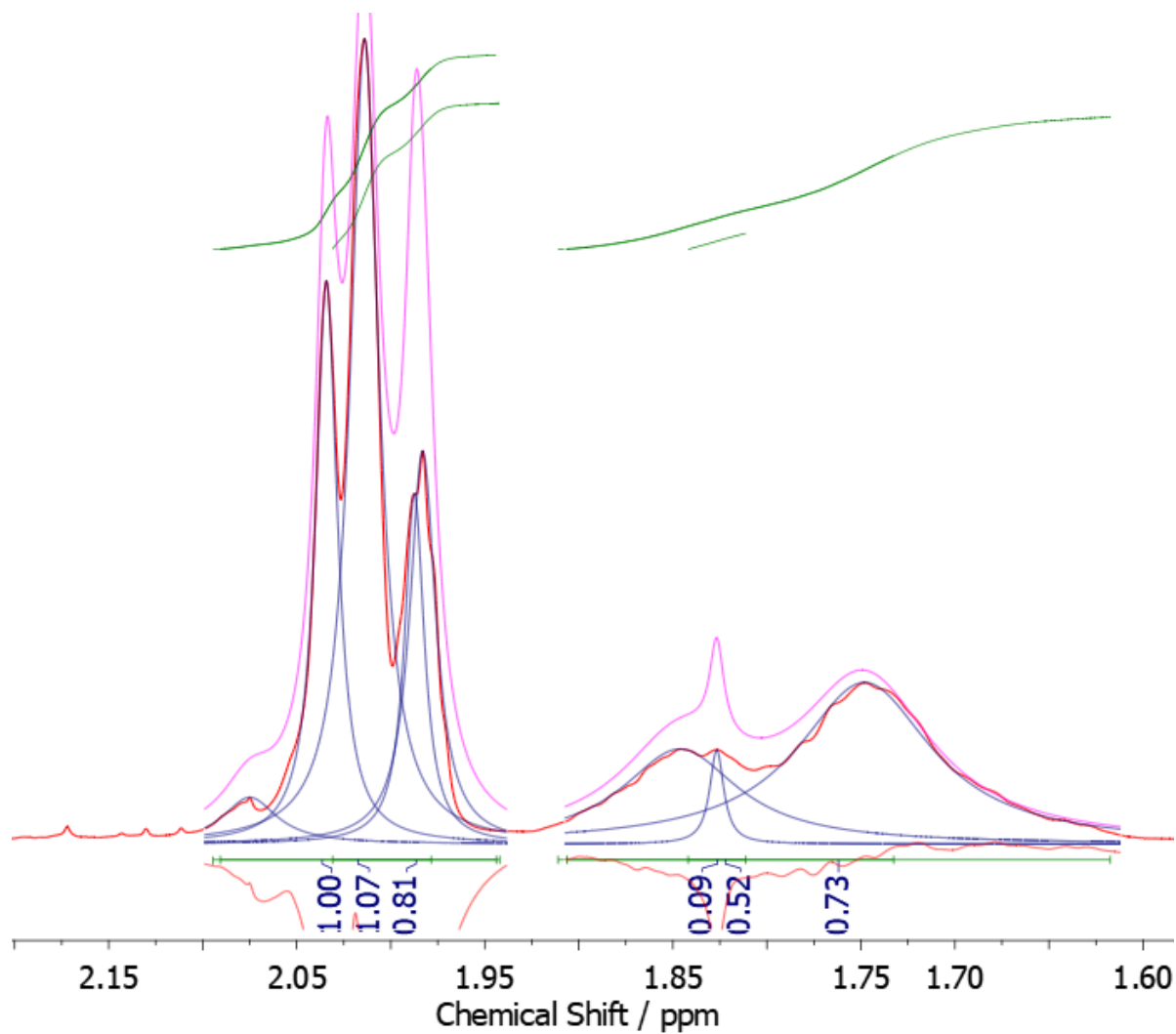


Fig A4.21: <sup>1</sup>H NMR spectra of PVAc isolated from MOF. Regions between 1.6 – 2.1 ppm have been expansion to show curve fitting and integral analysis.

# Appendix

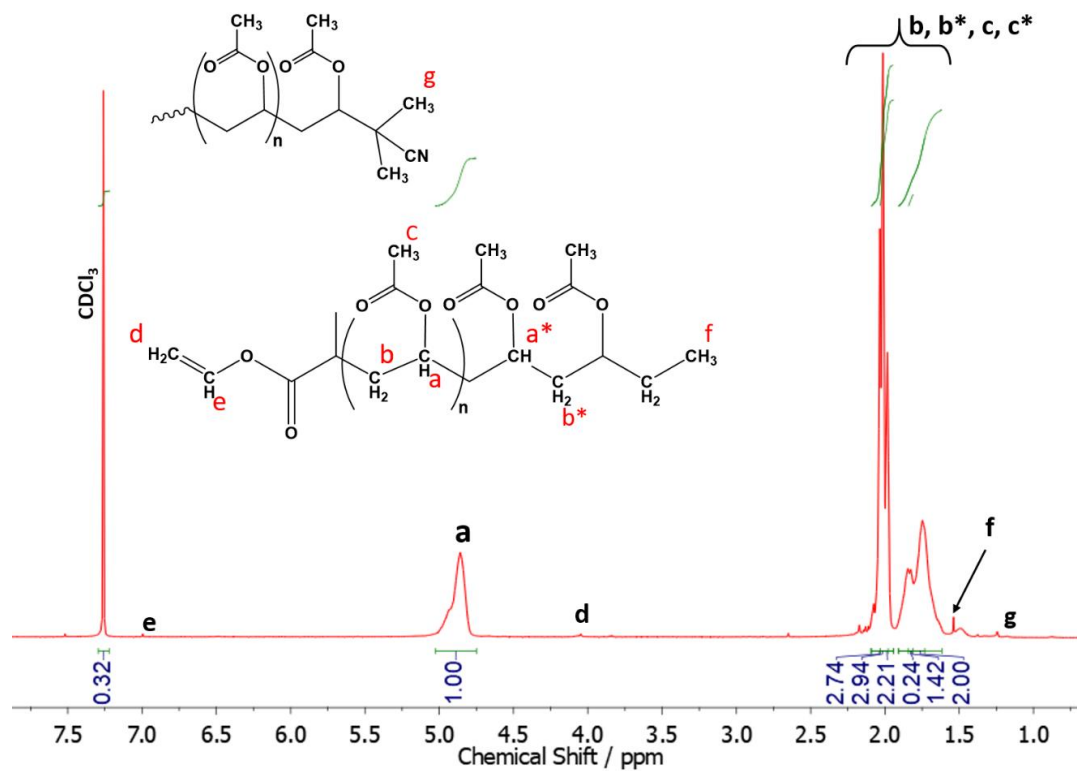


Fig A4.22:  $^1\text{H}$  NMR spectra of PVAc isolated from MOF with detailed assignments.



# Appendix

Absorbance band (cm <sup>-1</sup> )	Assignment
2973 and 2926	$\nu(\text{C-H})$
1729	$\nu(\text{C=O})$
1433	$\delta(\text{C-H})$
1370	
1225	$\nu(\text{C-O})$
1120	$\nu(\text{C-C})$
1018	
945	
795	$\delta(\text{C-H})$
632	
604	

Table A4.25: Characteristic absorbance bands and their assignments for PVAc.

Absorbance band (cm <sup>-1</sup> )	Assignment
2960	$\nu_{as}(\text{C-H})$
2900	$\nu_s(\text{C-H})$
1725	$\nu_s(>\text{C=O})$
1470 – 1485	$\delta_{ip}(\text{C-H})$
1415 – 1395	$\delta_{oop}(\text{C-H})$
1295 – 1275	$\nu_{as}(\text{O-C-O})$
1245 – 1235	$\nu_s(\text{O-C-O})$
1193	CH <sub>2</sub> Deformation
1163	
1047	$\delta(\text{C-O})$
940 – 960	

Table A4.26: Characteristic absorbance bands and their assignments for PCL.

# Appendix

Absorbance band (cm <sup>-1</sup> )	Assignment
3430	$\nu(\text{OH})$ from water
2930	$\nu_s(\text{C-H})$
1659	$\nu_s(\text{COO})$
1590	$\nu_{as}(\text{COO})$
1453	$\delta_{oop}(\text{C=O})$
1419	$\nu_{as}(\text{COO})$
1375	$\nu(\text{C=C})$
1252	$\nu(\text{C=O})$
1107	$\delta_{ip}(\text{C-H})$
935	$\delta_{oop}(\text{C-H})$
494	$\nu(\text{Cu-O})$
1617, 1545	$\delta(\text{OH})$ from water

Table A4.27: Characteristic absorbance bands and their assignments for HKUST-1.

		23 Na [He]		63 Cu [He]	
<i>Sample Name</i>	<i>Comment</i>	<i>Conc. [ ug/l ]</i>	<i>Conc. RSD</i>	<i>Conc. [ ug/l ]</i>	<i>Conc. RSD</i>
S-Blank		13.65	8.04	0.80	28.28
S-Blank		14.51	9.45	0.74	3.71
Sample 1	PVAc-KM185	24,086.53	3.59	1818.76	3.80
Sample 2	PVAc-KM186	23,383.12	0.81	1824.84	3.03
Sample 3	PCL-KM190	7,143.45	3.92	2,486.96	1.78
Sample 4	PCL-KM191	7,752.84	4.12	2,566.96	1.81
Sample 5	PCL-KM192	7,245.85	4.08	2,356.92	1.76

Table A4.28: ICP-AES analysis of isolated polymers from polymer@HKUST-1 composite.

# Appendix

		<b>23 Na [He]</b>		<b>66 Zn [He]</b>	
<i>Sample Name</i>	<i>Comment</i>	<i>Conc. [ ug/l ]</i>	<i>Conc. RSD</i>	<i>Conc. [ ug/l ]</i>	<i>Conc. RSD</i>
Sample1	KM205-PVAc	19,672.73	0.68	4,079.04	3.39
Sample1	KM205-PVAc	18,968.94	6.69	3,998.40	1.90
Sample2	KM206-PCL	8,152.84	4.39	2,686.96	2.10
Sample2	KM206-PCL	8,117.85	6.51	2,756.92	2.14

Table A4.29: ICP-AES analysis of isolated polymers from polymer@MOF-5 composite.

# Appendix

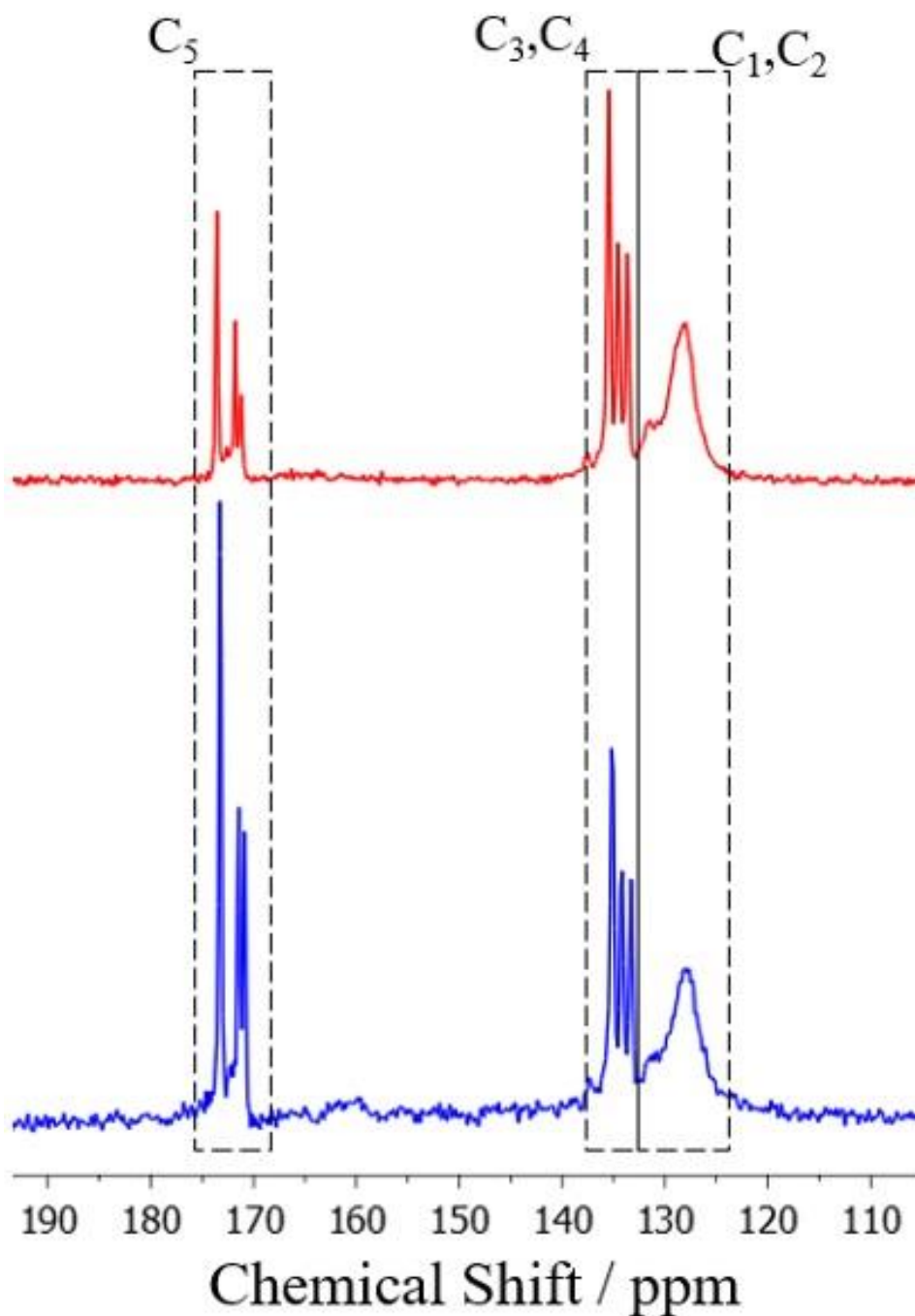


Fig A5.1:  $^1\text{H}$ - $^{13}\text{C}$  MAS NMR spectrum of MOF-5 (a) CP and (b) HPDEC. Expansion of the range 120 – 180 ppm is shown.

# Appendix

## A5.1: Data Processing in Gudrun.

### Sample Background

Sample background measurement is essential and must be made in every case. It is not possible to run Gudrun without these data files. Essentially, this measurement is taken with radiation beam on but with no sample container in the scattering position. Such a measurement captures the incident beam on the detectors which is later subtracted in the first step of the data analysis.

### Purge Detectors for Time-of-Flight Diffraction

The NIMROD instrument has 2,268 detectors positioned in large arrays and it is highly unlikely that each detector will be working for the duration of each sample run. Thus, it is essential that these detectors be removed at the time of data analysis. This is executed by running PURGE and must be performed prior to processing any data. Running PURGE produces a list of bad detectors as a **spec.bad** file and Gudrun excluded the number of detectors at the time of preparing the final differential cross-section. Further information about the PURGE process can be found in Section 3.3 in the Gudrun manual.<sup>2</sup>

### Calculation of Attenuation and Multiple Scattering Factors

To calculate the attenuation and multiple scattering factors, it is necessary to have the total cross section for materials of the samples and the containers. The sample cross-sections, provided that the attenuation and multiple scattering cross-sections are not too large, tabulated single atom values for scattering cross-section can be used with sufficient accuracy in place of their precise values. To a reasonable approximation, the neutron cross section is independent of neutron wavelength with the exception near nuclear resonance values and when the sample has strong Bragg scattering of significant elasticity effects, as with the case of H and D containing samples. Away from a resonance, the neutron adsorption cross-section is a linear function of wavelength.<sup>3</sup> The most recent tabulations were compiled by Sears in 1992, but many online resources are available including the NIST neutron cross-section database.<sup>4,5</sup>

# Appendix

## Deadtime Corrections

Counting detectors have an intrinsic deadtime ( $\tau$ ), which is the minimum time between the scattering events that is needed by the detector to classify two events as distinct events. Such a correction is executed before running the data analysis as one of the pre-set input parameters.

## Data Calibrations – Vanadium Background.

To define the diffraction data on an absolute scale, a vanadium sample is run as a background. Vanadium has a small coherent scattering length and thus, any distinct scattering from Bragg reflections are very weak compared to single atom scattering.<sup>6</sup> For data analysis, vanadium's atomic mass means that inelastic effects with the material will be small and can be estimated using an approximate model to model for the inelasticity.<sup>7</sup> Running the vanadium calibration sample before the analysis sample, using the same beam operation conditions allows a parallel comparison for background subtraction with accuracy.

## Data Processing

Upon placing the data on an absolute scale and assuming the multiple scattering and attenuation corrections have been estimated, it is possible to remove multiple scattering. The final step includes dividing by the number of atoms in the beam to give the differential scattering cross section of the sample per atom of the sample. For powdered or crystalline particles where the container is not fully packed with the sample, *tweak factor* is introduced as one of the input parameters on Gudrun. (Described at length in the next)

## Flat-plate Containers

The flat plate containers are made of a titanium-zirconium (TiZr) alloy. This alloy has a small coherent cross-section and takes advantage of the opposite phase of scattered neutrons by Ti and Zr. It is necessary to have materials that have no or negligible coherent cross-section to avoid Bragg reflections from the container that are difficult to subtract from the diffraction data.<sup>8</sup> The

# Appendix

difference in Bragg reflections arise because the front of the container facing the incident beam and the back of the container corresponds to slightly different scattering angles at the detectors. When the container is measured filled with sample following an empty run, the neutron attenuation by the sample causes the Bragg peaks from the front of the container to be attenuated preferentially compared to those from the rear, causing an apparent shift in the position of the peak, as seen at the detector.

Two cells with path length 1 mm and 2 mm were used during the experiment. Further details of the container cells is given in Table A5.2.

Path Length (mm)	Upstream and Downstream Thickness (cm)	Pressure Rating (bar)	Container Label
1	0.05	10	Cell B
			Cell C
2	0.1	10	Cell A
1	0.05	100	Cell D
			Cell H
2	0.1	100	Cell E
			Cell G

Table A5.1 Physical parameters of the flat-plate containers.

## Running Gudrun and input parameters.

GudrunN consist of tabbed windows consisting of one tab for each of INSTRUMENT, BEAM, NORMALISATION, and SAMPLE BACKGROUND. The INSTRUMENT tab allows to specify the number of parameters for a particular run and is specific to an instrument with the instrument. The BEAM tab allows to specify aspects of incident neutron beam, sample geometry, and the scattering detector. The sample container may be a CYLINDRICAL or a FLATPLATE

# Appendix

type of container and defines the sample geometry. There are different inputs that need to be defined for each of the cells, step sizes for the CYLINDRICAL attenuation and the number of slices for the FLATPLATE multiple scattering correction. ‘Normalisation’ in GudrunN refers to the process of data input on an absolute scale of the cross section per unit solid angle. For this purpose, a sample of vanadium of identical geometry as the sample is usually used due to its large and flat incoherent differential cross section ( $\sigma_{\text{inc}} = 5.07 \text{ barn}$ ).<sup>9</sup> NORMALISATION tab allows defining the data files for the vanadium data such as composition, dimensions, density, and its corresponding background files. For an experiment, there are only one set of INSTRUMENT, BEAM and NORMALISATION tabs and cannot be removed. SAMPLE BACKGROUND tab may be more than one for any given sample. The sample background may be different from the normalisation background which is the background with no sample or reference material in the beam, while the sample background may include the background from a furnace or cryostat, should the experiment call for such modifications.

The only parameters for the SAMPLE BACKGROUND tab are the data files which store the data for this background. Two additional types of tabs are possible, namely one or more SAMPLE tabs, and up to three CONTAINER tabs that would eventually contain the scattering data input files for each sample. The SAMPLE tab consists of the *.raw* data files. Along with the data files, the SAMPLE tab contains other input parameters that are specific to each samples:

1. The sample **Tweak Factor**: By definition, the tweak factor is the division of number of atoms in the beam to give a total differential cross section of the sample per atom of the sample. In essence, it is the reciprocal of the packing fraction, which affects the attenuation and multiple scattering: a packing fraction of 0.75 would translate into a tweak factor of 1.5. It should be noted that sample tweak factor and container tweak factor are two distinct values as it is used to modify the specific number density by dividing that density with the tweak factor. This modified density is employed to calculate the attenuation and multiple scattering corrections, as well as the number of atoms in the beam for the final normalisation of the cross section to barns per steradian per atom (b/sr/atom).

# Appendix

2. Normalisation correction factor is used as a correction that considers that the normalisation geometry may not be consistent with that of the sample. The final normalisation may either be ‘nothing’,  $\langle b \rangle^2$  or  $\langle b^2 \rangle$ .
3. The ‘top hat’ width is a number used to remove single atom background scattering before performing Fourier transform. If the value is negative, the final differential cross section is averaged from the  $Q$  value to the maximum  $Q$  value, and average level subtracted from the data prior to the Fourier. If the value is zero, there is no background subtraction and thus, no Fourier transform is performed.
4. Both  $h(r)$  and  $d(r) = 4\pi\rho rh(r)$  are produced following performing Fourier transform and give outputs with extension **.mgor01** and **.mdor01** respectively. The former gives the Fourier transform of **.mint01** which is the merged differential scattering cross section AFTER post processing using the top hat function and deconvoluting the function in real space that is defined in the SAMPLE tab. The latter gives the function  $4\pi\rho rh(r)$ .
5. The minimum and maximum radius used for cleaning up the Fourier transform,  $r_{min}$  and  $r_{max}$  respectively. The broadening of r-space, minimum and maximum wavelength of any resonance, and exponential amplitude and decay constants are described in the Gudrun manual.<sup>10</sup>

The CONTAINER tab consists of information regarding the dimensions, upstream and downstream thickness that is the path length of the cell, atomic composition for the material of construction of the cell. The cells are made of a titanium-zirconium alloy, taking advantage of the opposite phase of scattered neutrons by Ti and Zr. These materials are needed to avoid Bragg reflections from the container that may be hard to subtract at the time of data processing. The neutron attenuation from the sample that causes the Bragg peaks from the front of the container to be attenuated preferentially compared to those from the rear, causing an apparent shift in the peak positions in the detector. Hence, the container is measured empty first and then filled with

# Appendix

samples. By doing this, it is possible to subtract the scattering that arises from the container when empty, compared to when it is filled with samples.

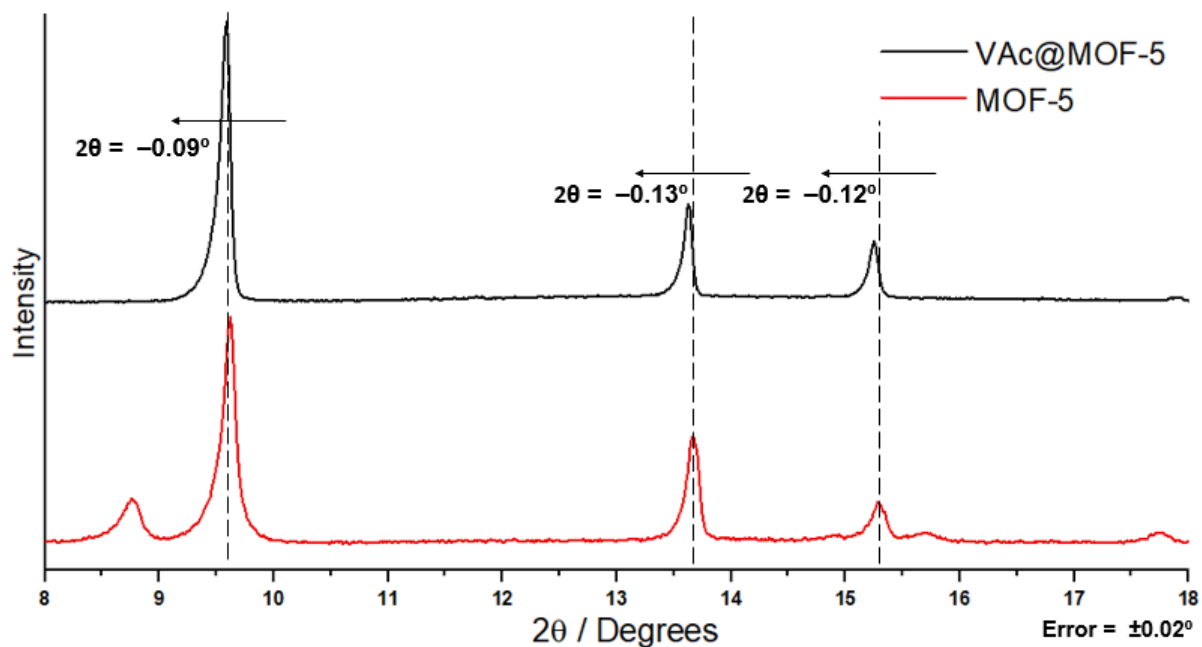


Fig A5.2: Expansion for PXRd pattern ( $2\theta = 8\text{--}18^\circ$  range) synthesised MOF-5 and VAc@MOF-5. Black arrows indicate the direction of shift for peaks.

# Appendix

## References

- 1 J. E. Mark, *The Polymer Data Handbook*, Oxford University Press, Oxford, vol. 1, Ed. 2, 2009.
- 2 ISIS Gudrun - Routines for reducing total scattering data, <https://www.isis.stfc.ac.uk/Pages/Gudrun.aspx>, (accessed January 7, 2021).
- 3 H. J. A. M. Heijmans, *Advances in Imaging and Electron Physics*, Academic Press, Massachusetts, Ed. 2, 2021.
- 4 V. F. Sears, *Neutron News*, 1992, **3**, 26–37.
- 5 Neutron scattering lengths and cross sections, <https://www.ncnr.nist.gov/resources/n-lengths/>, (accessed January 11, 2021).
- 6 G. W. Stanton, J. C. Dore and N. J. Hance, *Nucl. Instrum. Methods Phys. Res. A: Accel. Spectrom. Detect. Assoc. Equip.*, 1977, **141**, 259–261.
- 7 A. K. Soper, *Mol. Phys.*, 2009, **107**, 1667–1684.
- 8 J. R. Santisteban, L. Edwards, A. Steuwer and P. J. Withers, *J. Appl. Crystallogr.*, 2001, **34**, 289–297.
- 9 Vanadium - Neutron Scattering Lengths and cross sections, <https://www.ncnr.nist.gov/resources/n-lengths/elements/v.html>, (accessed January 8, 2021).
- 10 A. K. Soper, *RAL Report RAL-TR-2011-013*.